Instrumental progress to test General Relativity in the Galactic Center

Felix Benjamin Widmann

München 2022

Instrumental progress to test General Relativity in the Galactic Center

Felix Benjamin Widmann

Dissertation
der Fakultät für Physik
der Ludwig-Maximilians-Universität
München

vorgelegt von
Felix Benjamin Widmann
aus Stuttgart

München, den 08.09.2021

Erstgutachter: Professor Dr. Reinhard Genzel
Zweitgutachter: PD Dr. Ortwin Gerhard
Tag der mündlichen Prüfung: 08.11.2021

CONTENTS

LIST OF FIGURES

LIST OF TABLES

ZUSAMMENFASSUNG

Im Zentrum unserer Galaxie befindet sich das supermassereiche Schwarze Loch Sgr A* mit einer Masse von etwa vier Millionen Sonnenmassen. Es ist das uns nächstgelegene supermassive Schwarze Loch, und erlaubt uns Schwarze Löcher und ihren Einfluss auf die Umgebung zu studieren. Mehrere Dutzend Sterne befinden sich auf gebundenen Bahnen um dieses Schwarze Loch. Diese Sterne und ihre Bewegung um Sgr A* bieten die einzigartige Möglichkeit, die Allgemeine Relativitätstheorie in einem extremen Gravitationspotential zu untersuchen.

Diese Arbeit konzentriert sich auf die jüngsten Fortschritte in der astronomischen Instrumentierung und wie sie sich auf die wissenschaftlichen Entdeckungen aus dem galaktischen Zentrum ausgewirkt haben. Durch eine überarbeitete Datenreduktion und Kalibrierung verbessern wir die gemessenen Radialgeschwindigkeiten von Sternen. Außerdem verbessern wir die Messungen weiter, indem wir die optischen Aberrationen im interferometrischen Instrument GRAVITY berücksichtigen. Der dadurch entstandenen Datensatz der Umlaufbahn des Sterns S2 um Sgr A* ermöglicht uns die präziseste Entfernungsmessung zum galaktischen Zentrum, die je durchgeführt wurde. Wir verwenden diesen Datensatz auch um Abweichungen vom Einsteinschen Äquivalenzprinzips zu messen. Wir stellen fest, dass wir Abweichungen ausschließen können, die größer als 5 % sind. Dies findet in einem Potential Bereich statt in dem solche Messungen bisher unmöglich waren.

Im letzten Teil dieser Arbeit stellen wir Studien zur Verbesserung des GRAVITY-Instruments vor, wodurch wir neue Beobachtungsmodi zur Verfügung stellen. Wir zeigen eine umfangreiche Studie zur instrumentellen Polarisation in GRAVITY. Indem wir die instrumentellen Effekte kalibrieren, können wir GRAVITY als polarimetrisches Instrument einsetzen. Dies ist für die Untersuchung von Sgr A* von großer Bedeutung, da die Emission des Schwarzen Lochs stark polarisiert ist. In ähnlicher Weise kalibrieren wir einen weiteren Beobachtungsmodus, der es uns ermöglicht, direkte Astrometrie zwischen zwei Quellen durchzuführen, die sich nicht im selben interferometrischen Sichtfeld befinden. Mit diesem Verständnis systematischer Effekte und der Kalibrierung neuer Beobachtungsmodi ermöglichen wir bessere Beobachtungen des galaktischen Zentrums mit GRAVITY, da sie uns erlauben die Akkretionsprozesse um Sgr A* in Zukunft besser untersuchen. Dies wird unser Verständnis von supermassiven schwarzen Löchern und der Allgemeinen Relativitätstheorie weiter voran bringen.

SUMMARY

At the center of our Galaxy lies the supermassive black hole Sgr A* with a mass of around four million solar masses. It is the closest supermassive black hole known and offers an excellent opportunity to study black holes and their impact on their environment. Several tens of stars are on bound orbits around this black hole. These stars and their motion around Sgr A* offer a unique possibility to study General Relativity in an extreme gravitational potential.

This work presents recent improvements in astronomical instrumentation and how they have impacted scientific discoveries from the Galactic Center. We are able to significantly improve the measured radial velocities of stars by improving data reduction and calibration of the spectrograph SINFONI. We further improve the measurements by considering optical aberrations in the interferometric beam combiner, GRAVITY. By modeling and calibrating these aberrations, we refine the dataset of the orbit of the star S2 around Sgr A*. With these improvements, we achieve the most precise distance measurement to the Galactic Center to date. We subsequently use the dataset to constrain violations of the Einstein Equivalence Principle. We can exclude violations larger than 5 % in a mass regime, for which no such test has been possible before.

In the last part, we present work to improve the GRAVITY instrument and make new observing modes available to better study the physics around supermassive black holes. We show an extensive study of the instrumental polarization of GRAVITY. By calibrating the instrumental polarization effects, we open up the possibility of using GRAVITY as a polarimetric instrument. This is of great importance for the studies of Sgr A* as the emission from the black hole is highly polarized, and adding polarimetry to the unique sensitivity of GRAVITY allows us to better study the accretion processes around Sgr A*. Similarly, we calibrate another observing mode, which allows us to do direct astrometry between two sources that are not in the same interferometric field of view. The better understanding of systematic effects and the calibration of new observing modes developed as part of this thesis will allow us to further sharpen our understandings of supermassive black holes and General Relativity.

Part I

SETTING THE STAGE

1 SCOPE OF THIS THESIS

The very center of our Galaxy is the home of a supermassive black hole inside a dense cluster of stars. The black hole is called Sagittarius A*, is at a distance of around 28 thousand light-years, and has a mass of four million solar masses. It is the closest supermassive black hole and offers many possibilities to study the black hole and the influence on its surroundings. The Galactic Center has been studied for over forty years and has proven that black holes do indeed exist. A primary driver for a better scientific understanding of Sagittarius A* and its surroundings has been the improvement of existing instrumentation and development of new instruments.

The work collected in this thesis shows how improvements in the understanding of instrumental effects can lead to immense scientific progress. To demonstrate this I divided the thesis into three main parts:

- This thesis starts with a brief introductory part about the Galactic Center and the instruments that are discussed in the following: SINFONI and GRAVITY (chapter 2 and chapter 3)
- The second part presents two examples of how instrumental progress opens the possibility for new results. I show the improvements in radial velocity measurements with SINFONI (chapter 4), which was an essential factor for the precise measurement of the distance to Sagittarius A* (chapter 5). This distance measurement is improved even further with the correction of optical aberrations, as presented in chapter 6. The second part is concluded with the test of the Equivalence Principle in chapter 7, which was only possible due to the improvements in data reduction and analysis.
- The third part of this work gives an outlook and shows how we can offer new observation modes with GRAVITY by understanding systematic effects. We study the instrumental polarization in chapter 8 to enable polarized observations with GRAVITY. Chapter 9 outlines the calibration of optical aberrations needed for a dual-beam astrometric measurement with GRAVITY.

THE GALACTIC CENTER 2

The center of our Galaxy offers the possibility to study processes in galactic nuclei and the effects a supermassive black hole has on its surroundings. The Galactic Center hosts a dense star cluster, several different gas streams, and the supermassive black hole Sagittarius A* (hereafter Sgr A*) in the very center (Genzel et al., 2010). The most dominant gas feature is a bundle of ionized gas streams, which orbit Sgr A* and is called the *minispiral* (see e.g. Lo and Claussen, 1983; Paumard et al., 2004; Zhao et al., 2009; Tsuboi et al., 2017). The minispiral is surrounded by the *circum-nuclear disk*, a dense ring of molecular gas with a size of approximately 3 parsec (pc) (see e.g. Becklin et al., 1982; Guesten et al., 1987; Christopher et al., 2005; Montero-Castaño et al., 2009). Within that ring sits the nuclear star cluster (see Figure 2.1 and Genzel et al., 2010). This cluster is composed of late-type giants and supergiants but also contains a comparably large number of early-type stars. This was a surprising finding as it is not clear whether the young stars formed around the supermassive black hole or were brought in there by other processes. The origin of the young stats is still an ongoing debate, labeled as *the paradox of youth*. Several of these stars seem to be on an ordered rotation in a clockwise disk around the black hole (Lu et al., 2006; Lu et al., 2009), but also other disk features have been discovered (Bartko et al., 2009; Bartko et al., 2010; Yelda et al., 2013). The dynamical structure is a result of the formation from an infalling cloud of gas approximately six million years ago (Bonnell and Rice, 2008; Hobbs and Nayakshin, 2009). Within the central arcsecond around Sgr A* the stellar picture changes yet again as there are several tens of so-called *S-stars* which are on close orbits around the black hole. They do not show an ordered rotation but have isotropically distributed orbits (Gillessen et al., 2009a; Gillessen et al., 2017). The connection of the different components of gas and stars, the origin of the different populations of stars, and the influence of Sgr A* on all the components is a rich research field in the Galactic Center science.

For this work I focus predominately on the supermassive black hole itself and on the S-stars around it. The central object was first discovered as a compact radio source by Balick and Brown, 1974. During the following years, the size of the emission region was constrained, by very long baseline interferometry to around 40 µas (Krichbaum et al., 1993; Shen et al., 2005; Doeleman et al., 2008; Bower et al., 2014; Issaoun et al., 2019). It was also found that the radio source Sgr A* shows no intrinsic motion in comparison to extragalactic sources (Reid and Brunthaler, 2004; Reid, 2009), which constrains the mass to above $4 \cdot 10^5$ solar masses.

At the end of the 1970s the group of Charles Townes started observing the innermost parsec of the galaxy in the mid-infrared (see e.g. Wollman et al., 1977; Lacy et al., 1980). They used spectroscopy to measure the velocity of ionized gas components. Analyzing the gas motions in these observations, they found that the core of the Milky Way must contain a mass of 3-4 million solar masses. It was at that time concluded that this mass could be a central massive black hole (Crawford et al., 1985), an idea developed earlier by Lynden-Bell and Rees, 1971. Two groups later supported this conclusion with the help of near-infrared imaging of the Galactic Center stars. Our group at MPE in Germany, first used the 3.5 m New Technology Telescope (NTT) and later the 8 m Very Large Telescope (VLT) to determine proper motions of stars as close as 0.1 arcseconds (as) to Sgr A* (Eckart and Genzel, 1996; Eckart and Genzel, 1997). We used speckle imaging for these first near-infrared observations, which is a very short exposure imaging technique. Speckle imaging became available at that time due to new developments in infrared detectors. A second group at UCLA came to a similar conclusion using the 10 m Keck telescope (Ghez et al., 1998). Both groups concluded that there must be a massive central object of several million solar masses, with the mass contained in a small region. This mass coincidences with the emission of the radio source Sgr A* to the accuracy of the coordinate system of 10 mas (Reid and Brunthaler, 2004; Reid, 2009). These findings of a massive central mass made any other explanation than a supermassive black hole unlikely.

The next step by both groups was to determine individual stellar orbits close to Sgr A*. With the implementation of adaptive optics (AO) at both the Keck observatory (Wizinowich et al., 2000) and the VLT (Rousset et al., 2003), both groups reached diffraction limited imaging. Even more substantial progress was made with the use of AO-supported spectroscopy as it allowed radial velocity measurements of the stars around Sgr A*. This is true for the long slit spectroscopy in case of the UCLA group (Ghez et al., 2003a), but even more so for the integral field spectroscopy, used by the MPE group (Eisenhauer et al., 2003). In 2005 OSIRIS was commissioned on the Keck telescope, which allowed the UCLA group to also use integral field spectroscopy in the Galactic Center. With the combination of astrometry and spectroscopy, it soon became possible to measure the orbits of individual stars around the central source. These very first orbits led to the firm conclusion that Sgr A* is indeed a supermassive black hole with a mass of around four million solar masses (Schödel et al., 2002; Schödel et al., 2003; Ghez et al., 2003a; Ghez et al., 2005; Eisenhauer et al., 2005).

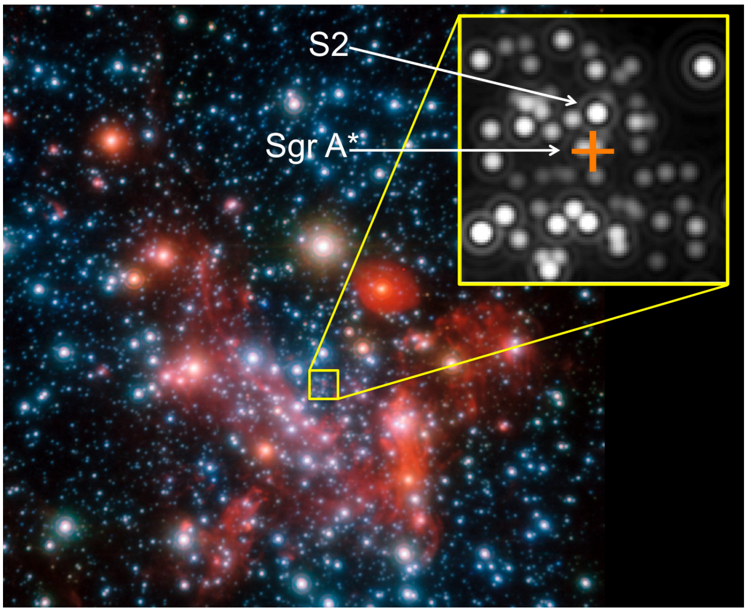

Figure 2.1: The inner region of the Galactic Center with the stellar star cluster. The inset shows Sgr A* and the close S-stars. Credit: ESO/MPE/S. Gillessen et al.

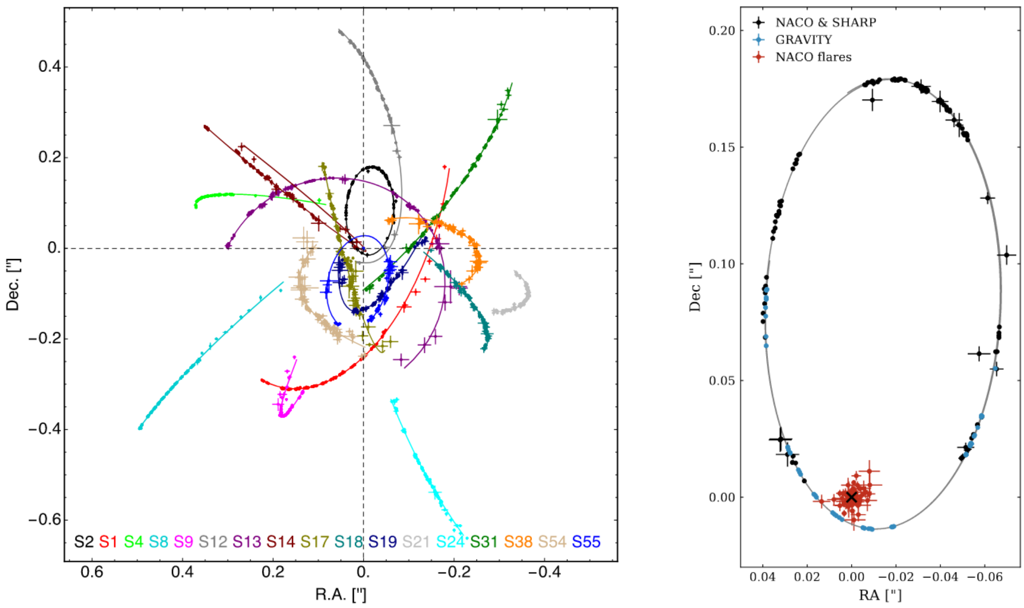

Figure 2.2: Orbits of the Galactic Center stars around Sgr A*. The left figure shows the 17 closest stars of the ones with known orbits, from Gillessen et al., 2017. The right figure shows the well known orbit of S2 from Gravity Collaboration et al., 2020a

The work of both groups has continued since. This led to the determination of over 40 individual orbits by now (Gillessen et al., 2017; Boehle et al., 2016). Figure 2.2 shows the orbits of the innermost stars. Another step forward in the astrometric measurements was made with the implementation of the interferometric instrument GRAVITY at the Very Large Telescope Interferometer (VLTI) (Gravity Collaboration et al., 2017). With the combination of the four 8 m telescopes at the VLT, GRAVITY can regularly achieve an astrometric precision of 50 µas, an improvement of roughly a factor of 10 in comparison to the best results from AO supported single-dish astrometry. However, the unique astrometric power of GRAVITY is not the only improvement. With the sensitivity and resolution of GRAVITY, it is possible to disentangle Sgr A* from other sources and observe emission from Sgr A* at almost all times (Gravity Collaboration et al., 2020e). The improved resolution also reduces the possibility of obtaining biased astrometric stellar positions due to confusion with other sources, which leads to a better orbit determination of the observed stars.

The best-known star in the central region is the star S2 (or S-02 in UCLA nomenclature). S2 is a massive star with an apparent magnitude of 14.2 in the astronomical K-Band (2.0 µm to 2.5 µm) (Martins et al., 2008). It orbits the central source every 16 years and has been observed regularly for 28 years (see right panel of Figure 2.2). S2 opens up the possibility to use the Galactic Center as a laboratory to study fundamental physics around a supermassive black hole. When we consider the star as a test particle in the extreme gravitational potential, it allows us to study the effects of general relativity on the stellar orbit. The first of those effects is the gravitational redshift, which results in a deviation from the emission one would expect in a purely Keplerian field. The redshift is in these experiments usually parameterized as an f-factor, which is zero for a pure Keplerain measurement and one if the measurement agrees with the redshift expected from general relativity. Both teams discovered the gravitational redshift in the data of S2, where we measured it as $f = 0.90 \pm 0.09|_{stat} \pm 0.15|_{sys}$ (Gravity Collaboration et al., 2018b) and the UCLA team as $f = 0.88 \pm 0.17$ (Do et al., 2019). With the addition of more astrometric data-points from the GRAVITY interferometer we improved this significance to $20\,\sigma$ in Gravity Collaboration et al., 2019. With the capabilities of GRAVITY, it was also possible to measure another effect of general relativity, the Schwarzschild precession, in the orbit of S2 (Gravity Collaboration et al., 2020a). The gravitational redshift and the Schwarzschild precession follow the predictions of general relativity and show that the Schwarzschild metric can describe the orbits of the stars around the black hole.

The orbits of the stars around Sgr A* and the relativistic effect in the orbits combined constitute the current best evidence of the existence of a supermassive black hole. This research led to the awarding of the Nobel Prize in Physics in 2020 to Reinhard Genzel and Andrea Ghez for *"for the discovery of a supermassive compact object at the centre of our galaxy"*.

While the results from the Galactic Center over the last decades have been spectacular, there are many discoveries still to come. With the current interferometric observations from the VLTI, there is still a lot to study in the Galactic Center. We are continuously pushing GRAVITY to new limits as we understand the instrument better. With the improved understanding, we can limit the uncertainties due to systematic effects. Furthermore, the Galactic Center offers so many more possibilities to study general relativity and black hole accretion.

In Gravity Collaboration et al., 2018a and Gravity Collaboration et al., 2020c we have shown that we can measure orbital motions of matter at few gravitational radii distance around Sgr A* with GRAVITY. These motions occur during the flaring state of the black hole and probe the accretion flow close to the event horizon. By analyzing those flares with orbital motions we can constrain the properties of the accretion flow as well as the properties of the black hole itself. An important tool for the analysis of the flares is the polarimetry, as shown in Gravity Collaboration et al., 2018a and Gravity Collaboration et al., 2020b. Polarimetry helps us to understand the observed data of Sgr A* as well as to probe the magnetic field around Sgr A*, which is closely coupled to the accretion processes. We developed a full calibration of the polarimetric observing mode of GRAVITY, which will help us to better analyze the polarimetric data from GRAVITY.

We are also discovering even fainter stars (Gravity Collaboration et al., 2021) in the vicinity of Sgr A*. To study those faint stars on their orbits and to better observe the Sgr A* flares, we need a new observing mode, which is currently still dominated by systematic effects. With the calibration of the known systematic effects it becomes possible to study stars further out and reach the highest possible precision with GRAVITY.

With the results from the last years and the ongoing science projects, the Galactic Center maintains its status as a unique laboratory for general relativity and black hole accretion. It allows us to learn more about the closest supermassive black to us and to study the effects of general relativity in stellar orbits. Over the last 40 years, the progress in the Galactic Center science has been closely coupled to the advancement in instrumentation and continues to do so. This thesis shows how the two are coupled and what future possibilities we will have with an increased understanding of the instruments used.

3 INSTRUMENTS

The work in this thesis is based to a large degree on improvements to the instruments SINFONI and GRAVITY. SINFONI is an integral field spectrograph with which we derived the radial velocities of the stars in the Galactic Center. GRAVITY is an interferometric beam combiner used to get the positions of the stars closest to the black hole in the Galactic Center. The following section will shortly present both of those instruments, their main working principle and the subsystems relevant to this work.
Apart from GRAVITY and SINFONI, much Galactic Center data was taken with the near-infrared imager NACO at the VLT. NACO is not as precise as GRAVITY but has a much larger field of view and was used to get the positions of many stars over a large area. NACO was the first instrument to observe the Galactic Center with adaptive optics. It was the main instrument for astrometry (measuring positions for objects on sky) for almost twenty years and played a crucial role in the determination of stellar orbits around Sgr A*. As NACO is less relevant for this work, I will focus on GRAVITY and SINFONI.

3.1 SPECTROSCOPY WITH SINFONI

The first instrument I introduce is SINFONI, the instrument we used to measure the radial velocities of stars. SINFONI is a combination of an AO module and the integral field spectrograph SPIFFI (Eisenhauer et al., 2003; Bonnet et al., 2004). SPIFFI was installed at the Very Large Telescope (VLT) in 2003, and the AO module was added a year later. SINFONI was decommissioned in 2019, and SPIFFI is currently being upgraded to become a part of the new instrument ERIS (Davies et al., 2018).

An integral field spectrograph produces 2D spatially resolved spectra of the target region. For the Galactic Center this means that one can observe a field of 0.8 x 0.8 arcseconds and gets a spectrum of each star in the field (for an example of a typical Galactic Center observation with SINFONI see Figure 3.1).

The working principle of SINFONI as an integral field unit is illustrated in Figure 3.2. SINFONI works with an image slicer consisting of 32 plane mirrors (Tecza et al., 2000). Those mirrors cut the field into 32 slices and align them next to each other to form a long slit. This sliced image is then spectrally

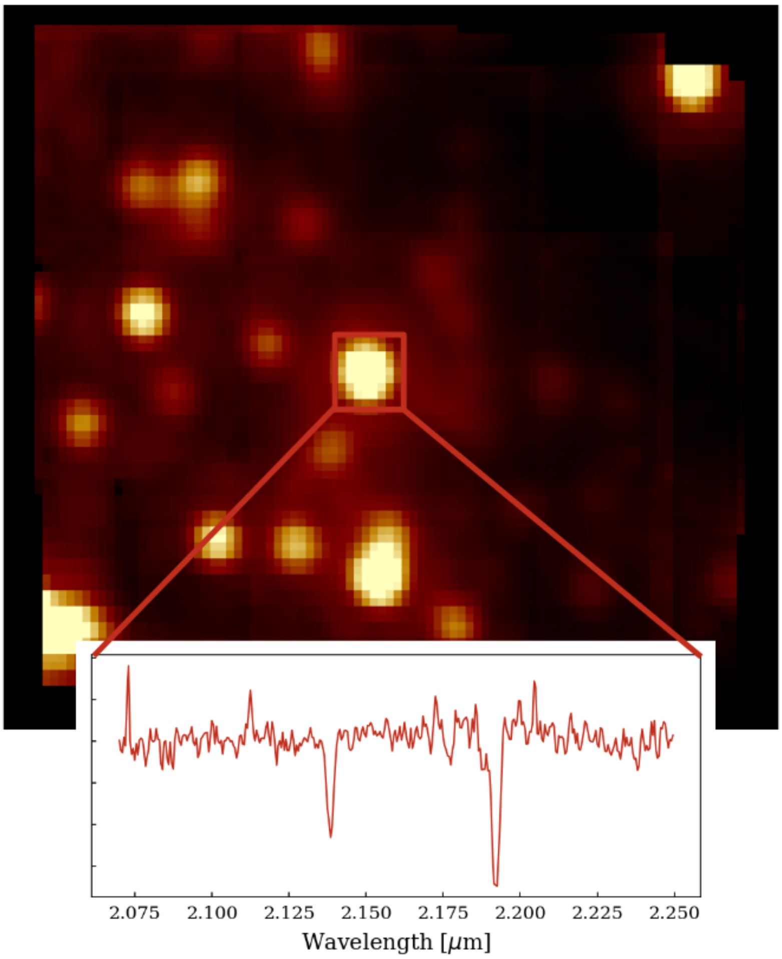

Figure 3.1: Example of a Galactic Center observation with SINFONI. The field of the integral field spectrograph is shown on top and the insert shows the extracted spectrum for the star S2.

resolved with a grism. The result is then 32*64 individual spectra which are measured with a detector. In the data processing, the individual spectra can be extracted and transformed into a 3D cube with two spatial coordinates and the third dimension containing the spectrum of each pixel in the image.

For the measurement of the velocity of a star, one selects the pixels in which the star's signal is present and averages them. For the background correction on uses pixels without any stellar signal and subtracts them from the averaged star signal. This gives a stellar spectrum as shown in Figure 3.1. The example spectrum is of the star S2, which shows clear emission features from Hydrogen and Helium. To get the velocity, one needs to measure the wavelength at which the spectral features occur in the observed spectrum λ and compare them to

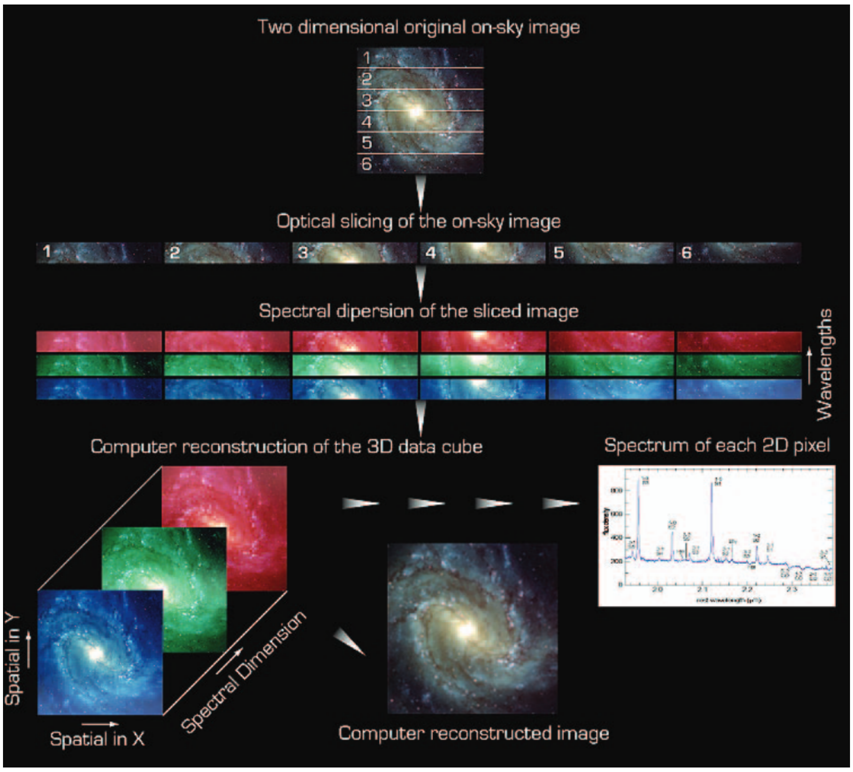

Figure 3.2: Principle of an observation with SINFONI (from Bonnet et al., 2004)

the rest wavelengths of the same features in a vacuum λ_0. The radial velocity is then calculated with the simple Doppler formula:

$$v_r = \frac{\lambda - \lambda_0}{\lambda_0} \cdot c \tag{3.1}$$

The measurement of λ can be either done with a simple Gaussian fit or with the comparison to a template spectrum (for more details, see chapter 4). The Doppler formula used for the Galactic Center stars (Equation 3.1) does not involve any relativistic effects, as they are part of the model of the orbit, which is then fitted to the data (for more details, see Lindegren and Dravins, 2003 or the discussion in the appendix of chapter 6).

Over the 15 years of its lifetime, SINFONI was a workhorse for Galactic Center observations. For the target S2 alone, it produced 94 data points and was a crucial part in the detection of the gravitational redshift on the orbit of S2 around Sgr A* (Gravity Collaboration et al., 2018b). Chapter 4 describes the improvements we made to the SINFONI data reduction and the extraction of velocities from the measured spectrum. This work ultimately brought the SINFONI precision to the level needed for its data to play a role in the extremely precise distance measurement to the Galactic Center (chapter 5) and to enable the first-ever test of the Einstein Equivalence principle close to a supermassive black hole (chapter 7).

3.2 INTERFEROMETRY WITH GRAVITY

To measure the position of sources on the sky (the astrometry), we use the interferometric beam combiner GRAVITY. I start this section with a short summary of the general concept of interferometry before discussing the properties of GRAVITY itself and how we use it to observe the stars and the black hole in the Galactic Center.

3.2.1 PRINCIPLE OF INTERFEROMETRY

The spatial resolution of a telescope corresponds to the smallest angular separation at which two objects can be distinguished from each other. The resolution of a single telescope is limited by the size of the aperture. A telescope's aperture alters the incoming light wave, which directly relates to the resolution of a telescope. For a single telescope the resolution is given by

$$\Delta\Theta = 1.22 \cdot \frac{\lambda}{D}. \tag{3.2}$$

This fundamental limit can be overcome by not using a single telescope but an array of telescopes. The principle of such an interferometer is closely related to the double-slit experiment by Thomas Young from the year 1802: If coherent light from a point source passes two slits, an interference pattern will occur. This effect was originally used to prove the wave nature of light, as the interference pattern is due to two electromagnetic waves, propagating from the two slits and reaching the screen with different relative path lengths. These different path lengths then lead to constructive or destructive interference for the different positions along the screen. The intensity distribution for the two slit of a single point source is given by:

$$I \propto (1 + \cos(k\alpha B)) \tag{3.3}$$

where α is the angle between the straight line from the two slits and the observed point at the screen. k is the wavenumber, and B the separation of the slits. In the case of an astronomical interferometer the resolution of the observation is given by the angle at which one moves half a fringe on the detector. Following Equation 3.3 this is given by:

$$\Delta\Theta = \frac{\lambda}{2B} \tag{3.4}$$

where B is the baseline, which is the distance between two telescopes. The resolution of an interferometer is not dependent on the telescope's diameter but on the distance between the telescopes, which is usually much larger. Interferometers overcome the fundamental resolution limit of single-dish telescopes. The disadvantage is that an interferometer does not directly provide images or spectra as a single dish telescope. The observable in the case of an interferometer is the complex visibility.

The measured complex visibility of an interferometer is given by the Van Cittert-Zernike theorem. It states that the intensity distribution of the source on sky and the complex visibility as a function of the baseline are connected with a Fourier transformation (For a full derivation of this theorem see e.g. Monnier, 2003; Glindemann, 2011; Thompson et al., 2017). For monochromatic star light one can then write the interferometer response of a source in the source plane as the complex visibility $V(u, v)$, given by the Fourier transformation of the brightness distribution $I(x, y)$ on sky. The Van Cittert-Zernike theorem is given by the following equation:

$$V(u, v) = |V|e^{-i\phi} = \frac{\int\int dxdy I(x, y) e^{-i2\pi(xu+yv)}}{\int\int dxdy I(x, y)} \tag{3.5}$$

The complex visibility V is usually measured in the (u,v)-plane which is parallel to the sky plane (x,y) and contains the projected baseline. Each baseline and spectral channel defines one point in the (u,v)-plane at which the interferometer measures the complex visibility.

It follows that the visibility is a two-dimensional Fourier transformation of the position on the sky, weighted with the intensity at this position. With the measured visibility one can then either use model fitting to the data to infer the source distribution on sky or use an inverse Fourier transformation to get the image of the sky. The second approach is usually done in interferometric imaging, but is difficult due to the the incomplete information in the (u,v)-plane (Högbom, 1974; Monnier and Allen, 2013). For the work in this thesis only the approach of model fitting to the observed data is used.

Observables in interferometry: The observed complex visibility can naturally be divided into two observables. The first one is the visibility amplitude, which carries the information about the fringe contrast. For a point source, the visibility amplitude is constant at one, while it drops off towards longer baselines for extended sources. In the work I present here, we often use model fitting to the visibility amplitudes. For example, we calculate the expected amplitude for a binary system and then fit the separation and brightness of the two sources to the data.

The second observable is the visibility phase, which is apart from the increased resolution the second significant advantage of an interferometer. In contrast to a single-dish telescope, it is possible to measure phase information with an interferometer. The fringe phase includes information about the spatial structure of the observed source, as well as information about the position of the source on the sky. This allows us to do astrometry with an interferometer. The main issue of phase measurements with an interferometer is that the atmosphere and internal variations in the interferometer influence the measured phase. There are usually two ways to overcome this limitation: either to phase reference the observed phases to a known point source or to not use absolute phase but the so-called closure phase.

The closure phase is the simpler way to measure accurate phases. It is calculated for a triangle of three telescopes by adding up the phase measurement of three baselines, which then form a triangle:

$$\Phi_{1,2,3} = \Phi_{1,2} + \Phi_{2,3} + \Phi_{3,1} \tag{3.6}$$

The significant advantage of the closure phases is that all errors which occur at one individual telescope drop out in Equation 3.6. The measurement is insensitive to variations in the light path of one telescope or aberrations in the atmosphere. In general, the closure phases of a symmetric source are zero and become non-zero for asymmetric source distributions (for more information see e.g. Monnier, 2003; Monnier and Allen, 2013). The disadvantages of the closure phase measurements are that one only gets one measurement for each triangle of telescopes and not for each baseline, as usual for the visibility measurements. This decreases the number of measurements, especially for interferometers with a small number of telescopes. The second significant disadvantage is that the measurement is translation invariant. In the case of the VLTI one gets four closure phase measurements from the six baselines. This means that we can only do relative astrometry of sources that are observed in one beam at the same time. For an astrometric measurement of a single source, we need to go to phase referenced observations.

The second possibility to overcome the instrumental and atmospheric influences on the phase is the phase-referenced observing (see e.g. Shao and Colavita, 1992). In this mode, a point source is observed simultaneously with the science target, and an internal metrology system monitors the changes in the optical path between the two light paths. This is an ability that the GRAVITY instrument offers. The phase referenced observing is the most complex observing mode for GRAVITY.

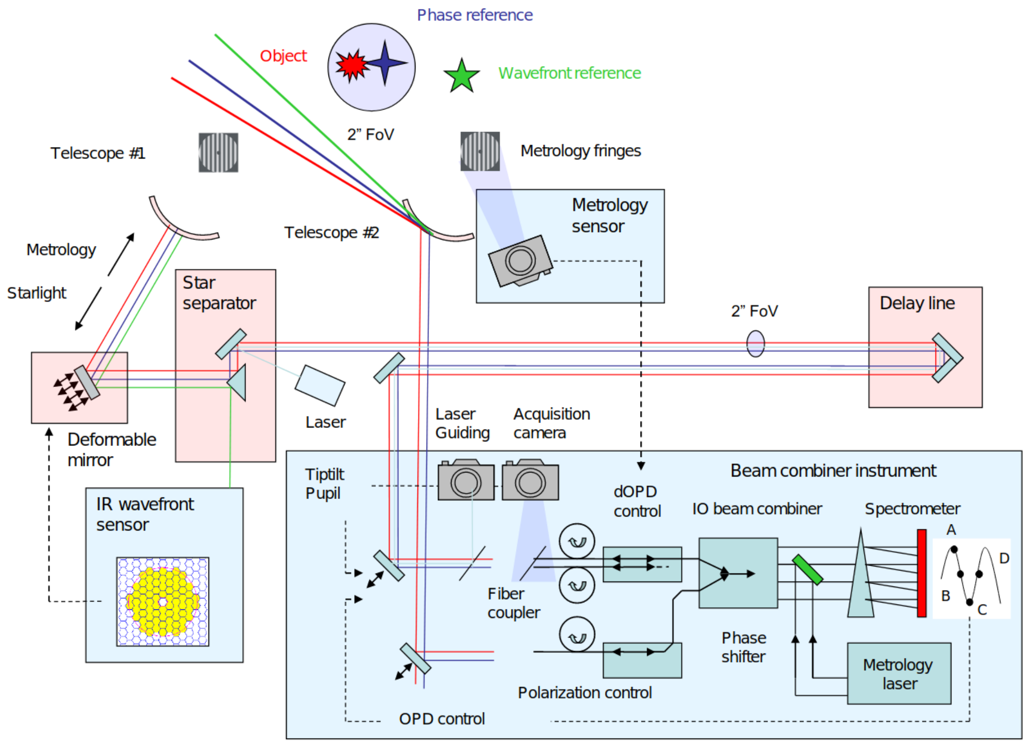

Figure 3.3: Schematic overview of the GRAVITY instrument with the working principle illustrated for two telescopes. The light path of the three observed object is shown in different colors: the science object in red, the phase reference in blue, and the AO target in green. The different subsystems of GRAVITY are shown in the blue shaded boxes and the used VLTI infrastructure in the orange shaded boxes (from Gravity Collaboration et al., 2017)

.

3.2.2 GRAVITY

GRAVITY is an interferometric beam combiner located at the Very Large Telescope Interferometer (VLTI) in Paranal, Chile (Gravity Collaboration et al., 2017). It operates in the astronomical K-Band between 2.0 µm and 2.5 µm. GRAVITY can be used to combine either the light of the four 8.2 m Unit Telescopes (UTs) or the four 1.8 m Auxiliary Telescopes (ATs). With baselines up to 130 m, the maximum spatial resolution of GRAVITY is on the order of 3 mas as given by Equation 3.4. The goal of GRAVITY was to provide phased referenced astrometry and imaging of targets fainter than 16 m_K, much fainter than for any other optical interferometer.

The basic principle of GRAVITY with all its subsystem is shown in Figure 3.3: In a typical observation, three targets need to be specified. One has to select a bright star for the adaptive optics (AO) system, a point source for the fringe-tracker (FT) to phase reference, and a science target. The light of the AO target is separated from the science beam by the star separator at the telescope level and then fed into an AO system. For the UTs, the AO is done either by the MACAO system in the visible (Arsenault et al., 2003) or the CIAO system in the near-infrared (Kendrew et al., 2012). Both systems are located in the Coudé room below the UTs. In the case of the ATs, the AO system NAOMI is used, which operates in the optical (Woillez et al., 2019).

The second light beam is brought to the VLTI delay lines. This light then enters GRAVITY with a field of view of 2 as for the UTs and 4 as for the ATs. At the GRAVITY beam combiner entrance is a K-mirror, which derotates the field, followed by a half-wave plate that ensures a stable polarization input or enables the possibility to do polarimetry with GRAVITY. In the fiber coupler, the light of the science and FT targets is then split and coupled into individual fibers (Pfuhl et al., 2014). Those run to the fiber control unit where rotators align the polarization for maximum fringe contrast, and fibered delay lines that can be stretched to compensate for differential optical delays between the FT and science target. After that, the interference happens in an integrated optics chip (Jocou et al., 2014; Perraut et al., 2018). The fringe-tracking light is then brought to the fringe-tracking detector, which runs with a frequency up to 1 kHz and measures the phase and group delay. The fringe-tracker is used to measure the optical path difference (OPD) between two telescopes, which is primarily due to atmospheric turbulence (Lacour et al., 2019). This OPD is then compensated via the delay lines in the VLTI and piezo mirrors in GRAVITY (labeled as OPD control in Figure 3.3). This compensation of the OPD enables a stable fringe detection in GRAVITY and allows for arbitrarily long integration times on the science target. The science light is measured with a different detector. It can be used with three different grisms with a resolving power of 22, 500, or 4500.

Several more subsystems are running in GRAVITY to allow for a full phase referencing between the fringe-tracking and the science light. A pupil laser is launched from the four spiders of each telescope and is detected by the acquisition camera in GRAVITY (Amorim et al., 2012). With the help of a 2x2 Shack-Hartmann sensor, GRAVITY tracks the lateral and longitudinal movement of the pupil. The pupil motion is then in real-time corrected by the internal pupil actuators in the fiber coupler and by the curvature mirror in the VLTI delay line. This enables a stable pupil position during an observation.

A second subsystem is the metrology system (Lippa et al., 2016). A laser at 1908 nm is launched in the fiber coupler and follows the light path of the science and FT light backward. The interference pattern between the science and FT part of the metrology laser is then measured by photodiodes on the spiders of each UT. These measurements allow to measure the differential optical path difference (dOPD) between the two beams and are crucial to phase reference

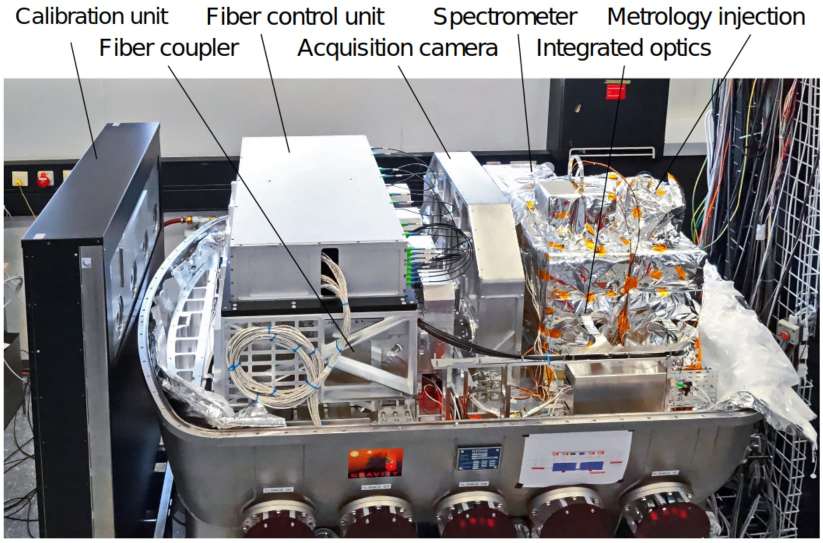

Figure 3.4: Picture of the open GRAVITY beam combiner with an overview of the different subsystems (from Gravity Collaboration et al., 2017)

.

the science light to the fringe-tracking measurement. A picture of the open cryostat of GRAVITY with all its subsystems is shown in Figure 3.4.

GRAVITY had its first light in 2017 and has since been producing exceptional results in several fields. In the Galactic Center, as well as for the observation of exoplanets in the off-axis mode, where the science target is separate from the fringe-tracker, GRAVITY can reach an astrometric precision of the order of 30 µas. In terms of sensitivity, we could show that we can successfully detect stars as faint as 19.8 m_K (Gravity Collaboration et al., 2021).

3.2.3 GRAVITY AND THE GALACTIC CENTER

For observations of the Galactic Center, the full potential of GRAVITY is used by observing in the so-called off-axis mode. In this mode, we use a dedicated fringe-tracking star and also a separate AO star, as shown in Figure 3.5. As the AO target, we use IRS7, a 6.5 m_K star. IRS7 is observed with the CIAO adaptive optics system. We have several possible stars for the fringe-tracking target but usually use IRS16C, a single star with a magnitude of 9.7 m_K. With this star, we are well above the fringe-tracker's sensitivity limit, which ensures stable fringe-tracking in good conditions. In the off-axis case, we then can point to targets within a 2 as range from the fringe-tracker. This mode allows us to directly observe the flux variable black hole Sgr A*.

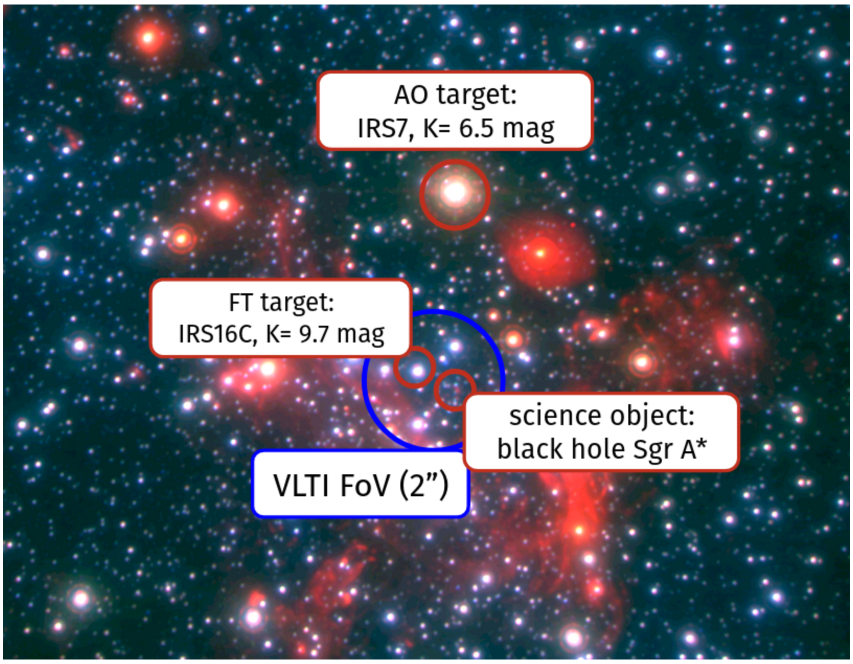

Figure 3.5: Explanation of the observing mode for GRAVITY in the Galactic Center

With GRAVITY, we get different observables and can get astrometric measurements in different ways. When there are several targets in the field of view of the science fiber, we can use model fitting to find the distances between the sources (see e.g. Gravity Collaboration et al., 2020e). This fitting is usually done to the visibility amplitude and the closure phases. As these observations use the entire field of view, they are affected by field-dependent aberrations in the optical path. We demonstrate with the measurement of the distance to the Galactic Center that we get reliable measurements when calibrating for those effects. If there is only one source in the field of view, the closure phases are zero, and the visibility amplitudes are one. Therefore, we cannot use those quantities to get an astrometric measurement. In this case, we have to use the visibility phases referenced to the fringe-tracking star. This referencing is done with the help of the GRAVITY metrology system, which again can be influenced by aberrations in the light path. In order to enable the phase referenced astrometry as an individual observing mode, we, therefore, need another set of calibration measurements (more details in chapter 9).

Part II

DECISIVE ROLE OF CORRECTING INSTRUMENTAL EFFECTS TO STUDY GENERAL RELATIVITY

4 REVISED RADIAL VELOCITY MEASUREMENTS

To measure the orbit of a star in three dimensions, one needs information about the astrometry and the velocity in the direction of the line of sight. This velocity, called radial velocity, is extracted from the spectrum of the star. A star has spectral lines, which shift according to the Doppler shift when the star moves along the line of sight. They shift towards bluer wavelengths if the star moves towards the observer or to redder wavelengths if the star moves away from the observer. For the measurement of relativistic effects in the orbits of stars around the supermassive black hole Sgr A* it is, therefore, essential to get the best possible velocity from the stellar spectrum. We changed some parts in our treatment of the SINFONI data reduction and velocity extraction from the spectrum to achieve the best velocity measurement. In the following, we outline the most significant changes in the wavelength calibration and velocity extraction and the effect of the changes on the measured velocities. As this work was done with the pericenter of the bright star S2 upcoming, it is mostly based on spectra of S2. However, all the techniques can be applied to all the other stars in the Galactic Center.

4.1 WAVELENGTH CALIBRATION

The software package which we use to reduce SINFONI data is called spred (Schreiber et al., 2004). We used spred as a starting point and made some changes to improve the wavelength calibration. An essential step to measure reliable velocities is to precisely calibrate the wavelength axis of an observed spectrum of a star. The calibration is usually done in a two-step process. In the first step, we use data from a calibration lamp that was taken during the daytime. This lamp has strong emission lines. In our case, this is a Xenon lamp within SINFONI. The lines in the observed spectrum are measured, and a dispersion relation is fitted, using the measured positions on the detector and the theoretical lines of the lamp. In the case of spred a polynomial of fifth order is used. This dispersion relation gives a first wavelength calibration of the pixels on the detector.

In the second step, the OH emission lines are used to create an improved calibration. OH lines are produced by OH radicals in the upper atmosphere. The radicals are created in a reaction between atomic hydrogen and ozone.

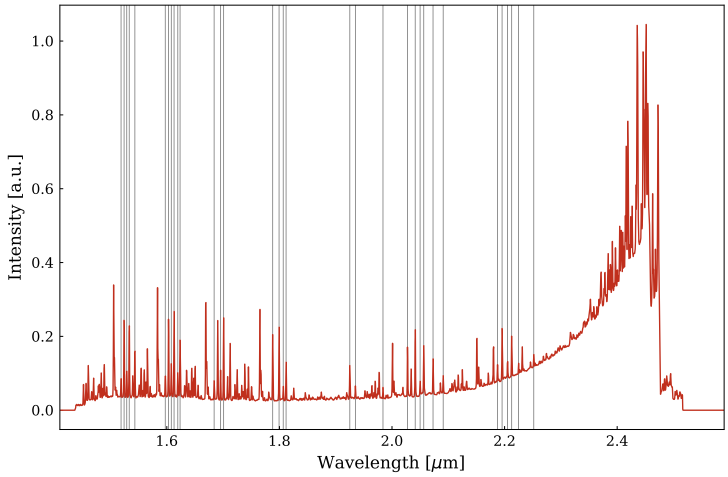

Figure 4.1: Example sky spectrum taken with SINFONI. The gray background lines show the OH lines which are used in the wavelength calibration.

The OH lines are strongest between 1 µm to 2.5 µm, and they are variable over short timescales. Because of the variability, they are a nuisance in infrared astronomy. Even if they can be removed from the final data, their variability adds noise to the spectrum. Often some signal remains in the spectrum, as the lines cannot be entirely removed (Osterbrock et al., 1996; Davies, 2007).

However, as the OH lines are strong lines at fixed wavelengths, one can use them for wavelength calibration (Osterbrock et al., 1996; Rousselot et al., 2000). In our case, we used the average over all sky frames, which shows strong OH emission lines. The lines outshine any background signal in the sky frames. For an example of a sky spectrum, see Figure 4.1. In this spectrum, one sees the OH line on top of the black body spectrum of the sky. We then used a selection of the lines to improve the wavelength calibration. Using the OH lines atlas from Rousselot et al., 2000 we created the maximum set of lines, which were clearly detectable as single lines. Many OH lines are doublets and triplets, which we cannot resolve with the spectral resolution of SINFONI. By only selecting the lines that were clear single lines, we reduced the number of lines used in the original spred pipeline by removing five lines. After carefully selecting the lines, there were 33 lines left, which we show as grey vertical lines in Figure 4.1.

The theoretical OH lines are used to create a synthetic spectrum, which is then cross-correlated with the actual sky spectrum. The second step, therefore, only adds a slight shift to the wavelength calibration. The primary dispersion relation is taken from the calibration with the internal lamp. While the cross-correlation process was already present in the original spred package, the cross-correlation was poorly implemented, which added a negative bias to the

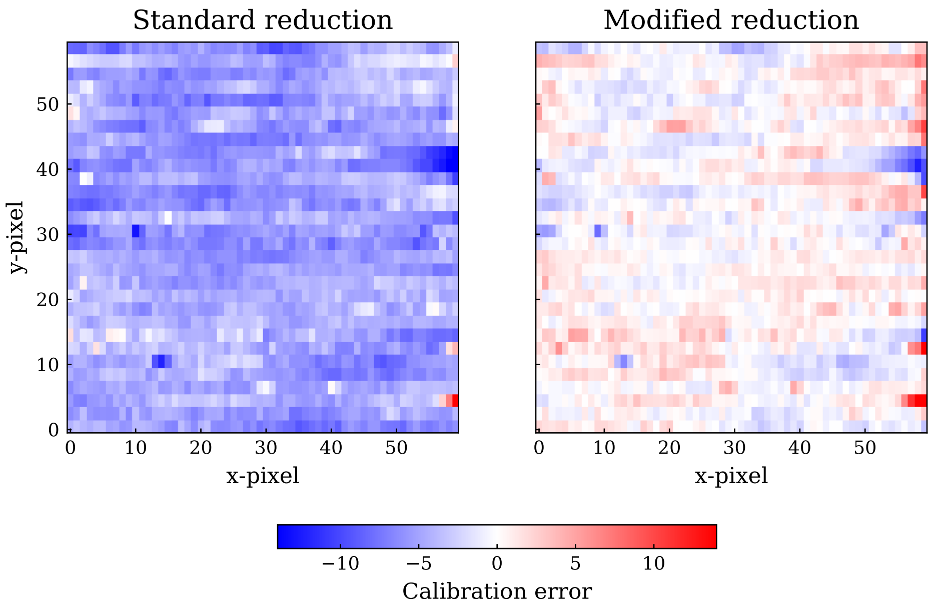

Figure 4.2: Example for the improvement in calibration with the improved pipeline. The left plot shows the calibration error for each spatial pixel for the original reduction and the right plot for the modified reduction.

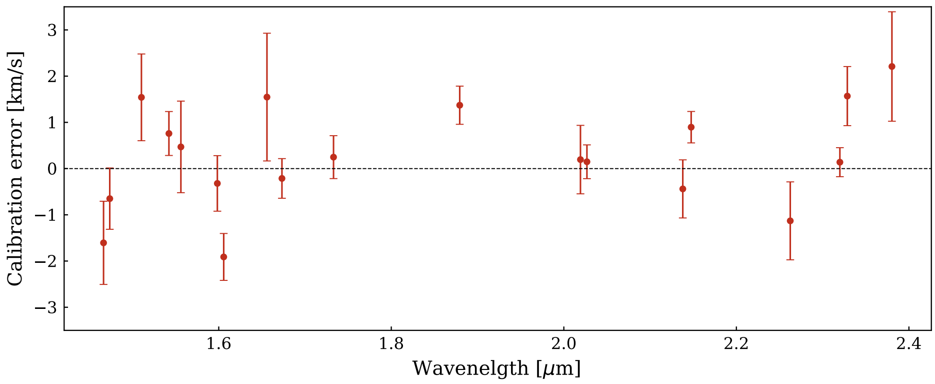

Figure 4.3: Remaining calibration error for a typical SINFONI data-cube. Each used OH line is fitted over the full data-cube and the deviation from the theoretical line position is shown here.

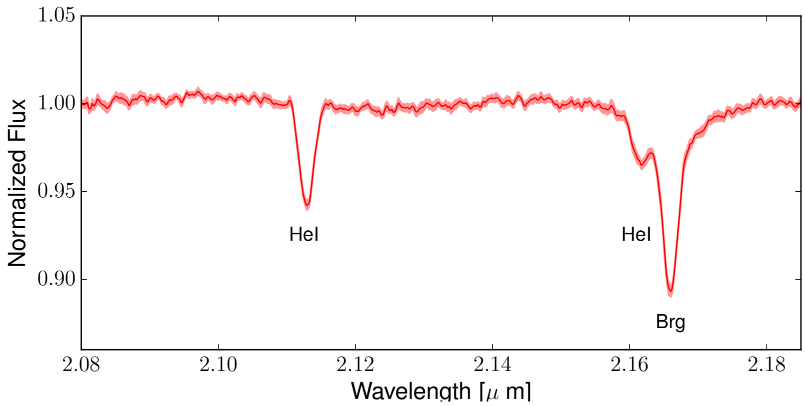

Figure 4.4: High signal-to-noise spectrum of the star S2 in the astronomical K-Band. The spectrum has been produced by combining data from 12 years of observations (adapted from Habibi et al., 2017).

final wavelength calibration. This negative bias can be nicely seen in Figure 4.2, where we show the calibration error for each spatial pixel in a SINFONI cube. For Figure 4.2 we took a combined and fully calibrated sky cube and measured the position of the OH lines at each spatial pixel. The average deviation from the nominal wavelength is shown in the figure. The average error in the original spred implementation is on the order of $-5\,\mathrm{km\,s^{-1}}$. With the better cross-correlation and the improved OH line selection, the average error in the improved reduction is $0.25\,\mathrm{km\,s^{-1}}$ which is very close to zero. This shows that we can remove the bias due to the calibration with the new scheme. In terms of uncertainty Figure 4.3 shows the measurement error in the OH line for a typical sky cube. We see that there is still some uncertainty in the calibration but no clear trend or bias anymore. For such a typical cube we estimate the calibration uncertainty on the final measured velocities to be smaller than $2\,\mathrm{km\,s^{-1}}$.

4.2 VELOCITY EXTRACTION

With the upcoming pericenter of the star S2 in mind (Gravity Collaboration et al., 2018b) we also decided to improve the velocity extraction from the spectrum. S2 has a magnitude of 14.2 and is one of the brightest stars in the region close to Sgr A* (Martins et al., 2008). It has an orbital period of 16.05 yr and had its closest encounter with Sgr A* in May 2018. S2 is an early type star, which has two dominant absorption features in the K-band. The strongest line is the Brγ line (hydrogen transition n = 7 - 4) with a vacuum wavelength of 2.1661 µm. The second feature is the helium line around 2.1125 µm. This line is not a single feature but a blend of the He I triplet at 2.1120 µm (3p ^{3}P^0 – 4s

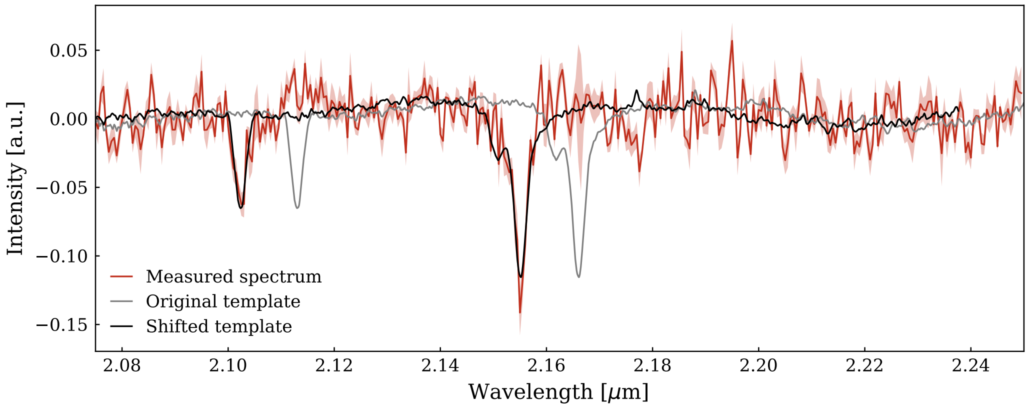

Figure 4.5: Example for the fitting of the template spectrum to the SINFONI data. The red spectrum is the one measured from SINFONI with the uncertainty from the pixel extraction showing in light red. The grey spectrum is the combined spectrum from Habibi et al., 2017 at zero velocity and the black one is the same spectrum shifted to the fitted velocity of $-1492\,\mathrm{km\,s^{-1}}$

.

^{3}S) and the He I singlet at 2.1132 µm (3p ^{1}P^0 – 4s ^{1}S). The weighting of the two features depends on the atmospheric parameters and the rotational velocity of the star (Habibi et al., 2017). In an individual spectrum at our resolution, they appear as a single feature. In a typical observation of one hour, the helium and hydrogen feature can be detected at $> 5\sigma$. A combined spectrum with a high signal-to-noise ratio (SNR) from Habibi et al., 2017 is shown in Figure 4.4. On the left shoulder of the hydrogen line is another helium line at 2.161 µm, which is much weaker than the hydrogen line and in an individual dataset just above the noise level.

Traditionally the velocity of S2 was measured by just fitting a Gaussian to the Brγ to get the wavelength λ at which the line is measured and the radial velocity is calculated with the doppler formula shown in Equation 3.1. However, the Gaussian fit approach ignores the information from the Helium features in the spectrum. In our new approach, we used the combined spectrum from Habibi et al., 2017, shown in Figure 4.4, as a template and did a cross-correlation with the measured spectrum. The cross-correlation has the advantage that the fit takes the different features in the S2 spectrum and their distance to each other into account. However, as the Doppler shift is not a simple shift of the template spectrum, the approach is more complicated. We first obtain a guess of the measured velocity from a traditional cross-correlation. We then shifted the template spectrum to that velocity using the formula from Equation 3.1. As this shift includes a regridding of the spectrum, we did this to the template spectrum and not the measured one, as it introduces a small amount of noise.

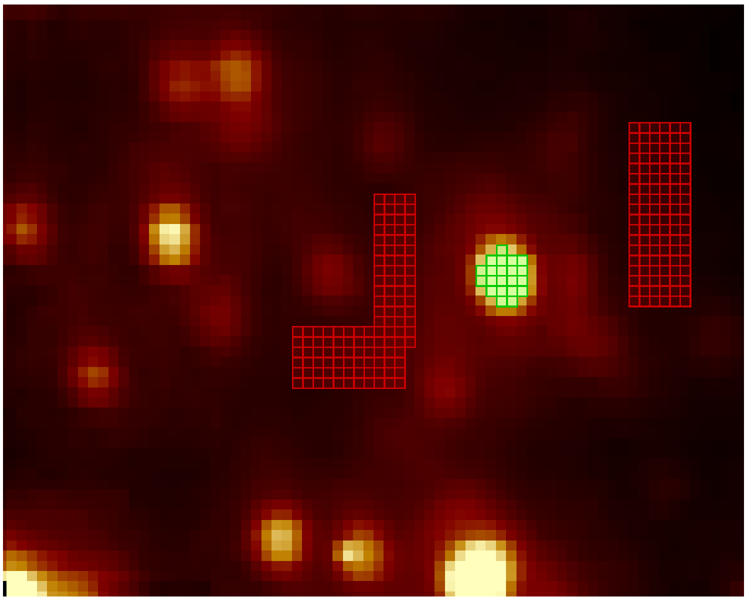

Figure 4.6: Typical extraction of a spectrum from the spatial axis of the integral field unit. The green pixel show the selection for the object and the red ones the selection for the background subtraction.

We then iteratively repeated these steps until the measured velocity was stable. The total velocity by which the template spectrum needed to be shifted is then the measured velocity of S2. An example for such a fit is shown in Figure 4.5.

In terms of uncertainty, there are three components to a velocity measurement with an integral field spectograph: the uncertainty from the wavelength calibration, the uncertainty from the selection of spatial pixels for the star and background position, and the fit uncertainty. The error from the wavelength calibration was set to $2\,\mathrm{km\,s^{-1}}$, as motivated by the previous section. The selection of the pixels adds uncertainty as the galactic center is a very crowded field with several stars and gas flows. Therefore, it is not always clear what pixels have star flux in them and where to put the pixels for the background subtraction without adding a signal from the gas flows. A typical extraction for S2 is shown in Figure 4.6. To quantify the impact of different extractions, we usually created eight spectra with different pixel selections and measured the velocity for all of them. The standard deviation from the measurements with different masks gives then the uncertainty from the pixel selection. For the fit uncertainty, we determined the formal fit error σ, but also measured a signal to noise (SNR) dependent uncertainty. The SNR is measured from the depth of the Brγ line for the signal, and the noise is estimated from a part of the spectra without emission lines. We fitted a power law to the dependence of the fit error σ on the SNR and found a relation of $\sigma \propto \mathrm{S/N}^{-0.92}$. The data and

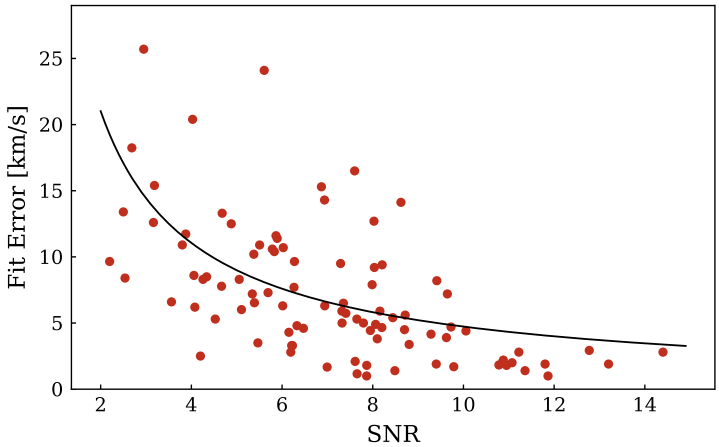

Figure 4.7: Relation of the SNR of the spectrum and the uncertainty from the velocity fit. The red points are the datapoints and the black line the fitted powerlaw with an exponential of -0.92

.

the fit are shown in Figure 4.7. The 1/(S/N) behavior is consistent with the uncertainty of a centroid fit (Fritz et al., 2010).

However, the fit error, the S/N uncertainty, and the standard deviation over the different masks are strongly correlated. Therefore, we used the largest of the three as the fitting uncertainty. The calibration uncertainty is then added to that value to get the full error on the measurement. This full procedure was used from 2018 on, but we also re-reduced the full data-set of radial velocities taken between October 2004 and the end of 2019 for the work presented in chapter 5. In the re-reduction we got an uncertainty of $\sim 7\,\mathrm{km\,s^{-1}}$ for the very best data-sets and a median uncertainty of $12.3\,\mathrm{km\,s^{-1}}$. This was an improvement by 46% compared to the previous set of radial velocity data. The uncertainty in the measurement is in comparison to other radial velocity measurements still comparably big. With the newest high resolution spectrographs uncertainties well below $\mathrm{m\,s^{-1}}$ are possible. For the spectrocopy of S2 we are limited by the broad spectral lines and also by the fact that we only have two lines in the K-Band. For old stars, where one sees a forest of thin metal lines in the K-Band this measurement can still be significantly improved. Despite those limitations the rederived radial velocities of S2 allowed us to better constrain the orbit of S2, which ultimately led to a new and improved distance measurement to the Galactic Center, presented in chapter 5, and to the first-ever test of the Einstein Equivalence Principle around a supermassive black hole, which is presented in chapter 7.

A GEOMETRIC DISTANCE MEASUREMENT TO THE GALACTIC CENTER BLACK HOLE WITH 0.3% UNCERTAINTY

5

Original Publication: GRAVITY Collaboration, R. Abuter, A. Amorim, M. Bauböck, J.P. Berger, H. Bonnet, W. Brandner, Y. Clénet, V. Coudé du Foresto, P.T. de Zeeuw, J. Dexter, G. Duvert, A. Eckart, F. Eisenhauer, N.M. Förster Schreiber, P. Garcia, F. Gao, E. Gendron, R. Genzel, O. Gerhard, S. Gillessen, M. Habibi, X. Haubois, T. Henning, S. Hippler, M. Horrobin, A. Jiménez-Rosales, L. Jocou, P. Kervella, S. Lacour, V. Lapeyrère, J.-B. Le Bouquin, P. Léna, T. Ott, T. Paumard, K. Perraut, G. Perrin, O. Pfuhl, S. Rabien, G. Rodriguez Coira, G. Rousset, S. Scheithauer, A. Sternberg, O. Straub, C. Straubmeier, E. Sturm, L.J. Tacconi, F. Vincent, S. von Fellenberg, I. Waisberg, F. Widmann, E. Wieprecht, E. Wiezorrek, J. Woillez & S. Yazici
Main Authors: F. Widmann, S. Gillessen
DOI: 10.1051/0004-6361/201935656

Abstract: We present a 0.16% precise and 0.27% accurate determination of R_0, the distance to the Galactic Center. Our measurement uses the star S2 on its 16-year orbit around the massive black hole Sgr A* that we followed astrometrically and spectroscopically for 27 years. Since 2017, we added near-infrared interferometry with the VLTI beam combiner GRAVITY, yielding a direct measurement of the separation vector between S2 and Sgr A* with an accuracy as good as $20\,\mu$as in the best cases. S2 passed the pericenter of its highly eccentric orbit in May 2018, and we followed the passage with dense sampling throughout the year. Together with our spectroscopy, in the best cases with an error of 7 km/s, this yields a geometric distance estimate of $R_0 = 8178 \pm 13_{\text{stat.}} \pm 22_{\text{sys.}}$ pc. This work updates our previous publication, in which we reported the first detection of the gravitational redshift in the S2 data. The redshift term is now detected with a significance level of 20σ with $f_{\text{redshift}} = 1.04 \pm 0.05$.

5.1 INTRODUCTION

Measuring distances is a key challenge in astronomy. While many distance estimators rely on secondary calibration methods, the basis for the whole distance ladder is laid by a few methods. These methods all compare an angular scale on sky with a size that is known in absolute terms. Foremost is of course the parallax method. It compares an observed reflex motion on the sky, measured in angular units with the size of Earth's orbit. Recently, Gaia improved the number and quality of available parallaxes substantially (Gaia collaboration 2018). However, Gaia works in the optical and at moderate spatial resolution and does not provide any parallaxes toward the crowded and highly dust-obscured center of the Milky Way. The extinction can be overcome by observing at longer wavelengths, in the near-infrared (NIR, $1 - 5\,\mu$m). Very large telescopes with adaptive optics (AO), and recently, interferometry between large telescopes (GRAVITY collaboration 2017), overcome the stellar crowding. This allowed us to determine the orbits of 40 stars around the central massive black hole with periods between 13 and a few thousand years (Gillessen et al. 2017). These stars offer another direct method of determining a distance. The distance to the Galactic Center (GC), R_0, can be determined by comparing the radial velocities (measured in km/s) of these stars with their proper motions (measured in mas/yr). The measurement is direct because this can be done for individual stellar orbits, as opposed to using a sample of stars together with a dynamical model like in van de Ven et al., 2006 for the globular cluster ω Cen or in Chatzopoulos et al., 2015 for the Milky Way nuclear cluster.

Most suitable for the orbit method is the star S2 on a 16-year orbit (the second shortest period known so far, Meyer et al., 2012), with a semimajor axis $a \approx 125\,$mas. S2 has an apparent K-band magnitude of $m_K \approx 14$, which is bright enough for spectroscopy. It is a massive, young main-sequence B star (Ghez et al., 2003b; Martins et al., 2008; Habibi et al., 2017) that offers a few atmospheric absorption lines in the observable parts of the spectrum. Several works used S2 to measure the distance to the GC. The first measurement was in Eisenhauer et al., 2003, who reported $R_0 = 7940 \pm 420\,$pc. Eisenhauer et al., 2005 updated this value to $R_0 = 7620 \pm 320\,$pc. Ghez et al., 2008 reported $R_0 = 8400 \pm 400\,$pc, and Gillessen et al., 2009a differed slightly with $R_0 = 8330 \pm 350\,$pc. More recently, Boehle et al., 2016 measured $R_0 = 7860 \pm 140 \pm 40\,$pc, and Gillessen et al., 2017 obtained $R_0 = 8320 \pm 70 \pm 140\,$pc. Here and in what follows, the first error is statistical, and the second error is systematic. All these measurements rely on AO data. For general recent overviews of R_0 determinations, see Genzel et al., 2010 and Bland-Hawthorn and Gerhard, 2016.

The star S2 passed the pericenter of its orbit in May 2018, an event that we followed in detail with astrometry and spectroscopy (Gravity Collaboration et al., 2018b). The primary goal of these observational efforts was the detection of relativistic effects in the orbital motion. However, the data also allow for an unprecedentedly accurate measurement of R_0 because of the large swing in radial velocity (from +4000 to -2000 km/s) and the large orbital phase that was covered in 2018. Gravity Collaboration et al., 2018b presented the detection of the gravitational redshift from Sgr A* in the S2 spectra. Our previous analysis included data up to end of June 2018. It addressed the question whether the gravitational redshift and Doppler terms are in agreement with the predictions of Einstein's theory of relativity. At the same time, our orbital solution also included the most precise determination of R_0 so far, $R_0 = 8122 \pm 31\,\mathrm{pc}$, where the error is only statistical. Several authors studying the Milky Way structure have used this result (McGaugh, 2018; Drimmel and Poggio, 2018; Mróz et al., 2019; Eilers et al., 2019). Here, we update our value for R_0, using data up to the end of 2018, and we apply the relativistic corrections assuming General Relativity is correct. This yields one fit parameter less. We also investigate the systematic error on R_0 from our measurement, which we did not consider in Gravity Collaboration et al., 2018b.

5.2 DATA

Gravity Collaboration et al., 2018b used 45 AO-based astrometric points (after down-sampling), 77 radial velocities, and 30 GRAVITY interferometric data points. The present study adds ten epochs of radial velocity measurements from late June 2018 to late September 2018, and ten epochs of GRAVITY astrometry. Furthermore, we reanalyzed our radial velocity data from SINFONI and the GRAVITY astrometry, implementing an improved understanding of the respective systematic effects. This also led to a slightly different data selection and different grouping of the observations.

For the SINFONI data we revisited the wavelength calibration, yielding an improved wavelength dispersion solution. Where possible, we determined the radial velocities by template fitting. The uncertainties are a combination of formal fit error, wavelength error, and the error introduced by selecting a certain extraction mask in the field of the integral field unit. For the details see section 5.A.

For the GRAVITY data we replaced the manual frame selection with an objective outlier-rejection and included the (minor) effect of atmospheric differential refraction. The data analysis includes data selection, binary fitting, correction for atmospheric refraction, outlier rejection, nightly averaging, correction for effective wavelength, adding systematic errors, and error scaling. We report the details in section 5.B.

Overall, our new data set consists of 169 AO-based astrometry points between 1992 and 2019, 91 radial velocities between 2000 and 2019, and 41 GRAVITY-based astrometry points in 2017 and 2018.

Our AO data set samples the on-sky motion of S2 at high cadence. The distance between subsequent data points is typically smaller than the size of the point spread function. Any confusion event with unrecognized faint stars thus might affect several data points, leading to correlated measurements. As in Gravity

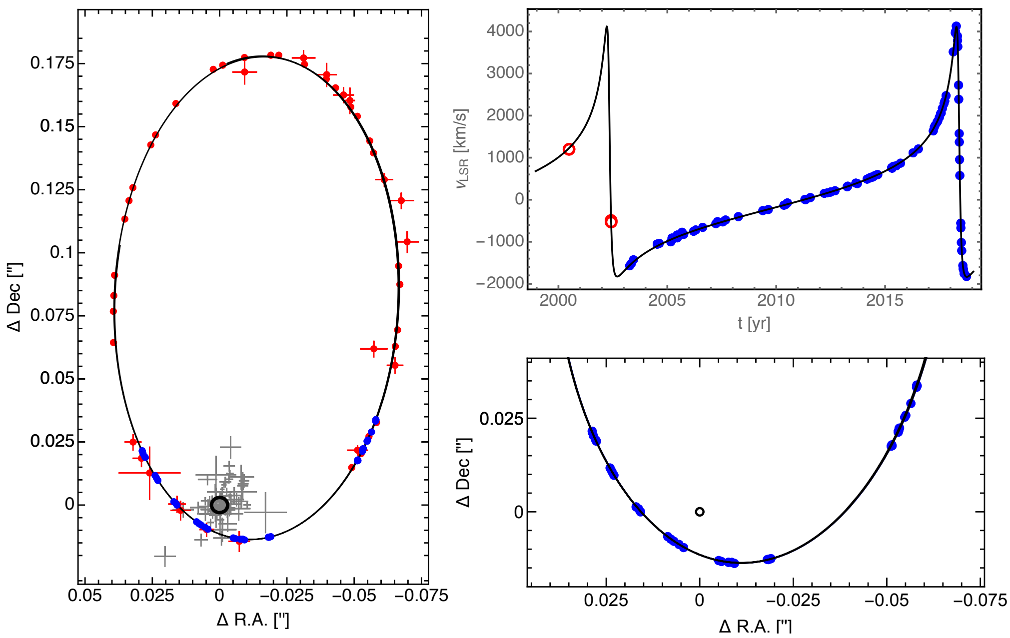

Figure 5.1: Orbit of S2. Left: On-sky view of the astrometric data (red: AO data, blue: GRAVITY data) in the down-sampled version with the best-fit orbit (black ellipse). The black circle marks the position of Sgr A*. The locations of previous AO-based flares agree with that position (gray crosses). Right top: Radial velocity data of S2 together with the best-fit orbit. The blue data are from the VLT, the red are earlier epochs from the Keck data set (Ghez et al., 2008). Right bottom: Zoom into the on-sky orbit in 2017 and 2018, showing the GRAVITY data that have error bars smaller than the symbol size.

Collaboration et al., 2018b, we therefore down-sampled the AO data set into intervals of constant arc length on the sky, and we down-weighted these AO data by a factor two in order to take the additional uncertainty due to unseen confusion events into account. Furthermore, we omitted the 2018 data where additional confusion with Sgr A* affects the data, leading to 48 AO-based astrometric data points. We also developed a different approach for the same problem, namely a noise model (see sec. 5.3). This gives a second data set, in which we used all 169 AO-based astrometric points.

5.3 ANALYSIS

We used the same techniques as in Gravity Collaboration et al., 2018b and Gillessen et al., 2017. The analysis essentially consists of one step: determining the best-fit orbit for the data given, and the corresponding uncertainties. We employed a χ^2-minimization to determine the best-fit, and for the uncertainties, we used the standard error matrix approach, a Markov chain Monte Carlo (MCMC) sampler and a bootstrapping technique. The latter bootstraps an artificial data set by drawing from the original data separately for the AO astrometry, the radial velocities, and the GRAVITY data. In order to avoid problems that might arise because the AO points are correlated, we used the down-sampled data set for the bootstrapping.

For a different approach with the AO data, we implemented a noise model of the type presented in Plewa and Sari, 2018 for the AO-based astrometry. Such a model has the advantage that it estimates the additional amount of error and the correlation length from the data themselves, avoiding any prior choices on how to treat the data. In our implementation, we exchanged the temporal correlation length of Plewa and Sari, 2018 with a spatial one. The underlying reason for a correlation between different data points is confusion with unseen stars that can be described naturally by a length scale in the image plane. Because S2 has a widely varying proper motion, a temporal correlation length is less suited. This model adds two additional fit parameters: the spatial correlation length and the typical confusion amplitude, which correspond to the down-sampling and down-weighting in the other data set. We note that fitting the noise model is feasible only when we also use the GRAVITY data, otherwise, its parameters are too degenerate with the other 13 parameters. We did not exclude all 2018 data for this data set, but only the epochs at which Sgr A* apparently affected the position measurements, as visible in an elongated source structure or excess flux of S2. We also analyzed a third data set excluding all AO astrometry. Perhaps somewhat surprisingly, the two years of GRAVITY data already are the much stronger constraint for the orbit compared to the past 27 years of AO imaging data.

Compared to the analysis in Gravity Collaboration et al., 2018b, we included in the calculation of the transverse Doppler effect the apparent proper motion of Sgr A* to the southwest of $(-3.151, -5.547)$ mas/yr, a reflex of the solar motion around the Milky Way center (Reid and Brunthaler, 2004). This corresponds to $v_\odot \approx 250\,\mathrm{km/s}$, while S2 at pericenter reaches an on-sky motion of $v_{\mathrm{S2}} \approx 7320\,\mathrm{km/s}$. Because in the Doppler formula a term of type $(v_{\mathrm{S2}}+v_\odot)^2 \approx v_{\mathrm{S2}}^2(1 + 2v_\odot/v_{\mathrm{S2}})$ occurs, the proper motion of Sgr A* leads to a small but noticeable correction. We parameterized the strength of the combined redshift and transverse Doppler effect with an artificial parameter f_{redshift} such that $f_{\mathrm{redshift}} = 0$ corresponds to classical physics, while $f_{\mathrm{redshift}} = 1$ corresponds to the effects occurring as predicted by General Relativity. Including the proper motion of Sgr A* induces a change of $\Delta f_{\mathrm{redshift}} = +0.038$, and a change in distance of $\Delta R_0 = +6\,\mathrm{pc}$.

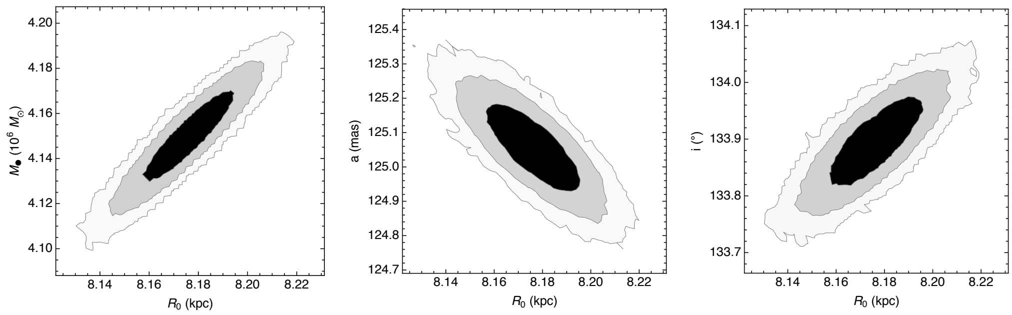

Figure 5.2: Selected posterior densities as obtained from the MCMC sampler with N=200000, here for the noise model data set. The contour lines mark the 1, 2, and 3σ levels. We only show the diagrams with the strongest correlations. All parameters are well determined (see section 5.D).

5.4 RESULTS

5.4.1 DISTANCE TO THE GALACTIC CENTER

If the fit has as few free parameters as possible, the estimate for R_0 is the most precise. We therefore assumed that General Relativity holds and fixed the parameter $f_{\text{redshift}} = 1$. We further used the Rømer delay and included the first-order correction from the Schwarzschild metric. The coordinate system parameters only apply to the AO astrometry because GRAVITY directly measures the vector S2 - Sgr A*.

We list our best-fit results in Table 5.1 and show the best fit in Figure 5.1. The error bars we report are the formal fit errors from the error matrix. The three data sets yield completely consistent parameters within the formal uncertainties. The reduced χ^2 values by construction of the errors are close to 1 (section 5.A and section 5.B).

The noise model has two additional free parameters, the noise amplitude $\sigma = 0.83 \pm 0.15\,\text{mas}$ and the spatial correlation length $\lambda = 21.2 \pm 3.8\,\text{mas}$. These numbers define by how much a certain data point is expected to be off from the model, given the other data. The correlation length is on the same order of magnitude as the AO point spread function radius, and the amplitude is reasonable. Our best-fit σ corresponds to a perturbing star of $m_K \approx 17$ at a distance of our best-fit λ (Plewa and Sari, 2018).

Using the MCMC sampler, we obtained the full 13-dimensional posterior distribution. All parameters are well constrained, and Figure 5.2 shows the diagrams with the strongest parameter correlations: mass versus R_0, semimajor axis versus R_0, and inclination versus R_0. The most probable value agrees with the best-fit value, and the 1σ uncertainty from the posterior is 13 pc, which

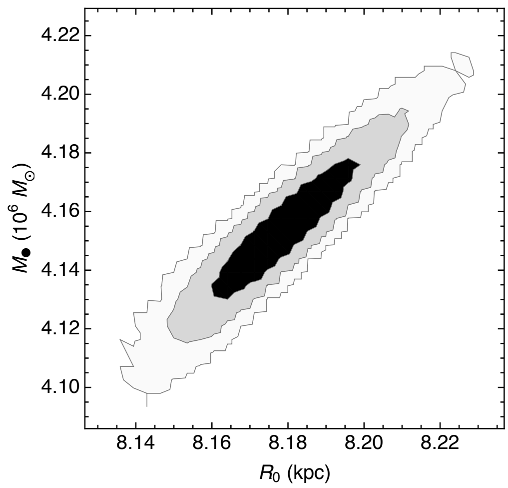

Figure 5.3: Posterior distribution for R_0 and mass from our bootstrap sample. The contour lines mark the 1, 2, and 3σ levels.

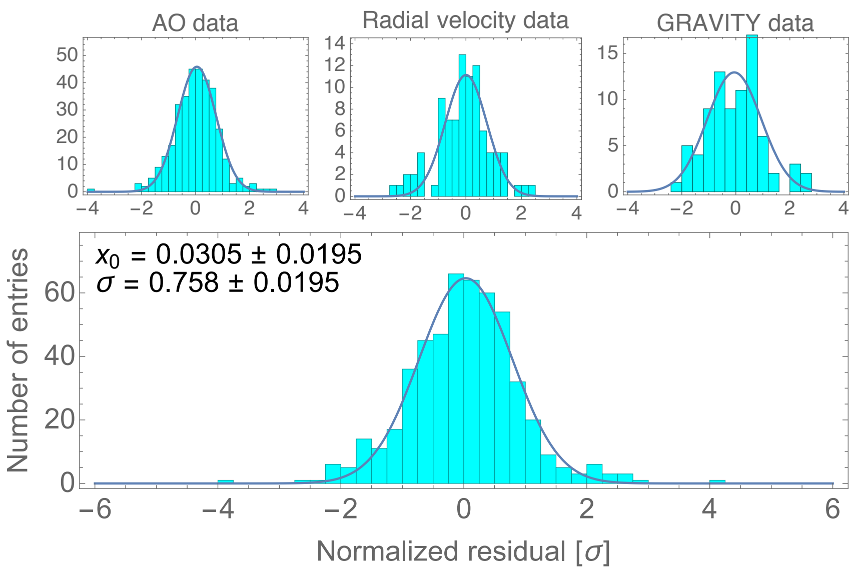

Figure 5.4: Histograms of the normalized residuals, the ratio of residual to error for each data point. Top row: Individually for the three subsets of data. Bottom: Combined data set.

Table 5.1: Best-fit parameters for our three data sets. The parameters x_0, y_0, vx_0, and vy_0 describe the location and motion of the mass in the coordinate system of the AO data in R.A. and Dec. Because GRAVITY directly measures the separation vector, we do not need to include such coordinate system offsets for the GRAVITY data. The third velocity vz_0 is the offset of the motion in the radial direction along the line of sight, the negative sign means a blueshift or a motion toward the observer. The parameters $(a, e, i, \Omega, \omega, t_{\text{peri}})$ are the classical orbital elements semimajor axis, eccentricity, inclination, position angle of ascending node, longitude of pericenter, and the epoch of pericenter passage. The orbital elements are defined as the osculating orbital elements at $t = 2010.0$, i.e., the conversion to position and velocity is done at that epoch assuming a Kepler orbit.

Parameter	**down-sampled data**	**noise model fit**	**GRAVITY only**
R_0 [pc]	8179 ± 13	8178 ± 13	8175 ± 13
mass [$10^6\,\mathrm{M}_\odot$]	4.154 ± 0.014	4.152 ± 0.014	4.148 ± 0.014
x_0 [mas]	-1.04 ± 0.36	-0.65 ± 0.36	N.A.
y_0 [mas]	-0.47 ± 0.35	-0.73 ± 0.35	N.A.
vx_0 [μas/yr]	68 ± 31	68 ± 32	N.A.
vy_0 [μas/yr]	158 ± 31	108 ± 31	N.A.
vz_0 [km/s]	-3.3 ± 1.5	-3.0 ± 1.5	-2.8 ± 1.5
a [mas]	125.072 ± 0.084	125.066 ± 0.084	125.065 ± 0.086
e	0.884282 ± 0.000064	0.884293 ± 0.000064	0.884288 ± 0.000064
i [°]	133.911 ± 0.052	133.904 ± 0.052	133.883 ± 0.053
Ω [°]	228.067 ± 0.041	228.075 ± 0.041	228.091 ± 0.041
ω [°]	66.250 ± 0.035	66.253 ± 0.035	66.257 ± 0.035
t_{peri} [yr] - 2018	0.3790 ± 0.0014	0.3790 ± 0.0014	0.3789 ± 0.0014
UTC date	19.5.2018 09:53	19.5.2018 09:51	19.5.2018 09:47
red. χ^2	0.82	1.10	1.00

is fully consistent with the estimate from the error matrix. We furthermore estimated our errors by bootstrapping (and refitting each artificial data set). For this, we used the down-sampled data set because here the most important correlation between data points is removed. Figure 5.3 shows the resulting distribution for N = 20000 bootstraps. The most likely value agrees with the best-fit value, and so do the error bars: $R_0 = 8178^{+13}_{-12}\,\mathrm{pc}$.

Figure 5.4 shows the normalized residual (residual divided by the error) distributions for each of the three subsets of data and for the whole data set. The distributions are well behaved and reasonably close to a Gaussian with mean 0 and width 1.

The size of the R_0 error of $13/8178 \approx 0.16\%$ is comparable to what a simple estimate yields. R_0 is directly related to the ratio of proper motion (arc length divided by time) and radial velocity. The most constraining part of the orbit is the pericenter swing, which we followed with GRAVITY in 2017 and 2018.

- The arc length is $\approx 150\,\mathrm{mas}$, more than $1000\times$ larger than the median 2D error of the 41 GRAVITY points[1]. The astrometric precision is thus at the 0.01% level and does not contribute significantly to the statistical error.

- The median error of the radial velocity data in 2017 and 2018 is 14.4 km/s, and we have 35 data points. The mean absolute radial velocity of our data in 2017 and 2018 is 2300 km/s. The spectroscopic precision is thus at the 0.1% level. It dominates the measurement error, and it is of the same magnitude as the actual statistical error on R_0.

We conclude that $R_0 = 8178 \pm 13_{\mathrm{stat.}}\,\mathrm{pc}$. However, we still lack an estimate for the systematic error.

5.4.2 SYSTEMATIC ERRORS

Our estimate for R_0 is direct and as such does not depend on intermediate calibration steps. Any systematic error is directly related to how accurately we understand the instruments we use, that is, how accurate are the on-sky positions we measure and how accurate are the radial velocities. Figure 5.2 shows the strongest parameter correlations for R_0 from the posterior distribution

[1] The median 1D error of the 2018 GRAVITY data is $60\,\mu\mathrm{as}$, and for 2017 it is $145\,\mu\mathrm{as}$. These numbers already take into account the scatter from night to night. The uncertainties for individual data points within a single night are smaller (Gravity Collaboration et al., 2018a). The difference in median error between 2017 and 2018 is caused by the improvement in fiber positioning implemented for 2018. The median error over the whole data set of 41 points is $86\,\mu\mathrm{as}$ 1D, or equivalently, $121\,\mu\mathrm{as}$ 2D.

of the 13-dimensional fit. They are with mass, semimajor axis, and inclination. These correlations can be understood qualitatively.

- R_0 is inversely proportional to the semimajor axis a. A biased determination of a in angular units would bias R_0 because the radial velocity data determine a in absolute units; for S2, $a \approx 1023\,\mathrm{AU}$. The slope of the correlation in Figure 5.2 (middle) confirms this, $R_0 \times a \approx 1023\,\mathrm{AU}$. The instrumental reason why a could be biased is an error in the image scale. A scale error of 1% would imply a distance error of $\approx 80\,\mathrm{pc}$.

- The inclination i would be biased if the image scale were off in one dimension only. The MCMC shows a sensitivity of R_0 to i of $3.75°/\mathrm{kpc}$. At the inclination of S2, the sensitivity of the scale change to a change in i amounts to $1.2\%/°$.

- Kepler's third law, $GM = 4\pi^2(a \times R_0)^3/P^2$ (where the semimajor axis a is measured in angular units), shows that our mass measurement is equivalent to determining the period P because the nominator $a \times R_0$ is a constant, see above. The MCMC shows a sensitivity of R_0 to M of $1.4 \times 10^3\,M_\odot/\mathrm{pc}$ at the best-fit R_0, corresponding to $\approx$ 1day / pc for the sensitivity to P. We note that the error we make in measuring the period due to the uncertainty in the underlying data is captured in the statistical error on R_0. What matters here would be a systematic error in measuring time, which we can exclude at the relevant level. The mass-distance degeneracy is not a source of potential systematic error.

We conclude that if the parameter degeneracies were to introduce a systematic error on R_0, it would originate from an error in the astrometry. Furthermore, we note that the GRAVITY data completely dominate our astrometry (see Table 5.1), and that the AO + GRAVITY data sets yield the same result as the GRAVITY-only fit. This means that the uncertainty in the GRAVITY astrometry dominates the systematic error from the astrometry. In section 5.C we show that we estimate this uncertainty to be 19 pc or 0.24%.

When we used the GRAVITY astrometry, we assumed that the near-infrared (NIR) counterpart of Sgr A* is at the position of the center of mass. Gravity Collaboration et al., 2018a reported that the flaring emission from Sgr A* moves in a circular pattern with a radius of a few Schwarzschild radii, $\approx 50\,\mu\mathrm{as}$. The flares are compact regions of transiently heated electrons that emit synchrotron light, powered probably by magnetic reconnection events (Dodds-Eden et al., 2009). They occur very close to the innermost stable circular orbit, and orbital motion of a few $10\,\mu\mathrm{as}$ has been proposed since their discovery (Genzel et al., 2003; Broderick and Loeb, 2005; Hamaus et al., 2009). Observationally, the center of motion matches the position of the mass to within $\approx 50\,\mu\mathrm{as}$. We

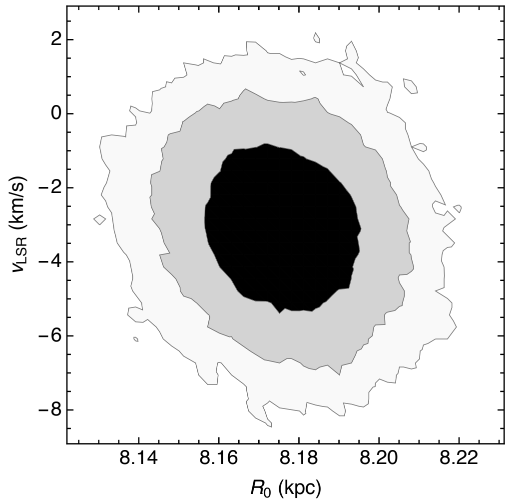

Figure 5.5: Posterior distribution for R_0 and the offset in radial velocity. The contour lines mark the 1, 2, and 3σ levels.

used this as uncertainty on our assumption and estimated the effect on R_0 by artificially displacing the mass by that amount. This yields changes in R_0 of $+8$ pc, -8 pc, -6 pc, and $+5$ pc to the north, south, east, and west. We include 6 pc in the systematic error for the assumption that GRAVITY directly measures the separation vector between S2 and mass center.

With full coverage of the orbit, the measurement of R_0 is no longer degenerate with the offset vz_0 in radial velocity (Figure 5.5, cf. Ghez et al., 2008). A general offset in the radial velocity would be absorbed fully into vz_0, but it would not affect our measurement of R_0. The zeroth order of the wavelength calibration is thus not a source of systematic error. The leading order could only be the first order, that is, the dispersion solution.

Our spectra are calibrated with a higher order polynomial, using multiple atmospheric lines in the same spectra as calibration points. From the residuals of our dispersion solution at these calibration points, we estimated the systematic uncertainty in the wavelength axis to 2.5 km/s over the range relevant for S2. Together with the mean absolute radial velocity in 2017 and 2018 (2300 km/s), we obtain a systematic error of 0.11% or 9 pc.

Taken together, we thus estimate our systematic error on R_0 to be 22 pc. Our main result is

$$R_0 = 8178 \pm 13_{\text{stat.}} \pm 22_{\text{sys.}}\ \text{pc}.$$

The statistical error is dominated by the measurement uncertainties of the radial velocities, and the systematic error by the GRAVITY astrometry.

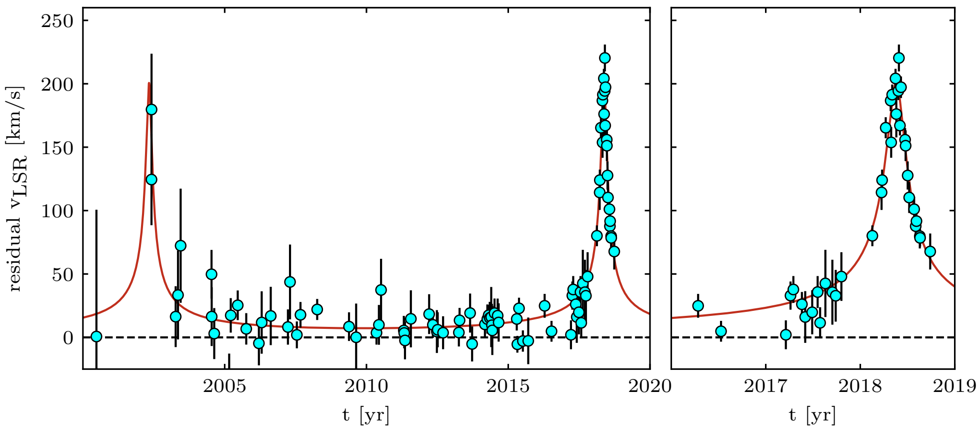

Figure 5.6: Update of the posterior analysis of Gravity Collaboration et al., 2018b. The panels show the residuals of the radial velocity data to the best-fit orbit in which post-fit the redshift and transverse Doppler effect were turned off (line at 0, $f_{\text{redshift}} = 0$). The 2018 data show a highly significant excursion. The red line gives the orbit with $f_{\text{redshift}} = 1$. General relativity is an excellent description for the residuals.

5.4.3 UPDATE ON THE GRAVITATIONAL REDSHIFT IN S2

With the new data sets in hand, we repeated the posterior analysis of Gravity Collaboration et al., 2018b to determine the combined effect of gravitational redshift and transverse Doppler effect. Using an orbit model including the first-order correction due to the Schwarzschild metric and including the Rømer delay, we find $f_{\text{redshift}} = 1.047 \pm 0.052$ for the noise model fit and $f_{\text{redshift}} = 1.036 \pm 0.052$ when we use the down-sampled data set. Figure 5.6 shows the radial velocity residuals to the classical part of the true best-fit orbit. For this we set $f_{\text{redshift}} = 0$ without refitting after fitting with $f_{\text{redshift}} = 1$. We compared these residuals to the true model (i.e., with the effects turned on,$f_{\text{redshift}} = 1$). We exclude that purely Newtonian physics can describe our data at a significance level of 20σ.

5.4.4 DISTANCE ESTIMATE WITHOUT RADIAL VELOCITIES

Our GRAVITY measurement also provides the first direct distance measurement from orbital motion without the need for radial velocities. The key for this is the Rømer effect: The light travel time across the orbit causes astrometric points to appear slightly ahead or lagging behind the orbit, depending on whether S2 is in front of or behind Sgr A*. For a Keplerian orbit with astrometric data only and no light-time travel effect, the distance cannot be determined. The best-fit mass and distance are degenerate along a line $M \propto R_0^3$. Because the light travel time across the orbit between 2017 and 2018 (where we have

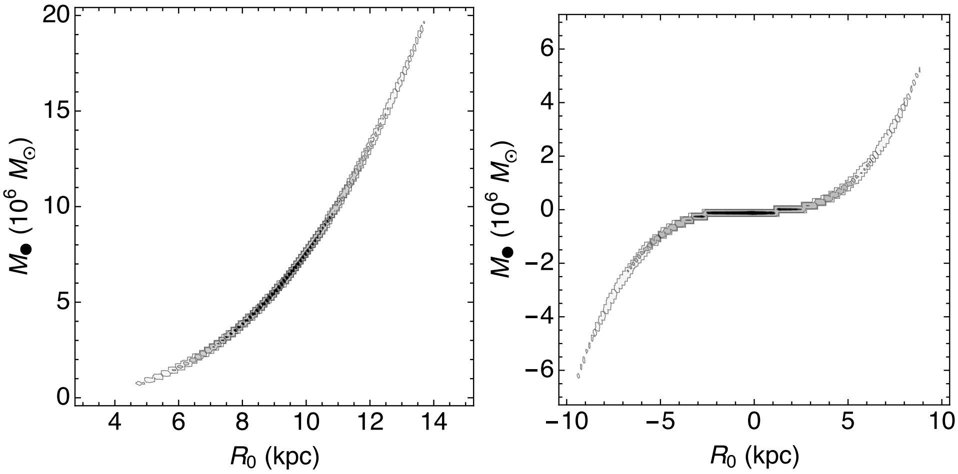

Figure 5.7: Posterior distributions for the data set without radial velocities. Left: Using the correct orbit model. Right: Using an orbit model that neglects the Rømer effect. In this plot we allowed negative distances (and correspondingly negative masses) to avoid having a bound of the parameter space at 0, where the actual maximum of the distribution falls.

GRAVITY data) is about three days and because we can detect the daily motion of S2 in the GRAVITY data, our astrometry breaks the degeneracy. Figure 5.7 (left) shows that this is indeed the case. The best-fit distance for this case is $R_0 = 9.5 \pm 1.5\,\mathrm{kpc}$, consistent with our best estimate. To our knowledge, Anglada-Escudé and Torra, 2006 were the first to propose this type of distance measurement, but we are not aware of an application anywhere so far.

If we were to ignore the Rømer effect for the purely astrometric data set, we would not obtain as a return a fully degenerate mass-distance relation. Instead, the fit then tries to become as small a distance as possible (figure 6, right), that is, in the sense of a limit, we obtain $R_0 \to 0$. This is where the light travel time effect is minimal, as imposed by the wrong orbit model without Rømer delay. This just shows in a different way that our astrometry requires a finite speed of light and thus can estimate R_0.

5.5 DISCUSSION

The best estimate for R_0 from Bland-Hawthorn and Gerhard, 2016 using only their set of ten independent best measurements that did not invoke Sgr A* is $R_0 = 8210 \pm 80\,\mathrm{pc}$, in perfect agreement with our value. This means that Sgr A* is indeed at the center of the Milky Way bulge.

Our value of R_0 together with the proper motion of Sgr A* of $6.379 \pm 0.026\,\mathrm{mas/yr} = 30.24 \pm 0.12\,\mathrm{km/s/kpc}$ from Reid and Brunthaler, 2004 implies $\Theta_0 + V_\odot = 247.4 \pm 1.4\,\mathrm{km/s}$, where Θ_0 is the rotation speed of the local standard of rest (LSR) and $V_\odot$ is the peculiar solar motion toward $l = 90°$. The error on $\Theta_0 + V_\odot$ is composed roughly equally of the error in the proper motion of Sgr A* and the uncertainty in R_0. This constraint on $\Theta_0 + V_\odot$ is compatible with the recent determination from Hayes et al., 2018, who found $\Theta_0 + V_\odot = 253 \pm 6\,\mathrm{km/s}$ from Gaia astrometry of the Sgr stream.

Bland-Hawthorn and Gerhard, 2016 estimate $V_\odot = 11 \pm 2\,\mathrm{km/s}$, but to take into account the radial variations in the median v_ϕ seen by Gaia Collaboration et al., 2018, we used a total uncertainty of $4\,\mathrm{km/s}$. Together with our estimate for $\Theta_0 + V_\odot$ this implies $\Theta_0 = 236.9 \pm 4.2\,\mathrm{km/s}$. From combining Gaia DR2 and APOGEE data, Eilers et al., 2019 found $\Theta_0 = 229 \pm 6\,\mathrm{km/s}$, where the error is the reported systematic uncertainty. Wegg et al., 2019 used Gaia DR2 and RR Lyrae stars to derive $\Theta_0 = 217 \pm 6\,\mathrm{km/s}$. Using trigonometric parallaxes of high-mass star-forming regions, Reid et al., 2014 find $\Theta_0 = 240 \pm 8\,\mathrm{km/s}$.

Another remarkable result is the fact that the offset in the radial velocity, vz_0, is small and consistent with zero. The offset absorbs any possible systematic offset in the radial velocity.

- The surface gravity of S2 contributes $\Delta vz_0 = GM_{\mathrm{S2}}/r_{\mathrm{S2}}c = 1.6\,\mathrm{km/s}$ (Lindegren and Dravins, 2003), where we used r_{S2}, the radius of S2, and M_{S2}, its mass, from Habibi et al., 2017.

- The contribution of the Galactic potential can be approximated by $\Delta vz_0 = v_\odot^2/c \ln(R_0/R_{\mathrm{S2}})$, where $v_\odot$ is the Sun's circular galactocentric speed and R_{S2} is the galactocentric radius of S2 (Lindegren and Dravins, 2003). The approximation surely does not hold inside the sphere of influence of Sgr A* ($\approx 3\,\mathrm{pc}$), where the massive black hole dominates the potential. However, because of the logarithm in the expression, the actual effective value for R_{S2} does not matter strongly. With $v_\odot \approx 230\,\mathrm{km/s}$ and $R_{\mathrm{S2}} = 3\,\mathrm{pc}$, we obtain $\Delta vz_0 = 1.4\,\mathrm{km/s}$, and when we use the apocenter distance $R_{\mathrm{S2}} = 0.009\,\mathrm{pc}$, the number is $\Delta vz_0 = 2.4\,\mathrm{km/s}$.

- Frame-dragging by a maximally spinning black hole might contribute an average $\lesssim 0.2\,\mathrm{km/s}$ to the redshift (Angélil et al., 2010; Grould et al., 2017).

- Light bending and Shapiro delay reach $\lesssim 4\,\mathrm{km/s}$ (Angélil et al., 2010) but are highly peaked around pericenter and flip sign, so that they do not induce a bias on vz_0.

- Contributions from the solar system are around $3\,\mathrm{m/s}$, and thus negligible.

A similarly sized offset in vz_0 might arise from the uncertainty of the construction of the LSR, which by its original definition should not include a motion component in the radial direction, $U_{\mathrm{LSR}} = 0$. The LSR correction applied to our data uses the values from Schönrich et al., 2010, who reported $U_\odot = 11.10^{+0.69}_{-0.75}\,\mathrm{km/s}$, where $U_\odot$ is the solar motion in the direction of the GC. In their review, Bland-Hawthorn and Gerhard, 2016 concluded that this was $U_\odot = 10.0 \pm 1.0\,\mathrm{km/s}$. The variations in the median radial velocity of stars measured by Gaia Collaboration et al., 2018 in the nearby disk suggest that U_{LSR} is uncertain on the scale of several km/s.

Furthermore, an offset in vz_0 could be due to the intrinsic motion of Sgr A* with respect to the Milky Way. Reid and Brunthaler, 2004 measured the motion of Sgr A* perpendicular to the Galactic plane to be $0.4 \pm 0.9\,\mathrm{km/s}$. For the third dimension, the motion along the Galactic plane, Reid et al., 2009 reported $-7.2 \pm 8.5\,\mathrm{km/s}$, and the update in Reid et al., 2014 implies tighter constraints around $2 - 3\,\mathrm{km/s}$. The expected "Brownian motion" of Sgr A* that is due to scattering with stars in its vicinity is even slightly smaller than these limits with $0.2\,\mathrm{km/s}$ (Chatterjee et al., 2002; Merritt et al., 2007).

The parameter vz_0 is the sum of these offsets. Our fit results and the two redshift terms yield a value of $\approx -6 \pm 6\,\mathrm{km/s}$. The uncertainty on this number is larger than the fit error because of the systematic uncertainties, such as the actual value for the Galactic potential that is used for S2, but also the systematic uncertainties in the wavelength calibration. The most likely reason why the sum is small is that the summands are small. Under this hypothesis, we conclude that to within a few km/s, Sgr A* is at rest at the center of the Milky Way and that the LSR is moving tangentially. The value is lower than might be expected from the combined effect of Galactic bar and spiral arms; however, their quantitative effect on the velocity streamlines at the solar position is not well known.

Our data very strongly constrain the angular diameter of Sgr A*. Because mass and R_0 are correlated, the constraint is stronger than what simple error propagation would yield. We find $R_S/R_0 = 10.022 \pm 0.020_{\mathrm{stat.}} \pm 0.032|_{\mathrm{sys.}}\,\mu\mathrm{as}$. The combined uncertainty corresponds to 50000 km at our R_0. This sets a strong prior for the analysis of data obtained from global millimeter very long baseline interferometry that aims at resolving Sgr A* (Falcke et al., 2000; Doeleman et al., 2009).

A potential caveat of our analysis might be that the physical model of the orbit is too simple. So far, S2 did not reveal any signs of binarity. For GRAVITY, S2 is an unresolved point source (Gravity Collaboration et al., 2017). The resolution of GRAVITY in GC observations is about $2.2\,\mathrm{mas} \times 4.7\,\mathrm{mas}$, excluding a source extension larger than or a companion farther away than $\approx 1\,\mathrm{mas}$. Chu et al., 2018 used the radial velocity data of S2 and reported an upper limit of $M_{\mathrm{companion}} \sin i \le 1.6 M_\odot$ for periods between 1 and 150 days. Longer periods would not be stable against tidal break-up. Furthermore, the motion of either S2 or Sgr A* could be affected by as yet unknown massive objects in the GC. To some extent, such a perturbation can always be absorbed into the orbital elements (Gualandris et al., 2010), resulting in biased estimates for the parameters. According to our current knowledge, S2 is a suitable probe for R_0. It is an ordinary massive main-sequence star of type B0 - B3 (Ghez et al., 2003b; Martins et al., 2008; Habibi et al., 2017). The atmospheric absorption lines we used are expected to be fair tracers of the motion of the star, together with its (unresolved) photocenter.

The value from Boehle et al., 2016, $R_0 = 7.86 \pm 0.14 \pm 0.04\,\mathrm{kpc}$, disagrees with our result. However, it comes from a combined fit of the stars S2 and S38. The S2-only result of these authors is $R_0 = 8.02 \pm 0.36 \pm 0.04\,\mathrm{kpc}$, which is completely consistent with our result. Furthermore, we note that combining different stars in the orbit fit tends to change the parameter mass and R_0 by rather large amounts (Gillessen et al., 2017) because small inconsistencies in the data sets are amplified by the fact that in the mass-R_0 plane two narrow, curved posterior distributions are combined. The statistical error of a combined fit does not catch this and could thus miss part of the true uncertainties.

Overall, we used accurate radial velocities from SINFONI and proper motions from GRAVITY of the star S2 as it orbits Sgr A* to set the absolute size of the orbit and determine the distance to the GC with unprecedented accuracy to $R_0 = 8178\,\mathrm{pc}$. The statistical error is only 13 pc and is dominated by the measurement errors of the radial velocities. The systematic error of 22 pc is dominated by the calibration uncertainties of the astrometry. Our analysis also demonstrates that the relative velocity of the LSR along the line of sight to Sgr A* is consistent with zero to within a few km/s, implying that Sgr A* is at rest in the GC and the LSR is moving tangentially. The addition of further SINFONI and GRAVITY data taken in 2018 also allowed us to increase the significance of the previously published measurement of the gravitational redshift caused by Sgr A* to 20σ.

ACKNOWLEDGMENTS

We are very grateful to our funding agencies (MPG, ERC, CNRS, DFG, BMBF, Paris Observatory, Observatoire des Sciences de l'Univers de Grenoble, and the Fundação para a Ciência e Tecnologia), to ESO and the ESO/Paranal staff, and to the many scientific and technical staff members in our institutions who helped to make NACO, SINFONI, and GRAVITY a reality. S.G. acknowledges support from ERC starting grant No. 306311 (PROGRESO). F.E. and O.P. acknowledge support from ERC synergy grant No. 610058 (BlackHoleCam). J.D., M.B., and A.J.-R. were supported by a Sofja Kovalevskaja award from the Alexander von Humboldt foundation. A.A. and P.G. acknowledge support from FCT-Portugal with reference UID/FIS/00099/2013.

APPENDIX

5.A RADIAL VELOCITIES FROM SINFONI

For the SINFONI data we improved the wavelength calibration. Explicitly, we modified our atmospheric line list that serves as reference for the wavelength calibration by excluding double lines or lines with a low signal-to-noise ratio (S/N) following the line atlas of Rousselot et al., 2000. We also improved the fine-tuning of the spectrum to the OH lines, leading to an improved wavelength dispersion solution. With these changes, we typically achieved a calibration error of below 2 km/s, measured by the residuals of the OH lines. With the improved data reduction, we re-reduced all available data since October 2004. The earlier data (two epochs in 2004 and one in 2003) were obtained during commissioning time and need a dedicated calibration procedure, which we did not repeat. We combined data from different nights when the expected velocity change was smaller than the calibration error. We omitted one measurement from 2008 with low S/N (from a single ten-minute exposure) and included one more epoch from 2009 and 2015 each and two more from 2010 and 2011 each. We split up data that previously were combined into one cube into two epochs in two occasions, in 2013 and 2015.

For spectra in which both the He-I line (2.112 μm) and Brackett-γ (2.166 μm) lines are unaffected by atmospheric residuals, we used template fitting to determine the radial velocities. For this we fit the long-time average S2 spectrum (Habibi et al., 2017) to the data. For spectra with sufficient S/N and no artifacts (e.g., from imperfect atmosphere correction), template fitting yields more accurate velocities. When either of the lines showed artifacts, we fit a double-Voigt profile to the other unaffected line.

The errors are a combination of fit error and wavelength calibration uncertainty. The fit error is obtained from the formal fit error σ, the S/N, and by varying the pixel selection. For the S/N-related error we established a relation between σ and S/N of $\sigma \propto \mathrm{S/N}^{-0.92}$. The 1 / S/N behavior is consistent with the uncertainty of a centroid fit (Fritz et al., 2010). To assess the impact of different background subtractions and extraction regions, we extracted eight spectra for each observation and determined the standard deviation of the radial velocities from the different masks. Because these three error estimates are strongly correlated, we used the largest of the three as fit error. We linearly added the wavelength calibration error to obtain a preliminary error.

These preliminary errors establish the relative weight of the different radial velocities. Using these, we obtained a preliminary orbit fit, which showed that we overestimated the errors because the residuals around the best preliminary fit are on average 76.8% of the errors. Thus we rescaled the errors by that factor.

With this improvement of the SINFONI analysis, we reach an error of $\approx 7\,\mathrm{km/s}$ for the best data. The median error is $12.3\,\mathrm{km/s}$, which is an improvement by 46% compared to the previous set of radial velocity data.

5.B ASTROMETRY FROM GRAVITY DATA

5.B.1 DATA SELECTION

We started from all observations of Sgr A* or S2 (793 exposures, each $30 \times 10\mathrm{s} = 5\,\mathrm{min}$ on source, i.e., a total of 66 hours on source), regardless of observing conditions and instrument performance.

In 2017, S2 was still at a distance of $54 - 67\,\mathrm{mas}$ from Sgr A*, which is comparable to the photometric field of view (FWHM$\approx 65\,\mathrm{mas}$), and too little flux from Sgr A* was injected into the fibres of the exposure pointing on S2 for a reliable interferometric binary signature (Perrin and Woillez, 2019). We therefore only considered the observations centered on Sgr A* (261 exposures). We furthermore rejected all Sgr A* observations for which the instrument internal pupil control (Gravity Collaboration et al., 2017) reported an error $> 6\,\mathrm{cm}$ for any of the telescopes (12 exposures) or for which the pointing of any telescope was too far from Sgr A* (83 exposures). We used a box spanning ΔR.A.$= -45\,...10\,\mathrm{mas}$, ΔDec.$= -30\,...30\,\mathrm{mas}$ around Sgr A*, which especially avoided pointings toward the opposite side of S2. This selection keeps 166 exposures in 2017.

For 2018, we had 373 exposures on Sgr A*. Again, we rejected exposures with pupil errors $> 6\,\mathrm{cm}$ (18 exposures). Because of a newly introduced laser-metrology guiding with substantially improved pointing accuracy, we rejected exposures already when the estimated pointing error for any telescope was outside Δ R.A. / Δ Dec.$= -10\,...10\,\mathrm{mas}$ around Sgr A* (35 frames). Because S2 was always closer than $23\,\mathrm{mas}$ to Sgr A* during our March - June 2018 observing campaigns, both sources were well within the photometric field of view. We also used the 43 exposures centered on S2 that were obtained during this period. Out of these observations, we rejected three exposures because of a pupil error $> 6\,\mathrm{cm}$, and five exposures because of a pointing error larger Δ R.A. / Δ Dec.$= -10\,...10\,\mathrm{mas}$. This yields a total of 355 exposures in 2018.

5.B.2 BINARY FITTING AND CORRECTION FOR ATMOSPHERIC REFRACTION

In a second step, three independent subgroups fit the individual exposures with a binary model as described in Gravity Collaboration et al., 2018b; Gravity Collaboration et al., 2018a, using three different codes ("Waisberg (W)", "Pfuhl (P)", "Rodriguez-Coira (R)"). The codes differ in detail in the relative weighting of closure-phases, visibilities, and square visibilities, the free fit parameters (e.g., color of Sgr A* or flux ratio per telescope), and the numerical implementation (e.g., least-squares minimization or MCMC), but give overall consistent results for the binary separations.

We furthermore corrected each binary fit for the differential atmospheric refraction between the comparably "blue" S2 and "red" Sgr A* (see Appendix A7.4 of Gravity Collaboration et al., 2018a). Because Sgr A* was in its faint quiescent state for most of our observations, we used the redder low-flux spectral index $S_\nu \propto \nu^{-1.6}$ from Witzel et al., 2018 for the subsequent analysis. With $S_\nu \propto \nu^2$ for S2, and for the given effective spectral resolution of 127 nm (low-resolution mode of GRAVITY), the difference in effective wavelength between S2 and Sgr A* is $\Delta\lambda = 2.2\,\mathrm{nm}$, and the resulting atmospheric differential refraction is $\Delta R = 45\,\mu\mathrm{as}\ /\ \mathrm{nm} \times \Delta\lambda \tan z = 99\,\mu\mathrm{as} \tan z$, where z is the zenith distance. Because we typically observed the GC close to zenith, the atmospheric differential refraction was on average only $30\,\mu$as, and often with opposite signs during a night, which resulted in a mean correction of ΔR.A. $= -1\,\mu$as and ΔDec.$= -5\,\mu$as.

5.B.3 OUTLIER REJECTION AND NIGHTLY AVERAGING

For each of the three sets of binary fits we determined a preliminary orbit for error scaling and outlier rejection. We rejected observations for which the residuals were outside the 80% quantile constructed in the 2D error-normalized position residual plane[2]. The final data set contains 818 (W), 795 (P), and 737 (R) binary fits, corresponding to about 400 exposures of five minutes each, that is, about 33 hours on source. We combined these and derived nightly (error-weighted) mean and standard errors (with variance weights). Only in the few cases when we had fewer than ten binary-fits per night (26/27 March 2017, 28/29 March 2017, 10/11/12 July 2017) did we combine several nights to one average. The statistical 1D astrometric error of these combined nightly averages is between $10 - 110\,\mu$as.

[2]The 80% quantile area was constructed using the Mathematica-based quantile regression package https://raw.githubusercontent.com/antononcube/MathematicaForPrediction/master/QuantileRegression.m, Version 1.1, written by Anton Antonov.

5.B.4 CORRECTION FOR EFFECTIVE WAVELENGTH, SYSTEMATIC ERROR, AND FINAL ERROR SCALING

In a last step we corrected the nightly average separation for the effective wavelength shift of 2.3 nm (0.1%) between the wavelength calibration with our 2800 K calibration lamp and the very red highly dust obscured S2/Sgr A* data (see Appendix A7.2 in Gravity Collaboration et al., 2018a).

To account for the systematic error in the wavelength calibration, which we estimate to be 1/20 detector pixel, or equivalently, 2.5 nm, we added in square the corresponding scale error of 0.11%. This error in the effective wavelength translated into an astrometric error of about 10 μas for the time around peri-passage, and up to ΔR.A. $= 66\,\mu$as and ΔDec. $= 33\,\mu$as for March 2017, when the S2-Sgr A* distance was largest in our observations.

Finally, to account for unknown additional errors, we scaled the GRAVITY astrometric errors by a factor 2.2 to match the residuals of a best-fitting preliminary orbit. The resulting astrometric errors around the S2 peri-passage in our data from 24 April - 27 June 2018 are ΔR.A. $= 22 - 101\,\mu$as and ΔDec. $= 38 - 112\,\mu$as, with a mean of 51 μas and 60 μas, respectively.

5.C SYSTEMATIC ERROR OF THE GRAVITY ASTROMETRY

We obtained the GRAVITY astrometry in the single-field mode. S2 and Sgr A* were close enough in 2017 and 2018 to be fed into the interferometer by a single fiber, the acceptance aperture of which was matched to the telescope point spread function of ≈ 65 mas. The two sources appear as an interferometric binary to GRAVITY, which means that none of the more complex dual-beam aspects of the instrument (Gravity Collaboration et al., 2017) enter the measurement. The standard equation of interferometric astrometry $\Delta\mathrm{OPD} = \vec{s} \times \vec{B}$ sets the effective image scale, where $\vec{B}$ is the baseline and $\vec{s}$ is the separation vector that is to be measured. The accuracy of the interferometric baselines and how well we can measure the OPD thus set the accuracy of $\vec{s}$.

The value for the baseline length to use is the so-called "imaging baseline" in the sense of Woillez and Lacour, 2013 and Lacour et al., 2014. The telescope position is then defined by the photocenter of the entrance pupil plane appodized by the fiber mode in the pupil plane. While the telescope geometry is known to the millimeter level, the active mirrors controlling the fiber mode to pupil overlap are more critical and actually limit the baseline accuracy. A systematic error occurs from how well the fiber mode is aligned with the reference point of the pupil tracker. A vignetting of the pupil would also bias the baselines. For an error estimate we used the stability of the pupil position, assuming that the alignment uncertainties overall are at that level. It amounts to 4 cm in the primary mirror space. For the mean baseline length of 81.2 m, an error of 4 cm corresponds to 0.05% or 4 pc on R_0.

The wavelength accuracy of the effective wavelengths sets the accuracy of the OPD. From the standard calibrations of GRAVITY, we estimate that the wavelength accuracy of the interferogram pixels is 0.11% or 9 pc on R_0. This is owing to the faintness of S2 (for interferometric standards), which dictates that we need to observe S2 in low-resolution mode with $R \approx 22$, which corresponds to a wavelength sampling of 50 nm/pixel.

When the results from the three subgroups and fitting codes are analyzed separately, the standard deviation in the best estimate R_0 is 16 pc. This takes care of the uncertainty in the binary model fit to the GRAVITY data. The difference between the objective outlier rejection and the manual frame selection of GRAVITY collaboration (2018a) results in a difference in R_0 of 15 pc. For this estimate, we carried forward the analysis of Gravity Collaboration et al., 2018b with the new data up to the end of 2018 and included the atmospheric refraction effects. This error, however, is not independent of the error from the fitting by subgroups, and we include the larger of the two (16 pc).

The color difference of S2 and Sgr A* is not known very well, and we include the difference in R_0 determined with and without correction of the atmospheric differential dispersion in our error. It amounts to 5 pc. Adding the different contributions in quadrature, we conclude that the total systematic error on the astrometry is 19 pc, which corresponds to 0.24%.

5.D FULL POSTERIOR DENSITY

In Figure 5.8 we show the full set of posterior densities as obtained from the MCMC sampler with N=200000 for the down-sampled data set. All parameters are well determined.

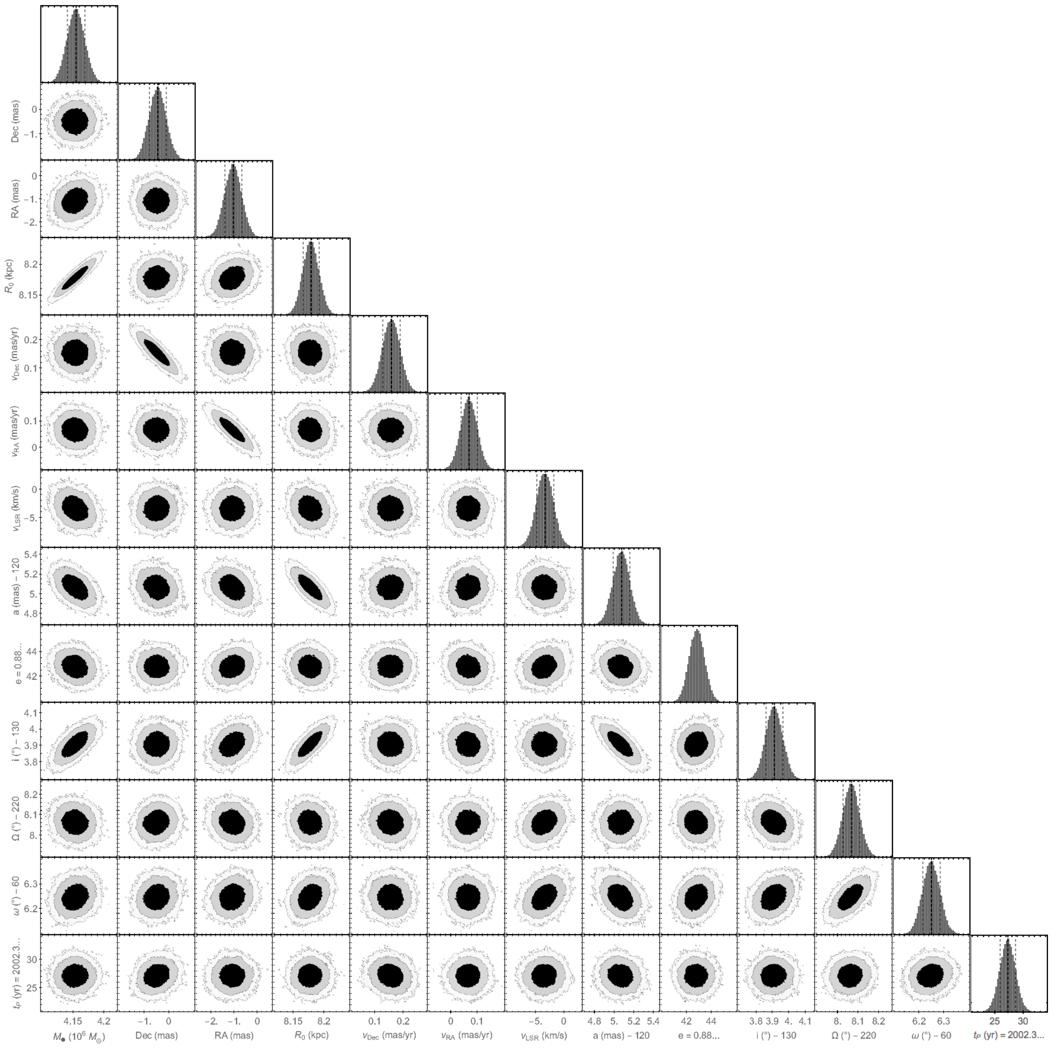

Figure 5.8: Full set of posterior densities as obtained from the MCMC sampler with N=200000, here for the down-sampled data set. The contour lines mark the 1, 2, and 3σ levels.

IMPROVED GRAVITY ASTROMETRIC ACCURACY FROM MODELING OF OPTICAL ABERRATIONS 6

Original Publication: GRAVITY Collaboration, R. Abuter, A. Amorim, M. Bauböck, J.P. Berger, H. Bonnet, W. Brandner, Y. Clénet, R. Davies, P.T. de Zeeuw, J. Dexter, Y. Dallilar, A. Drescher, A. Eckart, F. Eisenhauer, N.M. Förster Schreiber, P. Garcia, F. Gao, E. Gendron, R. Genzel, S. Gillessen, M. Habibi, X. Haubois, G. Heißel, T. Henning, S. Hippler, M. Horrobin, A. Jiménez-Rosales, L. Jochum, L. Jocou, A. Kaufer, P. Kervella, S. Lacour, V. Lapeyrère, J.-B. Le Bouquin, P. Léna, D. Lutz, M. Nowak, T. Ott, T. Paumard, K. Perraut, G. Perrin, O. Pfuhl, S. Rabien, G. Rodríguez-Coira, J. Shangguan, T. Shimizu, S. Scheithauer, J. Stadler, O. Straub, C. Straubmeier, E. Sturm, L.J. Tacconi, F. Vincent, S. von Fellenberg, I. Waisberg, F. Widmann, E. Wieprecht, E. Wiezorrek, J. Woillez, S. Yazici, A. Young, G. Zins
Corresponding Authors: F. Widmann, J. Stadler
DOI: 10.1051/0004-6361/202040208

Abstract: The GRAVITY instrument on the ESO VLTI pioneers the field of high-precision near-infrared interferometry by providing astrometry at the $10 - 100\,\mu$as level. Measurements at such high precision crucially depend on the control of systematic effects. Here, we investigate how aberrations introduced by small optical imperfections along the path from the telescope to the detector affect the astrometry. We develop an analytical model that describes the impact of such aberrations on the measurement of complex visibilities. Our formalism accounts for pupil-plane and focal-plane aberrations, as well as for the interplay between static and turbulent aberrations, and successfully reproduces calibration measurements of a binary star. The Galactic Center observations with GRAVITY in 2017 and 2018, when both Sgr A* and the star S2 were targeted in a single fiber pointing, are affected by these aberrations at a level of less than 0.5 mas. Removal of these effects brings the measurement in harmony with the dual beam observations of 2019 and 2020, which are not affected by these aberrations. This also resolves the small systematic discrepancies between the derived distance R_0 to the Galactic Center reported previously.

6.1 INTRODUCTION

The distance to the Galactic Center (GC), R_0, can be measured directly from stellar orbits around Sgr A*, the radio source associated with the GC massive black hole (MBH) (see e.g. Genzel et al., 2010; Bland-Hawthorn and Gerhard, 2016, for a recent overview of alternative methods). To this end, the star's proper motion, given in angle per unit time, is compared to its radial velocity, obtained in absolute length per units time from spectroscopic observations. The GC distance then follows directly as a scaling parameter between the two measurements. Most suited to measure R_0 is S2, a massive young main sequence B-star on a 16-year orbit with semi-major axis $a \simeq 125\,\mathrm{mas}$ and apparent K-band magnitude $m_k \simeq 14$ (Ghez et al., 2003b; Eisenhauer et al., 2005; Martins et al., 2008; Gillessen et al., 2009b; Gillessen et al., 2017; Habibi et al., 2017). During its pericenter passage in 2018, S2 was closely monitored in astrometry and spectroscopy (Gravity Collaboration et al., 2018b; Do et al., 2019). In particular, the GRAVITY instrument (Gravity Collaboration et al., 2017) directly measured the distance between S2 and Sgr A* during the fly-by at high angular resolution of around $30\,\mu\mathrm{as}$. The combination of ultra-high astrometric precision from near-infrared interferometry and the spectroscopic precision of $\lesssim 10\,\mathrm{km/s}$ allowed to determine the GC distance at the unprecedented precision of $< 1\%$ (Gravity Collaboration et al., 2019).

Operating in the K-band, GRAVITY combines the light from either the four Unit Telescopes (UTs) or Auxiliary Telescopes (AT) of the ESO Very Large Telescope Interferometer (VLTI). Fringe tracking on a bright reference object allows for minute-long integration times on the fainter science target and for the measurement of differential complex visibilities. The instrument's extremely high angular resolution of $\simeq 3\,\mathrm{mas}$ results in very accurate astrometry with error bars between $10\,\mu\mathrm{as}$ and $100\,\mu\mathrm{as}$ (Gravity Collaboration et al., 2017). However, the latest R_0 measurement in Gravity Collaboration et al., 2020a indicates a possible systematic difference with earlier determinations (Gravity Collaboration et al., 2018b; Gravity Collaboration et al., 2019). While the shift is small, of $\mathcal{O}\,(1\%)$ only, it is nevertheless significant due to the high precision of the measurement.

The difference in the measured GC distance coincides with a change in the observing mode. GRAVITY observes the Galactic Center with two different methods, depending on the separation between Sgr A* and S2. Close to pericenter passage, i.e. in 2017 and 2018, the sources are detected simultaneously in a single fiber pointing in the so-called single-beam mode. In later epochs, their separation exceeds the fiber's field of view (FOV), and S2 and Sgr A* are targeted individually. This is referred to as dual-beam mode.

In single-beam mode, it is not possible to align the two sources with the fiber center. Hence, to further improve the GRAVITY astrometry, we conducted an analysis of how optical aberrations affect the visibility measurement across the full field of view. A similar concept of field-dependent errors already exist in radio interferometry, where it is known as direction dependent effects (DDEs) (see e.g. Bhatnagar et al., 2008; Smirnov, 2011; Smirnov and Tasse, 2015; Tasse et al., 2018, and references there in). The DDEs can arise either at the instrument level from the antenna beam pattern or at the atmospheric level such as from the ionosphere. In particular for the latest generation of interferometers (e.g. VLA, Meerkat, LOFAR) with a wide FOV and a large fractional bandwidth DDEs cannot be neglected. However, to our knowledge there is no equivalent discussion in the context of optical/near-IR interferometry.

Indeed, our analysis shows that small optical imperfections in the beam combiner induce field-dependent phase errors that reflect in the inferred binary separation. We developed an analytical model to describe this effect, and verified it by application to a dedicated test-case observation. Applied to the GC observations, the model induces a shift in the S2 relative position of order $0.1 - 0.2$ mas in 2018 and ~ 0.5 mas in 2017 in both right ascension (R.A.) and declination (Dec.). Despite being small, the change is non-negligible at the high astrometric accuracy achieved by GRAVITY. We can show that the corrected 2017 and 2018 data is in harmony with the dual-beam observations of 2019 and 2020. Further, when retroactively applying the correction to the data sets used in Gravity Collaboration et al., 2018b; Gravity Collaboration et al., 2019, the ensuing GC distance is fully consistent with the latest result (Gravity Collaboration et al., 2020a).

We introduce the analytical model in section 6.2 and compare it to calibration measurements in section 6.3. Verification from the binary test-case and the improved S2 position are presented in Sec. section 6.4, while we discuss the implications for the GC distance in section 6.5. Finally, we conclude in section 6.6.

6.2 FORMAL DESCRIPTION OF STATIC ABERRATIONS

Formal description of static aberrations and their impact on visibility measurements Static aberrations along the instrument's optical path affect the measured visibilities by introducing a complex, field-dependent factor for each telescope. We express this gain in its polar representation and decompose it into a phase map $\phi_i(\vec{\alpha})$ and an amplitude map $A_i(\vec{\alpha})$. Here, the index i labels the telescope and $\vec{\alpha}$ denotes positions in the image plane. Phase and amplitude maps lead to a modification of the observed complex visibilities V^{obs}

from the well-known van Cittert-Zernike theorem (c.f. Equation 6.23). As we demonstrate in the following, they are given by

$$V^{\mathrm{obs}} = \frac{\int d\vec{\alpha}\, A_i\left(\vec{\alpha}\right) A_j\left(\vec{\alpha}\right) O\left(\vec{\alpha}\right) e^{-2\pi i\, \vec{\alpha}\cdot\vec{b}_{i,j}/\lambda + i\left(\phi_i\left(\vec{\alpha}\right)-\phi_j\left(\vec{\alpha}\right)\right)}}{\sqrt{\int d\vec{\alpha}\, A_i^2\left(\vec{\alpha}\right) O\left(\vec{\alpha}\right)\ \int d\vec{\alpha}\, A_j^2\left(\vec{\alpha}\right) O\left(\vec{\alpha}\right)}}\,, \tag{6.1}$$

where $\vec{b}_{i,j}$ is the baseline vector between the two telescopes and $O\left(\vec{\alpha}\right)$ denotes the intensity distribution of the observed astronomical object.

In this section, we show how the phase- and amplitude-maps follow from optical aberrations. To this end, we start from the overlap integral, which determines the electromagnetic field from a single telescope arriving at the beam combiner. Subsequently, we propagate the effect of static aberrations from the overlap integral to the measured complex visibility to arrive at a rigorous derivation of Equation 6.1. Finally, we account for the superposition of static and turbulent aberrations, to obtain a formalism which is applicable in realistic observation scenarios.

6.2.1 STATIC, FIELD-DEPENDENT ABERRATIONS AT FIBER INJECTION

Single mode fibers transport the light collected by each telescope E_{tel} to the beam combiner instrument. The overlap integral between light and the fiber mode E_{fib} then determines the transmitted electric field (Neumann, 1988),

$$E\left(\vec{\beta}\right) = E_{\mathrm{fib}}\left(\vec{\beta}\right) \times \eta = E_{\mathrm{fib}} \times \int d\vec{\xi}\, E_{\mathrm{tel}}\left(\vec{\xi}\right) E_{\mathrm{fib}}^{*}\left(\vec{\xi}\right)\,. \tag{6.2}$$

Here, we assume a normalized fiber mode $\int d\vec{\xi} \left|E_{\mathrm{fib}}\left(\vec{\xi}\right)\right|^2 = 1$ and express image-plane positions by two-dimensional vectors, $\vec{\xi}$ and $\vec{\beta}$. Following the description of Perrin and Woillez, 2019, the overlap integral is converted to the pupil plane by the Parseval-Plancharel theorem,

$$\eta = \int d\vec{u}\ \mathcal{F}^{-1}\left[E_{\mathrm{obj}}\right] P\left(\vec{u}\right)\ \mathcal{F}^{-1}\left[E_{\mathrm{fib}}^{*}\right]\left(\vec{u}\right)\,, \tag{6.3}$$

where $\mathcal{F}^{-1}$ denotes the inverse Fourier transform, i.e. transformation from the image to the pupil plane, and E_{obj} the light emitted by the astronomical object. The latter is connected to $\mathcal{F}^{-1}\left(E_{\mathrm{tel}}\right)$ by multiplication with the pupil function $P\left(\vec{u}\right)$, corresponding to a convolution in the image plane. In the most simple case of a single point source located at $\vec{\alpha}_0$, the light is described by a pure phase $\mathcal{F}^{-1}[E_{\mathrm{obj}}^{\mathrm{ps}}] = \exp\left(-2\pi i\, \vec{u}\cdot\vec{\alpha}_0\right)$. The pupil- and image-plane coordinates, $\vec{\xi}$ and $\vec{u}$ respectively, are Fourier-conjugate to each other and chosen to be dimensionless. That is, any length scale in the pupil plane is given by λu where λ refers to the wavelength and $u = |\vec{u}|$. For discussion, we convert the dimensionless image plane coordinates $\vec{\xi}$ to the corresponding angular separation in UT observations. In an aberration-free scenario, the pupil function of a spherical telescope with diameter $2r_{\mathrm{tel}}$ and central obscuration $2r_{\mathrm{cent}}$ simply is

$$\tilde{P}\left(\vec{u}\right) = \begin{cases} 0 & \text{if} \quad u \leq r_{\mathrm{cent}}/\lambda \\ 1 & \text{if} \quad r_{\mathrm{cent}} < u \leq r_{\mathrm{tel}}/\lambda \\ 0 & \text{if} \quad u > r_{\mathrm{tel}}/\lambda \end{cases} . \tag{6.4}$$

Optical aberrations multiply the pupil function by a position-dependent, complex phase, and we here consider the case of purely static aberrations. These are characterized by an optical path difference (OPD) $d_{\mathrm{pup}}\left(\vec{u}\right)$ in the pupil plane that can be expanded in terms of Zernike polynomials Z_n^m,

$$d_{\mathrm{pup}}\left(\vec{u}\right) = \sum_{n=0}^{n_{\max}} \sum_{m=-n}^{n} A_n^m \, Z_n^m \left(\lambda \vec{u}/r_{\mathrm{tel}}\right) . \tag{6.5}$$

We adopt the convention that Z_n^m is dimensionless and the coefficient A_n^m corresponds to the term's root mean square over the unit circle. Defining the turbulence-free complex fiber mode apodised by the pupil function as

$$\Pi_{\circledcirc} = e^{2\pi i \, d_{\mathrm{pup}}(\vec{u})/\lambda} \, \tilde{P}\left(\vec{u}\right) \, \mathcal{F}^{-1}\left[E_{\mathrm{fib}}^{*}\right]\left(\vec{u}\right) , \tag{6.6}$$

the overlap integral reads

$$\eta = \int d\vec{u} \; \mathcal{F}^{-1}\left[E_{\mathrm{obj}}\right]\left(\vec{u}\right) \, \Pi_{\circledcirc}\left(\vec{u}\right) . \tag{6.7}$$

The overlap integral obviously depends on the fiber profile which, for a perfectly aligned ideal single-mode fiber, is

$$\mathcal{F}^{-1}\left[\tilde{E}_{\mathrm{fib}}^{*}\right] = \exp\left(-\frac{\lambda^2 u^2}{2\,\sigma_{\mathrm{fib}}^2}\right) . \tag{6.8}$$

GRAVITY was designed for optimal fiber injection (Pfuhl et al., 2014), which is obtained for $\sigma_{\mathrm{fib}} = 2r_{\mathrm{tel}}\sqrt{2\ln 2}/\left(\pi\epsilon\right)$ (Wallner et al., 2002). Here, the parameter ϵ is of order unity and describes the pupil shape.

From comparison between model predictions and the calibration measurements in subsection 6.3.2, we find that pupil-plane distortions alone are not sufficient to describe the observed aberration pattern. We also need to account for optical errors in the focal plane. Misalignment of the optical fiber, as well as higher order aberrations at fiber injection, introduce a complex phase to Equation 6.8 and can distort the amplitude of the fiber profile.

To illustrate the effect of focal plane aberrations, we first consider the three types of misalignment depicted in Figure 6.1: (A) Lateral misplacement of the fiber by $(\delta x, \delta y)$, which in the pupil plane produces a phase slope $\vec{\xi}_{\mathrm{fib}} = (\delta x/f,\, \delta y/f)$, with f being the focal length. (B) Fiber tilt by an angle $\vec{\varphi}_{\mathrm{fib}} = (\varphi_1, \varphi_2)$ with respect to the optical axis of the system which shifts the back-propagated fiber mode by $\vec{u}_{\mathrm{fib}} = \vec{\varphi} \cdot f/\lambda$. And (C), a defocus or axial fiber misplacement by δz that introduces an additional phase curvature $\exp\left[\pi\, i \delta z \lambda / f^2\, u^2\right]$. Taking all three effects into account, the generalized fiber profile, projected to the pupil, is (Wallner et al., 2002)

$$\begin{aligned}\mathcal{F}^{-1}\left[E^*_{\mathrm{fib}}\right] = \mathcal{F}^{-1}\left[\tilde{E}^*_{\mathrm{fib}}\right](\vec{u} - \vec{u}_{\mathrm{fib}}) \\ \times \exp\left\{-2\pi\, i \left[\frac{\pi \delta z}{2 f^2}\left(\vec{u} - \vec{u}_{\mathrm{fib}}\right)^2 - \vec{\xi}_{\mathrm{fib}} \cdot \left(\vec{u} - \vec{u}_{\mathrm{fib}}\right)\right]\right\} .\end{aligned} \tag{6.9}$$

By rearranging the phase term in the pupil plane, one can decompose it into a piston, tip-tilt and defocus

$$d^{\mathrm{piston}}_{\mathrm{fib}}\left(\vec{u}\right) = -\lambda \left(\frac{\delta z \lambda}{f^2}\, \vec{u}_{\mathrm{fib}} + \vec{\xi}_{\mathrm{fib}}\right) \cdot \vec{u}_{\mathrm{fib}} - \frac{\delta z}{4 f^2}\,, \tag{6.10}$$

$$d^{\mathrm{tip-tilt}}_{\mathrm{fib}}\left(\vec{u}\right) = \lambda \left(\frac{\delta z \lambda}{f^2} \vec{u}_{\mathrm{fib}} + \vec{\xi}_{\mathrm{fib}}\right) \cdot \vec{u}\,, \tag{6.11}$$

$$d^{\mathrm{defocus}}_{\mathrm{fib}}\left(\vec{u}\right) = -\frac{\delta z}{4 f^2}\left(2\lambda^2 \vec{u}^2 - 1\right) . \tag{6.12}$$

The phase terms in Equation 6.10 to 6.12 thus affects the overlap integral in the same way as the lowest-order aberrations in $d_{\mathrm{pup}}\left(\vec{u}\right)$. For the coordinate shift of the Gaussian profile, on the other hand, there is no such correspondence, and it alters the way in which the optical fiber scans the pupil-plane aberrations.

During GRAVITY observations, the misplacement term (A) depends on the performance of the fiber tracker but also on the uncertainty of the source position. In particular for exoplanet observations, the latter can be sizable. Fiber tilt (B) is controlled by the GRAVITY pupil tracker, and the adaptive optics calibration is one example that impacts the defocus (C).

While lateral misplacement (A) and defocus (C) describe the misplacement of a point-like fiber entrance, fiber tilt (B) accounts for the alignment of the fiber's surface. This surface can exhibit irregularities beyond a simple tilt, which lead to a position-dependent OPD in the focal plane, $d_{\mathrm{foc}}\left(\vec{x}\right)$, as illustrated in Figure 6.1. Generally, aberrations from optical elements not conjugated to the pupil are field-dependent and known as Seidel aberrations. In this context, $d_{\mathrm{foc}}\left(\vec{x}\right)$ arising in the focal plane constitutes an extreme example. Still, it is possible to decompose the focal plane distortions into a series of Zernike polynomials, in analogy to Equation 6.5. In this representation, axial fiber

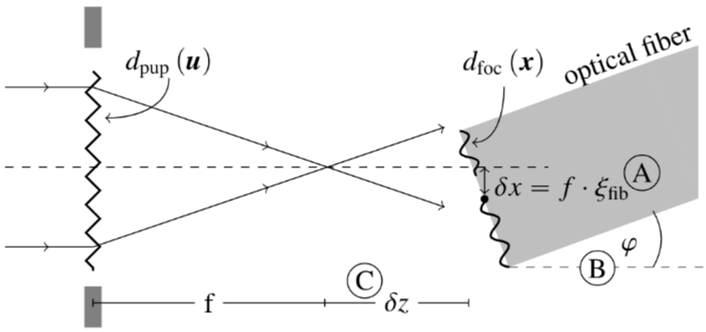

Figure 6.1: Schematic depiction of the pupil and focal plane aberrations which enter the overlap integral. Both effects in combination are required to describe the aberration patterns observed in calibration measurements. The lowest-order aberrations in the pupil function are shown explicitly, which are (A) lateral fiber misplacement, (B) fiber tilt and (C) defocus. Their effect is further explained in the text.

offset (C) and fiber tilt (B) simply correspond to the lowest-order coefficients, and higher-order terms amount to a generalization of Wallner et al., 2002. Again, the phase terms introduced in $\mathcal{F}^{-1}\left[\tilde{E}^*_{\mathrm{fib}}\right]$ by higher order aberrations are degenerate with $d_{\mathrm{pup}}(\vec{u})$, but the amplitude distortions need to be modeled explicitly by themselves.

Finally, for a single point source, located at $\vec{\alpha}_0$ in the image plane, the overlap integral averaged over a time scale much longer than the source's coherence time $\langle ... \rangle_{\mathrm{obj}}$ is

$$\langle \eta^{\mathrm{ps}} \rangle_{\mathrm{obj}} \propto \int d\vec{u}\; e^{-2\pi i\, \vec{u}\cdot\vec{\alpha}_0} \Pi_{\circledcirc}(\vec{u}) = \mathcal{F}\left[\Pi_{\circledcirc}\right](\vec{\alpha}_0)\ . \tag{6.13}$$

Evaluation of the Fourier transform as function of $\vec{\alpha}_0$ results in a two-dimensional complex map. We show several examples of such maps in Figure 6.2, assuming different Zernike coefficients to determine $d_{\mathrm{pup}}(\vec{u})$. The perfect Airy pattern, obtained in the limit of zero aberrations, exhibits zero phase in the central part and a phase jump by 180° at $|\vec{\alpha}| \simeq 1.22\,\lambda/(2r_{\mathrm{tel}})$. Anti-symmetric terms, such as tilt, coma and trefoil (not shown), only alter the location and shape of the phase jump, while defocus (not shown), astigmatism and higher order terms produce smooth phase gradients. For a general choice of $d_{\mathrm{pup}}(\vec{u})$ and in the absence of focal-plane aberrations, there is a saddle point where the phase maps average to zero, but significant phase shifts are encountered at larger radii.

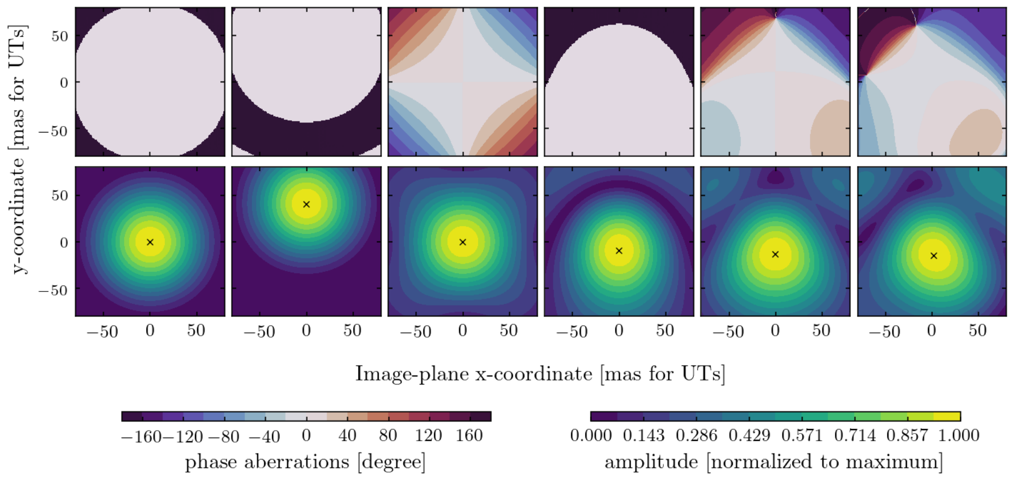

Figure 6.2: Example phase screens (top) and amplitude maps (bottom) in the image plane induced by low-order Zernike aberrations in the pupil plane at a wavelength of $\lambda_0 = 2.2\,\mu$m. From left to right the considered aberrations are: perfect Airy pattern, vertical tilt of 0.4 µm RMS, vertical astigmatism of 0.2 µm RMS, vertical coma of 0.2 µm RMS, and combination of astigmatism, coma and trefoil (with RMS 0.2 µm, 0.2 µm, and 0.1 µm, respectively). The rightmost panel also considers an additional fiber tilt with 0.2 µm RMS.

Focal-plane aberrations break the radial symmetry of the fiber profile. Still, if the perturbations are small enough, the phase maps show a saddle point, but its value differs from zero and its location may be shifted. In any case, the transmitted amplitude is deformed and/or misplaced from the perfect Airy case. Pupil-plane aberrations typically widen the amplitude, while image-plane aberrations have the opposite effect. They lead to a widening of the fiber in the pupil plane and correspondingly to a narrower image-plane profile. The exact scaling relation for the position of the Airy ring remains true only approximately in the presence of higher-order aberrations such that maps at two different wavelengths, λ_1 and λ_2, can be related by

$$\langle \eta^{\mathrm{ps}} \rangle_{\mathrm{obj}} (\alpha_0, \lambda_1) \simeq \langle \eta^{\mathrm{ps}} \rangle_{\mathrm{obj}} \left(\alpha_0 \frac{\lambda_2}{\lambda_1}, \lambda_2 \right) . \tag{6.14}$$

6.2.2 EFFECT ON VISIBILITY MEASUREMENTS AND ASTROMETRY

The overlap integral defines the electromagnetic wave transmitted to the beam combiner from each of the four telescopes. After pairwise beam combination, the complex visibilities are obtained from the inference pattern $I_{i,j}$,

$$I_{i,j} = \int d\vec{\beta} \left\langle \left| E_i \left(\vec{\beta}\right) + E_j \left(\vec{\beta}\right) \right|^2 \right\rangle_{\mathrm{obj}} \tag{6.15}$$

$$= \left\langle |\eta_i|^2 \right\rangle_{\mathrm{obj}} + \left\langle |\eta_j|^2 \right\rangle_{\mathrm{obj}} + 2\Re \left\langle \eta_i \eta_j^* \right\rangle_{\mathrm{obj}} , \tag{6.16}$$

where i and j denote the telescopes involved in the measurement and I is the intensity. The complex pupil function enters each of these terms. Focusing on the single-telescope component first, we find from Equation 6.7

$$\left\langle |\eta_i|^2 \right\rangle_{\mathrm{obj}} = \int d\vec{\alpha}\ \mathcal{F} \left[\Pi_{\circledcirc,i} \otimes \Pi_{\circledcirc,i}\right] (\vec{\alpha})\ O(\vec{\alpha})$$

$$= \int d\vec{\alpha}\ \left| \mathcal{F} \left[\Pi_{\circledcirc,i}\right] (\vec{\alpha}) \right|^2 O(\vec{\alpha}) , \tag{6.17}$$

where the $\otimes$-operator denotes auto-correlation, and $O(\vec{\alpha}) = |E_{\mathrm{obj}}(\vec{\alpha})|^2$ is the brightness distribution of the observed astronomical object which obeys

$$\left\langle \mathcal{F}^{-1} \left[E_{\mathrm{obj}}\right] (\vec{u})\ \mathcal{F}^{-1} \left[E_{\mathrm{obj}}\right]^* (\vec{v}) \right\rangle_{\mathrm{obj}} = \mathcal{F}^{-1} \left[O(\vec{\alpha})\right] (\vec{u} - \vec{v}) . \tag{6.18}$$

Similarly, the inference term is given by

$$\left\langle \eta_i \eta_j^* \right\rangle_{\mathrm{obj}} = \int d\vec{\alpha}\ \mathcal{F} \left[\Pi_{\circledcirc,i} \otimes \Pi_{\circledcirc,j}\right] (\vec{\alpha})\ O(\vec{\alpha})\, e^{-2\pi i\, \alpha \cdot \vec{b}_{i,j}/\lambda}$$

$$= \int d\vec{\alpha}\ \mathcal{F} \left[\Pi_{\circledcirc,i}\right] (\vec{\alpha})\ \mathcal{F} \left[\Pi_{\circledcirc,j}\right]^* (\vec{\alpha})\, O(\vec{\alpha})\, e^{-2\pi i\, \alpha \cdot \vec{b}_{i,j}/\lambda} , \tag{6.19}$$

where $\vec{b}_{i,j}$ is the baseline vector.

All optical aberrations discussed previously are encoded in the back-projected apodized pupil, which is a complex field-dependent function. Expressing the pupil function in its polar representation,

$$\mathcal{F} \left[\Pi_{\circledcirc,i}\right] = A_i(\vec{\alpha})\, e^{i\phi_i(\vec{\alpha})} , \tag{6.20}$$

we refer to A_i as the telescope-dependent "amplitude map" and to ϕ_i as the "phase map". Note that these quantities are closely related to the photometric and the interferometric lobes, $L_i(\vec{\alpha}) = A_i^2(\vec{\alpha})$ and

$$L_{\mathrm{i,j}}(\vec{\alpha}) = A_{\mathrm{i}}(\vec{\alpha})\, e^{i\phi_{\mathrm{i}}(\vec{\alpha})}\, A_{\mathrm{j}}(\vec{\alpha})\, e^{-i\phi_{\mathrm{j}}(\vec{\alpha})} , \tag{6.21}$$

respectively.

From the measured inference pattern, the complex visibilities are obtained as

$$V^{\mathrm{obs}}\left(\vec{b}_{i,j}/\lambda\right) = \left\langle \eta_i \eta_j^* \right\rangle_{\mathrm{obj}} \Big/ \sqrt{\left\langle |\eta_i|^2 \right\rangle_{\mathrm{obj}} \left\langle |\eta_j|^2 \right\rangle_{\mathrm{obj}}} \,. \tag{6.22}$$

By contrast, in an ideal, aberration-free setting, the van-Cittert-Zernike theorem relates the complex visibilities to the object's brightness distribution

$$V^{\mathrm{mod}}\left(\vec{b}_{i,j}/\lambda\right) = \frac{\int d\vec{\alpha}\; O\left(\vec{\alpha}\right) e^{-2\pi i\, \alpha\cdot \vec{b}_{i,j}/\lambda}}{\int d\vec{\alpha}\; O\left(\vec{\alpha}\right)} \,. \tag{6.23}$$

Comparison of Equation 6.22 and Equation 6.23 readily suggests that static aberrations at fiber injection distort both the measured visibility phases and amplitudes. We thus need to adapt the interferometric equation accordingly. To make this effect even more explicit, we first consider the case of a single, unresolved object at position $\vec{\alpha}_0$,

$$V^{\mathrm{obs}}_{\mathrm{ps}}\left(\vec{b}_{i,j}/\lambda\right) = \frac{L_{i,j}\left(\vec{\alpha}_0\right)}{\sqrt{L_i\left(\vec{\alpha}_0\right) L_j\left(\vec{\alpha}_0\right)}}\, e^{-2\pi i \vec{\alpha}_0\cdot \vec{b}_{i,j}/\lambda} \,. \tag{6.24}$$

In the aberration-free case, the phase and amplitude maps of either telescope are given by the perfect Airy pattern shown in the very left panel of Figure 6.2, and $\phi_{i/j}\left(\vec{\alpha}_0\right)$ equals zero or 2π. The presence of static aberrations introduces a phase shift by $\phi_i\left(\vec{\alpha}_0\right) - \phi_j\left(\vec{\alpha}_0\right)$. For an interferometric binary with positions $\vec{\alpha}_1$, $\vec{\alpha}_2$ and flux ratio f^{bin} the measured visibility becomes

$$V^{\mathrm{obs}}_{\mathrm{bin}} = \frac{L_{i,j}\left(\vec{\alpha}_1\right) e^{-2\pi i \vec{\alpha}_1\cdot \vec{b}_{i,j}/\lambda} + f^{\mathrm{bin}} L_{i,j}\left(\vec{\alpha}_2\right) e^{-2\pi i \vec{\alpha}_2\cdot \vec{b}_{i,j}/\lambda}}{\sqrt{\left[L_i\left(\vec{\alpha}_1\right) + f^{\mathrm{bin}} L_i\left(\vec{\alpha}_2\right)\right]\left[L_j\left(\vec{\alpha}_1\right) + f^{\mathrm{bin}} L_j\left(\vec{\alpha}_2\right)\right]}} \,. \tag{6.25}$$

Finally, for a generic extended object with an intensity distribution $O\left(\vec{\alpha}\right)$ the van-Cittert-Zernike theorem generalizes to the expression stated at the beginning of this section, in Equation 6.1

$$V^{\mathrm{obs}} = \frac{\int d\vec{\alpha}\, L_{i,j}\left(\vec{\alpha}\right) O\left(\vec{\alpha}\right) e^{-2\pi i\, vec\alpha\cdot \vec{b}_{i,j}/\lambda}}{\sqrt{\int d\vec{\alpha}\, L_i\left(\vec{\alpha}\right) O\left(\vec{\alpha}\right)\; \int d\vec{\alpha}\, L_j\left(\vec{\alpha}\right) O\left(\vec{\alpha}\right)}} \,.$$

Single point sources typically are observed at the fiber center, where fiber injection is highest and the phase distortions are close to zero. In situations where a very precise alignment is not possible, like for example in exoplanet observations, the visibilities can pick up some small contribution from the phase maps. For binaries with a separation comparable to the fiber width, a configuration in which the phase and amplitude maps are irrelevant cannot be obtained in principle. In this case, the effect of static aberrations needs to be modeled and corrected for in the data analysis.

6.2.3 INTERPLAY WITH TURBULENT ABERRATIONS

To this point, we have not considered the effect of time varying phase aberrations. These are introduced by atmospheric turbulence or time-varying imperfections in the optical system such as tip-tilt jitter from the adaptive optics. Their effect is to multiply the static pupil function by another, time dependent phase

$$P_{\circledcirc} = \Pi_{\circledcirc}\, e^{i\phi^{\mathrm{turb}}(\vec{u},t)} \,. \tag{6.26}$$

To see how time-dependent aberrations affect the visibility measurement, we briefly recap the arguments of Perrin and Woillez, 2019. Assuming that the detector integration time by far exceeds the coherence time of phase fluctuations, the long-time average $\langle ... \rangle_{\mathrm{turb}}$ over the telescope lobes is

$$\begin{aligned} \langle L_{\mathrm{i}}\,(\vec{\alpha})\rangle_{\mathrm{turb}} &= \left\langle \left|\mathcal{F}\left[P_{\circledcirc,i}\right](\vec{\alpha})\right|^2 \right\rangle = \\ &= \mathcal{F}\left[\left(\Pi_{\circledcirc,\mathrm{i}} \otimes \Pi_{\circledcirc,\mathrm{i}}\right)(\vec{u})\, e^{-\frac{1}{2}D_\phi(\vec{u})}\right] \,, \end{aligned} \tag{6.27}$$

$$\begin{aligned} \langle L_{\mathrm{i,j}}\,(\vec{\alpha})\rangle_{\mathrm{turb}} &= \langle \mathcal{F}\left[P_{\circledcirc,\mathrm{i}}\right](\vec{\alpha})\rangle_{\mathrm{turb}} \langle \mathcal{F}\left[P_{\circledcirc,\mathrm{j}}\right](\vec{\alpha})\rangle^*_{\mathrm{turb}} \\ &= \mathcal{F}\left[\left(\Pi_{\circledcirc,\mathrm{i}} \otimes \Pi_{\circledcirc,\mathrm{j}}\right)(\vec{u})\, e^{-\sigma_\phi}\right] \,, \end{aligned} \tag{6.28}$$

where $D_\phi\,(\vec{u})$ is the structure function of the turbulent phase (Roddier, 1981), which saturates to $2\sigma_\phi$ on large scales. Two assumptions underlie these expressions, first that the fluctuations are stationary and second that the baseline between the telescopes is long enough for the respective apertures to become uncorrelated. As in Perrin and Woillez, 2019, we assume both to be fulfilled.

In the case of GRAVITY observations, atmospheric phase variations across the telescope apertures are corrected by the adaptive optics system and the turbulent aberrations are dominated by tip-tilt jitter. Thus, the turbulent phase is

$$\phi_{\mathrm{i}}^{\mathrm{turb}} = 2\pi\, \vec{t}_{\mathrm{i}}(t) \cdot \vec{u} \,, \tag{6.29}$$

where the two directions of $\vec{t}_{\mathrm{i}}(t)$ are independent and follow a Gaussian distribution with zero mean and variance σ_t^2. The structure function then becomes $D_t\,(\vec{u}) = (2\pi\sigma_t u)^2$, and the photometric lobe is given by

$$\langle L_{\mathrm{i}}\,(\vec{\alpha})\rangle_{\mathrm{turb}} = \left|\mathcal{F}\left[\Pi_{\circledcirc,\mathrm{i}}\right](\vec{\alpha})\right|^2 \circledast \exp\left(-\frac{\alpha^2}{2\,\sigma_t^2}\right) \,, \tag{6.30}$$

where $\circledast$ denotes convolution. In case of the interferometric lobe, we further assume that the jitter is uncorrelated between telescopes which yields

$$\langle L_{\mathrm{i,j}}\left(\vec{\alpha}\right)\rangle_{\mathrm{turb}} = \left(\mathcal{F}\left[\Pi_{\circledcirc,i}\right] \circledast e^{-\frac{\alpha^2}{2\sigma_t^2}}\right)^* \left(\mathcal{F}\left[\Pi_{\circledcirc,j}\right] \circledast e^{-\frac{\alpha^2}{2\sigma_t^2}}\right) . \tag{6.31}$$

These turbulent lobes replace the static expressions of the previous sections in the prediction of the observed visibility, i.e. in Equation 6.1, Equation 6.24 and Equation 6.25. The tip-tilt jitter acts like a Gaussian convolution kernel on the static maps, which is applied to the amplitude map squared in case of the photometric lobe but to the full complex map in the case of the interferometric lobe.

6.3 CHARACTERIZATION OF THE GRAVITY BEAM COMBINER

Measurement and characterization of aberrations for the GRAVITY beam combiner GRAVITY observes the Galactic Center in its so-called dual-field mode, which requires the presence of a bright reference target (IRS 16C) within 2" of the actual science targets, Sgr A* and S2. The field at each telescope is split, and reference and science source are separately injected into the fringe tracking (FT) and science channel (SC) fibers. Short detector integration times on the FT allow for the optical path delay to be constantly adjusted for atmospheric turbulence in order to maintain a high fringe contrast. The science channel then measures a differential visibility phase with respect to the fringe tracker on each baseline.

Phase and amplitude maps are inherently single-field effects in the sense that they individually affect the fringe tracker and the science channel for each telescope separately. Based on the optical layout of the fiber coupler (Pfuhl et al., 2014), there is no reason to expect equal aberrations on the SC and FT. However, the fringe tracking object is a bright, unresolved source which is actively tracked by the fiber center in closed loop, such that the phase distortions introduced from static aberrations are small. Moreover, any possible phase distortion from the fringe tracker cancels in the analysis of closure phases or induces a global shift without affecting the binary separation in the analysis of visibility phases. However, a description of the SC phase and amplitude maps is essential to robustly measure a binary separation in the science channel.

Here we report on measurements with the GRAVITY Calibration Unit (Blind et al., 2014a) and on our subsequent analysis to extract SC phase and amplitude maps. We then fit the static-aberration model from subsection 6.2.1 to those maps in order to demonstrate its validity and to obtain compressed representation of the aberrations in form of a small number of Zernike coefficients.

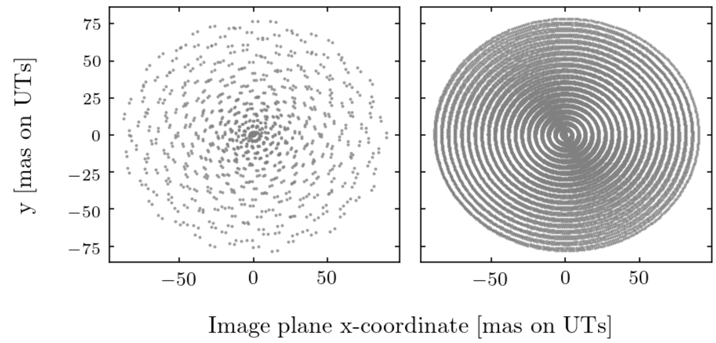

Figure 6.3: Examples of the scanning pattern applied in the Calibration Unit measurements. SC aberration maps where obtained with a slow modulation frequency (left). For the corresponding FT measurement, a faster scanning was used, and the right panel only shows a single iteration of in- and out-spiral.

6.3.1 PHASE MAP MEASUREMENTS WITH THE CALIBRATION UNIT

The GRAVITY Calibration Unit, which we use for the measurement of static aberrations, is directly attached to the beam combiner and creates the light of an artificial science and fringe tracker star. By modulating the voltage on GRAVITY's positioning mirror, the position of that star relative to the fiber can be changed. We scan the FOV out to $\sim 70\,\mathrm{mas}$ in a pattern of in- and out-spiral, which is applied simultaneously to the FT and SC on one single telescope at a time, see Figure 6.3.

In normal observation mode, GRAVITY controls the differential OPD between science channel and fringe tracker by its laser metrology and the common path to the telescopes by fringe tracking. During the phase map calibration measurement, however, fringe tracking is not possible because the fringes are lost at the margins of the scanning region. Instead, the common path from the telescope to the instrument drifts in time. Thus the determination of the aberration pattern from the absolute FT and SC phase requires a drift correction. On the FT, the short detector integration time with maximum sampling frequency of $1\,\mathrm{kHz}$ allows one to resolve fast modulation of the source position and the full FOV can be scanned within $\sim 15\,\mathrm{s}$. Over this short time span, the drift is well described by a constant velocity, which we fit and subtract from the data. On the SC, in contrast, the minimum detector integration time is $0.13\,\mathrm{s}$ and a full scan of the FOV takes $2-3\,\mathrm{minutes}$, too long to model the drift by a simple polynomial fit. Instead, we obtain the science channel aberrations via a detour and first analyze the differential, drift-free SC-FT

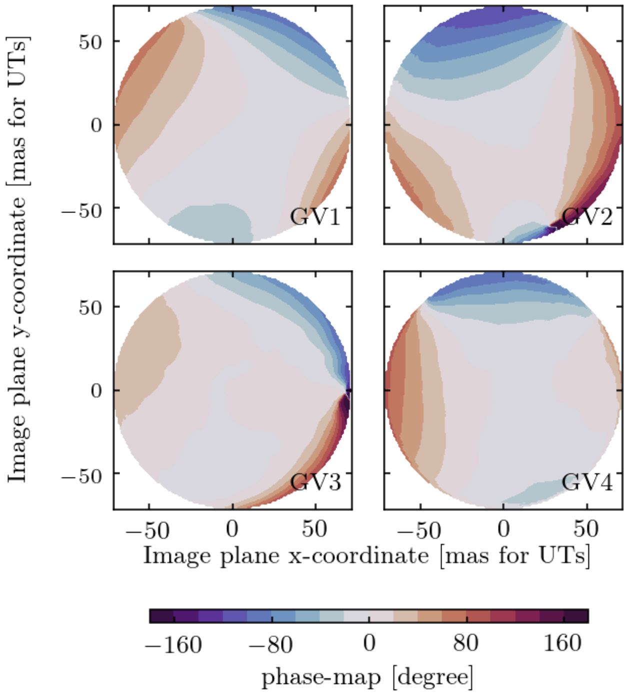

Figure 6.4: Science channel phase maps reconstructed by the procedure of subsection 6.3.1 from the Calibration Unit measurement on 03/03/20 for all four GRAVITY beams.

phase. The pure science channel aberrations then follow from knowledge of the absolute fringe tracker phase.

The data are reduced by the standard GRAVITY pipeline and we obtain the correlated flux in six FT spectral channels (ranging from $1.99-2.38\,\mu\mathrm{m}$) and in medium resolution for the SC (233 wavelength bins in the range $1.97-2.48\,\mu\mathrm{m}$). With the chosen setup, where the source position is varied on only one of the two beams forming a baseline, the measured correlated flux is given by

$$\left\langle \eta_i^{\mathrm{ps}}\left(\vec{\alpha}_0\right)\left(\eta_j^{\mathrm{ps}}\left(\vec{0}\right)\right)^*\right\rangle_{\mathrm{obj}} = A_i\left(\vec{\alpha}_0\right)e^{i\phi_i(\vec{\alpha}_0)}\,A_j\left(\vec{0}\right)e^{-i\phi_j(\vec{0})}\,. \qquad (6.32)$$

Thus, the measurement directly scans the phase and amplitude maps on the modulated channel. Potential offsets in the accompanying non-modulated beam, $\phi_j\left(\vec{0}\right) \neq 0$, can only cause a global phase shift, which we fit and remove in the subsequent analysis. Finally, we consider the amplitude maps normalized to their maximum value, such that $A_\mathrm{j}\left(\vec{0}\right)$ has no impact on our result.

In summary we apply the following analysis steps to obtain the FT and the differential SC-FT phase and amplitude maps.

1. We fit and subtract a linear time drift from the phases measured in each spectral channel and on each baseline.
2. Phases and amplitudes are binned on a spatial grid with resolution 1 mas and averaged over all periods of in- and out-spiral available.
3. The image plane coordinates do not align perfectly with the amplitude maximum, i.e. the source position for which the coupling to the fiber is most efficient. We correct for this effect by fitting a Gaussian profile and shifting the coordinate origin to its maximum.
4. Interpolation over the gridded data gives one phase and amplitude map per spectral channel and baseline.
5. All spectral channels are combined into a single map at reference wavelength $\lambda_0 = 2.2\,\mu$m, by applying the approximate coordinate scaling from Equation 6.14. Here, we verified that the individual maps are consistent over the full spectral range. Cross-validation with simulated maps shows that the error introduced by the approximate scaling relation is small, apart from the very margins of the map. It further cancels between channels above and below λ_0 to a very good degree.
6. From consideration of all baselines, three maps are available for each telescope. We again verify their consistency and average them into a single phase and amplitude map.

This method results in a FT and a differential SC-FT map for each telescope. Subtracting the former from the latter, we finally arrive at the desired SC phase map, which is shown in Figure 6.4. The amplitude map on the SC, on the other hand, is measured directly.

The Calibration Unit measurement was performed twice with a four month break, in late-2019 and early-2020, and we use the data to construct two independent sets of maps. These agree very well in the qualitative features and structures displayed. On the quantitative level the maps display moderate differences of the order of $\sim 10°$, which are smaller at the center and increase towards the map's margins.

6.3.2 REPRESENTATION IN THE PUPIL PLANE

Analyzing the Calibration Unit measurement as described in the previous subsection, we obtain the phase and amplitude maps on a grid discretizing the image plane. We use this result to infer the underlying pupil-plane and fiber aberrations, $d_{\mathrm{pup}}(\vec{u})$ and $d_{\mathrm{foc}}(\vec{u})$, in their Zernike representation. To this end, we developed a simulation tool that creates complex maps of image-plane distortions from a set of Zernike coefficients according to Equation 6.5, Equation 6.6 and Equation 6.13.

For the fit we consider the two Calibration Unit measurements from 2019 and 2020 separately and combine the phase and amplitude maps for each telescope into a complex map. We then minimize the square absolute difference to the model prediction summed over all pixels with respect to the input coefficients. Due to the nature of the approximate coordinate scaling (step 5 of the analysis pipeline), at a map's edge only the smallest wavelengths contribute. We limit the radius to which the data is considered in the fit to $\alpha_{\mathrm{max}} \times \lambda_{\mathrm{low}}/\lambda_{\mathrm{high}}$. With α_{max} being the size of the full map and λ_{low} and λ_{high} the wavelength of the lowest and highest channel, respectively. This choice ensures equal participation of all channels in the fit.

The optical layout of observations with the Calibration Unit has some important differences with the on-sky situation, for which the phase maps will be applied later. Namely, the lack of a central obscuration and an enlarged outer stop $r_{\mathrm{GCU}} = 9.6\,\mathrm{m}/2$ alter the shape of the pupil defined in Equation 6.4. As a consequence, the Calibration Unit pupil illuminates image-plane aberrations out to a slightly larger radius. We choose to normalize the Zernike polynomials by $r_{\mathrm{tel}} = 8.0/2\,\mathrm{m}$, i.e. the telescope area covered by the secondary mirror, to optimize our parameterization for the on-sky case. Image plane distortions, on the other hand, are normalized over the image-plane fiber width at λ_0, $\tilde{\sigma}_{\mathrm{fib}} = \epsilon\lambda_0/\left(4r_{\mathrm{tel}}\sqrt{\ln 2}\right)$, i.e.

$$d_{\mathrm{foc}}(\vec{\alpha}) = \sum_{n=0}^{n_{\mathrm{max}}} \sum_{m=-n}^{m} B_n^m\, Z_n^m\left(\vec{\alpha}/\tilde{\sigma}_{\mathrm{fib}}\right) . \tag{6.33}$$

Of the different types of maps constructed, the fringe tracker provides the cleanest system and thus gives an important benchmark point for the agreement between model and data. We thus use the FT-maps to determine the order n_{max} to which Zernike polynomials in the pupil- and focal-plane aberrations are considered. Successively increasing the fit order, we find that pupil-plane aberrations with $n_{\mathrm{max}} = 6$ and focal-plane aberrations with $n_{\mathrm{max}} = 2$ provide satisfactory model consistency, while still allowing for manageable convergence times. Increasing the Zernike order in the pupil plane is especially important to reduce phase residuals at larger radii, while the central part of the maps can also be described by polynomials of lower order. Fits without focal-plane aberrations manage to reproduce the phase structure to a satisfactory degree, but show poor consistency between the phase and the amplitude data. Finally, an additional parameter accounts for the overall amplitude scaling between

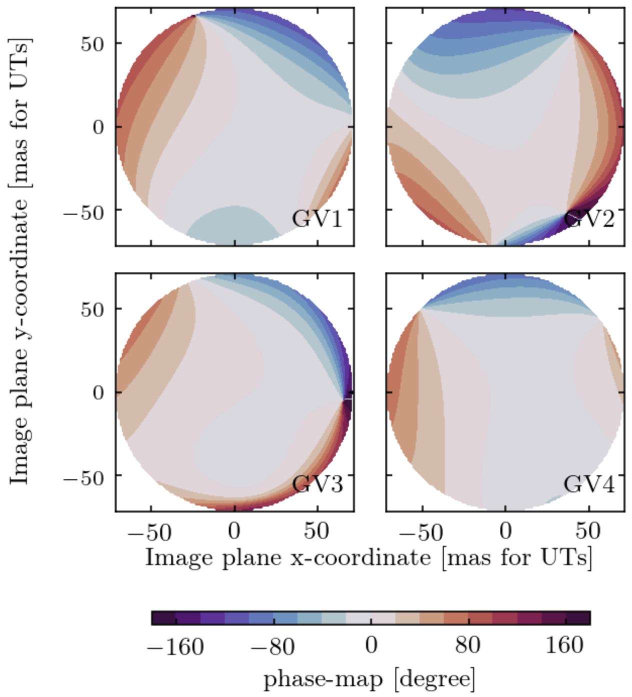

Figure 6.5: Science channel phase maps obtained from fits to the differential SC-FT maps, measured on 03/03/20 for all four GRAVITY beams.

measured and predicted maps, such that each fit constrains at least 34 degrees of freedom. The phase RMS achieved for the fringe tracker fits is of order $\sim 1°$ for all beams and data sets; extrapolation of the fit result to the full map radius yields an RMS of a few degrees.

In principle, it is possible to directly fit the SC maps by the same procedure employed for the FT. However, by further refining the analysis we can remove additional systematic effects from the SC maps. Creating the maps, we corrected for misalignment of the image plane coordinates with the amplitude maximum (step 3 in the analysis pipeline). This shift, however, is not guaranteed to be identical on SC and FT, and as a result there can be a small offset between the FT phase entering the differential SC-FT measurement. To describe this effect, we fit a differential map, predicted from two sets of Zernike coefficients, to the SC-FT maps. The latter of this two sets of parameters is largely fixed to the previously obtained FT coefficients, and only the tip-tilt terms are allowed to vary. The SC parameters, on the other hand, are all free, such that the fit eventually determines the desired SC maps and the offset between the two channels.

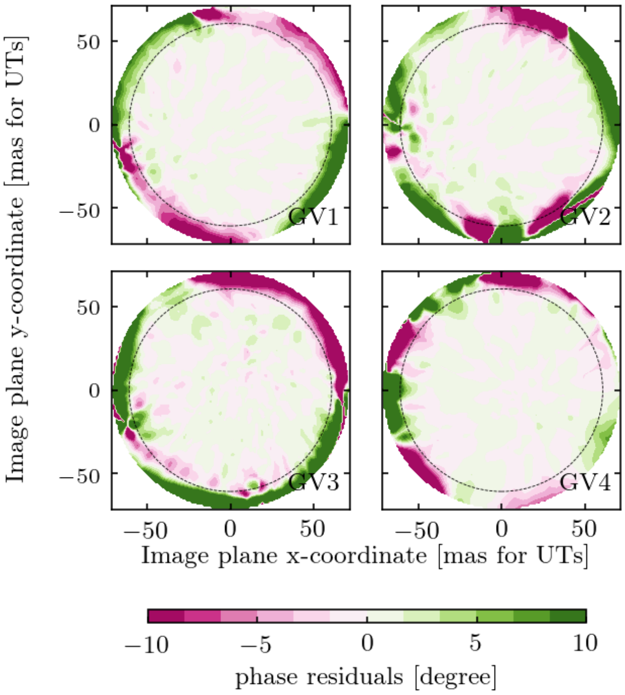

Figure 6.6: Phase residuals of the fit to the differential SC-FT map measured on 03/03/20 for all four GRAVITY beams. Only the data within the dashed circle is considered in the fit; at larger radii the cancellation of wavelength-dependent scaling errors is not guaranteed.

From the best-fit coefficients of the differential SC-FT fit, which we summarize in section 6.A, we reconstruct a complex SC map. Its phase is displayed in Figure 6.5. As expected, the structure agrees very well with the maps obtained by direct evaluation of the Calibration Unit measurement in Figure 6.4. Residuals between measured and fitted SC-FT map, shown in Figure 6.6, are low over the full radius considered for the fit. We obtain a best-fit RMS of $1° - 2°$ for most beams and data sets and two slightly worse results with RMS $\sim 3°$ and $\sim 5°$. Going to larger radii, the disagreement between fit and data starts to increase. This can be caused either by wavelength-dependent errors or by higher-order aberrations, beyond those considered for the fit. Indeed, in optimizing $n_{\max}$, we noted that every increase improved the extrapolation to large separations. However, at such large off-axis distances, fiber damping becomes very significant, resulting in a poor signal-to-noise ratio. Thus, we consider the Zernike decomposition up to 6th order sufficient for our applications.

6.4 APPLICATION TO GRAVITY OBSERVATIONS

Static, field-dependent aberrations affect the visibility measurement whenever the size of an observed object is comparable to the fiber FOV. Here, we apply the formalism developed in section 6.2 alongside the characterization of aberrations from section 6.3 to observations of two different binary systems. First, as a proof of concept, we consider a test-case binary observed with the Auxiliary Telescopes (ATs), where the system's position in the FOV was systematically varied and thus screened over the phase and amplitude maps. Second, we apply the aberration-correction to GC observations with the UTs from 2017 and 2018. During those epochs, close to pericenter passage, S2 and Sgr A* where observed simultaneously in a single fiber pointing.

The data considered in either analysis consists of visibility amplitudes, squared visibilities and closure phases with a relative weighting of (1:1:2). To infer the sources' separation, we fit a binary model based on Equation 6.25, which we extend to account for the effect of finite spectral resolution and for a homogeneous background with flux ratio f^{bkg} relative to the first binary component,

$$
\begin{aligned}
V_{\mathrm{bin}}^{\mathrm{obs}}\left(\frac{\vec{b}_{i,j}}{\lambda}\right) = & \left(\tilde{A}_i\left(\vec{\alpha}_1\right)\tilde{A}_j\left(\vec{\alpha}_1\right)V_\lambda\left[\left(\vec{b}_{i,j}\cdot\vec{\alpha}_1-\vec{d}_{i,j}\left(\vec{\alpha}_1\right)\right),\nu_1\right]\right. \\
& \left.+\ \tilde{A}_i\left(\vec{\alpha}_2\right)\tilde{A}_j\left(\vec{\alpha}_2\right)V_\lambda\left[\left(\vec{b}_{i,j}\cdot\vec{\alpha}_2-\vec{d}_{i,j}\left(\vec{\alpha}_2\right)\right),\nu_2\right]\right) \\
\cdot & \left(\prod_{x=i,j}\left[\tilde{L}_x\left(\vec{\alpha}_1\right)V_\lambda\left(\vec{0},\nu_1\right)+f^{\mathrm{bin}}\tilde{L}_x\left(\vec{\alpha}_2\right)V_\lambda\left(\vec{0},\nu_2\right)\right.\right. \\
& \left.\left.+\ f^{\mathrm{bkg}}V_\lambda\left(\vec{0},\nu_{\mathrm{bkg}}\right)\right]\right)^{-\frac{1}{2}}
\end{aligned}
\tag{6.34}
$$

Phase distortions enter this expression via the OPD correction $d_{i,j}=\left(\tilde{\phi}_i-\tilde{\phi}_j\right)\times\lambda/2\pi$. Further, the point-source visibility averaged over a spectral channel is

$$
V_\lambda\left(\vec{d},\nu\right)=\int d\lambda\,P\left(\lambda\right)\left(\frac{\lambda}{2.2\,\mu m}\right)^{-1-\nu}e^{-2\pi i\,d/\lambda}\,. \tag{6.35}
$$

The spectral bandpass $P\left(\lambda\right)$ is given by a top hat function. The source positions $\vec{\alpha}_1$ and $\vec{\alpha}_2$, the flux ratios f^{bin} and f^{bkg} as well as the spectral index of the central component (ν_1) and the background flux (ν_{bkg}) are free fit parameters, while the companion's spectral slope is fixed to $\nu_2=3$.

Finally, $\tilde{A}_{i/j}$, $\tilde{\phi}_{i/j}$ and $\tilde{L}_{i/j}$ in Equation 6.34 refer to the phase maps, amplitude maps and the photometric lobes as they are encountered in on-sky observations. Those have two important differences with the Calibration Unit measurement. Firstly, while the pupil-plane representation of the aberrations is the same for both settings, the presence of a central obscuration and the smaller outer stop

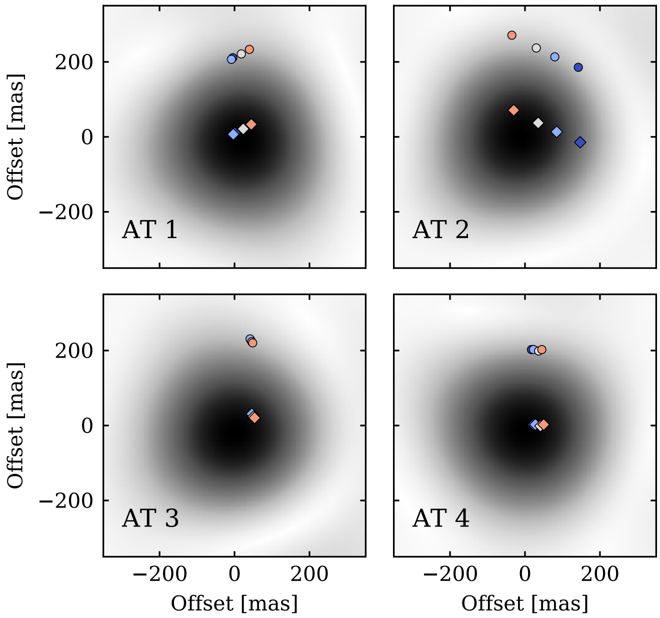

Figure 6.7: Illustration of the AT binary test observations, showing the position of the two binary components (circles and diamonds, respectively) relative to the fiber profile (gray shading). Color gradients are chosen in accordance with Figure 6.8. For this test, the fiber position was varied on AT2 only, but kept fixed on the other three telescopes.

affects the realization of the maps in the image plane. This is conveniently captured by using the Zernike coefficients found in subsection 6.3.2 to create a new set of maps with adjusted pupil configuration. Secondly, the maps are subject to turbulent smoothing according to Equation 6.30 and Equation 6.30.

6.4.1 VERIFICATION FOR A BINARY TEST-CASE

The test-case observations, carried out with the ATs in astrometric configuration, targeted HIP 41426, a binary with K-band magnitude $m_{\mathrm{K}} \simeq 5.393$ at R.A. = 8:26:57.75 h, Dec. = −52:42:17.8 (Cutri et al., 2003). The system has an approximate separation of 200 mas. Its position relative to the GRAVITY fiber was kept fixed for three of the four telescopes and varied in 24 steps between ±400 mas on AT2. At each offset, ten frames with a 6 s integration time were taken. The setup is illustrated in Figure 6.7, which shows both binary components relative to the fiber profile on all four telescopes. The shift was applied along the x-axis in the frame of the GRAVITY pupil, whose rotation with respect to the field results in a diagonal movement on the sky.

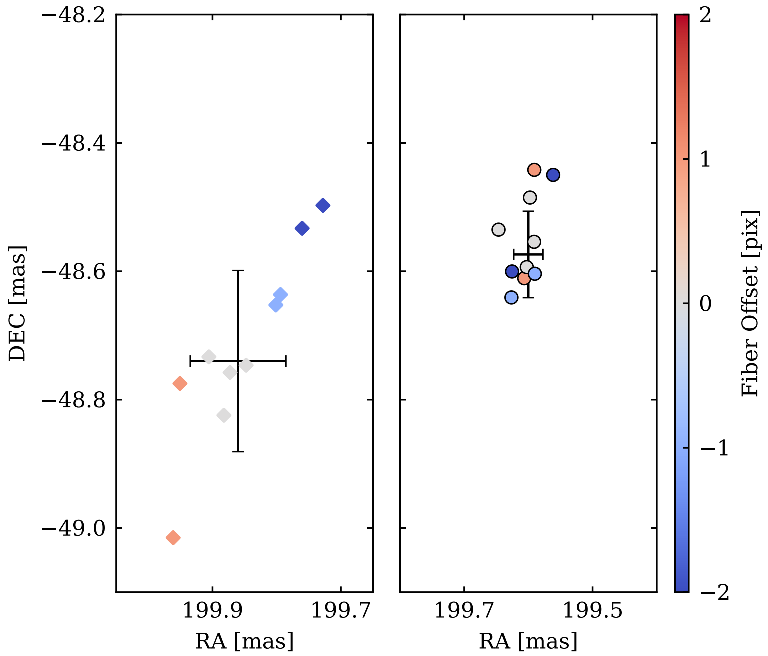

Figure 6.8: Binary separation inferred for a varying fiber offset on AT2 with (right panel) and without (left panel) application of the phase and amplitude maps. Each data point shows the average over two polarization states, and the range of offsets corresponds to $\pm 200\,\mathrm{mas}$, approximately.

We use the Zernike coefficients obtained for the SC in subsection 6.3.2 to produce phase and amplitude maps tailored to observations with the ATs. In this case, the pupil, c.f. Equation 6.4, is defined by $r_{\mathrm{tel}} = 1.82\,\mathrm{m}/2$ and $r_{\mathrm{cent}} = 0.14\,\mathrm{m}/2$. After beam collimation, ATs and UTs illuminate the same section on the GRAVITY mirrors, such that the pupil-plane phase screen can simply be scaled to the AT radius, i.e. $r_{\mathrm{tel}} = 1.82\,\mathrm{m}/2$ also applies in the Zernike decomposition of Equation 6.5. To authenticate the impact of correct aberration modeling, we compare our results to a second, no-map analysis. In this latter scenario, we set all phase maps to zero and all amplitude maps to one, i.e. $\tilde{\phi}_{i/j} = 0$, $\tilde{A}_{i/j} = 1$.

For too large fiber offsets, the signal-to-noise ratio on AT2 is poor due to large fiber damping and we consequently discard these data. The remaining pointings are shown in Figure 6.7, and the corresponding separation, measured from a binary fit to the data according to Equation 6.34, is given in Figure 6.8.

The AT binary test-case clearly validates our aberration corrections. Different configurations yield consistent results only if phase and amplitude maps are considered in the analysis. Including the correct aberration model in the analysis clearly shifts the result and reduces the scatter. Even more importantly, however, the separation found in the no-map analysis systematically depends on the fiber position; it is largest for positive fiber-offsets and smallest for offsets in the negative direction. With application of the aberration-correction, this systematic is largely removed.

We consider the binary test-case observations primarily as a proof of concept and therefore forgo a full analysis of the measurement's systematic error as carried out for the GC. Such uncertainties arise from the accuracy to which the phase maps can be determined and from the uncertainty of the atmospheric smoothing kernel. Further, there can be minor differences in the phase and amplitude maps between AT und UT observations, and our treatment is optimized to the UT scenario.

As the shift in its central value indicates, the binary separation is large enough that even at perfect fiber pointing at least one source lies in a region of the FOV where aberration-induced phase errors are significant. Accurate astrometry thus is not a question of precise fiber alignment but is only possible with a consistent treatment of the pupil-plane distortions in the analysis.

6.4.2 THE SEPARATION BETWEEN S2 AND SGRA*

Having verified our approach to correct for aberration-induced systematic errors, we also apply it to Galactic Center observations with GRAVITY. During 2017 and 2018, i.e. close to pericenter passage, S2 and Sgr A* where observed simultaneously in a single fiber pointing. In particular during 2017, when the off-axis distance of S2 was larger, the aberration correction improves the inferred binary separation. In 2019, in contrast, the Sgr A*-S2 separation exceeds the single telescope beam size of about 60 mas, and GRAVITY observes both sources separately in so called dual-beam mode. Their separation is then obtained by calibrating Sgr A* with S2 and fitting a point source model to its visibilities (see Gravity Collaboration et al., 2020a for details). In this configuration, each source can be well aligned with the fiber center, such that field-dependent aberrations do not impact the measurement.

To derive the aberration-induced shift of the S2 position, we examine a subset of the GRAVITY data used in Gravity Collaboration et al., 2019. In particular, we apply stricter quality cuts and demand a high signal-to-noise ratio. Phase and amplitude maps are generated from the coefficients obtained in subsection 6.3.2 by accounting for the specific geometry of UT-observations, i.e. $r_{\text{tel}} = 8.0\,\text{m}/2$ and $r_{\text{cent}} = 0.96\,\text{m}/2$. The residual turbulent tip-tilt is between 10 mas and 15 mas per axis (Perrin and Woillez, 2019). In total, we consider four different realizations of the aberration maps which are given by the independent analysis of the two calibration measurements in 2019 and 2020 each convolved with the minimum and maximum smoothing assumption. A representative example for

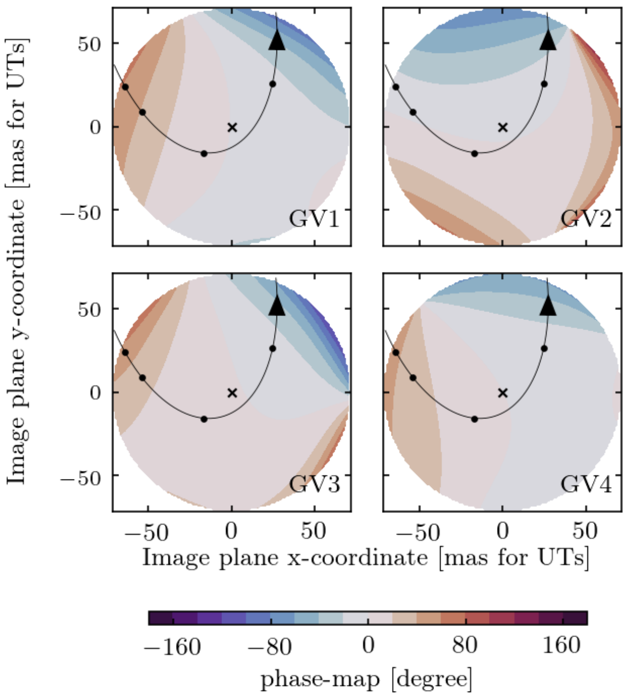

Figure 6.9: The orbit of S2 relative to the phase maps as applied for the GC analysis (measurement from 03/03/20, $\sigma_t = 10\,\mathrm{mas}$). Dots indicate the position of S2 on 2017.2, 2017.6, 2018.2 and 2018.7, respectively, while the cross marks Sgr A*.

the phase maps applied in the GC analysis is shown in Figure 6.9 in relation to the orbit of S2.

Our main result, the difference in S2 position with and without aberration-corrections averaged per month, is shown in Figure 6.10. As expected, the correction is largest in early-2017 and smallest around peri-center passage in May 2018. Further, the mean corrections per epoch obtained with the four different realizations of the aberration maps are consistent over the full observational period.

As the orbit of S2 smoothly scans over the phase and amplitude maps (see Figure 6.9), we also expect a smooth variation in the position-correction. Indeed, the time-dependence in Figure 6.10 is well described by a second-order polynomial fit

$$\Delta\mathrm{R.A.} = \left(-0.44\,\tau^2 + 0.11\,\tau + 0.04\right)\,\mathrm{mas}\,, \tag{6.36}$$

$$\Delta\mathrm{Dec.} = \left(0.41\,\tau^2 - 0.47\,\tau - 0.06\right)\,\mathrm{mas}\,, \tag{6.37}$$

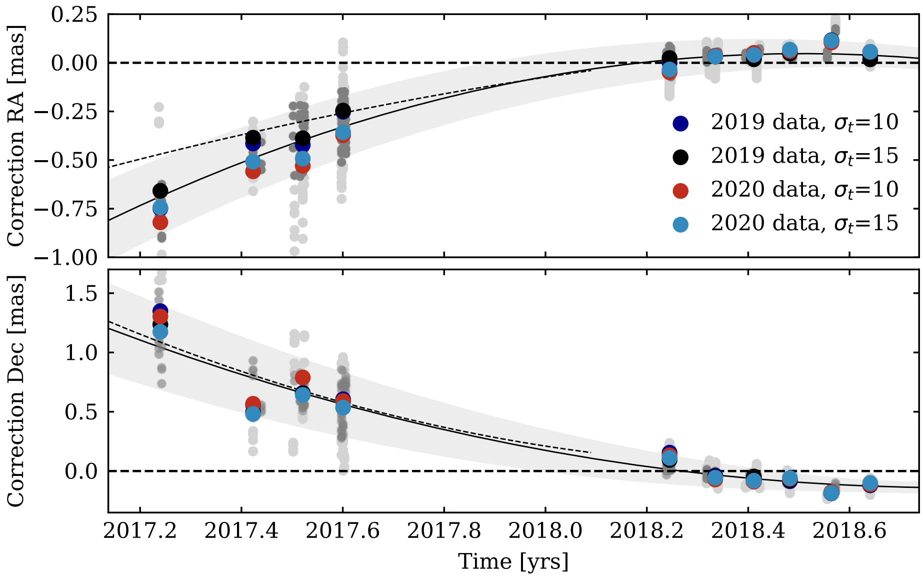

Figure 6.10: The difference in S2 position obtained from an analysis with and without application of the aberration corrections. Colored dots indicate the epoch-wise mean for different realizations of the phase and amplitude maps, gray dots the results for individual observations. From these, we determine a mean position-correction as function of time with a corresponding upper and lower limit as indicated by the black solid line and the gray band. The thin dashed line, finally, represents the correction applied in Gravity Collaboration et al., 2019.

where $\tau = t/\text{years} - 2018.4$ refers to the shifted observation date in years.

In addition to the mean correction per epoch, Figure 6.10 also shows the individual file-by-file results as gray dots. These give some insight into the uncertainty of the aberration-correction. When we fit the orbit of S2, any such uncertainty must to be propagated as source of systematic error. We construct a upper and a lower estimate of the correction, containing 67% of the files per epoch. This is shown in Figure 6.10 as a gray band.

Apart from the systematic error, we also need to account for the statistical uncertainty of the S2 position. That is, as the phase and amplitude error changes when the S2 position is varied within its errorbars, we need to propagate this effect to the final correction. To this end, we take the position error of the original, un-corrected data point from which we draw 100 realizations and shift the aberration maps by it. We then derive the correction from each realization independently and use their scatter to estimate the statistical error of the S2 position correction. The resulting mean statistical uncertainty per epoch is small, between 10 μas and 30 μas, but we nevertheless also account for it in the orbit fitting.

A further check is to ask the question, what correction makes the 2017 and 2018 GRAVITY positions optimally match to the rest of the S2 data. To this end, we included a scaling factor $f_{\rm corr}$ in the correction we apply, such that $f_{\rm corr} = 1$ is our best correction and $f_{\rm corr} = 0$ is no correction. This parameter we can then include in the orbit fit (see subsection 6.5.1). The best fit yields $f_{\rm corr} = 0.99 \pm 0.06$, i.e. identical to the correction we have derived purely from calibration data. This gives an independent confirmation of our concept and the resulting aberration correction: Our correction yields the most consistent S2 orbit.

The aberration correction presented here constitutes a further refinement of the analysis in Gravity Collaboration et al., 2020a. There, we applied the measured aberration maps as shown in Figure 6.4 directly, rather than the fitted decomposition in terms of pupil-plane Zernike polynomials. To account for the widening of the maps, which occurs when projecting from the enlarged stop on the Calibration Unit to the telescope pupil, in addition to the effect of turbulence, we applied a smoothing kernel of $\sigma_t = (19 \pm 5)$ mas. The resulting best-estimate for the correction is depicted in Figure 6.10 as dashed line. Both methods give consistent results, affirming the robustness of the approach. The only sizable deviation is in 2017.2, when S2 was observed at a separation comparable to the maximum radius for which we obtained the calibration measurement (see Figure 6.9). This case shows the strength of the Zernike decomposition, which allows for a well-defined extrapolation.

6.5 RESULTS

6.5.1 DETERMINATION OF THE S2 ORBIT

In the following we evaluate the effect of the aberration correction on the S2 orbit. The data used is similar to Gravity Collaboration et al., 2020a and described in detail in section 6.B. We employ the same fitting procedure as in Gravity Collaboration et al., 2020a, using a 13-parameter, Post-Newtonian orbit model. Six of those parameters describe the Kepler orbit (a, e, i, ω, Ω, $t_{\rm peri}$), and another six describe the reference frame relative to the AO spectroscopy and assumed Local Standard of Rest (LSR) correction, (x_0, y_0, R_0, $\dot{x}_0$, $\dot{y}_0$, $\dot{z}_0$). Here, R_0 is the distance to the GC, the prime focus of this work, and $M_\bullet$ the central mass. The best-fit parameters are given in Table 6.2.

For determining the systematic uncertainty, we follow the approach in Gravity Collaboration et al., 2019 of varying our assumptions and tracing the associated

misalignment between mass and IR-emission	12 pc
wavelength calibration of SINFONI	9 pc
GRAVITY astrometry	29 pc
baseline accuracy	4 pc
wavelength accuracy	9 pc
model & data selection	9 pc
atmospheric differential dispersion	5 pc
aberration-correction	23 pc
metrology correction	10 pc

Table 6.1: Contribution to the systematic errors affecting the measurement of R_0, for details see Gravity Collaboration et al., 2019. Adding all contributions quadratically, we find a total systematic uncertainty of 33 pc.

changes in R_0. Compared to our earlier work, we also include the uncertainty due to the aberration correction, as given by the gray band in Figure 6.10. The individual contributions are given in Table 6.1. It turns out that the aberration correction is the dominant contributor to the systematic error. The total systematic uncertainty is 33 pc when adding the contributions quadratically.

Our best estimate of the Galactic Center distance thus is

$$R_0 = 8275 \pm 9|_{\text{stat.}} \pm 33|_{\text{sys.}} \ \text{pc} \,. \tag{6.38}$$

6.5.2 COMPARISON TO PREVIOUS RESULTS

Our previous determinations of the GC distance in Gravity Collaboration et al., 2018b, Gravity Collaboration et al., 2019 and Gravity Collaboration et al., 2020a were biased by the field-dependent aberrations. Taking them into account brings all our measurements into agreement as shown in Figure 6.11 and Table 6.3. We further note the following:

- In contrast to Gravity Collaboration et al., 2020a, we also apply a correction for the 2018 data, where S2 and Sgr A* were close to each other and close to the field center. Yet, the small aberration corrections lead to a small upward correction of R_0 of around 30 pc, comparable to the systematic error.

parameter	value
a [mas]	124.982 ± 0.034
e	0.884215 ± 0.000058
i [deg]	134.685 ± 0.029
ω [deg]	66.259 ± 0.030
Ω [deg]	227.175 ± 0.029
P [yr]	16.0458 ± 0.0013
t_{peri} [yr]	2018.378990 ± 0.000082
x_0 [mas]	-0.79 ± 0.10
y_0 [mas]	0.00 ± 0.11
$\dot{x}_0$ [mas/yr]	0.0780 ± 0.0091
$\dot{y}_0$ [mas/yr]	0.0342 ± 0.0094
$\dot{z}_0$ [mas/yr]	-2.6 ± 1.4
$M_\bullet$ [$10^6\,M_\odot$]	4.297 ± 0.013
R_0 [pc]	8274.9 ± 9.3

Table 6.2: Orbital parameters of S2 with their statistical uncertainties.

Phasemaps	None	2017 only	2017 and 2018
GRAV. coll 2018	$\mathbf{8122 \pm 31}$		$8231 \pm 16 \pm 24$
GRAV. coll. 2019	$\mathbf{8178 \pm 13 \pm 22}$		$8275 \pm 13 \pm 31$
GRAV. coll. 2020		$\mathbf{8249 \pm 9 \pm 45}$	$8275 \pm 9 \pm 33$
this work		$8246 \pm 9 \pm 33$	$\mathbf{8275 \pm 9 \pm 33}$

Table 6.3: Published values of R_0 **(bold)** and the corresponding values if the aberrations are taken into account (right column). All values in pc.

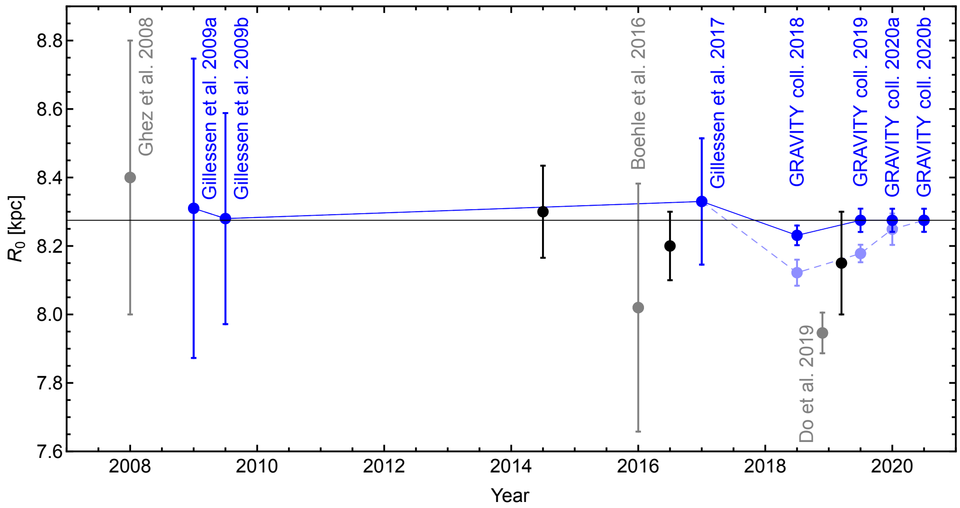

Figure 6.11: Measurements of the Galactic Center distance over time with a focus on studies of the S2 orbit. Blue points show results obtained with the SINFONI, NACO and GRAVITY data with (dark blue) and without (light blue) application of the aberration corrections. Gray R_0 determinations are based on data from the Keck observatory. For comparison, we show in black results based on the statistical parallax of the nuclear star cluster (Chatzopoulos et al., 2015) and from modeling the Milky Way dynamics based on observations of molecular masers (Reid et al., 2019). Bland-Hawthorn and Gerhard, 2016, finally, give the GC distance based on a combination of various methods.

- The orbit is particularly sensitive to the pericenter data. This leads to the effect that the statistical uncertainty decreases strongly with time, while the systematic uncertainty even increases slightly during this time frame, since varying the assumptions then leads to stronger variations in the fit result.

6.5.3 COMPARISON WITH FURTHER S2-BASED RESULTS

We estimate that the accuracy of our VLT-based result is at the 40 pc level. However, it deviates significantly from the Keck-based value reported in Do et al., 2019, with the difference being at the 300 pc level. Since both works use the orbit of S2 around Sgr A* for the determination of R_0, it is important to investigate where the discrepancy is arising, and we address this in section 6.C. Overall, we conclude that the combination of

- a difference in the radial velocity data and
- a modest offset of the Keck coordinate system in the declination direction

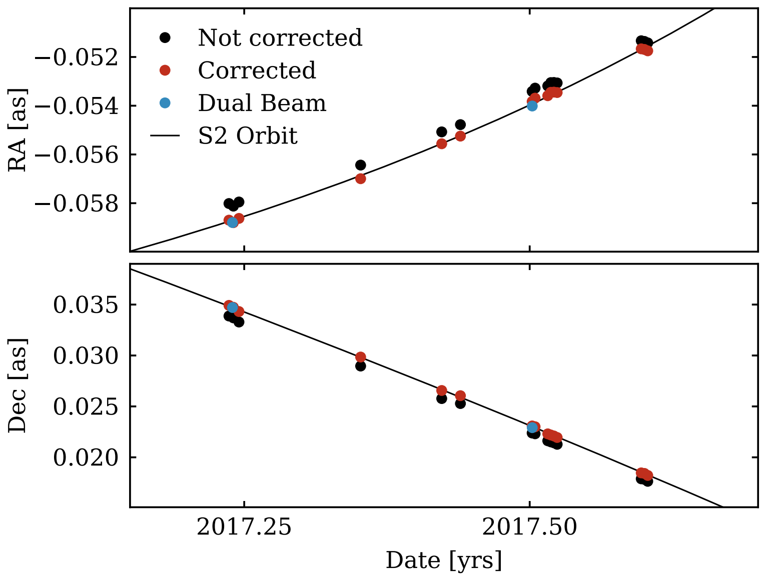

Figure 6.12: Detailed view of the S2 orbit in 2017. Dual-beam points do not suffer from aberration-related systematic errors and agree very well with our corrected data points.

might explain the discrepancy. Both effects contribute roughly 50%.

About 20% of the radial velocity difference can be attributed to the Doppler formula in StarKit used implicitly by Do et al., 2019. The remaining 80% are unexplained and could be in either the Keck or the VLT data.

The origin of the coordinate system offset is unclear as well. Trying to explain the offset with a shift of the VLT coordinate systems is much harder than imposing a shift of the Keck one due to the high precision of the GRAVITY data.

6.6 CONCLUSIONS

GRAVITY delivers high-resolution astrometry which, in combination with spectroscopic data, allows for a very precise determination of the Galactic Center distance. The values inferred from different epochs (Gravity Collaboration et al., 2018b; Gravity Collaboration et al., 2019; Gravity Collaboration et al., 2020a) show a small discrepancy at the 1% level, which nevertheless is significant due to the high precision of the measurement.

We were able to relate this shift to optical aberrations introduced in the instrument, which lead to a field-dependent distortion of the visibility phase. Their effect is the stronger, the further off-axis an object lies within the FOV. In particular Galactic Center observations close to the S2 pericenter passage are affected, where S2 and Sgr A* are detected simultaneously in a single fiber pointing but at a separation comparable to the FOV. In earlier and later epochs, in contrast, we employed the so-called dual-beam method and targeted each source individually. In this case, as for most other GRAVITY science observable, each source can be well centered and aberration corrections become irrelevant. The dual-beam observation mode was also assumed to derive the astrometric error budget in Lacour et al., 2014, which did not include the effect of phase maps for this precise reason.

The full analytical description which we developed here allows us to propagate the effect of optical aberrations at fiber injection to the measured visibilities. Fitting this model to dedicated calibration measurements confirms its validity and enables us to account for the effect in the data analysis. We further verify the approach with dedicated test-case observations.

The formalism which we developed is applicable beyond GRAVITY to any optical/near-IR interferometer where aberrations are introduced in the pupil or the focal plane. There have been several cases in the literature with more than one object lying in the interferometer's FOV, for example some Keck (Colavita et al., 2013), CHARA (Brummelaar et al., 2005) or NPOI (Armstrong et al., 1998) results on binary stars. How severely aberrations affect an observation, however, depends not only on their strength for a particular instrument but also on the off-axis distance considered and on the statistical noise in the measurement. In the example of GRAVITY on the UTs, the mean phase error introduced at 20 mas separation is $4-5$ degrees per telescope and increases to $14-20$ degrees at 50 mas. While a binary test case as presented in subsection 6.4.1 can serve as a general strategy to diagnose whether aberration-induced systematics are an issue, dedicated calibration measurement are required for their correction in the analysis for each individual instrument.

With the results from the GRAVITY Calibration Unit measurements and our refined analysis scheme, we are able to further improve the separation between S2 and Sgr A* in 2017 and 2018, introducing shifts up to 0.5 mas caused by the phase aberrations. In Figure 6.12, we show a detailed view of the S2 orbit in 2017, where we have also included two dual-beam measurements that do not suffer from phase aberrations. Indeed, the improved data agrees very well with these positions.

Of all orbital parameters, the distance to the Galactic Center R_0 is most strongly affected by the change in the S2 position. This can be easily understood if one views R_0 as the scaling factor between angular and proper velocity. As such, the field-dependent phase errors discussed in this work fully explain the shift between earlier R_0 measurements with GRAVITY data. Applying the analysis scheme developed here lifts any such discrepancies (see subsection 6.5.2). In particular Figure 6.11 demonstrates that belatedly corrected data sets of earlier publications give fully consistent results whose accuracy increases with time.

APPENDIX

6.A LIST OF ZERNIKE COEFFICIENTS

The Zernike coefficients obtained by fitting the Calibration Unit measurements from late-2019 and early-2020 are summarized in Table 6.4 and Table 6.5, respectively. We provide the science channel results for all for GRAVITY beams (GV1 to GV4) in units of μm according to the definitions in Equation 6.5 and Equation 6.33, where A_n^m labels pupil-plane aberrations and B_n^m those in the focal plane.

6.B DATA

We use the data set presented in Gravity Collaboration et al., 2020a with the following changes:

- Each single-beam astrometric position is corrected according to Equation 6.37, and we add the statistical error of this correction in quadrature, which increases the individual uncertainties by around 15 μas.

- We corrected the radial velocity of the epoch 2018.1277, which was 13 km/s too high in the previous data set.

- Further, we are able to add one interferometric position measurement of S2 from early March 2020. Like in 2019, the separation between S2 and Sgr A* exceeds the fiber field of view, and hence a dual-beam measurement needed to be employed.

Our data set consists of 128 AO-based astrometric points, 58 GRAVITY-based astrometric points and 97 radial velocities, of which the first three before 2003 are from Do et al., 2019.

	GV1	GV2	GV3	GV4
A_0^0	-0.005	-0.028	-0.019	-0.014
A_1^{-1}	0.000	0.008	0.062	-0.014
A_1^1	0.021	-0.030	0.053	0.022
A_2^{-2}	0.009	-0.009	0.028	0.010
A_2^2	-0.010	-0.012	0.015	-0.035
A_2^0	-0.034	-0.012	-0.016	-0.002
A_3^{-1}	0.032	-0.042	0.028	0.065
A_3^1	0.032	0.071	0.081	0.013
A_3^{-3}	-0.056	0.011	0.032	0.021
A_3^3	0.013	-0.017	-0.026	0.054
A_4^{-2}	-0.005	-0.020	-0.036	-0.016
A_4^2	-0.049	-0.014	-0.046	-0.034
A_4^{-4}	0.011	-0.005	0.049	0.002
A_4^4	-0.005	-0.006	-0.029	-0.012
A_4^0	-0.039	-0.001	-0.023	-0.019
A_5^{-1}	0.011	0.030	0.013	0.014
A_5^1	-0.003	-0.026	0.032	-0.032
A_5^{-3}	0.018	-0.026	-0.015	-0.013
A_5^3	-0.020	0.002	-0.026	-0.030
A_5^{-5}	0.013	-0.018	0.008	-0.027
A_5^5	0.003	-0.003	0.047	-0.002
A_6^{-6}	-0.003	0.009	0.018	-0.001
A_6^6	-0.009	0.013	-0.019	0.015
A_6^{-4}	-0.002	0.004	-0.017	0.002
A_6^4	0.021	0.000	0.018	0.018
A_6^{-2}	0.001	-0.001	0.002	-0.000
A_6^2	0.003	0.002	0.003	0.002
A_6^0	0.024	0.001	0.024	0.007
B_1^{-1}	0.010	0.113	0.065	0.033
B_1^1	0.035	-0.043	0.062	0.042
B_2^0	-0.006	-0.011	0.005	0.007
B_2^{-2}	-0.045	0.053	-0.086	0.024
B_2^2	0.011	0.033	-0.004	0.031

Table 6.4: Zernike coefficients for science channel aberrations fitted to the calibration measurement on 03/11/19. All coefficient are given in units of μm.

	GV1	GV2	GV3	GV4
A_0^0	-0.009	-0.059	-0.019	-0.027
A_1^{-1}	-0.018	0.034	0.066	-0.003
A_1^1	0.008	0.016	0.045	0.043
A_2^{-2}	0.008	-0.005	0.047	0.006
A_2^2	-0.012	-0.010	0.019	-0.023
A_2^0	-0.043	-0.012	-0.024	0.012
A_3^{-1}	0.020	-0.039	0.038	0.075
A_3^1	0.042	0.079	0.063	0.026
A_3^{-3}	-0.031	0.009	0.029	0.023
A_3^3	-0.001	-0.006	0.022	0.032
A_4^{-2}	-0.028	-0.049	-0.042	-0.014
A_4^2	-0.030	-0.052	-0.019	-0.017
A_4^{-4}	0.014	-0.014	0.023	-0.014
A_4^4	-0.004	-0.001	-0.016	-0.016
A_4^0	-0.049	-0.027	0.001	-0.023
A_5^{-1}	0.022	0.026	-0.000	-0.000
A_5^1	-0.014	-0.031	0.034	-0.041
A_5^{-3}	0.005	-0.027	-0.011	-0.017
A_5^3	-0.007	-0.005	-0.025	-0.017
A_5^{-5}	0.004	-0.015	0.008	-0.007
A_5^5	-0.008	0.001	0.058	0.004
A_6^{-6}	-0.006	0.018	0.040	0.014
A_6^6	0.001	0.008	-0.002	0.008
A_6^{-4}	0.013	0.017	-0.005	0.001
A_6^4	0.012	0.021	0.014	0.015
A_6^{-2}	-0.001	0.002	0.003	0.001
A_6^2	-0.001	-0.001	0.006	0.004
A_6^0	0.030	0.007	0.016	0.009
B_1^{-1}	0.002	0.115	0.036	0.023
B_1^1	0.068	-0.032	0.086	0.035
B_2^0	-0.004	-0.000	0.004	0.015
B_2^{-2}	-0.027	0.035	-0.076	0.012
B_2^2	0.043	0.065	-0.040	0.008

Table 6.5: Zernike coefficients for science channel aberrations fitted to the calibration measurement on 03/03/20. All coefficient are given in units of μm.

6.B.1 DUAL-BEAM MEASUREMENT IN 2020

Due to the limited observability of the GC in early March and expecting observations in the following months, we did not attempt to observe Sgr A* in March 2020, but only pointed to S2 and to our usual calibrator star R2, with the aim of testing the stability of the GRAVITY astrometry. Pointings to Sgr A* were planned for later in the year. They had to be canceled due to the pandemic-related closure of the VLT(I) from mid-March on. To still determine the S2 – Sgr A* separation vector from this observation, we need to proceed in two steps and first measure the S2 – R2 distance, then we reference R2 to Sgr A*.

The distance between S2 and R2 is measured with the dual-beam method (subsection 6.4.2), where we calibrate the S2 files with R2. In addition to the 2020 measurement, this separation is also available for 56 epochs in the years 2017, 2018 and 2019. It can be measured very precisely due to the brightness of the two stars. Since the S2 – Sgr A* vectors have already been determined in Gravity Collaboration et al., 2020a, we can also refer R2 to Sgr A* in those earlier epochs. We then fit a simple quadratic function for the time evolution of the R2 coordinates relative to Sgr A* and extrapolate it to March 2020. Given the large number of data and the small time range to extrapolate for, the extra uncertainty introduced is well below the $100\,\mu$as level.

We derive the S2 position in 2020 from the four scientifically usable exposures as their mean. We assign an error of $150\,\mu$as to each coordinate for this data point, reflecting both the smaller number of files compared to what we typically had available in 2019 and the extra uncertainty due to the additional step of referencing via R2. The new data point falls well onto the expected orbit, but its error bar is too large to have a significant impact on the fitted parameters.

6.C ANALYSIS OF THE DIFFERENCE BETWEEN DISTANCE DETERMINATIONS FROM KECK AND VLT DATA SETS

While we believe our determination of R_0 is accurate to the 40 pc level, we note that the value published in Do et al., 2019 is discrepant at the 300 pc level. Both teams use the orbit of the star S2 around Sgr A* for the R_0 determination, and hence it is natural to ask where the differences are.

6.C.1 DATA

Beyond our ("VLT") data set (section 6.B), we use the Keck data set published in Do et al., 2019. We apply the NIRC2 radial velocity offset of $+80\,\mathrm{km/s}$

as determined in Do et al., 2019 to the NIRC2 data, i.e. we add 80 km/s to these radial velocities. Unlike Do et al., 2019, we then don't fit for this offset. Further, we drop the last astrometric data point (epoch 2018.67148268), as suggested by the authors in a private communication. The data set consists of 45 astrometric points and 116 radial velocities, of which 41 are actually from the VLT data set between 2003 and 2016. The published table also includes one radial velocity from the epoch 2019.3567, which possibly was not part of the data set actually used in Do et al., 2019.

6.C.2 THE DIFFERENCE IN R_0

We fit the orbit with a simple, 13-parameter model: The six orbital elements of the star (corresponding to the initial conditions of the star in phase space), six parameters for the position and velocity of the MBH, and the mass of the MBH. The fits are done using the relativistic corrections as in Gravity Collaboration et al., 2020a, i.e. we fix $f_{\mathrm{RS}} = f_{\mathrm{SP}} = 1$. For this non-Keplerian motion, the meaning of the orbital elements is that they are osculating at a reference epoch, for which we choose T=2010.35, close to the apocenter passage time of S2.

For fitting the VLT data set, we use the same approach as in Gravity Collaboration et al., 2020a: For the GRAVITY data, we assume that the astrometry directly refers the S2 positions to the mass center, as we directly measure the separation vector between the two objects interferometrically. For the NACO (AO-imaging based) data, we allow for a coordinate system offset, on which we set priors following the work from Plewa et al., 2015, and we include the NACO flare positions as an additional constraint for locating the mass. This fit yields

$$\begin{aligned} R_0 &= 8274.9 \pm 9.3\,\mathrm{pc} \\ a &= 124.982 \pm 0.034\,\mathrm{mas} \\ i &= 134.685 \pm 0.029^\circ \\ \Omega &= 227.175 \pm 0.029^\circ, \end{aligned} \tag{6.39}$$

where a is the semi-major axis, i the inclination and Ω the position angle of ascending node of the S2 orbit, and the errors are the statistical fit uncertainties. The VLT astrometry is dominated by the GRAVITY points, as illustrated by dropping all AO data points, which results in $R_0 = 8276 \pm 10\,\mathrm{pc}$.

Fitting the Keck data set with the same 13-parameter model as used for Equation 6.39 yields

$$\begin{aligned} R_0 &= 7935 \pm 44\,\mathrm{pc} \\ a &= 126.64 \pm 0.27\,\mathrm{mas} \\ i &= 133.78 \pm 0.15^\circ \\ \Omega &= 227.66 \pm 0.13^\circ. \end{aligned} \tag{6.40}$$

This is not the exact same number as in Do et al., 2019, where $R_0 = 7959 \pm 59\,\mathrm{pc}$ is reported. The small (and statistically insignificant) difference is most likely due to the noise model which Do et al., 2019 include in their analysis, which we do not have readily available. Applying the noise model at hand (Plewa and Sari, 2018; Gravity Collaboration et al., 2019) yields $R_0 = 7965 \pm 56\,\mathrm{pc}$. Hence, the value reported by Do et al., 2019 lies between the two numbers we get by re-fitting their data. In the following, we will use for simplicity, and for equal treatment of the data, the value and approach as in Equation 6.40. We have thus a difference of $\Delta R_0 = 340 \pm 45\,\mathrm{pc}$.

6.C.3 COMPARING, COMBINING & ADJUSTING THE ASTROMETRY

Already, Gillessen et al., 2009a noticed that a simple attempt to compare the astrometric data sets by plotting them on top of each other fails. One needs to allow for an offset and a drift between the two coordinate systems (i.e. four parameters Δx, Δy, Δv_x, Δv_y). This yields thus a 17-parameter fit. Comparing the best-fitting parameters in Equation 6.39 and Equation 6.40 shows that they differ in Ω significantly. This parameter is fully degenerate with the angular orientation (called β here) of the coordinate system. Hence, the difference in Ω suggests that the two astrometric data sets are rotated with respect to each other.

Therefore we extend the combination scheme by an additional, fifth parameter, $\Delta\beta$, resulting in a 18-parameter fit. With this we fitted both data sets simultaneously, omitting the 41 VLT radial velocities from the Keck data set, whist dropping also the three Keck ones in the VLT data set. This fit matches the two coordinate systems ideally onto each other and results in

$$\begin{aligned} R_0 &= 8260 \pm 9\,\mathrm{pc} \\ a &= 125.00 \pm 0.03\,\mathrm{mas} \\ i &= 134.66 \pm 0.03^\circ \\ \Omega &= 228.16 \pm 0.03^\circ \\ \Delta\beta &= 0.32 \pm 0.05^\circ, \end{aligned} \tag{6.41}$$

Note that the value of $\Delta\beta$ matches the difference $\Delta\Omega$. We conclude that indeed the Keck and VLT data are rotated with respect to each other. The other parameters are very similar to Equation 6.39, which is due to the considerably smaller astrometric uncertainties of the GRAVITY data compared to the adaptive optics data.

With the best-fit coordinate system difference in hand, we can transform the Keck astrometric data into the VLT coordinate system and vice versa. We choose to do the former, since the VLT data set is more directly calibrated by the interferometric data. After applying the coordinate system difference to the Keck data, we can fit them again with a 13-parameter model. This yields the exact same best-fit parameters as in Equation 6.40 (with the exception of Ω, of course). Hence, transforming the astrometry does not change the more fundamental differences between the two orbits, while a direct comparison is now feasible. The value of Ω can be omitted in the following.

6.C.4 DISCREPANCY IN THE RADIAL VELOCITY DATA

Chu et al., 2018 have investigated the consistency of the radial velocity data between the Keck and VLT data sets for the years 2000 to 2016, and they concluded that the data are in agreement with each other. We have repeated the exercise, now also extending into the time of the pericenter passage in 2018 (Figure 6.13). To our surprise, the radial velocities differ systematically from ≈ 2011 on, and the difference gets larger as the radial velocity increases ever more. The difference reaches $\approx 50\,\mathrm{km/s}$ in 2018, just before the star swung through pericenter [1].

Hence, it is an obvious question to ask what influence the radial velocities have on R_0? For this, we swapped the radial velocities between the two data sets. Using the VLT-set together with the Keck astrometry yields

$$\begin{aligned} R_0 &= 8094 \pm 32\,\mathrm{pc} \\ a &= 126.08 \pm 0.21\,\mathrm{mas} \\ i &= 134.0 \pm 0.13^\circ \end{aligned} \tag{6.42}$$

Vice versa, using the Keck radial velocities together with the VLT astrometry yields $R_0 = 8214 \pm 14\,\mathrm{pc}$. Given that the Keck radial velocity set contains 35% VLT radial velocities, the fit in Equation 6.42 is the cleaner test. We thus explain roughly half of the difference in R_0 with the radial velocity data, i.e. 159 pc.

[1] Also, there is one obvious outlier in the Keck data, the earliest 2018 point. We have checked that dropping this measurement does not change the Keck-fit result in any significant way.

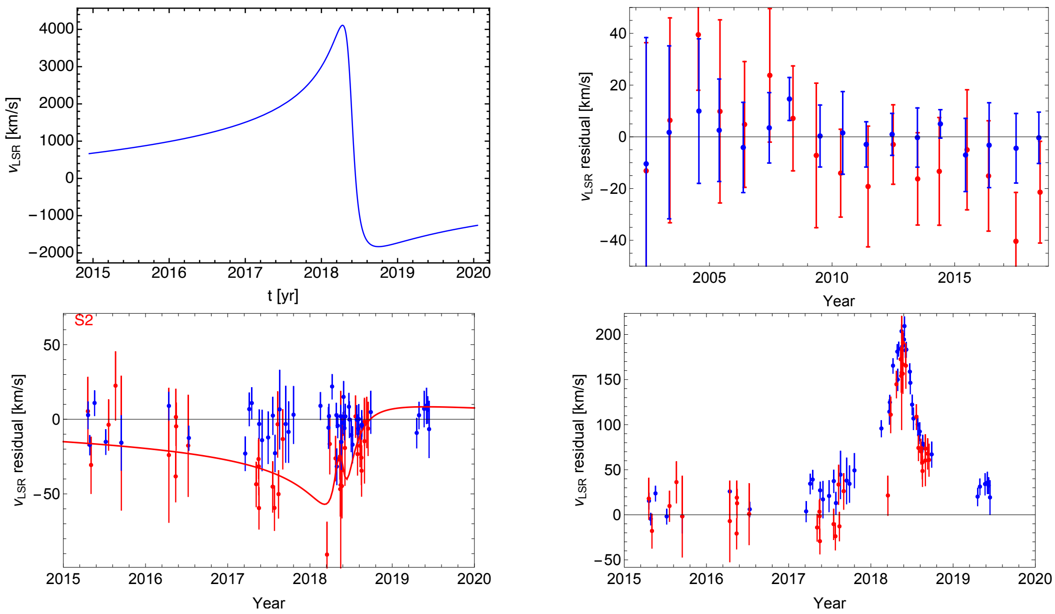

Figure 6.13: Comparison of the radial velocity data sets. Blue points are data from the VLT data set, red from the Keck data set. Top left: Radial velocity as a function of time for the VLT fit (Equation 6.39). Top right: Yearly averages of the residua of the two data sets to the fit from Equation 6.39. By construction the VLT data thus scatter around 0. The Keck data deviate systematically from 2011 on, and the discrepancy increases in the later years. Bottom left: The same as the left panel, but zooming in to the period 2015 - 2020, and showing all individual data points. The best fit Keck orbit corresponding to Equation 6.40 is the red line. Apparently, the difference is largest, when the radial velocity gets largest (in the year 2018 at pericenter passage). Bottom Right: Both data sets show a clear peak in radial velocity in 2018 when comparing with the Keplerian part of the VLT fit (Equation 6.39), i.e. both data sets clearly detect the redshift term.

Why do the radial velocities differ? So far, we can only offer an explanation for $\approx 20\%$ of the radial velocity difference: We applied the stellar atmosphere model-based fitting with the StarKit package used in Do et al., 2019 also to the VLT spectroscopy. We found a significant difference for large radial velocities, which we were able to trace down to the Doppler formula used by the StarKit package. While both Do et al., 2019 and Gravity Collaboration et al., 2020a state that the spectroscopic observable is $v_r = z\,c$, i.e. the redshift of a given spectrum, the StarKit package actually applies a Doppler formula which includes the longitudinal, relativistic correction: $\lambda' = \lambda_0 \sqrt{\frac{1+v_r/c}{1-v_r/c}}$. In this form, the Doppler formula ignores the (significant) tangential motion v_t of S2. In order to apply a relativistic correction one needs to use the full

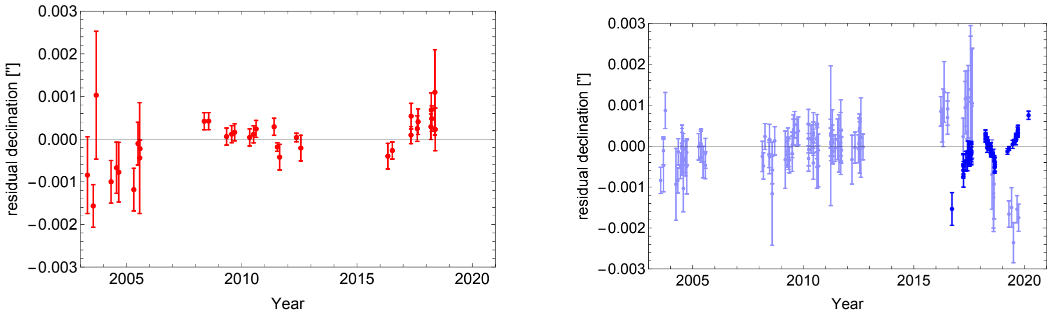

Figure 6.14: Comparison of the astrometric residual after forcing an offset in declination such that the fit to Keck data set matches the VLT one (left) and such that the fit to VLT data set matches the Keck one (right). Lighter blue corresponds to AO data from the VLT data set, darker blue to the GRAVITY data.

Doppler formula $1 + z = \frac{1+v_r/c}{\sqrt{1-(v_r^2+v_t^2)/c^2}}$ (Lindegren and Dravins, 2003). For this correction, however, the spectroscopic information is not sufficient. One cannot, in general, Doppler-correct a spectrum in a relativistic way without knowing the other motion component. Further, even if one would apply the full correction, one would in the following of course not be able to fit for the relativistic redshift anymore.

The difference between the two formulae is small at velocities much smaller than the speed of light, but becomes important close to peri-center, when S2 reaches a velocity of nearly 8000 km/s. Still, it amounts to ≈ 25 km/s at most and thus is smaller than the observed difference in Figure 6.13. This difference is also visible in Fig. 1 of Do et al., 2019: The plotted model spectra are slightly more redshifted than what the underlying data suggest. Changing the Keck radial velocities accordingly yields a fit with $R_0 = 7972 \pm 44$ pc, i.e. accounting for 37 pc of the 159 pc.

Further checks did not yield any clues why there remains a significant difference in the radial velocities. We note:

- We checked whether the time stamps are assigned consistently between the two data sets, and did not find a difference.
- Figure 6.13 bottom right shows that both data sets clearly show the redshift peak around pericenter.

6.C.5 DISCREPANCY IN THE ASTROMETRY

Comparing the fits in Equation 6.39 and Equation 6.40 shows that they not only differ in R_0, but also in the size of the semi-major axis a. We find

$\Delta a/a = 1.28 \pm 0.22\,\%$. The same is not true for the semi-minor axis though, $\Delta b/b$ is consistent with 0. Interestingly, the projected ellipses as given by the astrometric data in the plane of sky agree in both semi-major and semi-minor axes to within 0.17%. Hence, the inclinations i need to differ, which Equation 6.39 and Equation 6.40 confirm. We find in accordance with the above $1 - \sin(i_{\mathrm{VLT}})/\sin(i_{\mathrm{Keck}}) \approx 1.3\%$.

The inclination of the ellipse determines where the projected center of mass is located. Given the orientation of the S2 orbit and the disagreement in a but not in b hints towards an offset of the center of mass in the declination direction. Indeed, we can show that introducing an offset to either y or v_y (the mass position and velocity in declination) can explain the remaining discrepancy. Starting from the fit of the transformed Keck data set, we fix v_y to its best fit value of $-0.15\,\mathrm{mas/yr}$. All other parameters are left free again for a subsequent fit. Additionally using the VLTI velocities in this fit instead of the Keck ones yields:

$$\begin{aligned} R_0 &= 8277 \pm 28\,\mathrm{pc} \\ a &= 124.76 \pm 0.16\,\mathrm{mas} \\ i &= 134.63 \pm 0.11^\circ\,. \end{aligned} \tag{6.43}$$

This fit yields thus from the Keck astrometry the same value for R_0 as the VLT fit. Also note, that indeed semi-major axis a and inclination i have moved to the VLT values by forcing v_y to have an offset. Since the mass position is parametrized with a time origin at T=2000.0, the best fit y also changes, from $-0.972\,\mathrm{mas}$ to $1.234\,\mathrm{mas}$. The systematic uncertainty on y and v_y estimated by Do et al., 2019 are $1.16\,\mathrm{mas}$ and $0.066\,\mathrm{mas/yr}$ respectively. Hence, the difference one needs to enforce is within $\approx 2\sigma$ of the systematic uncertainty, and the residuals in Figure 6.14 (left) appear to be acceptable. Essentially the same can be achieved by forcing an offset to y and leaving v_y free instead.

Can one can turn the argument around and apply a similar offset to the VLT data in order to lower the VLT-based value of R_0? In a first attempt we applied the same offset to the VLT AO data. However, even an offset 10 x larger (i.e. $1.2\,\mathrm{mas/yr}$), changes R_0 only by $\approx 30\,\mathrm{pc}$. This is not surprising, since the VLT astrometry is completely dominated by the GRAVITY data. Thus, we instead tried varying v_y and y for the GRAVITY data, giving up the assumption that the GRAVITY source directly is the mass center. Also, we exchanged the VLT radial velocities for the Keck ones. We find that we need to change v_y by $-1.4\,\mathrm{mas/yr}$ in order to get a distance similar to the Keck value:

$$\begin{aligned} R_0 &= 7928 \pm 16\,\mathrm{pc} \\ a &= 126.89 \pm 0.05\,\mathrm{mas} \\ i &= 133.51 \pm 0.03^\circ\,. \end{aligned} \tag{6.44}$$

The fit achieves the lower R_0 by tilting the orbit similar to the fit from Equation 6.40. The enforced change of v_y is unrealistically large ($12\times$ larger than what was needed for the Keck data), Also, the GRAVITY data show very strong and systematic residuals of up to 0.5 mas (Figure 6.14 right), and the reduced χ^2 of the fit increased from 1.50 to 2.63.

7 FIRST TEST OF THE EQUIVALENCE PRINCIPLE IN THE GALACTIC CENTER

Original Publication: A. Amorim, M. Bauböck, J.P. Berger, W. Brandner, Y. Clénet, V. Coudé du Foresto, P.T. de Zeeuw, J. Dexter, G. Duvert, M. Ebert, A. Eckart, F. Eisenhauer, N.M. Förster Schreiber, P. Garcia, F. Gao, E. Gendron, R. Genzel, S. Gillessen, M. Habibi, X. Haubois, Th. Henning, S. Hippler, M. Horrobin, Z. Hubert, A. Jiménez Rosales, L. Jocou, P. Kervella, S. Lacour, V. Lapeyrère, J.-B. Le Bouquin, P. Léna, T. Ott, T. Paumard, K. Perraut, G. Perrin, O. Pfuhl, S. Rabien, G. Rodríguez-Coira, G. Rousset, S. Scheithauer, A. Sternberg, O. Straub, C. Straubmeier, E. Sturm, L.J. Tacconi, F. Vincent, S. von Fellenberg, I. Waisberg, F. Widmann, E. Wieprecht, E. Wiezorrek, S. Yazici (GRAVITY Collaboration)
Corresponding Authors: F. Widmann, M. Habibi
DOI: 10.1103/PhysRevLett.122.101102

Abstract: During its orbit around the four million solar mass black hole Sagittarius A* the star S2 experiences significant changes in gravitational potential. We use this change of potential to test one part of the Einstein equivalence principle: the local position invariance (LPI). We study the dependency of different atomic transitions on the gravitational potential to give an upper limit on violations of the LPI. This is done by separately measuring the redshift from hydrogen and helium absorption lines in the stellar spectrum during its closest approach to the black hole. For this measurement we use radial velocity data from 2015 to 2018 and combine it with the gravitational potential at the position of S2, which is calculated from the precisely known orbit of S2 around the black hole. This results in a limit on a violation of the LPI of $|\beta_{He} - \beta_H| = (2.4 \pm 5.1) \cdot 10^{-2}$. The variation in potential that we probe with this measurement is six magnitudes larger than possible for measurements on Earth, and a factor ten larger than in experiments using white dwarfs. We are therefore testing the LPI in a regime where it has not been tested before.

7.1 INTRODUCTION

Since its publication in 1915 general relativity (GR) has been tested frequently and has so far passed all experimental tests (Will, 2014). Recently there has been an additional experiment in a new mass regime: For the first time it was possible to detect both the gravitational redshift and the transverse Doppler shift of a star moving on an elliptical orbit through the extreme gradient of the gravitational potential near a supermassive black hole (Gravity Collaboration et al., 2018b). This was possible by monitoring the orbit of the star S2 around the supermassive black hole Sagittarius A* (Sgr A*) over the last 26 years (see e.g. Ghez et al., 2008; Gillessen et al., 2009a; Gillessen et al., 2017). So far all data taken for this experiment show excellent agreement with the predictions from GR. This work expands the previous tests of this experiment by testing the Einstein equivalence principle (EEP). The EEP states the universality of the coupling of gravity to matter and energy. Tests of the EEP are of great importance as many alternative theories of gravity and theories unifying gravity with other interactions predict violations of the EEP at high energies (Damour, 1996; Flambaum and Shuryak, 2008). The EEP consists of three main principles: the weak equivalence principle (WEP), the local position invariance (LPI), and the local Lorentz invariance (Will, 1993; Will, 2014). From those three principles the local Lorentz invariance is best constrained, as no violations have been found down to $c_0^2/c^2 - 1 < 10^{-20}$ (Chupp et al., 1989; Will, 2014). It is therefore assumed to be valid for this work, while the the LPI is discussed in the following. The WEP or universality of free fall is not straight forward to test with our current approach (Angélil and Saha, 2011), which is discussed in more detail in the outlook.

7.2 GALACTIC CENTER EXPERIMENT

Located at the very center of our galaxy is the bright radio source Sgr A*. The nuclear star cluster around it has been observed with high-resolution near-infrared (NIR) speckle and adaptive optics (AO) assisted imaging and spectroscopy over the past 26 years. This led to orbit determinations for ≈ 45 individual stars (Schödel et al., 2002; Schödel et al., 2009; Ghez et al., 2003a; Ghez et al., 2008; Eisenhauer et al., 2005; Gillessen et al., 2009a; Gillessen et al., 2017; Meyer et al., 2012; Boehle et al., 2016; Fritz et al., 2016). These observations have demonstrated that the gravitational potential is dominated by a compact object at the center of the cluster. The mass of the object was measured by Gravity Collaboration et al., 2018b to be (4.10 ± 0.03) x 10^6 $M_\odot$.

The radio source Sgr A* is coincident with the center of mass to < 1 mas (Plewa et al., 2015), and is itself very compact, with an upper limit on the radius of 18 µas, based on very long baseline interferometry at a wavelength of 1.3 mm (Krichbaum et al., 1998; Doeleman et al., 2008; Johnson et al., 2017). In addition, Sgr A* shows, in comparison to extragalactic sources, no intrinsic motion (Reid and Brunthaler, 2004; Reid, 2009). This supports the interpretation that the compact radio source is coincident with the mass. Orbital motion of the centroids of the SgrA*'s near-infrared emission during bright 'flare states' suggest that the same mass inferred from the S2 orbit is also contained within 60 to 90 µas of the mean-position, or near the innermost stable orbit of a 4 million solar mass black hole (Gravity Collaboration et al., 2018a). This all leads to the conclusion that Sgr A* is indeed a supermassive black hole (Ghez et al., 2008; Genzel et al., 2010; Falcke and Markoff, 2013).

Of all the stars in the central cluster, the main-sequence B-star S2 is of special interest. With a near-infrared K-band magnitude of 14.2, S2 is one of the brightest stars in the innermost region around the black hole. It has an orbital period of 16.05 years and has its closest encounter with Sgr A* at a distance of 16.28 light hours or 14.45 mas. S2 also appears to be a single star (Martins et al., 2008; Habibi et al., 2017; Chu et al., 2018). The close encounter with Sgr A* and the comparatively short period make it the best available probe for post-Newtonian effects in the potential of the supermassive black hole (Gravity Collaboration et al., 2018b). One thing one might have to consider, is that S2 could come so close to the black hole that the star's properties change. However, the tidal disruption radius (Hills, 1975) of the star S2, based on its stellar parameters (Habibi et al., 2017), is 100 times smaller than the star's periapsis distance. Therefore, we do not expect any strong tidal interactions between the star and the black hole.

The GRAVITY Collaboration (Gravity Collaboration et al., 2018b) showed that the data from S2 fulfills the predictions of general relativity when the gravitational redshift and the relativistic Doppler effect are taken into account. In Gravity Collaboration et al., 2018b a scaling factor f for the first order parameterized post-Newtonian corrections (gravitational redshift and Doppler shift) is introduced, where f is zero for purely Newtonian physics and unity for GR. The measured f-factor of $f = 0.90 \pm 0.09|_{\text{stat}} \pm 0.15|_{\text{sys}}$ is significantly inconsistent with pure Newtonian dynamics. The resulting f-value is getting more robust with more data added to the dataset. The same analysis as in Gravity Collaboration et al., 2018b, but with additional data taken between June and September 2018, reduced the uncertainties in the f-value to $f = 0.97 \pm 0.05|_{\text{stat}} \pm 0.05|_{\text{sys}}$ (Gravity Collaboration et al., 2019).

7.3 LOCAL POSITION INVARIANCE

The main part of this work focuses on the LPI, which states that local non-gravitational measurements are independent of their location in spacetime. To test this we use the star S2 as it moves on its eccentric orbit through the gravitational potential of Sgr A*. A violation of the LPI would imply a coupling of fundamental atomic constants, such as the fine structure constant, to the gravitational potential. LPI experiments can therefore be used to constrain coupling constants of different atomic properties (Flambaum, 2007; Flambaum and Shuryak, 2008). As such couplings are expected to be nonlinear it is especially important to perform such experiments with strong changes in potential.

According to the LPI, the gravitational redshift of a clock moving through a weak gravitational field ($\Phi/c^2 \ll 1$) with a varying potential $\Delta\Phi$, depends only on the change of the potential: $\Delta\nu/\nu = \Delta\Phi/c^2$, where ν is the clock frequency and $\Delta\nu$ the shift due to the gravitational potential. The formula implies that the shift in frequency does not depend on the internal structure of the clock, which is another way to formulate the LPI. To test this assumption one introduces a violation to the formula, commonly parametrized as β:

$$\frac{\Delta\nu}{\nu} = (1+\beta)\,\frac{\Delta\Phi}{c^2} \tag{7.1}$$

To test the LPI with a single type of clock one needs to compare two identical clocks in different gravitational potentials. Alternatively one can measure the frequency change of two non-identical clocks moving through a time-dependent potential $\Phi(t) = \Phi_0 + \Delta\Phi(t)$. In this case a violation of the LPI would again be visible in the fractional frequency difference:

$$\Delta\left(\frac{\Delta\nu}{\nu}\right) = \frac{\Delta\nu_2}{\nu_2} - \frac{\Delta\nu_1}{\nu_1} = (\beta_2 - \beta_1)\,\frac{\Delta\Phi(t)}{c^2} = \Delta\beta\,\frac{\Delta\Phi}{c^2} \tag{7.2}$$

By measuring the frequency change of two clocks moving through a potential one can therefore constrain $\Delta\beta$. Such *null redshift experiments* are regularly done on Earth using the gravitational potential of the Sun, which varies over the timescale of a year, due to Earth's eccentric orbit (see e.g. Ashby et al., 2007; Agachev et al., 2011; Peil et al., 2013; Dzuba and Flambaum, 2017). The annual potential variation due to this eccentric motion is $\Delta\Phi/c^2 = 3.3 \cdot 10^{-10}$. The most stringent limit on a violation of the LPI so far is given by Ref. (Peil et al., 2013), from a comparison of hydrogen masers with rubidium clocks. From this measurement a value of $|\beta_H - \beta_{Rb}| = (2.7 \pm 4.9) \cdot 10^{-7}$ is measured. To get to such a low limit it is necessary to measure the frequency change of atomic transitions with a precision on the order of $\Delta\nu/\nu \approx 10^{-17}$. The most stringent astronomical tests of the LPI were done by a comparison of measured wavelength shift in white dwarf spectra directly to laboratory wavelengths, to get a constraint on variations of the fine structure constant Berengut et al., 2013; Ong et al., 2013; Bainbridge et al., 2017. In the experiments with white dwarfs a potential difference of approximately 10^{-5} is reached, which is much higher than that possible for earthbound experiments. However, it is still roughly an order of magnitude lower than the potential difference observed for S2 orbiting around Sgr A*.

7.3.1 MEASUREMENT

The data for the Galactic center experiment were mainly taken with the European Southern Observatory's Very Large Telescope and Very Large Telescope Interferometer, using the three instruments NACO (Lenzen et al., 1998; Rousset et al., 1998), SINFONI (Eisenhauer et al., 2003; Bonnet et al., 2004), and GRAVITY (Gravity Collaboration et al., 2017). The NACO images provided the time-dependent 2D projected positions of the stars in the nuclear star cluster. Those positions are then calibrated relative to the radio frame of the Galactic center (Reid et al., 2007). The unique astrometric precision of $\sim$ 50 µas obtained with GRAVITY directly adds the 2D projected separation of S2 and Sgr A* to the data set. SINFONI then adds spectroscopic measurements of the stars in order to measure their line-of-sight velocity (for more details on the data and the data analysis see Gravity Collaboration et al., 2018b). The combination of the data is then used to fit the full orbit of S2 around the central black hole (Gillessen et al., 2009a; Gravity Collaboration et al., 2018b). For this work we use the S2 orbit (Gravity Collaboration et al., 2018b) to calculate the gravitational potential at the position of S2. This is done by calculating the Newtonian potential for the separation $d(t)$ between S2 and Sgr A*: $\Phi(t) = GM/d(t)$, with M being the mass of the black hole. For this calculation we can neglect all other stars in the area, as their masses are negligible in comparison to Sgr A*. Furthermore we can use a Newtonian description for the potential, as the first relativistic correction term would be from the Schwarzschild metric, which is so small that it is not yet relevant for the orbit fit Alexander, 2005; Gillessen et al., 2009a. In the three years leading up to the pericenter passage of S2 around the super massive black hole Sgr A*, the gravitational potential experienced by the star changes by $\Delta\Phi/c^2 = 3.2 \cdot 10^{-4}$.

In addition to the gravitational potential Gravity Collaboration et al., 2018b the data used for this work are the K-Band (2.0 to 2.5 µm) spectra of S2 obtained with SINFONI. These spectra are used to measure the line-of-sight velocity of S2. In the K-band S2 has two dominant absorption features: The strongest line is the Brγ line (hydrogen transition n = 7 - 4) with a vacuum wavelength of 2.1661 µm. The second feature is the helium line around 2.1125 µm. This line is not a single feature but a blend of the He I triplet at 2.1120 µm (3p ^{3}P^0 – 4s ^{3}S) and the He I singlet at 2.1132 µm (3p ^{1}P^0 – 4s ^{1}S). The weighting of the two features depends on the atmospheric parameters and the rotational velocity of the star (Habibi et al., 2017). In an individual spectrum at our resolution they appear as a single feature. In a typical observation of 1 hour the helium and hydrogen feature can be detected at $> 5\sigma$. A combined spectrum with a high signal-to-noise ratio (SNR) from Ref. Habibi et al., 2017 is shown in Figure 7.1. On the left shoulder of the hydrogen line is another helium line at 2.161 µm, which is much weaker than the hydrogen line (flux ratio of 1 to 4 in

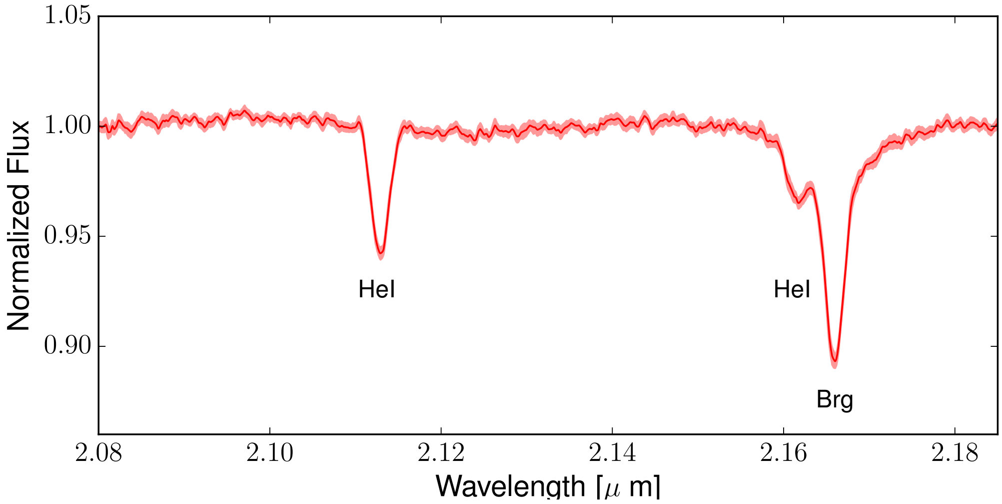

Figure 7.1: High signal-to-noise spectrum of the star S2 in the astronomical K-Band. The spectrum has been produced by combining data from 12 years of observations (adapted from Habibi et al., 2017).

the high SNR spectrum). In an individual dataset this line is just above the noise level. It is therefore not a dominant feature and does not influence the velocity measurement from the hydrogen line.

After extracting the spectrum of S2 from the SINFONI data, we usually measure the star's velocity with a combination of a fit to the Brγ line and a cross correlation of the whole K-band with the high SNR spectrum shown in Figure 7.1 (for more details see Gravity Collaboration et al., 2018b). For this work we use a slightly different approach. We divide the spectrum into two parts, one containing the He feature and the other one the Brγ line. Both parts are individually cross correlated with their corresponding part of the high SNR spectrum. By doing this we get two velocities for each spectrum: one from the helium line and one from the hydrogen line. In other words, we have a helium and a hydrogen clock moving through the varying gravitational potential during the pericenter passage of S2. By measuring the difference in frequency change for both clocks we are able to give an upper limit on the LPI violation during the pericenter passage. The values for the velocity difference $(\mathrm{v}_{He} - \mathrm{v}_H)/c = \Delta\nu_{He}/\nu_{He} - \Delta\nu_H/\nu_H$ are shown in Figure 7.2, together with the gravitational potential at the position of S2.

The uncertainty of the datapoints in Figure 7.2 is calculated from several contributions. The first is the calibration error of the wavelength. During the data reduction the wavelength calibration of each individual data frame is fine-tuned by a set of OH lines in the K-Band. The scatter of the line position from their expected velocity after the fine tuning is below $5\,\mathrm{km\,s^{-1}}$, which is then used as the uncertainty for the measured wavelength. This is calculated for each spectrum individually by fitting the atmospheric OH lines. A second contribution is the uncertainty of the cross correlation, determined from the uncertainty of the cross-correlation peak position. A third error originates from the extraction of the spectrum. As SINFONI is an integral field spectrograph the final result of the data reduction is a 3D cube, where two dimensions are the image axes and the third is the spectrum for each pixel. To get a spectrum of a star one has to select the source and background pixels in the image plane. This is the source of a third uncertainty as different masks can lead to slightly different results in the velocity. We account for this by calculating the velocity from different reasonable masks and use the scatter in the result as an estimate of uncertainty. The uncertainty of one velocity measurement is then the quadratic sum of these three contributions. This is done for Brγ and He I individually. The final value used in this analysis is then the difference of the two velocities with the quadratic sum of the uncertainties. This might slightly overestimate the error as the calibration error should be the same for both measurements, but is accounted for twice. However, this does not have a big influence as it is the least dominant error source.

To get an upper limit on the LPI violation we use Equation 7.2 to fit the potential to the data points shown in Figure 7.2. In the fit $\Delta\beta = \beta_{He} - \beta_H$ is left as a free parameter. The fitted value of $\Delta\beta$ is:

$$\Delta\beta = |\beta_{He} - \beta_H| = (2.4 \pm 5.1) \cdot 10^{-2} \tag{7.3}$$

Where the given error is the 1 σ confidence interval of the fit. We can place an upper limit on the violation of the LPI in the strong gravitational field of the supermassive black hole of $\Delta\beta \leq 5 \cdot 10^{-2}$. The result is consistent with $\Delta\beta = 0$. The fit is shown together with the data in Figure 7.2. The χ^2 analysis of the fit shows a reduced χ^2 of 0.91. In comparison, $\beta = 0$ results in a χ^2_{red} of 0.89. Under the assumption that the χ^2 distribution is approximately Gaussian it has a variance of $\sigma = \sqrt{2/N} = 0.22$. Therefore both values for χ^2_{red} lie within the one sigma range of $\chi^2_{red} = 1$ and the χ^2_{red} values cannot be used to distinguish between the models.

While our result is not competitive with current experiments on earth, the change in gravitational potential experienced by S2 on its orbit from early 2015 to its pericenter passage in May 2018 is $\Delta\Phi/c^2 = 3.2 \cdot 10^{-4}$. This is a regime which has not been reached by any other experiment and we therefore test the LPI at a potential difference which has not been tested before this work (see Figure 7.3) (Will, 2014).

As mentioned in the introduction, a violation of the LPI would imply a coupling of fundamental atomic constants to the gravitational potential. Atomic clock measurements are therefore used to constrain coupling constants of different

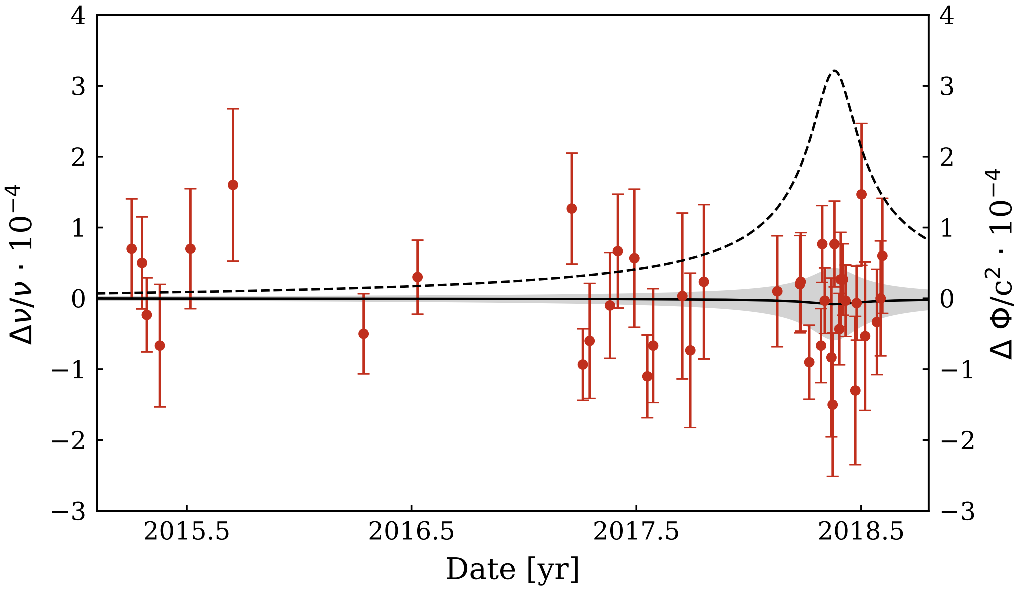

Figure 7.2: Difference in frequency change for the helium and the hydrogen line as red dots. The dimensionless gravitational potential is shown as a dashed black line. The solid black line shows $\Delta\beta \cdot \Delta\Phi/c^2$, where $\Delta\beta$ is fitted to the data. The gray area shows the 3 sigma values from the fit.

atomic properties (Flambaum and Shuryak, 2008). This can for example be done for the coupling of the fine structure constant α (Dzuba and Flambaum, 2017) or for the electron-to-proton mass ratio m_e/m_p and the ratio of the light quark mass to the quantum chromodynamics length scale Peil et al., 2013. In principle one could also use our measurement of β to constrain these coupling constants. However, a single measurement of $\Delta\beta$ is not sufficient for that. One can overcome this by combining different measurements from different atomic species (Peil et al., 2013), or by using computational techniques to calculate the relativistic perturbation of the energy levels for the observed transitions (Dzuba and Flambaum, 2017). In the present case, the S2 helium absorption line is a doublet and the transitions are not isolated enough that a specific model of the transition would yield further information. We therefore cannot make any further statements than the pure limit on the violation of the LPI.

7.4 OUTLOOK

This measurement demonstrates that the data from stars orbiting a black hole can be used for testing the LPI. Looking forward this also opens possibilities for the next pericenter passage of S2 in 2034. At that point the Extremely Large

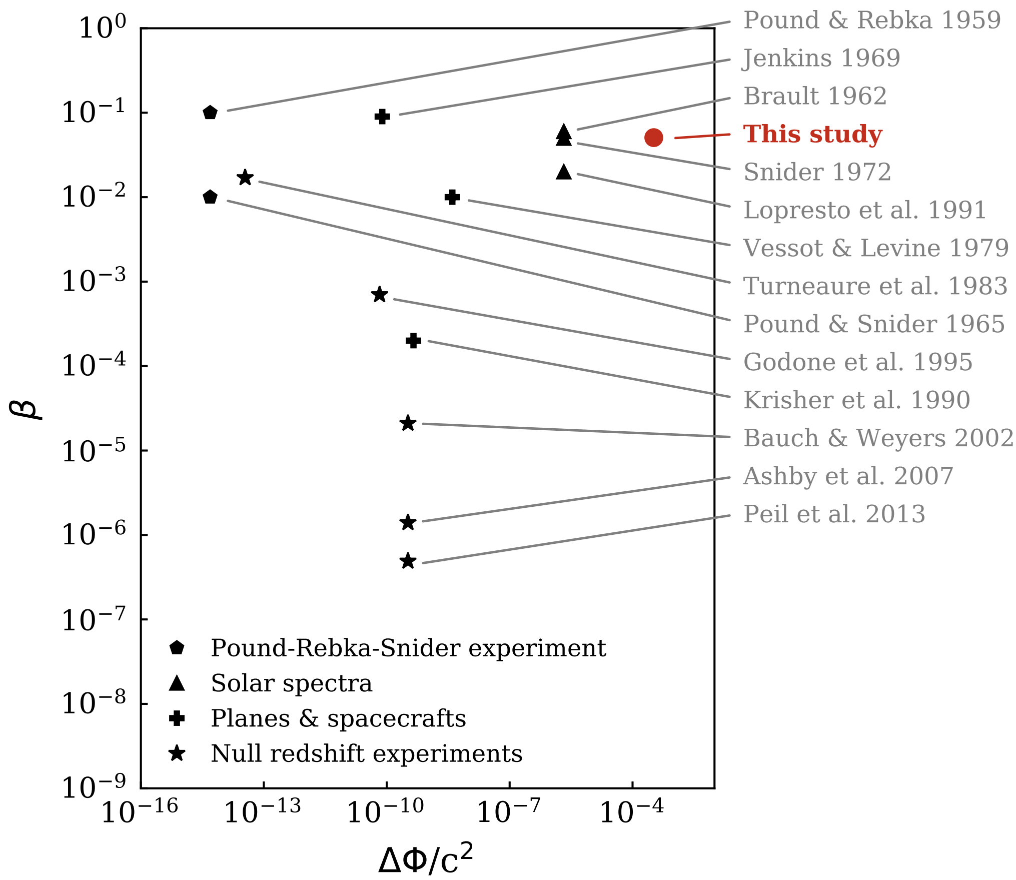

Figure 7.3: Comparison of selected tests of the LPI with gravitational redshift. Plotted is the variation in potential, which is tested against the measured limit on a violation. The different symbols mark the Pound-Rebka-Snider experiments (Pound and Rebka, 1959; Pound and Snider, 1965), tests from solar spectral lines (Brault, 1962; Snider, 1972; Lopresto et al., 1991), tests on rockets and spacecrafts (Jenkins, 1969; Vessot and Levine, 1979; Krisher et al., 1990), and null redshift experiments (Turneaure et al., 1983; Godone et al., 1995; Bauch and Weyers, 2002; Ashby et al., 2007; Peil et al., 2013)

Telescope (ELT) will be fully operational. With a telescope diameter of more than four times the one from the VLT, the ELT will collect more than twenty times more light. The first light instrument MICADO (Davies et al., 2016) will include a slit spectrograph with a resolving power of R $\geq$ 10000. This is more than six times higher than what we currently achieve with SINFONI (R = 1500 in the used mode). One can therefore use the ELT to measure S2's spectrum with higher resolution and with higher SNR. This would allow a velocity measurement of S2 in the H-Band, which currently has a too low SNR for velocity measurements from individual data frames. In the H-Band there is a narrow helium line (He I at 1.7002 µm) as well as a series of hydrogen lines (Habibi et al., 2017), which can be used to significantly improve the velocity measurement. Unlike hydrogen, the He lines are not sensitive to the stellar pressure broadening, providing sharper atomic lines to measure the velocity with high accuracies.

With the high sensitivity of the ELT it is also possible to make the same measurement for fainter late type (K & M type) stars. The infrared spectrum of these stars shows several sharp metal lines, including different isotopes, as well as series of rotational–vibrational bands of CO molecule (Wallace and Hinkle, 1997). With a high resolution spectrograph such as the planned HIRES (Marconi et al., 2016), with a resolving power of R = 130000 and a very high calibration accuracy a velocity measurement of the order of $\mathrm{m\,s^{-1}}$ would be possible. This would allow a measurement of $\frac{\Delta\nu}{\nu}$ in the order of 10^{-8}. For a star on a similar orbit as S2 this would translate in a factor of 10^4 more restrictive limit on the LPI and velocities from different atoms could be used to directly constrain coupling parameters. Interesting stars for this are for example S21 or S38 which are both in a comparably short orbit around SgrA* (37 and 19 years, see Gillessen et al., 2017), or even fainter stars in closer orbits which might be discovered with the ELT.

This would also open the possibility to test the third part of the EEP, the WEP, also known as universality of free fall. It states that inertial and gravitational mass are equivalent. In principle, one can use a gravitational redshift experiment to test the WEP, under the assumption that special relativity is fully valid Schiff, 1960. However, in order to do so one has to precisely know the gravitational field, as otherwise a violation could be absorbed as a constant factor in the gravitational potential. A solution for this could be to use different stars around Sgr A*. In this case one star can be used to test the WEP and the others to measure the mass of Sgr A* separately Angélil and Saha, 2011. At the moment this would be a rather imprecise measurement, as the current best mass measurement of Sgr A* is from S2 itself. This is a problem which is very likely to be solved with future observations and facilities. One solution would be the discovery of a star in closer orbit around SgrA*, either with GRAVITY Waisberg et al., 2018 or the ELT. The combination of S2 and a closer star can then be used to measure the mass of SgrA* and test the WEP individually. However, even without a star on a very close orbit, the ELT will allow more precise measurements of the already observed orbits of S-stars. With better orbit measurement of other close S-stars, such as S38, one can then test the WEP.

7.5 CONCLUSION

With this paper we continued the analysis of the data presented by the GRAVITY Collaboration (Gravity Collaboration et al., 2018b) to give constraints on the LPI. We used the helium and hydrogen transitions in the spectrum of S2 as individual clocks, to give a constraint on a violation of the LPI. The results are consistent with the LPI and give an upper limit to a violation of $5 \cdot 10^{-2}$. This limit is in absolute numbers less stringent than the current most precise tests (Peil et al., 2013). Our experiment however tests the LPI close to a central black hole with 4 million solar masses, in a potential which is 10^6 times larger than accessible to terrestrial experiments. It is currently the most extreme test of the LPI and is fully consistent with it.

ACKNOWLEDGMENTS

GRAVITY is developed in a collaboration by the Max Planck Institute for extraterrestrial Physics, LESIA of Paris Observatory/CNRS/Sorbonne Université/University Paris Diderot and IPAG of Université Grenoble Alpes/CNRS, the Max Planck Institute for Astronomy, the University of Cologne, the CENTRA—Centro de Astrofisica e Gravitação, and the European Southern Observatory. We are very grateful to our funding agencies (MPG, ERC,CNRS, DFG, BMBF, Paris Observatory, Observatoire des Sciences de l'Universde Grenoble, and the Fundação para a Ciência e Tecnologia), to ESO and the ESO/Paranal staff,and to the many scientific and technical staffmembers in our institutions who helped to make NACO, SINFONI, and GRAVITY a reality. S.G. acknowledges support from ERC starting grant No. 306311. F. E. and O. P. acknowledge support from ERC synergy Grant No. 610058 (Black-HoleCam). J. D., M. B., and A. J.-R. were supported by a Sofja Kovalevskaja award from the Alexander von Humboldt foundation. A. A. & P. G. acknowledge support from FCT-Portugal with reference UID/FIS/00099/2013.

Part III

UNVEILING NEW OBSERVING MODES FOR GALACTIC CENTER SCIENCE

8 POLARIZATION MODEL OF THE VLTI AND GRAVITY

The goal of this chapter is to characterize the polarization effects of the VLTI and the GRAVITY beam combiner instrument. This is useful for two reasons: to understand and correct the instrumental effects on polarimetric observations with GRAVITY, and to understand the systematic error introduced to the astrometry due to birefringence when observing targets with a significant intrinsic polarization. By using a model of the VLTI light path and its mirrors and combining this with dedicated experiments data we construct a full polarization model of the VLTI Unit Telescopes (UTs) as well as of GRAVITY. We first characterize all telescopes together, to construct a universal UT calibration model for polarized targets with the VLTI. In a second step we expand the model to study the differential birefringence between the four unit telescopes. With this we can constrain the systematic errors and the contrast loss for highly polarized targets. We show that there is no significant fringe loss, even if the science and fringe-tracker target have a significantly different polarization. Finally, we determine that the astrometric phase error in such an observation is smaller than 1°, even in the worst case. We also demonstrate that we can measure reliable polarization properties of astrophysical targets with GRAVITY, using observations of the galactic center star IRS 16C.
We show that it is possible to measure the intrinsic polarization of astrophysical sources with GRAVITY. For the galactic center star IRS 16C we are able to constrain the polarization degree to within 0.6 % and the polarization angle within 5°, while being consistent with the literature values. With this work we enable the use of the polarimetric mode with GRAVITY for the community and outline the steps necessary to observe and calibrate polarized targets with GRAVITY.

8.1 INTRODUCTION

Polarization is an important part of the information contained in electromagnetic radiation of astronomical sources. The use of polarimetric observations enables a better understanding of the source of radiation as well as its environment. Polarimetric observations are nowadays used over a very broad range of science cases and more and more instruments are equipped with a polarimetric mode (see e.g. Witzel et al., 2011; Dorn et al., 2014; Norris et al., 2015; van

Holstein et al., 2020). With the enormous success of the VLTI beam combiner instrument GRAVITY over the last years in various science fields, interest in polarimetric observations with GRAVITY and the VLTI has also grown. The fundamental capabilities of GRAVITY to make polarimetric observations have already been shown by observing the polarization of flares from the supermassive black hole SgrA* (Gravity Collaboration et al., 2018a; Gravity Collaboration et al., 2020b). With the help of the polarization data it was possible to constrain the magnetic fields around SgrA*. Similarly the EHT collaboration has studied the magnetic fields around the black hole M87* with their recently released polarimetric image (Event Horizon Telescope Collaboration et al., 2021). But not only the study of magnetic field is enabled by polarimetry, but also many other research areas profit from the availability of polarization measurements. For example disks around young stellar objects can be studied with the help of polarimetry (Hunziker et al., 2021), or measurements of dust properties of evolved stars benefit from a polarization measurements (Ireland et al., 2005; Norris et al., 2012b; Haubois et al., 2019). For a more complete overview see Elias et al., 2008 and Trippe, 2014. To combine polarimetric measurements with the unique angular resolution of GRAVITY we want to characterize the polarization properties of GRAVITY and the VLTI.

Ideally, a telescope and its instrument would not alter the polarization of incoming light. In reality however, the optical train of a telescope introduces polarization signal. This can mean that a polarization signal is produced by the instrument or that the instrument alters the incoming polarization by introducing crosstalk, which mixes the incoming polarization states. In order to get rid of these effects, the telescope and its instrument must be carefully calibrated for their effect on the measured polarization signal. In this work we show the results of a series of measurements to calibrate the polarimetric properties of the VLTI. This includes the characterization of the amount of crosstalk between different polarization states as well as polarization introduced by the VLTI itself. In the case of an interferometer, this is a bit more difficult than for a single-telescope instrument, as there are a significantly higher number of reflections, and one also has to account for both of the rotations of the telescope, in elevation as well as in azimuth. For this reason polarimetric observations with optical interferometers are not common yet, but the foundations were laid in the erly 2000s (Elias, 2001; Elias, 2004) and first steps were done soon after (Ireland et al., 2005; Rousselet-Perraut et al., 2006) to study variable stars and circumstellar environments, and later also in aperture masking (Norris et al., 2012a; Norris et al., 2015). Today, similar to GRAVITY at the VLTI, also MIRC-X at CHARA is having its first polarimetric observations (Setterholm et al., 2020).

While the modelling is a bit more complicated for an interferometer than for a single telescope, there is no fundamental difference in the calibration model for the absolute polarization. We can use similar calibration models to those used in solar physics (see e.g. Beck et al., 2005; Harrington et al., 2019) and for the NACO and SPHERE instruments at the VLT (Witzel et al., 2011; van Holstein et al., 2020). We then use our test data to adapt the model and constrain the polarimetric properties of the VLTI. With this approach we construct a full calibration model to correct polarimetric observations.

Apart from the absolute effect the VLTI has on the polarization measurement, there is an additional effect which has to be considered for interferometers. If the light paths of the individual telescopes have different polarimetric properties, this can introduce differential birefringence between the different telescopes. The VLTI has been built with great care to make sure that the different light paths and reflections within are as similar as possible, but of course cannot be ideal, as there are imperfections in the trains, as well as individual upgrades such as the adaptive M2 mirror at UT4. These differential effects are important to understand, as differential birefringence leads to a loss of fringe contrast and therefore limits the sensitivity of an interferometer (Beckers, 1990; Rousselet-Perraut et al., 1996). Furthermore, differential effects can also introduce errors to the visibility phase and therefore limit the astrometric accuracy for polarized targets. This was already explored for a part of the VLTI by Lazareff et al., 2014b (hereafterL14) and is continued with this work.

While most of the light path and the reflections are similar for the Unit Telescopes (UTs) and the Auxiliary Telescopes (ATs), we focus solely on UT observations in this work. The derotation of the field is done in the ATs themselves, which adds more complexity to the polarization measurement. Furthermore, the ATs are not fixed in place, but can be repositioned. This could effect the polarization, especially if the telescopes are located on different sides of the delay line. Taking this into account as well as the scientific importance of the UTs, we decided to limit this study to the UTs.

First, we will recap the polarization conventions in section 8.2, before we discuss the instrumental polarization of the VLTI with the telescope model and the calibration measurements in sections 8.3 and 8.4. We then investigate the differential effects of the VLTI in section 8.5 and the polarization effects of GRAVITY itself in section 8.6.

8.2 CONVENTIONS

There are two different conventions for the description of polarization (Tinbergen, 2005). One is the Stokes formalism (with Stokes vectors and Mueller matrices) and the other the Jones formalism (with Jones vectors and Jones matrices). The Stokes formalism is often used to describe instrumental polarization effects, as the components of the Stokes vector directly relate to the measurable intensities. It can also describe partial polarization and has simple formulas to measure and calculate the fundamental properties of polarized light. The Stokes values are also easily measured using a half- and a quarter-wave plate. One disadvantage is that the Stokes formalism does not include phase information. We will therefore mostly use the Stokes formalism in this work, and only switch to the Jones formalism when the phase information is needed for the interferometric quantities.

8.2.1 STOKES FORMALISM

In the Stokes formalism the light and its polarization is described by a Stokes vector. For an electric field which is described by

$$\vec{E}(z,t) = \begin{pmatrix} E_x \\ E_y \end{pmatrix} e^{i(kz-\omega t)} = \begin{pmatrix} A_x \cdot e^{i\phi_x} \\ A_y \cdot e^{i\phi_y} \end{pmatrix} e^{i(kz-\omega t)}, \tag{8.1}$$

the Stokes vector is defined as

$$s = \begin{bmatrix} I \\ q \\ u \\ v \end{bmatrix} = \begin{bmatrix} \langle E_x^2 + E_y^2 \rangle \\ \langle E_x^2 - E_y^2 \rangle \\ \langle 2E_xE_y \cos\delta \rangle \\ \langle 2E_xE_y \sin\delta \rangle \end{bmatrix} = \begin{bmatrix} A_x^2 + A_y^2 \\ A_x^2 - A_y^2 \\ 2A_xA_y \cos\delta \\ 2A_xA_y \sin\delta \end{bmatrix}, \tag{8.2}$$

with $\delta = \phi_x - \phi_y$. As the absolute intensity is not important for the polarization properties we will in the following only consider normalized Stokes vectors:

$$S = \frac{s}{I} = \begin{bmatrix} 1 \\ Q \\ U \\ V \end{bmatrix}. \tag{8.3}$$

The first parameter is the intensity in the non-normalized Stokes vector and is one in the normalized Stokes vector. The second and third parameters, Q and U, represent linear polarization. Positive Q shows linear polarization in horizontal direction and negative Q in vertical direction. U is 45° rotated in **counterclockwise direction** with respect to Q, when looking into the beam of light. V describes circular polarization with positive V being **right handed** and negative V being **left handed**. In the normalizes Stokes vector Q, U and V range from -1 to 1.

The change of polarization for any optical system is described by a 4x4 real matrix, the Mueller matrix. For an input state S_{in} the output state S_{out} is calculated as follows:

$$S_{out} = M \cdot S_{in}. \tag{8.4}$$

One of the advantages of the Stokes parametrization is that it is very easy to calculate the essential polarization properties. From the Stokes parameters one can calculate the degree of polarization (DOP), the degree of linear polarization (DOLP) and the polarization angle (Θ_{pol}) as follows:

$$\text{DOP} = \sqrt{Q^2 + U^2 + V^2} \tag{8.5}$$

$$\text{DOLP} = \sqrt{Q^2 + U^2} \tag{8.6}$$

$$\Theta_{\text{pol}} = \frac{1}{2} \arctan\left(\frac{U}{Q}\right) + n\tfrac{\pi}{2} \tag{8.7}$$

where n is 1 for Q < 0 and otherwise 0.

8.2.2 JONES FORMALISM

For the analysis of differential effects between the telescopes we need a description of the propagated phase (see section 8.5), which is not possible with the Stokes formalism. For this case we will use the Jones formalism. In this formalism the state of polarization of an electric field is described by a complex Jones vector:

$$j = \begin{pmatrix} E_x \\ E_y \end{pmatrix} = \begin{pmatrix} A_x \cdot e^{i\phi_x} \\ A_y \cdot e^{i\phi_y} \end{pmatrix}. \tag{8.8}$$

A change in radiation is again described by a matrix, the 2x2 complex Jones matrix:

$$j_{out} = J \cdot j_{in}, \tag{8.9}$$

with the input Jones vector j_{in} and the output vector j_{out}. One of the main disadvantages of the Jones formalism is that Jones vectors always represent fully polarized light. To be able to deal with partially polarized light one has to use the coherence matrix of Jones vectors:

$$C = \begin{pmatrix} \langle E_x E_x^* \rangle & \langle E_x E_y^* \rangle \\ \langle E_y E_x^* \rangle & \langle E_y E_y^* \rangle \end{pmatrix} \tag{8.10}$$

They propagate as follows:

$$C_{out} = J \cdot C_{in} \cdot J^* \tag{8.11}$$

The degree of polarization of a state described by a Jones coherence matrix is (Gil, 2004):

$$\text{DOP} = \sqrt{\frac{2 \cdot \text{Tr}(C^2)}{\text{Tr}(C)^2} - 1}, \tag{8.12}$$

with the trace of the coherence matrix $\mathrm{Tr}(C)$.

Similar to the approach of L14, we use the coherence matrix of the observed source to model the interferometric response. For this we assume that we have a system, as it is for example present in GRAVITY, where the light is split in two orthogonal linear polarizations. The interferometric combination then happens for the light in both directions individually.

The response of an interferometer to an electromagnetic signal $\vec{e}$ depends on the instrumental polarization of the two telescopes in each baseline. For two telescopes m and n this response is given by (see e.g. Hamaker, 2000; Smirnov, 2011):

$$\begin{aligned} V_{m,n} &= 2\ \langle J_m \cdot E\,(J_n \cdot E)^H \rangle \\ &= 2\ J_m \cdot \begin{pmatrix} \langle E_x E_x^* \rangle & \langle E_x E_y^* \rangle \\ \langle E_y E_x^* \rangle & \langle E_y E_y^* \rangle \end{pmatrix} \cdot J_n^H \\ &= 2\ J_m \cdot C_{in} \cdot J_n^H \end{aligned} \tag{8.13}$$

This quantity $V_{m,n}$ has different names across literature. Defined as *coherency matrix* by Hamaker, 2000, *visibility matrix* by Smirnov, 2011 or *cross-coherence matrix* in L14, it is nothing other than the complex visibility in a matrix representation. Taking this into account, one can get the interferometric quantities by extracting the matrix quantities along a specific axis, as was already done in L14. The correlated flux F, the photometric flux I, the fringe contrast ν and the fringe phase Φ are calculated in the following way:

$$\begin{aligned} F^x_{m,n} &= \left| V^x_{m,n} \right| \\ I^x_{m,n} &= \frac{1}{2}\left(V^x_{m,m} + V^x_{n,n} \right) \\ \nu^x_{m,n} &= |V^x_{m,n}| / I^x_{m,n} \\ \Phi^x_{m,n} &= Arg(V^x_{m,n}) \end{aligned} \tag{8.14}$$

With this concept we have everything in hand to calculate the interferometric response to polarized targets, taking into account the instrumental polarization of the individual telescopes. We will use this in section 8.5 to determine the differential birefringence and phase loss of the VLTI.

8.3 VLTI MODEL

In order to build up a calibration model for the VLTI we first model the light path with all its mirrors. This is done only once and not for all Unit Telescopes (UTs) individually, as the light paths of the four UTs are almost

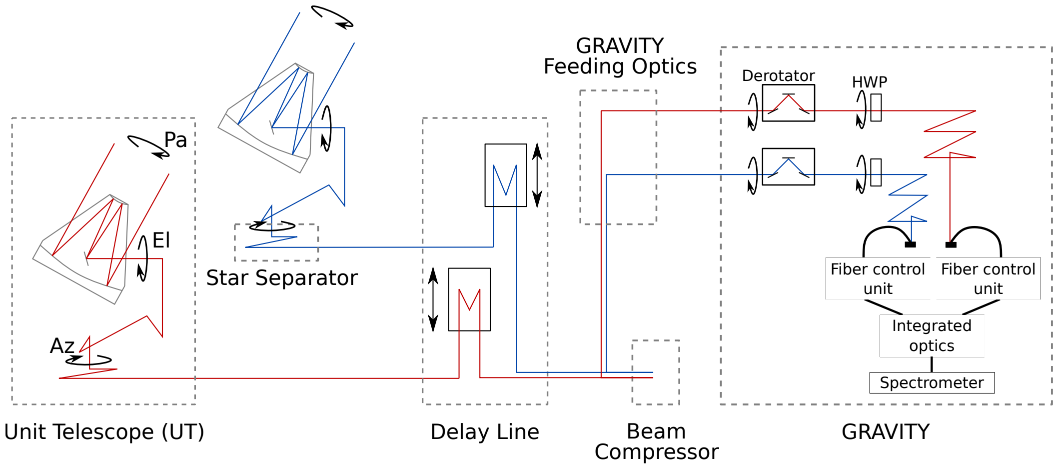

Figure 8.1: Schematic model of the VLTI light path. The light path is shown for two UTs in red and blue including GRAVITY. The rounded arrows indicate the possible rotations in the VLTI (for change in Azimuth (Az), Elevation (El) and paralactic angle (Pa)) and in GRAVITY (at the field derotator and the half-wave plate (HWP)). The straight arrows indicate the movement of the delay lines. The location of the star separator is only shown for the blue beam, but is in the same place for both telescopes. The fiber optics and elements within the GRAVITY beam combiner are only indicated here and further explained in section 8.6.

identical. The only differences are the distances between some mirrors and the directions of some 45° reflections in the delay line, both of which have no effect on the propagation of polarization. This assumption is later supported by our measurements. The overall model is based on what was previously developed by L14 (for more details see also: Lazareff et al., 2014a).

8.3.1 VLTI LIGHT PATH

The light path for two telescopes is shown in Figure 8.1. After the telescope itself, the light is sent to the Nasmyth platform by M3. It then travels to the center below the telescopes, where it is guided into the Coudé room. In the Coudé room it travels through the star separator where some of the light is directed into the adaptive optics system. As the the adaptive optics system is not sensitive to polarization and the light is not fed back, it is not relevant for the purpose of instrumental polarization. From there all light beams are sent to the delay lines. Here the positions of the mirrors change slightly for each telescope, but as the distances only differ in the direction of light propagation and all the reflections are identical, these differences do not affect the polarization. From the delay lines the light enters the VLTI lab, where it reaches the beam compressor, which adapts the beam size to fit the beam size required by GRAVITY. After the beam compressor the light continues to the VLTI switchyard, where it can be sent to the individual instruments. For GRAVITY there is one more reflection to feed the light into the instrument. In the instrument the light is derotated by a K-Mirror and a half-wave plate, before it is fed into the fiber coupler. More details on the exact components of GRAVITY are given in section 8.6.

8.3.2 MODELLING

An electromagnetic wave incident on a mirror can be decomposed into a component parallel (p-component) and a component perpendicular (s-component) to the plane of incidence. Reflections on a metallic mirror can introduce a linear polarization if the reflectivity of the two components is different, or a circular polarization when there is a different phase shift for the two components. The Mueller matrix which describes such a reflection is given by (see e.g. Collett, 1992):

$$M = \frac{1}{2} \begin{pmatrix} r_s^2 + r_p^2 & r_s^2 - r_p^2 & 0 & 0 \\ r_s^2 - r_p^2 & r_s^2 + r_p^2 & 0 & 0 \\ 0 & 0 & 2r_s r_p \cos(\delta) & 2r_s r_p \sin(\delta) \\ 0 & 0 & -2r_s r_p \sin(\delta) & 2r_s r_p \cos(\delta) \end{pmatrix} \tag{8.15}$$

where r is the reflection coefficient of each component and δ the relative retardation: $\delta = \phi_s - \phi_p$. r and δ can be directly calculated from the Fresnel formula:

$$\sin \Theta_i = n \sin \Theta_r, \tag{8.16}$$

where Θ_i and Θ_r are the incident and reflection angles and n the material dependent refractive index. While this is the original Fresnel formula the refractive index for metals is a complex number and therefore also the reflection angle Θ_r is complex and is not a regular angle anymore. With the incident angle and the complex Θ_r one can now calculate the reflectance:

$$R_s = -\frac{\sin(\Theta_i - \Theta_r)}{\sin(\Theta_i - \Theta_r)} = r_s \exp(i\phi_s), \tag{8.17}$$

$$R_p = \frac{\tan(\Theta_i - \Theta_r)}{\tan(\Theta_i - \Theta_r)} = r_p \exp(i\phi_p), \tag{8.18}$$

With the information of n and Θ_i one can therefore calculate the Mueller matrix for the reflection of a mirror.

For the model we use the positions of the individual mirrors as given by Michel, 2000. We show the notation for the mirrors, which we use in the following,

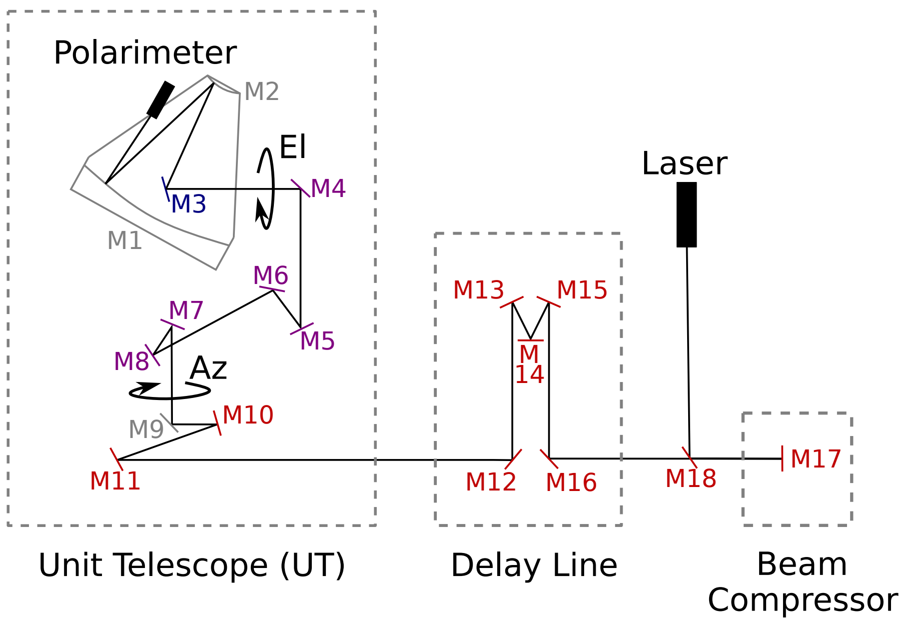

Figure 8.2: Simplified version of the VLTI light path from Figure 8.1 to show the modeling and the experimental setup. The black squares show the location where the laser is launched and where the polarimeter is mounted. The names of the mirrors used in the text are given. The color of the mirror number shows the grouping which was used for the fitting. Grey mirrors are not fitted in our calibration model.

in Figure 8.2. From the positions we can calculate the light path and the incident angle at each mirror. Together with the material of the mirrors this is enough to set up the VLTI model. However we implemented the following simplifications:

- We do not model M1 and M2 as the incidences are near normal and we can ignore their contribution.
- The star separator (see Figure 8.1) is not implemented as a special element in our model. As it is not rotating we instead approximated it with the initial positions of M10 and M11 from the VLTI setup before the implementation of the star separator, as given by Michel, 2000 (see also Figure 8.2).
- The reflection in delay line is done with cats-eye retroreflector. In our model we simplify this to three mirrors.
- The beam compressor is modeled as just one mirror, as all the incidences are almost normal.

The refractive indices of the mirrors are taken from the initial model from L14, as given in an online database [1]. For the three materials used here, they are:

- Gold: n $= 0.99 + 13.81i$
- Silver: n $= 0.77 + 13.41i$
- Aluminum: n $= 2.75 + 22.28i$

With this we can calculate the Mueller matrix for each individual mirror. To combine several Mueller matrices one can just take the product of them to get the combined Mueller matrix:

$$M = M_n M_{n-1} \cdots M_2 M_1 \tag{8.19}$$

Our model starts at M3 and goes all the way down into the VLTI lab until the GRAVITY feeding optics.

8.3.3 FIELD ROTATION

One additional issue one needs to take into account is that there are several fixed and varying field rotations in the path of the VLTI. These occur at the following points (see Figure 8.2):

- Between M3 and M4 there is a rotation due to the telescope movement in elevation (El). The rotation is $\phi = 90° - \mathrm{El}$, as an elevation of 0° corresponds to a zenith angle of 90°.
- Between M8 and M9 there is a rotation depending on the telescope's position in azimuth (Az). The rotation is given by $\phi = -(\mathrm{Az} + 18.98°) + 6.02°$. The 18.98° comes from the fact that the VLTI baselines are rotated by −18.98° compared to the east-west direction. As the zero position of the UTs is towards the south this introduces an offset in the azimuth position. The 6.02° comes from the mirror positions in the path.

All these rotations are identical for the light paths of the four UTs.

This leads to a rotation of the field in the light path by:

$$\begin{aligned} \Phi &= (90° - \mathrm{El}) - (\mathrm{Az} + 18.98°) + 6.02° \\ &= -\mathrm{El} - \mathrm{Az} + 77.04° \end{aligned} \tag{8.20}$$

These rotations are directly taken into account in our calibration model. In order to derotate the actual data, one also has to correct for the paralactic

[1] https://refractiveindex.info/

angle (Pa) and another 90° rotation due to a change of the reference system from the VLTI platform to the VLTI lab. This leads to a full field rotation Θ from the sky to the VLTI lab of:

$$\begin{aligned} \Theta &= 90^\circ + \mathrm{Pa} + \Phi \\ &= \mathrm{Pa} - \mathrm{El} - \mathrm{Az} + 167.04^\circ \end{aligned} \tag{8.21}$$

This is also what is stated in Gitton and Wilhelm, 2003, with the only difference being the sign of the azimuth angle. This is due to the fact that the angle is defined as East of South in Gitton and Wilhelm, 2003, while we use the convention of the ESO ISS system, which is East of North (Perraut and Berger, 2010).

A rotated optical element would usually be implemented by multiplying the Mueller matrix of the element with a rotation matrix R:

$$R(\Theta) = \begin{pmatrix} 1 & 0 & 0 & 0 \\ 0 & \cos 2\Theta & \sin 2\Theta & 0 \\ 0 & -\sin 2\Theta & \cos 2\Theta & 0 \\ 0 & 0 & 0 & 1 \end{pmatrix} \tag{8.22}$$

A rotated element is then traditionally described by $M_\Theta = R(-\Theta) \cdot M \cdot R(\Theta)$. We do this in a slightly different way. At each rotation we rotate our coordinate system accordingly. This way the field rotation as given in Equation 8.20 is automatically included in the final calibration Mueller matrix, which then depends on the telescope position. One must take into account that each metallic mirror introduces a 180° phase shift, which is equivalent to a change of coordinate system for a Stokes vector (Keller, 2002). One must then take into account that due to this change in coordinate system, rotations after an odd number of mirrors go into the total field rotation in the opposite direction. The full Mueller matrix of the VLTI, including all necessary rotations is then given by:

$$\begin{aligned} M_{VLTI} = \quad & R\left(90^\circ + \mathrm{Pa}\right) \cdot M_{M18} \ \cdots \ M_{M9} \\ & \cdot R\left(-(\mathrm{Az} + 18.98^\circ) + 6.02^\circ\right) \cdot M_{M8} \ \cdots \ M_{M4} \\ & \cdot R\left(90^\circ - \mathrm{El}\right) \cdot M_{M3} \end{aligned} \tag{8.23}$$

8.4 CALIBRATION MEASUREMENT

In order to verify and calibrate our model we took calibration data at the VLTI. As light source we used a high power Thulium Laser from IPG photonics with a laser wavelength of 1908 nm. The instrumental polarization is expected to change with the wavelength. That is why we used a laser at 1908 nm, in order

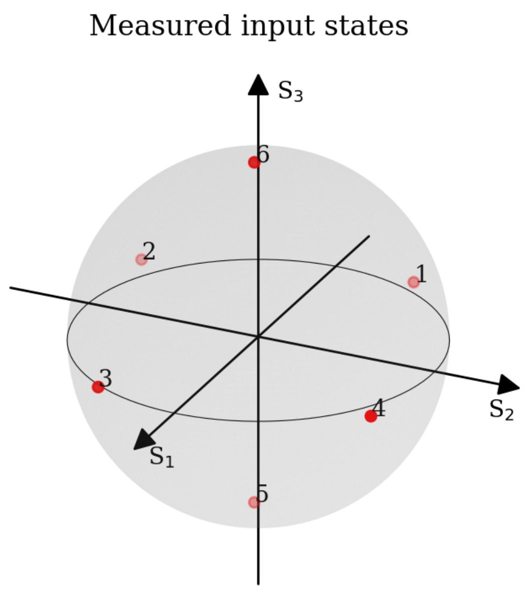

Figure 8.3: Visualization of the reference measurement of the six input states. Ideally the four linear states would lie on the equator, while the circular states are on the poles. The small deviations from that come from imperfect optics when setting up the input states.

to be as close as possible to the science wavelength of GRAVITY (between 2000 and 2500 nm). The differences over 500 nm should be small, as changes in the refractive index for the three materials are on the order of $\pm(0.1 + 2i)$ over this wavelength range. We can later use calibration observations on sky to verify that it is not a limiting factor. The polarization measurements were done with a PAX polarimeter from Thorlabs. This is a rotating-waveplate-based polarimeter which was customized by Thorlabs to work at NIR wavelengths. In order to have the full light path of the VLTI, we launched the laser in the VLTI lab, from the reference plates just in front of the GRAVITY feeding optics. With a linear polarizer, a half-wave and a quarter-wave plate we could modify the polarization of the laser and set it to arbitrary input states. The measurement head of the polarimeter was mounted onto a spider arm of one UT. This allowed us to measure the full light path at different telescope positions. For a sketch of the experimental setup see Figure 8.2.

In order to get the full polarization information the goal was to measure the Mueller matrix of the light path at different telescope positions. As a Mueller matrix has 16 free parameters, we needed at least four input states to determine the full matrix. As shown in Layden et al., 2012; Sabatke et al., 2000; Reddy et al., 2014, it is best to equally space the input states over the Poincaré sphere, which minimizes the error from the matrix inversion. The Poincaré sphere is a way to visualize polarization states (for an example see Figure 8.3, see also Collett, 1992). Fully polarized states lie on the sphere and partially polarized states are shifted towards the center of it. Fully linearly polarized states are shown on the equator and fully circular states on the two poles.

In order to keep our input states as simple as possible we used six different input states with equal distribution over the Poincaré sphere. The input states were four linearly polarized states with a distance of 45 degrees to each other and two fully circularly polarized states (left and right). The linear states were intentionally chosen to not coincide with the geometric axis of the light path (i.e. not 0°, 45°, ...). The six input states we used are the following:

- linear polarized at 75°
- linear polarized at 30°
- linear polarized at $-15°$
- linear polarized at $-60°$
- circular polarized, left handed
- circular polarized, right handed

The measured input states are also shown in Figure 8.3. The measurement was done for all four UTs with an average of 12 different telescope positions in altitude and azimuth. In order to test how well we can measure the polarization and how reproducible the input states are we did several test measurements. From those we conclude that the uncertainty on the polarization angle is on the order of 0.5° and 0.2 % for the degree of polarization. Those uncertainties are added to the error derived from the temporal scatter of each measurement.

8.4.1 FIRST RESULTS

The first test we did is if the degree of polarization is maintained or if we have significant depolarization in the light path of the VLTI. Overall we measure a degree of polarization of (98.1 ± 0.4) % and therefore a polarization loss of around 2 %. Such a small amount of depolarization is expected from scattering on dust in the optical train.

More interesting is the effect of instrumental polarization on the polarization angle and birefringence on the degree of linear polarization. For the polarization angle we look at the four linear input states, 100 % linearly polarized at 75°,

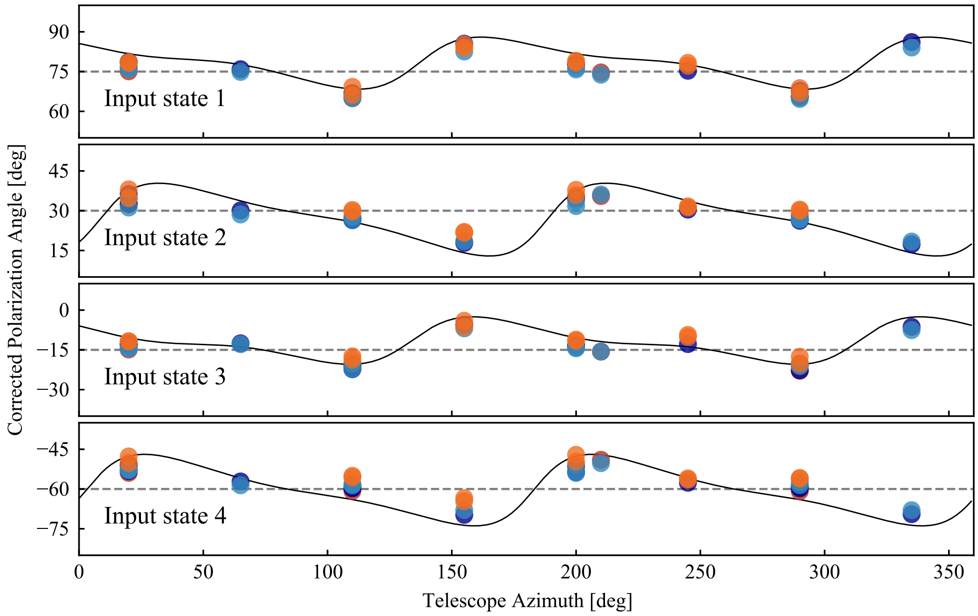

Figure 8.4: Measured polarization angles for the different telescope positions, only corrected by the geometric rotation of the field. The four panels show the data for each linear input states, with the different colors showing the data from the four UTs. The dashed line shows the input values for the polarization angles and the solid line the value expected from the model.

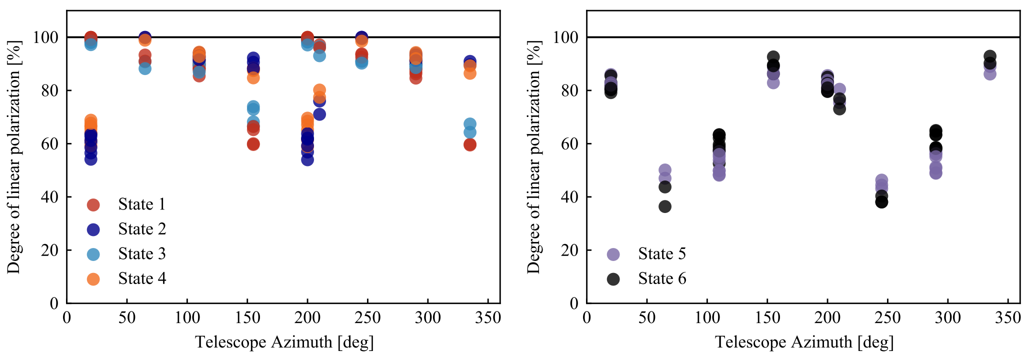

Figure 8.5: Measured degree of linear polarization for the different input states. Left: linear input states where the input degree of linear polarization is 100%. Right: circular states, where the input is fully circularly polarized, so 0% linear polarization.

-60°, -15°, and 30°. This measurement must be corrected for the field rotation, according to Equation 8.20, with an additional correction for the fact the polarimeter measurement head was mounted on the telescope spider, which is at an angle of 5.5° from the main axis.

The measured polarization angles as a function of azimuth position are shown in Figure 8.4. These data were taken at an elevation of 50° and 70°. As the change in elevation is not the dominant factor, the data is shown together. While the measured values lie around the input values, there is some modulation of around 15°. This is the instrumental polarization by the mirror train, which clearly depends on the telescope position. With the data we also show the prediction of the polarization angle by the polarization model from section 8.3. This illustrates that the data roughly follows the model and the amount of instrumental polarization we measure is nicely predicted by the model. The data from all telescopes is shown in one plot to illustrate that the telescopes behave very similar. The differences between the UTs will be discussed in section 8.5.

The third effect we can investigate is how much cross talk there is between the linear and circular polarization states, i.e. how elliptic the input states become. The result is shown in terms of degree of linear polarization in Figure 8.5. Here we see that the linear states, which should have 100 % linear polarization, have much lower values, going down to below 60 %, again depending on the telescope position. The inverse effect is clearly shown for the circular states, which reach very high values in degree of linear polarization with a maximum of 90 %.

From the calibration data one can conclude that the UTs behave very similarly and do not show significant depolarization. However we clearly see instrumental polarization, which would modify a polarization angle measurement by up to 15°. There is also strong crosstalk between linear and circular states, which could decrease the measured linear polarization degree by up to 40 %. Both effects are dependent on the telescope position.

8.4.2 FITTING THE CALIBRATION MODEL

From the comparison of model and data in Figure 8.4 we conclude that the model roughly predicts the measurement, but that there is still some discrepancy. To reach a full calibration model we improve the purely analytic VLTI model by fitting it to the obtained calibration data. The model includes 18 mirrors with two input values for the refractive indices and several rotations in the train. This proved to be almost impossible to fit to our sparse data. In order to overcome this, we group together all mirrors which have no rotation between them. These are the following:

- M3

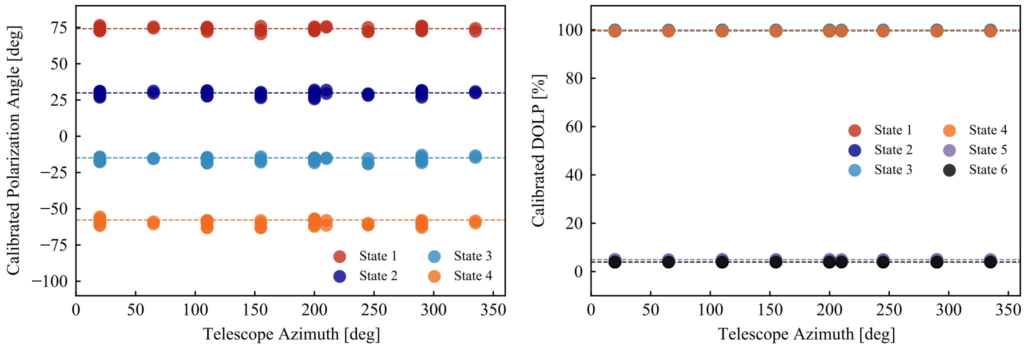

Figure 8.6: Test data calibrated with the fitted polarization model. The data are the same as in Figure 8.4 and Figure 8.5 but now calibrated. In both plots the data is shown as dots and the input states as dashed lines. The different colors show the different input states. The left plot shows the polarization angle and the right plot the degree of linear polarization.

- M4 to M8
- M9
- VLTI lab and delay lines (M10 to M18)

The groups of mirrors are also indicated in Figure 8.2 by different colors in the mirror notation. The groups rotate then with a change of elevation between M3 and M4, a change in azimuth between M8 and M9 and a constant field rotation after M9:

$$\begin{aligned} M_{VLTI} =& M_{Lab} \cdot R(90^\circ) \cdot M_{M9} \cdot R\left(-(\mathrm{Az} + 18.98^\circ) + 6.02^\circ\right) \\ & \cdot M_{M4-8} \cdot R(90^\circ - El) \cdot M_{M3} \end{aligned} . \tag{8.24}$$

The advantage of this approach is that the form of the Mueller matrix for a group of reflections stays the same as for a single reflection (see Equation 8.15). As the values in this matrix do not correspond to the values from a single Fresnel equation anymore we can modify the Mueller matrix to a simpler version (For the derivation see Harrington et al., 2019):

$$M = \frac{r_p}{2} \begin{pmatrix} 1+X^2 & 1-X^2 & 0 & 0 \\ 1-X^2 & 1+X^2 & 0 & 0 \\ 0 & 0 & 2X\cos(\delta) & 2X\sin(\delta) \\ 0 & 0 & -2X\sin(\delta) & 2X\cos(\delta) \end{pmatrix}, \tag{8.25}$$

where X is calculated from the reflection coefficients: $X = r_s/r_p$. The values for M9 were measured by L14, which leaves us with only six values to fit. Furthermore, the fitted matrices do not include rotations, which makes it

Table 8.1: Fitted values for X and δ. The given uncertainty is the one sigma confident interval of the fit. The vues for M9 are not fitted and therefore have no fitting uncertainty.

	X	δ [°]
M3	1.000 ± 0.006	170.1 ± 0.4
M4-M8	0.998 ± 0.006	144.4 ± 0.3
M9	0.944	165.0
M10-M18	0.917 ± 0.005	142.3 ± 0.3

possible to apply the model for each telescope position and in both propagation directions.

With the fitted values we therefore have a polarization model which calculates a Mueller matrix for the whole VLTI light path and depends on the telescope position. For an ideal mirror we assume $X = 1$ and $\delta = 180°$. The values we derived from the fit are given in Table 8.1. With the fitted calibration model we calibrated the test data set, shown in Figure 8.6. For the calibrated data the polarization angle of the input states is recovered well and the degree of linear polarization is 100 % for the linear input states and very low for the circular states, which matches the input states. If one compares the calibrated data with the original in Figure 8.4 and 8.5, this is a very clear improvement. This excellent result of the fitted model also validated the simplifications made in the model (see subsection 8.3.2).

With the fitted values the calibration model is a simple function of telescope position. We obtain a Mueller matrix for each telescope position, which describes the instrumental polarization of the VLTI. The sky polarization can be calculated from the measured Stokes vector and the Mueller matrix of the VLTI by applying Equation 8.4. In order to make this available to the community we put the calibration model into a small python package, which is available as VLTIpol at github[2].

8.5 DIFFERENTIAL EFFECTS

Apart from the absolute calibration of instrumental polarization, another important question is whether the differential birefringence between the telescopes causes errors in astrometric measurements. This topic was originally addressed by L14, however in their analysis they used small random perturbations of the telescopes in order to estimate the phase error and get the best alignment of the optical components in GRAVITY. We can now extend their analysis, as we

[2] `https://github.com/widmannf/VLTIpol`

do not have to work with random perturbations but have the measurements of the instrumental polarization for the four UTs. For this section we will switch to the Jones algorithm as this ultimately allows us to estimate the phase errors introduced by differential birefringence.

8.5.1 FITTING INDIVIDUAL TELESCOPES

Similar to the approach in subsection 8.3.2, we again fit the model to the calibration data. But this time we treat each telescope individually. The main principle of the model does not change: we reuse the model described in Equation 8.24. In this case, however we exchange the Mueller matrix with a Jones matrix. Using Fresnel calculus, the Jones matrix that describes the linear retardation as well as the reflection can be written as follows:

$$J = \frac{r_p}{2} \begin{pmatrix} r_s \cdot \exp(i\delta) & 0 \\ 0 & r_p \end{pmatrix} \tag{8.26}$$

All our measurements are of normalized Stokes vectors. One can convert them into Jones vectors with the following formula:

$$j = \frac{1}{\sqrt{2}} \begin{pmatrix} \sqrt{1+Q} \\ \sqrt{1-Q} \cdot \exp\left(i \arg(U+iV)\right) \end{pmatrix} = \begin{pmatrix} A_x \\ A_y \cdot e^{i\delta} \end{pmatrix} \tag{8.27}$$

As we do not have the full phase information in such a vector we have to allow for an additional phase for each input state. In the end, we fit

$$j_{out} = J \cdot \left(e^{i\phi} \cdot j_{in}\right), \tag{8.28}$$

where ϕ is an arbitrary phase factor which we ignore. For the Jones description of a mirror we must go back to three parameters per mirror group, instead of the two parameters from Equation 8.25. So for each of the three mirror groups we individually fit a reflection coefficient in the p and s directions as well as a phase difference between the two reflections. Furthermore, we split our data set into the individual telescopes, which divides the amount of available data for each fit by four.

The first result for the individual fits is shown in Figure 8.7, where the reflectivity in s and p direction, as well as the phase difference between s and p is shown. From this first look we can conclude, that in general all the values are similar. This confirms the initial assumption that the birefringence in the individual telescopes is on the same order. We see, however, some scatter in the reflection coefficients of the different telescopes. This means that we have some degree of differential attenuation in the VLTI, which leads to some loss in fringe contrast. The phase difference, however, is very stable over all telescopes. This is a good sign, as it indicates that we have very little differential retardance, which would

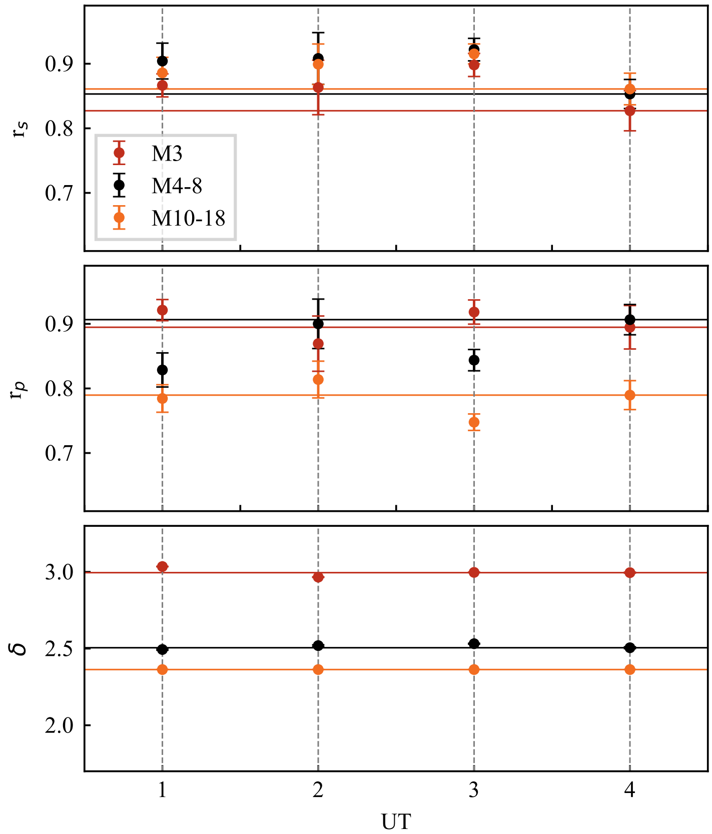

Figure 8.7: Comparison of the fitting values for the individual telescopes. The three plots show the reflectivity in the s and p directions, as well as the phase difference for each group of mirrors. The horizontal lines show the values from a fit to all telescopes at once. r_s, r_p and δ are defined in Equation 8.26.

show up as a phase error in the observations. We will look into both effects in more detail in the following.

While the errorbars on each of these values increase with the individual telescope fits we see a slightly improved Chi-squared for the values from the individual fits in comparison to the values from the four-telescope fit. We conclude that the fits are reliable despite the fewer data points going into them.

8.5.2 FRINGE CONTRAST

With the response of each individual telescope we can ask the question how much the different instrumental polarization in each light path influences the interferometric observations. For this we use the matrix representation of the visibilities (subsection 8.2.2). First we look at the loss in fringe contrast. We

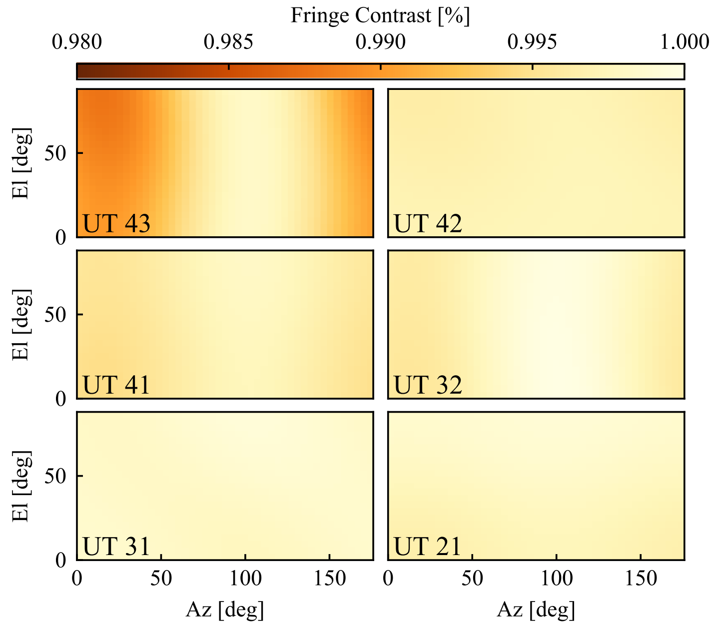

Figure 8.8: Fringe contrast in the six baselines shown for all possible telescope positions

assume that our fringe-tracking object is unpolarized. Nevertheless, instrumental polarization may introduce a small degree of polarization in the incoming light. As shown in Equation 8.14 one can calculate the fringe contrast by the quotient of correlated and total flux, basically asking the question how much of the total incoming light interferes. As the instrumental polarization depends on the position of the telescope we calculate the fringe contrast for a grid of telescope positions. This grid reaches from 0 to 90 ° in elevation and 0 to 180 ° in azimuth. In azimuth the telescopes can rotate between 0 and 360 °, but the polarization signal repeats after 180° so it is sufficient to calculate the values in this range.

The fringe contrast for all telescope positions is shown in Figure 8.8. For all baselines except UT 43 the fringe loss is always well below 1 %. Only for UT 43 the fringe loss reaches a maximum of 1.5 %. This is most likely caused by the fact that both reflectivities in s and p direction are different for UTs 4 and 3, while for all other combinations of telescopes the values are more similar (see Figure 8.7). However, also a contrast loss of $< 1.5\,\%$ is not really worrisome as we still reach a fringe contrast of 0.985 in the worst case. We can therefore conclude that we do not lose significant fringe contrast due to instrumental polarization.

8.5.3 EIGENVECTORS

Following L14, we use polarization eigenvectors to describe the polarization properties of the mirror train. A polarization eigenvector is defined as a linear input polarization which results in a linear output polarization. L14 have shown that each Jones matrix describing the VLTI has two distinct eigenvectors. They are generally not orthogonal to each other, but close to orthogonal. With the now measured Jones matrices for each telescope we confirm both findings. In order to minimize the phase error it was suggested by L14 that one should align one of the detector polarizations orthogonal to one of the output eigenvectors.

The effect of phase errors due to the differential birefringence depends on the direction of the detector in the instrument. We will therefore use GRAVITY as an example for now, but the findings are applicable to all instruments.

The two polarizations on the GRAVITY detector are horizontal and vertical. In GRAVITY there are fiber polarization rotators, which are set up in a way that a horizontal polarization in the VLTI lab corresponds to a horizontal polarization at the detector. We can therefore assume that there is no rotation of polarization in the GRAVITY light path, while there still might be additional birefringence, as we will discuss section 8.6.

By initial instrument alignment we can therefore assume that the two detector polarizations correspond to the same directions in the VLTI lab. As shown in Figure 8.12 there is an additional degree of freedom to adjust the polarization direction. In the fiber coupler of GRAVITY, just downstream of the K-Mirror, is a half wave plate, which could be used to overlay one of the output eigenvectors with the detector polarization. Currently the half wave plate rotates with the K-Mirror. This is done in order to reduce polarization effects on the metrology laser, which propagates backwards through the light beam. However, while this set-up reduces polarization effects for the metrology measurement, it is not ideal to minimize astrometric phase errors. In the following we will look into these phase errors and estimate how much they could be reduced with the optimal alignment.

8.5.4 PHASE ERRORS

The measured visibility phase is referenced to the fringe-tracking object. This can either be the same as the science target, or a nearby star. As discussed in L14 this can lead to a measurement error if the fringe-tracking and the science target have a different polarization state. In the case of two different targets the fringe-tracking object will most likely be a star and therefore unpolarized. In some cases the fringe-tracking source could be slightly polarized, due to foreground dust (see for example Buchholz et al., 2013) or intrinsic polarisation of for example a dusty giant (Haubois et al., 2019). However, this should only

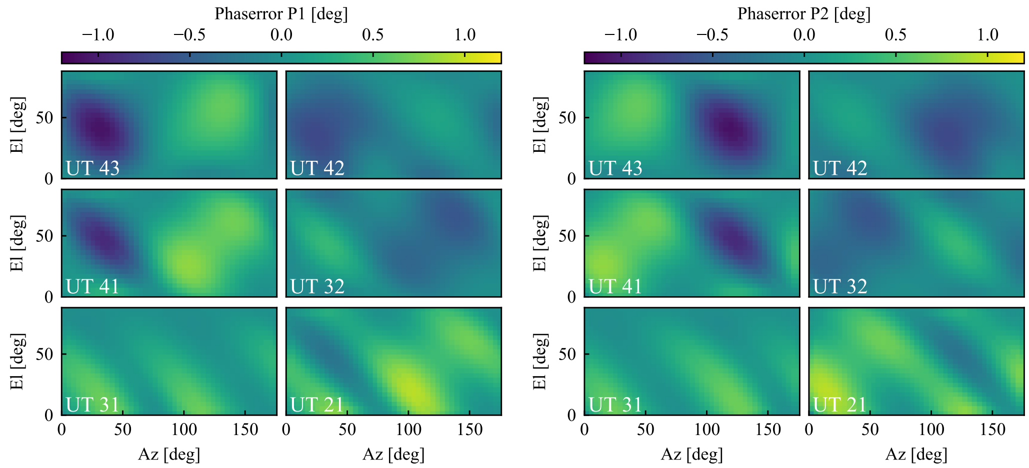

Figure 8.9: Error in the visbility phases due to differential birefringence for all telescope positions. The left two columns show the error for the first polarization P1 and the right two for the second polarization P2.

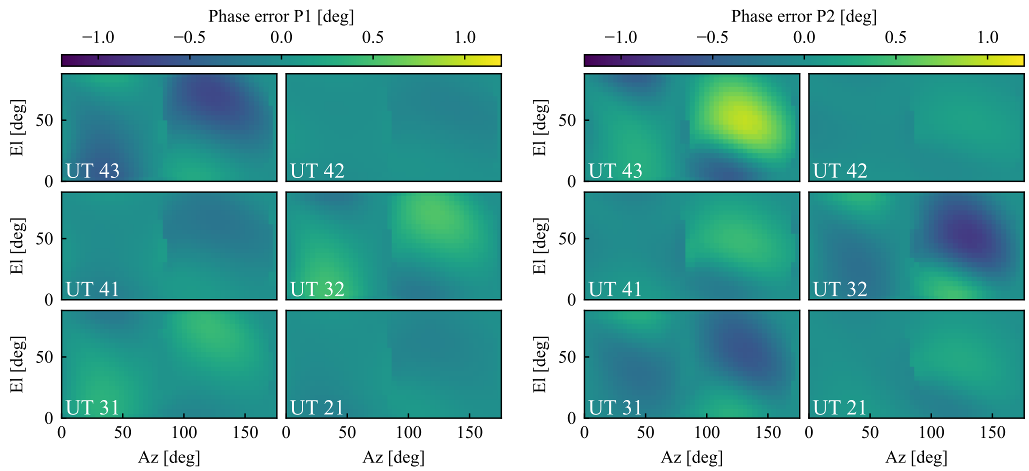

Figure 8.10: Same representation as in Figure 8.9, but this time the phase error if the GRAVITY half wave plates track the eigenvector of the individual telescopes.

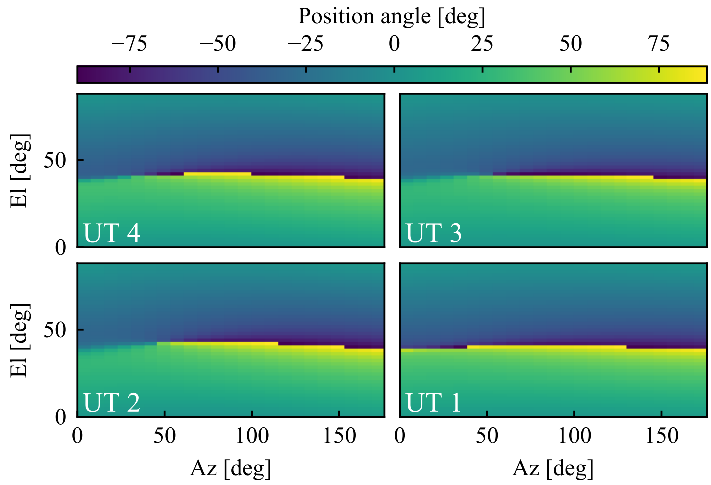

Figure 8.11: Eigenvector as applied in Figure 8.10 to minimize the phase errors.

be a few percent and is not relevant here as the science target can have a much higher polarization. In the case of an (almost) unpolarized fringe-tracking target and a highly polarized science target the polarimetric response of the mirror train is different for the two targets. This different instrumental polarization will therefore introduce a phase error, as the science phases are referenced to the fringe-tracking phases.

For the following tests we assumed a science target with a linear polarization of 30 %. This value is chosen, as it is a likely value for the Galactic Center super massive black hole Sgr A* in its flaring state (see e.g. Genzel et al., 2010), which is one of the most extreme levels of NIR polarization known in celestial bodies. Such a polarization state is represented by the following coherence matrix (see Equation 8.10):

$$C = \begin{pmatrix} 0.65 & 0 \\ 0 & 0.35 \end{pmatrix} \tag{8.29}$$

As shown in Equation 8.14 the measured phase of a target is just the argument of the visibility matrix. We calculate this for the unpolarized fringe-tracking object as well as for the slightly polarized science object and subtract the two phases from each other to take the phase referencing into account. As for the fringe contrast we again calculate this for each baseline and each telescope position and show the results in Figure 8.9. Theoretically there is another degree of freedom, which is the orientation of the polarization vector on sky. This is given by the intrinsic polarization of the source as well as the parallactic angle. However, as this is just a rotation it is redundant with the telescope azimuth and would just shift the pattern in Figure 8.9 to the left or right. We therefore ignore this for now.

As shown in Figure 8.9 there is a small phase error which depends on the telescope position. On average the error is of the order of 0.3°, with maximal values of 1.1°. However, the two polarizations show a somehow opposite pattern. If one averages the two polarizations, as one would probably do it for astrometry measurements anyway to increase the SNR, the phase error reduces. For the average value the mean phase error is 0.2°, with a maximum value of 0.8°. In the simplest case, a single point source, the phases relate to the position on sky with the following formula:

$$\Phi = 2\pi\vec{s} \cdot \vec{B}/\lambda \tag{8.30}$$

where Φ is the measured phase, $\vec{s}$ the measured position on sky and $\vec{B}$ the baseline length. Inverting this formula and using a baseline length of 100 m and a wavelength of 2.2 µm a phase error of 0.8° corresponds to an astrometric error of 10 µas.

It was already shown by L14 that this error can be improved if the output eigenvector of the telescope is aligned with the axis of the polarization measurement on the detector. We can confirm these previous results that each telescope always has two eigenvectors, which are roughly, but not exactly 90° apart. If one aligns one detector polarization with one eigenvector, the astrometric error of this measurement drops to 0. However, the second polarization still shows a significant phase error. From simulating all different options, we found that the lowest overall phase error can be achieved if one uses the average of the two eigenvectors angles:

$$\bar{\phi}_{EV} = \frac{1}{2}\left(\phi_{EV1} + \phi_{EV2} - \tfrac{\pi}{2}\right) \tag{8.31}$$

We can align the detector polarization with this vector by rotating the half-wave plate (HWP) by this angle. If we do so for each telescope individually we reach the phase errors as shown in Figure 8.10. One can see that the phase error has improved in comparison without the HWP rotation in Figure 8.9. The mean phase error in this case is significantly decreased to 0.1° with maximum values up to 0.9°. Again we can further improve this by averaging the two polarizations to mean values below 0.1° and a maximum error of 0.7°. We therefore see that while such an alignment improves the situation, it is only a small improvement if we work with the mean phase. In Figure 8.10 the biggest values can be seen in all baselines with UT3. This is due to the fact that for UT3 the two eigenvectors are less orthogonal than for the other telescopes. By averaging the two eigenvector angles this adds a slightly higher phase error than for the other baselines. In conclusion we find that one does not need to align the detector with the eigenvectors, as long as one uses the mean phase

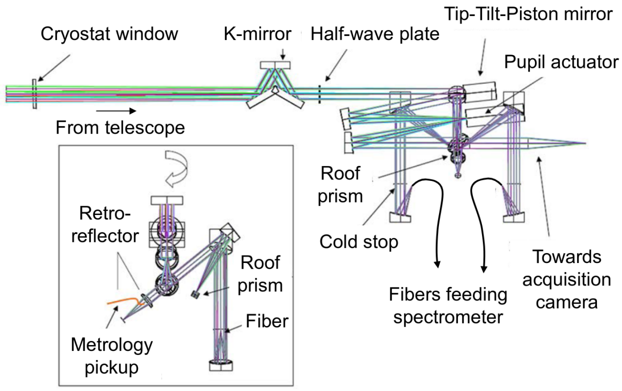

Figure 8.12: Schematic side and front view of the optical design of the GRAVITY fiber coupler. From Gravity Collaboration et al., 2017.

for the highest resolution astrometry, but the individual polarizations for the polarization measurement and the imaging.

However, it is also possible to implement an alignment with the direction of the eigenvalues. Figure 8.11 shows the angles used for the data in Figure 8.10, calculated from Equation 8.31. This angle is a pure telescope property and therefore does not depend on the polarization on sky or the parallactic angle. It could be implemented as a look-up table based on the derived values. However, as one can see in Figure 8.11 the angles are very similar for the four telescopes, but not identical. This means that one needs to aligns each telescope individually to get the smallest phase error. This might not be desired as then each telescope would have a different orientation of the polarization axis on the detector.

8.6 INSTRUMENTAL POLARIZATION OF GRAVITY

So far the results have been mostly independent of the interferometric instrument and generally valid for VLTI observations in the near infrared. However, in order to actually calibrate polarized observations, the instrument has to be taken into account as well. Here we discuss the instrumental polarization of the GRAVITY beam combiner. For a full overview about GRAVITY see Gravity Collaboration et al., 2017.

8.6.1 GRAVITY LIGHT PATH

In GRAVITY the light first passes the fiber coupler (Pfuhl et al., 2014). Part of the fiber coupler is a K-Mirror to derotate the field, a HWP and then some mirrors with tip-tilt, piston and pupil control. Behind that the light is split

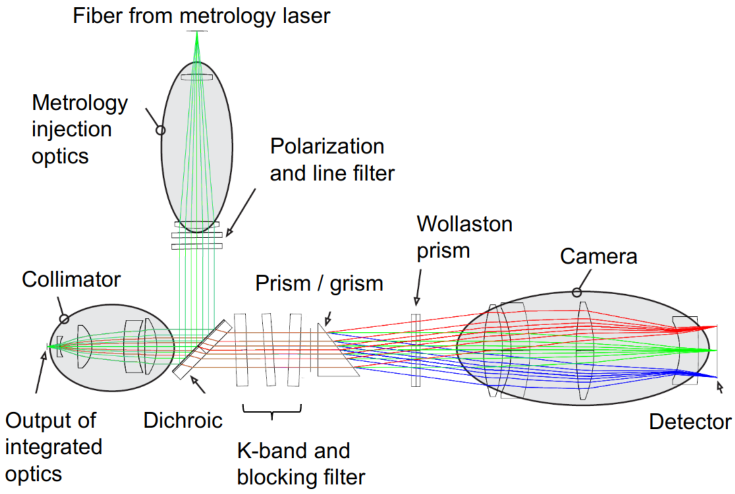

Figure 8.13: Optical design of the GRAVITY spectrometer. Most important for the polarimetric mode is the Wollston prism which can be moved in or out of the light path. From Gravity Collaboration et al., 2017.

into science and fringe-tracker and fed into optical fibers (Figure 8.12). The K-Mirror as well as the HWP rotate in a fixed way during the observation: The K-mirror is used as derotator and moves according to the field rotation described in Equation 8.20. With the derotation of the field it also derotates the sky polarization. However, in order to keep the light path of the backpropagating metrology system stable, the HWP rotates together with the K-mirror. This reverts the derotation of the polarization and the rotation correction described in subsection 8.3.3 and Equation 8.20 still has to be applied to a polarization measurement. The light is then fed into single-mode fibers and passes the fiber control unit, before it is fed into the integrated optics system (Jocou et al., 2014; Perraut et al., 2018) and then finally passed into the spectrometers (Straubmeier et al., 2014). In the spectrometers there are Wollaston prisms, which can be put into the light path to allow for a polarimetric measurement (see Figure 8.13) and split up the light into two polarizations (P1 and P2), with a 90° polarization angle between them.

There are some field rotations in the light path of GRAVITY. However, they do not have to be taken into account as the polarization angle on the spectrometer is calibrated with polarized light from the calibration unit. For this calibration a linear polarizer in the calibration unit is used. With the linearly polarized light from the calibration unit the Fibered Polarization Rotators in the fiber control unit of GRAVITY are then optimized to get a fully illuminated P2 spectrum on the detector. The polarization P1 is therefore horizontally polarized in the VLTI lab frame, or aligned with V, in the VLTI (V,W) coordinates.

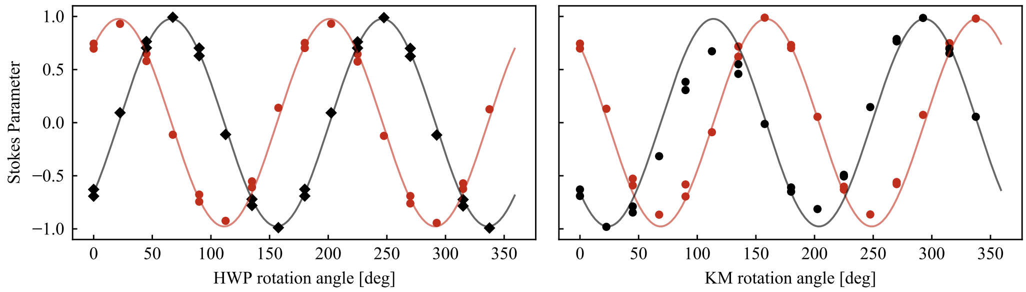

Figure 8.14: Measurement of the half-wave plate (left) and the K-Mirror (right) of GRAVITY. The points show the data points for Stokes Q (red) and Stokes U (black). The lines show the corresponding values for a ideal optical element.

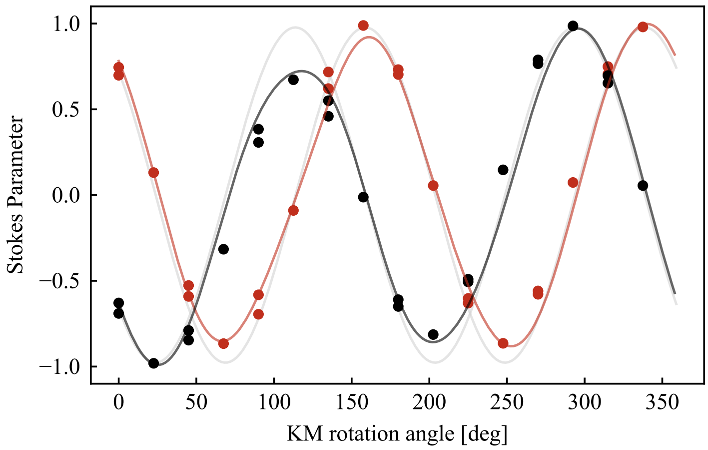

Figure 8.15: Fit of the K-Mirror Mueller matrix to the data. The dots show the data for Stokes Q (red) and Stokes U (black) the colored lines correspond to the fitted model and the grey lines to a ideal optical element.

For polarimetric measurements the instrumental polarization of some, or all of the components in GRAVITY has to be taken into account. This depends on the actual observation mode, as discussed in the following.

8.6.2 MEASUREMENTS OF INSTRUMENTAL POLARIZATION

In order to measure the instrumental polarization of GRAVITY we performed two individual experiments. The first one was done with the same polarimeter as the VLTI measurements. We put the polarimeter in front of one of the beams and used the metrology laser as a light source. In that setup we then rotated the half-wave plate as well as the K-Mirror individually. The measured Stokes Q and U values for both tests are shown in Figure 8.14. This measurement has a couple of disadvantages. First of all it mainly measures the carrier beam of the metrology: The light from the metrology laser is split into three beams before entering the GRAVITY light path. Less than 1 % of the light goes into the science and fringe-tracking beam and the rest into the carrier beam. It is therefore the main light source we used for this measurement. The disadvantage of this beam is that its polarization is not controlled and we only know about the orientation of the polarization from the installation phase of the instrument. The beam also does only enter the GRAVITY light path in the beam combiner, and we therefore do not get information about the other GRAVITY components from this measurement. However, we get a very good understanding of the rotated elements, namely the HWP and the K-Mirror. In Figure 8.14 one can see the data points and the response of an ideal HWP/K-Mirror under rotation. While the HWP shows very little birefringence, the K-Mirror shows clear deviations from an ideal derotator. We therefore assume that the HWP does not alter the polarization, apart from rotating it, while the K-Mirror does. With the data available it is possible to fit the full Mueller matrix of the K-Mirror while leaving the input polarization free. The free input polarization is important here, as we use the metrology laser as a light source, of which we do not know the exact polarization state. We therefore get a measurement of M_{KM} from this experiment. However, the derotators in GRAVITY show a small angle-dependent birefringence, which can lead to a loss in the degree of linear polarization of up to 20 %. We took this into account by allowing for an angle dependent loss in linear polarization. The fit result for the Mueller matrix with the angle-dependent birefrigence is shown in Figure 8.15.

With the results of this experiment we have all information in hand for a second measurement. In this second approach we used the light from the calibration unit of GRAVITY with its own linear polarizer. From this we get a constant and linearly polarized input source from the calibration unit. We then rotated the K-Mirrors of each beam from its initial position to 360°. At each location of the K-Mirror we took detector frames with the HWP at 0 as well as at 22.5°, to get a full polarization measurement (as will be described in more detail in the next section). With this experiment we can measure the output polarization of GRAVITY for a linear input polarization with rotating polarization angle, shown in Figure 8.16. With the measurement of M_{KM} from the previous experiment the polarization state after the HWP and the K-Mirror is well known. The remaining parts of GRAVITY do not have any rotating parts and we can therefore fit them with a single Mueller matrix: M_{GR}. As shown in Figure 8.16 the fit worked well and the instrument is well described. Interestingly the data is not too far of from an ideal response, showing that polarization is mostly preserved in GRAVITY.

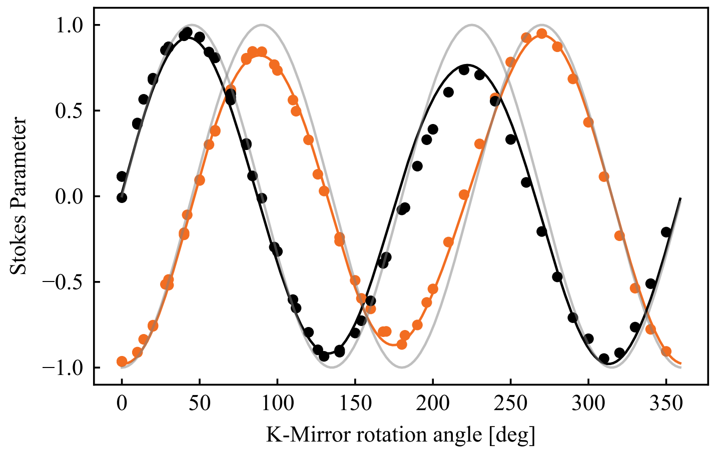

Figure 8.16: Measured polarization with GRAVITY for different rotations of the input vector. The points show the data points for Stokes Q (orange) and Stokes U (black). The colored lines show the corresponding values from the fitted Mueller matrix. The grey lines correspond to an ideal response of the instrument without instrumental polarization.

8.6.3 FULL CALIBRATION

With the results of the GRAVITY measurement we have all information in hand to calculate the full polarimetric response for an observation with GRAVITY and the VLTI. From the work presented in section 8.4 and especially Equation 8.24 we obtain the Mueller matrix of the VLTI, which depends on the elevation and azimuth of the telescope. Together with the Mueller matrix of the K-Mirror and the rest of GRAVITY this gives the full response:

$$\begin{aligned} M_{ALL} = &M_{GR} \cdot R(\Theta_{HWP}) \cdot M_{HWP} \cdot R(-\Theta_{HWP}) \cdot \\ &R(\Theta_{KM}) \cdot M_{KM} \cdot R(-\Theta_{KM}) \cdot M_{VLTI}(Az, El) \end{aligned} \tag{8.32}$$

Where R is the usual rotation matrix (Equation 8.22) with the position of the HWP (Θ_{HWP}) and K-Mirror (Θ_{KM}). For the half-wave plate we assume an ideal Mueller matrix:

$$M = \begin{pmatrix} 1 & 0 & 0 & 0 \\ 0 & 1 & 0 & 0 \\ 0 & 0 & -1 & 0 \\ 0 & 0 & 0 & -1 \end{pmatrix}. \tag{8.33}$$

Together with the VLTI model this is included in our calibration python package VLTIPOL, which can be used to get the full Mueller matrix of the VLTI and GRAVITY.

8.7 POLARIMETRIC MEASUREMENTS WITH GRAVITY

To observe with GRAVITY in a polarimetric mode one has to put the Wollaston prism into the light path. This gives measurements in two polarizations, P1 and P2. P1 is aligned with the horizontal axis in the VLTI lab (V axis in VLT definition) and P2 is 90° rotated from it. From the interferometric signal one can calculate the measured intensity and the first linear Stokes parameter Q:

$$I = I_{P1} + I_{P2}, \qquad Q = I_{P1} - I_{P2} \tag{8.34}$$

To retrieve U one has to rotate the HWP 22.5°, which rotates the polarization axis by 45°. Here one has to take into account that the GRAVITY HWP rotates in opposite direction than how the Stokes parameters are defined, which introduces a sign change:

$$U = -I_{P1}^{22.5} + I_{P2}^{22.5} \tag{8.35}$$

In order to reduce the effects of instrumental polarization one can measure the Stokes parameters as a double difference (Tinbergen, 1996; Canovas et al., 2011; de Boer et al., 2020). In this case both Q and U are measured twice, both for two HWP angles: Q with 0° and 45° and U with 22.5° and 67.5°. For the second measurement the sign of the Stokes component changes, but the instrumental polarization (IP) stays constant. The Stokes parameters are then calculated as:

$$Q = \frac{1}{2}\left[(I_{P1}^{0} - I_{P2}^{0}) - (I_{P1}^{45} - I_{P2}^{45})\right] = \frac{1}{2}\left(Q^{+} - Q^{-}\right) \tag{8.36}$$

$$U = \frac{1}{2}\left[(I_{P2}^{22.5} - I_{P1}^{22.5}) - (I_{P2}^{67.5} - I_{P1}^{67.5})\right] = \frac{1}{2}\left(U^{+} - U^{-}\right) \tag{8.37}$$

This way all the IP downstream of the HWP is removed (van Holstein et al., 2020). However, the double difference has the disadvantage that one needs four exposures to get one data point. For some special cases, where one has a quickly changing polarization state, this might not be usable (e.g. in Gravity Collaboration et al., 2018a). In this case one can still use Equations 8.34 and 8.35, but has to consider the full polarization effects of the optics after the HWP.

In the case of the double difference, one has to ignore the first term in Equation 8.32, but apart from that the effects are the same. With the calibration matrix from Equation 8.32 the measured polarization can then be calibrated:

$$S_{sky} = M_{ALL}^{-1} \cdot S_{GRAVITY}. \tag{8.38}$$

GRAVITY is not able to measure circular polarization. Therefore one has to assume V=0 for $S_{GRAVITY}$. As we have seen a significant birefringence from the VLTI, this would mean that some of the linear polarization is lost in this

Table 8.2: Polarization of degree (P) and angle (Θ) for IRS 16C

	P [%]	Θ [°]
Ott et al., 1999	4.0 ± 1.6	35 ± 19
Witzel et al., 2011	4.6	17.8
Buchholz et al., 2013	4.3 ± 0.6	25 ± 5
This work:		
2018-07-28	3.7 ± 0.6	19.2 ± 4.7
Average over all nights	3.7 ± 0.4	16.7 ± 3.0

analysis. Since this is strongly telescope dependent the importance of this effect has to be modeled for an individual observation to get an appropriate uncertainty on the results. However, under the assumption that the observed source emits only linear polarization one can use iterative approaches such as the one developed by Witzel et al., 2011 to recover the full amount of linear polarization. Another solution is to forward model the polarimetric property of the source (Gravity Collaboration et al., 2020b) to recover the full polarization information.

8.8 APPLICATION TO DATA

To test the polarization model described before we used the same data as presented in Gravity Collaboration et al., 2018a; Gravity Collaboration et al., 2020b. However, as shown in those papers the science target Sgr A* is not a good test target as it has a variable polarization state. During the observations of Sgr A* we used the star IRS 16C as the fringe-tracking target. IRS 16C has a brightness of $m_K = 9.55$ and is well known to be slightly polarized. It was for example observed in Ott et al., 1999; Witzel et al., 2011; Buchholz et al., 2013 and the studies found a consistent polarization of 4 % (see Table 8.2), most likely due to foreground polarization of the dust.

While the goal of the measurement was to measure the polarization of Sgr A*, the rotation of the HWP affects the fringe-tracking target in exactly the same way as it does the science target. We can therefore apply the full analysis to the measured fluxes of the fringe-tracking star, in order to measure its polarization. From the analysis described in this work we measure a polarization degree of $(3.7 \pm 0.6)\%$ at an angle of $(19.2 \pm 4.7)^\circ$ for the night 2018-07-28. These values are in perfect agreement with the other values from Table 8.2.

As IRS 16C is the usual fringe-tracking target for Galactic Center observations, there are several more data sets with polarization observations of the star.

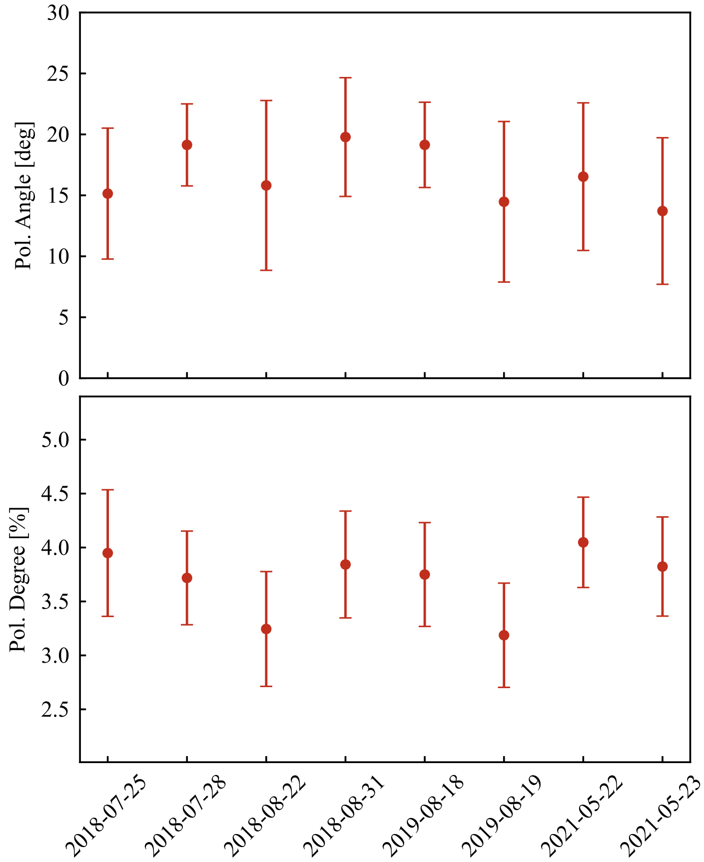

Figure 8.17: Polarization measurements of IRS 16C between 2018 and 2021. The top panel shows the polarization angle for each individual night and the bottom panel the polarization degree.

Figure 8.17 shows the polarization angle and polarization degree for eight nights between 2018 and 2021. The polarization state in each night is well measured with an average scatter of the polarization angle of 6° and 0.7 % for the polarization degree per night. This shows that the polarization calibration works well for different telescope orientations and that we are able to measure reliable polarization states with GRAVITY.

The fact that we can well measure the expected polarization of the fringe-tracking star clearly verifies our model and the polarimetric capabilities of GRAVITY. It also confirms the results from Gravity Collaboration et al., 2020b, where we already used the presented calibration model and could show clear and varying signal in the polarization of Sgr A*.

8.9 CONCLUSION

In this work we have presented the first full polarization study of the VLTI and GRAVITY. As expected, both the observatory as well as the instrument itself show effects of instrumental polarization. In both cases we characterized the effects and build up a calibration model to calibrate for the instrumental effects in observations. We have outlined the necessary steps in observation, data reduction and calibration to execute polarimetric measurements with GRAVITY. The capabilities were then demonstrated by remeasuring the polarization properties of the galactic center star IRS 16C, which is in excellent agreement with the literature.

We have also shown that differential birefringence between the light paths of the VLTI UTs is not a dominant error source, as the four lightpaths were constructed with great care in order to minimize differential birefringence. For a typical observation of a calibrated source our studies have shown a phase error due to differential birefringence of below 1°. Even for the extreme case with a 30 % polarized science target this results in only around 10 mas astrometric error. This error can be further reduced when using the average of the two polarizations for astrometry and the individual signal for poalrimetry. The fringe contrast in such a case is only reduced by around 1 %, which is not in a relevant regime.

We therefore demonstrated that observations with GRAVITY do not suffer from strong effects due to birefringence and that GRAVITY can be used for polarimetric observations. This can be done in very different ways. With IRS 16C we showed that GRAVITY can measure the polarization quantities of even slightly polarized targets with very good precision. One can also studying the temporal evolution of polarized targets, as it was done in Gravity Collaboration et al., 2018a; Gravity Collaboration et al., 2020b for a bright Sgr A* flare. Furthermore, the polarization information can not only be extracted for the full intensity, but also for the measured intensity in each spectral channel. One can therefore even map polarization changes over the spectral range of GRAVITY. As all of this comes together with the unprecedented resolution of GRAVITY this opens up a wide new range of possibilities to do polarimetry in the near-infrared.

GRAVITY DUAL-BEAM ASTROMETRY 9

The majority of the GRAVITY observations are done within a single science pointing. This can be astrometry between several sources in the field of view or imaging and studying the structure of extended objects. However, GRAVITY also offers astrometry between different science pointings or even between the fringe-tracking and the science target. For this so-called *"dual-beam astrometry"* one needs all subsystems which are included in GRAVITY. The metrology system is especially needed to measure differential optical path differences between the two targets. Dual-beam astrometry is a mode that GRAVITY offers, but some systematic effects must be considered due to its complexity. This section outlines the work done to analyze and characterize these systematic effects, which then fully enables dual-beam astrometry on short time scales.

9.1 DUAL-BEAM OBSERVATIONS

GRAVITY can perform astrometric measurements in between two different pointings of the science fiber. Such measurements are possible as all the measured visibility phases are referenced to the phases of the fringe-tracking target. This observing mode is usually called dual-beam or narrow-angle astrometry and requires a precise metrology system. This has been of big interest for the optical interferometry community for a long time (see e.g. Shao and Colavita, 1992). The technologies implemented in GRAVITY for the dual-beam astrometry and the metrology benefited greatly from earlier work for example at the Palomar Testbed Interferometer (Colavita et al., 1999), the Keck interferometer (Hrynevych et al., 2004) and the Navy Prototype Optical Interferometer (Hutter and Elias, 2003).

A good explanation of how the dual-beam observing mode works and why it is needed is shown with the Galactic Center science case as an example. GRAVITY has been engaged in a regular observing campaign to measure the distance vector between the star S2 and Sgr A* since its commissioning in 2016 (Gravity Collaboration et al., 2018b; Gravity Collaboration et al., 2019; Gravity Collaboration et al., 2020a). Before 2019, GRAVITY could detect both objects simultaneously with a single pointing. In this case, the visibility amplitude is not constant, and the closure phases are non-zero. Thus, all observables, such as

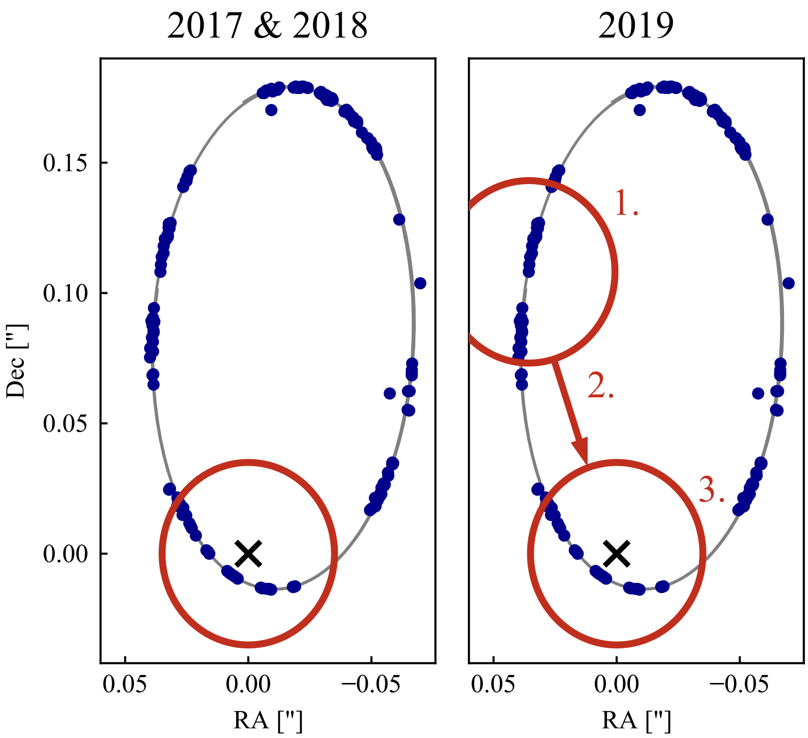

Figure 9.1: Illustration of the difference in observing strategy in 2017 & 2018 (left) compared to the 2019 observing strategy (right). In 2019, the S2 has moved to the edge of the interferometric field of view, which results in minimal flux coupling of the star if the GRAVITY fiber is pointed at Sgr A*. In consequence, in 2019, we: 1. point at the star S2 and take an exposure, 2. move the fiber to the Sgr A* location, and 3. do an exposure on Sgr A*. This way we can measure the distance between the two targets in consecutive exposures.

the distance vector and the flux of Sgr A*, can be inferred from interferometric binary model fitting (Gravity Collaboration et al., 2018b). It allows for direct measurement of the distance between the two sources, utilizing the advantages of the closure phase where scalar telescope-based systematic effects cancel out (see e.g. Monnier, 2003).

However, since the pericenter passage of S2 in 2018, this distance vector between S2 and Sgr A* has constantly been increasing. In 2019 S2 had moved so far out of the interferometric field of view (IFOV) that the residual flux injected during an observation is not enough to see a reliable binary signature in the data. We, therefore, adopted a new observing strategy in 2019, as illustrated in Figure 9.1. In this new mode, we first observe only S2 and afterward only Sgr A*. In order to measure the distance vector between the two sources, we derive the relative phase offset between them from the measured visibility phases. This is done by

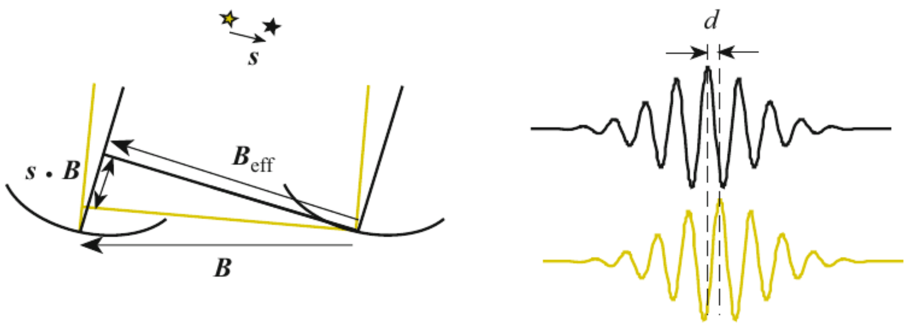

Figure 9.2: Principle of the phase referencing interferometry, adapted from Glindemann, 2011. The detected fringe packages show a phase shift d, from which the separation of the targets can be measured.

referencing the phases of the observed object to the phases of the fringe-tracker star.

Phase referencing means that we measure the phase difference of the fringe packets coming from the two stars (see Figure 9.2). With the knowledge that the fringe-tracking star is a point source and is well centered in the fringe-tracking fiber (which is made sure by GRAVITY control loops), we know that the phases of the fringe-tracking star are zero. This means that the difference of the measured phases is the phase of the science target, referenced to the fringe-tracker:

$$\Phi = \Phi_{SC} - \Phi_{FT} \tag{9.1}$$

This phase referencing is only possible if two objects are observed simultaneously, as many of the effects are time dependent.

However, a differential optical path difference (dOPD) between the fringe-tracker and the science target adds to the measured phase difference from Equation 9.1:

$$\Phi = \Phi_{SC} - \Phi_{FT} + \mathrm{dOPD} \tag{9.2}$$

There are two main contributions to the dOPD between the two targets. The first one is due to the different sky position of the targets, as illustrated in Figure 9.2, which contains the separation of the two targets:

$$\mathrm{dOPD} = \vec{S} \cdot \vec{B}, \tag{9.3}$$

with the separation between the two targets $\vec{S}$ and the baseline $\vec{B}$. This is the dominant dOPD in the phases. As $\vec{S}$ is on the order of milliarcseconds, the measured phases would not be usable as they would be larger than the coherence length of the light. This is why there is a subsystem in GRAVITY, which corrects for the dOPD introduced by the sky rotation. This correction is done with the fibered differential delay lines (FDDLs) in GRAVITY, which can introduce an optical path difference between the fringe-tracking and science sources. The FDDLs follow a calculated trajectory as given by Equation 9.3, to modulate how the dOPD changes due to sky rotation.

However, there is a second contribution to the dOPD, which is coming from instrumental effects. Two individual units detect the fringe-tracking light and the science light in GRAVITY. When those units are not perfectly identical, it will introduce an optical path difference between the two beams. This instrumental dOPD needs to be controlled to make reliable phase measurements with GRAVITY. This happens with the internal metrology system.

9.1.1 THE GRAVITY METROLOGY SYSTEM

The metrology system in GRAVITY is responsible for measuring instrumental dOPDs between the fringe-tracker and the science channel. In order to reach the desired astrometric precision of GRAVITY of 10 µas, this has to be done with a nanometer precision (Gillessen et al., 2012; Blind et al., 2014b).

The simple description of the metrology system is that a laser is launched backward through the entire GRAVITY and VLTI lightpath (for an overview, see Figure 9.3). This laser has a wavelength of 1908 nm to not interfere with the science light. Before entering the light path, the laser is split up with a fixed phase relation. One part is then fed into the science channel of each telescope and one part into the fringe-tracking channel. The two laser beams follow up the entire light path. After the reflection on the primary beam of the telescopes, they are measured with metrology diodes. The diodes are mounted at the spiders of each telescope. Each telescope has four diodes, and their signal is averaged to get a measurement at the center of the pupil plane. Ideally, one would make this measurement directly in the center, but the center of the telescope is obscured by the secondary mirror.

The metrology light beams from the science and the fringe-tracking channel interfere in the pupil plane of the telescope. This fringe pattern is then temporally sampled by the four diodes in the telescope spiders. From this measurement, the change in phase difference is extracted, which corresponds to a movement of the fringe pattern in the pupil plane. The changes in the phase then correspond directly to changes in the dOPD between the two light paths. Therefore, the absolute dOPD cannot be measured, but only changes of the dOPD.

The measurement at the telescope is usually referred to as telescope metrology and measures the full light path. There is another measurement at the entrance of the GRAVITY fiber coupler. In Figure 9.3 this measurement is shown as *Metrology Calibration Sensor*, but it is usually referred to as fiber coupler

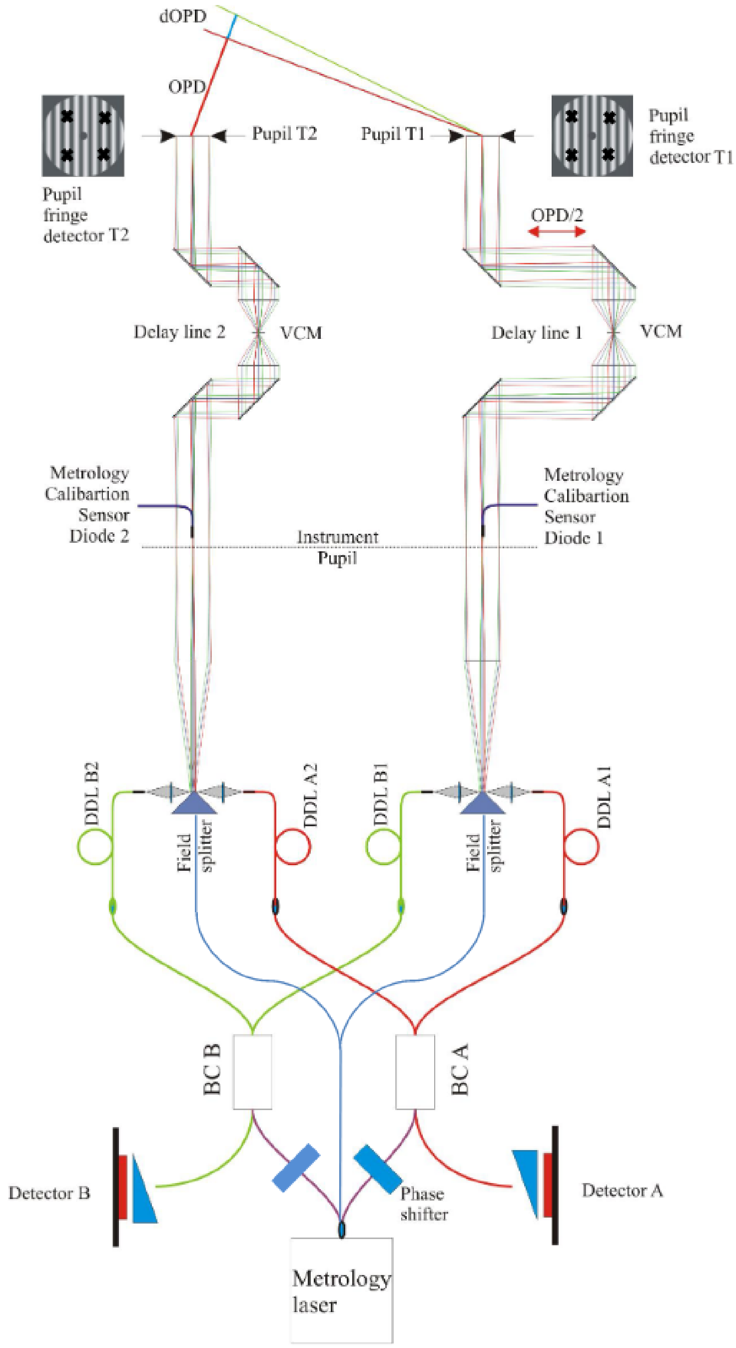

Figure 9.3: Overview of GRAVITY's metrology system, from Lippa et al., 2016. The principle of the metrology is system is shown for two telescopes. At the bottom the metrology laser is fed into the two beam combiner (BC) for the fringe-tracker and science channel. It then follows the light path of each telescope until it is measured in the pupil of the telescopes.

metrology. This measurement only covers GRAVITY itself, but due to the smaller beam size at the measurement point, it has a higher SNR and is used to run control loops in GRAVITY.

The final implementation of the metrology has not only two beams but three in total: one bright one, which is not going through the optical fibers, and two faint ones, which go through the entire light path. The scheme was implemented to reduce the noise from laser backscattering in the fibers and is discussed in detail in Lippa et al., 2016 and Lippa et al., 2018. In terms of the final measurement of the dOPD this three-beam scheme is not different, and we will not discuss it in further detail.

9.1.2 IMAGING PHASE

With the help of the metrology measurement we can now define the measured phase, starting from Equation 9.3. The final referenced phase is usually referred to as imaging phase. As defined in Equation 9.3, the main dOPD comes from the sky rotation. This is compensated by the FDDLs, which are hold in closed loop with the fiber coupler metrology, to make sure that the dOPD introduced by the FDDLs matches exactly the introduced dOPD:

$$\mathrm{dOPD}_{FDDL} = \vec{S} \cdot \vec{B}. \tag{9.4}$$

By adding the FDDL movement, the dOPD from the separation of the target is no longer part of the measurement. The dOPD introduced by instrumental effects are still contained in the measurement of the phase. These are measured by the metrology system and by subtracting the metrology measurement one gets rid of the instrumental effects. The metrology measurement also sees the dOPD, which is introduced by the stretching of the fibers with the FDDLs, as the metrology light passes through these fibers together with the science light. To take this into account one has to subtract the dOPD_{FDDL} from the metrology signal before calculating the final imaging phase:

$$\Phi_{imag} = \Phi_{SC} - \Phi_{FT} - (\mathrm{dOPD}_{MET} - \mathrm{dOPD}_{FDDL}). \tag{9.5}$$

Taking Equation 9.4 into account this converts to the normally used equation for the imaging phase:

$$\Phi_{imag} = \Phi_{SC} - \Phi_{FT} - \mathrm{dOPD}_{MET} + \vec{S} \cdot \vec{B}. \tag{9.6}$$

With Φ_{SC} and Φ_{FT} being the phase measured directly on the detectors and OPD_{MET} the dOPD measured by the metrology signal. As before $\vec{S}$ is the separation of science and fringe tracking target and $\vec{B}$ the baseline.

With the corrections of the different dOPD this means that if a point source is observed with the science beam and the point source is perfectly centered, the measured imaging phases are zero. Any deviation from zero shows an inaccuracy in the used separation vector or a more complicated source structure. In practice, more effects have to be taken into account, such as the dispersion of the fibers as the science and metrology wavelengths are not identical. However, the main principle of the imaging phase is the one given in Equation 9.6.

9.1.3 DUAL-BEAM IN THE GALACTIC CENTER

In the Galactic Center, we do not measure the distance between the fringe-tracker star and the science target, but we measure the vector between two separate science targets. This measurement is done by first observing S2 and then Sgr A*. We then calibrate all our phases with the phases of S2. As the phases are phase referenced to the fringe-tracker, they should be constant and zero if a point source is at the same position in the fiber as S2. This is ensured by the calibration with S2, which also solves the problem that the GRAVITY metrology system does not give the absolute dOPD directly. We do not do the full dual-beam astrometry with this observing scheme, but we still need the metrology system in the same way as we need continuously phase referenced measurements to do this measurement.

By calibrating the visibility phases of Sgr A* with the ones of S2, we create a phase center coordinate system anchored at the used separation vector. In other words, if the given vector, which is the amount by which we stretch the fibers from S2 to Sgr A*, would be perfect, we would measure zero OPD offsets, and the visibility phases would all be zero. However, if Sgr A* is slightly shifted, with respect to the pointing position, this introduces an OPD, and we measure non-zero phases, according to the simple formula:

$$\Phi = 2\pi \vec{s}_{PC} \cdot \vec{B}/\lambda \tag{9.7}$$

where $\vec{s}_{PC}$ is the position on sky which we fit and $\vec{B}$ the baseline vector. Fitting the S2-calibrated phases of Sgr A* with a point source model then gives the deviation of the phase center from the assumed orbit position. By combining this phase center offset with the assumed prior orbit, we get the absolute separation between S2 and Sgr A*:

$$\vec{s}_{S2-SgrA^*} = \vec{s}_{fibershift} + \vec{s}_{PC} \tag{9.8}$$

Where $\vec{s}_{S2-SgrA^*}$ is the separation of the two targets, we want to measure. $\vec{s}_{fibershift}$ is the separation vector which was applied to the FDDL with moving from S2 to the predicted position of Sgr A*. $\vec{s}_{PC}$ the fitted phase-center offset of Sgr A* from the predicted position. $\vec{s}_{PC}$ corresponds to the difference between the best fit separation between FT and SC and the assumed separation which is used for the FDDL control.

Be aware that in the observing mode we describe here, we find two different object separations. The first one is the distance from the fringe-tracking target to the science target (in our case from IRS16C to S2) which will be labeled with a capital $\vec{S}$. The second one is the separation from the calibration target observed with the science fiber (here S2) and the real science object (here Sgr A*). The separation between those two targets is marked with a small $\vec{s}$. In the observing mode of GRAVITY in the Galactic Center, we keep the fringe-tracking fiber on IRS16C and iterate the science fiber between S2 and Sgr A* to measure $\vec{s}$. As discussed before, it is also possible to measure the separation between fringe-tracking and science star ($\vec{S}$) with GRAVITY, but in this case, an additional measurement has to be used as the metrology zero point is unknown. This can be a swap between two bright targets, the observation of a known binary or also a longer time sequence of data from the observed object. Apart from this additional data, the systematic effects discussed in the following stay the same and are applicable in the same way to measuring $\vec{S}$ and $\vec{s}$.

In the dual-beam observing mode, we are more prone to systematic effects than in a measurement within a single pointing, as we cannot use the visibility amplitude information and must use absolute phases rather than closure phases. Absolute phases in the dual-beam mode are challenging to measure in interferometry, which is why most observations depend on closure phases and visibility amplitudes. However, with the metrology system of GRAVITY, it is possible to measure phase-referenced visibility phases. If the phases are well calibrated and the systematic effects are controlled, the determination of the position is simple since the many-parameter binary fit reduces to a simple two-parameter centroid fit.

9.2 SYSTEMATIC EFFECTS

In order to get the position of a single point source in an interferometric pointing, one can fit the calibrated data with the simple point source model given in Equation 9.7. However, to use the visibility phase, we have to rely on the capability of GRAVITY to produce fully phase-referenced dual-beam measurements. This means that the metrology measurement is now needed to calculate the science phase, in contrast to earlier binary observations. This has revealed additional systematic effects. We discuss these new effects and their correction in the following.

9.2.1 SEPARATION VECTOR CORRECTION

As detailed before, dual-beam astrometric observations require a prior estimate of the separation of the science target and the fringe-tracking star. Using this separation prior, we can compute the OPD corresponding to the difference in phase between the two objects. This OPD value is the physical value at which the FDDLs of GRAVITY are stabilized. Once such a value is chosen, the phase center coordinate system is fixed, and the deviation from the input separation can be measured. However, any deviation from the true separation leads to a systematic effect on the science phase. The differential delay lines compensate the OPD induced by the rotation of the earth, as given by Equation 9.3. However, any deviation $\vec{\Delta S}$ from the prior assumption of $\vec{S}$ leads to an incorrectly calculated compensation phase:

$$\Delta\vec{\Phi} = \vec{\Delta S} \cdot \vec{B} \tag{9.9}$$

Since the baseline separation $\vec{B}$ changes with earth rotation, the error on the compensation phase $\Delta\vec{\Phi}$ correspondingly also changes with time. This introduces a drift on the phase and, therefore, on the astrometry.

This effect can be calibrated out in the observing scheme, where we measure the distance between two different science targets. We regularly iterate between the target we calibrate with and the second one. If there are no systematic effects, the phases of the calibration target should stay zero. In practice, they drift due to the outlined effect. In Gravity Collaboration et al., 2020a we showed that we can correct the separation vector $\vec{S}$ by deriving $\Delta\vec{\Phi}(t)$ from the S2 exposures. We parameterize the science phase as a function of $\Delta\vec{\Phi}(t)$ and fit for the correction $\vec{\Delta S}$ which best removes this drift. This correction is added to $\vec{S}$, and the science phases are recomputed. Since $\Delta\vec{\Phi}(t)$ is derived only from exposures centered on S2, this procedure cannot introduce a bias on our Sgr A* astrometry.

9.2.2 METROLOGY SYSTEMATICS

For phase-referenced dual-beam astrometry, the phase of the science target is measured with reference to the fringe-tracker. For this, it is necessary to measure the dOPD between the light paths of the science and fringe-tracking targets with the metrology system. Under the assumption that the metrology traces variations in the light path, which the starlight would see, the measured dOPD is directly subtracted from the science phases (see Equation 9.6). However, this also means that any systematic effect of the metrology measurement is directly added to the science phase. Since the metrology signal is measured for each telescope individually, any systematic effect introduces a telescope-based error that will propagate to the baselines containing the respective telescope.

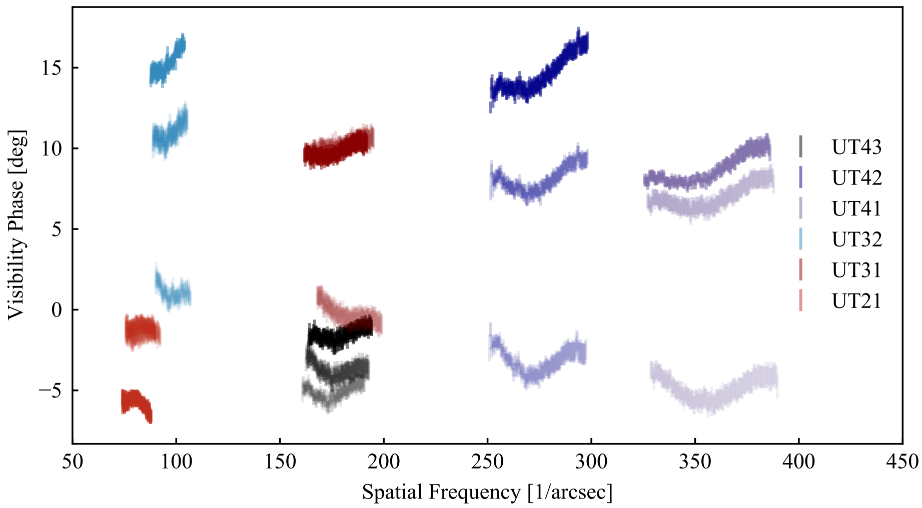

Figure 9.4: Phases of an observed point source from three consecutive exposures. The six colors show the different baseline. For each baseline three data sets are shown with decreasing color intensity over time.

Telescope-based errors are traditionally removed by using the closure phase instead of the visibility phase (Gravity Collaboration et al., 2018b; Gravity Collaboration et al., 2018a). However, as discussed in the previous section, this is not possible for phase-referenced observations in the dual-beam mode. For this reason, control of any metrology systematic is essential.

In order to verify this mode, we did test observations of known binary stars. In such a case one star is observed with the fringe-tracker and the other one with the science channel. In a perfect case we would assume that the visibility phases of the science target stay constant or maybe show a linear drift due to effects discussed in subsection 9.2.1.

Analyzing a lot of test observations indeed revealed that the visibility phase is affected by telescope-like systematic effects. Two effects are apparent:

1. A slow drift of the visibility phase as a function of time. This is shown in Figure 9.4, where the data from three consecutive exposures is shown, which is very obviously not stable over time. This can be introduced by the wrong separation vector, but even after fitting the separation vector there are drifts remaining. These drifts are therefore inconsistent with an offset point source and are true systematic effects.

2. Baseline inconsistencies for point sources. For an example see Figure 9.5, where a fit to one exposure is shown. The data is very clearly not described by a point source, despite that all other observables show no sign of an extended source structure.

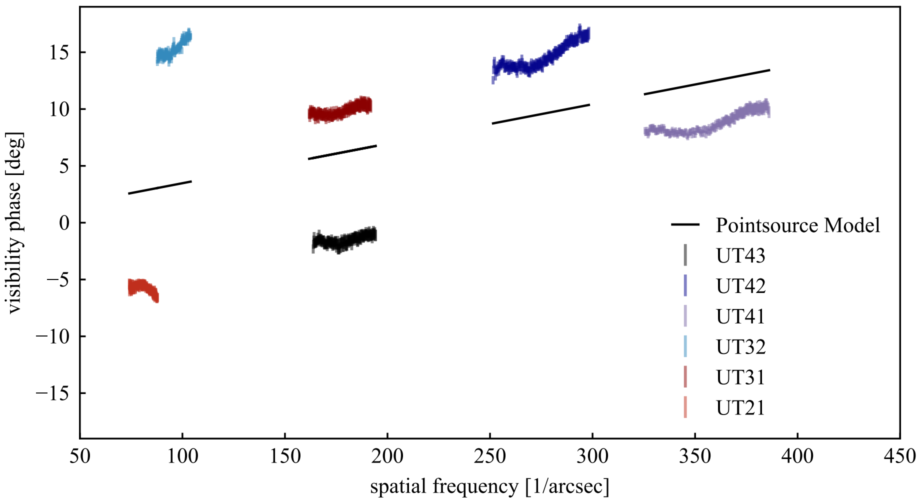

Figure 9.5: Point source fit to the data of the first exposure in Figure 9.4. The data for the six baselines is shown in color and the fit as a black line.

Both of these effects can be explained by introducing a single, varying systematic dOPD for each of the four telescopes. We find that the introduced systematic dOPD repeats over different nights. Furthermore, we find that the metrology signal shows the same systematic effects as the visibility phase. The metrology signal we look at here is the difference between the telescope and the fiber coupler metrology. This has the advantage that the strong drifts in the metrology, which are due to the stretching of the fibers in the FDDLs, is not seen in the signal. The systematic effects in phases and metrology can be nicely seen in the two consecutive nights of our test data set in Figure 9.6, where the metrology signal, as well as the science phase of one baseline for two nights, is shown. The data sets are shown as a function of the local stellar time (LST), as this means that for the same LST and the same target, the telescope positions are very similar. One can see that the signal repeats over both nights and is very similar in visibility and metrology phase. As the metrology signal is directly added to the measured visibility phase during the data reduction, we conclude that the systematic effect we observe comes from the metrology measurement. We deduce that the observed systematic effect can be explained by a previously known but unaccounted-for effect, the so-called metrology beam-walk systematic (as introduced in Shao and Colavita, 1992; Lacour et al., 2014).

The metrology beam-walk systematic

Similar to the bias introduced by optical aberrations in the measurement of the S2-Sgr A* separation (see chapter 6), we can trace this metrology error to

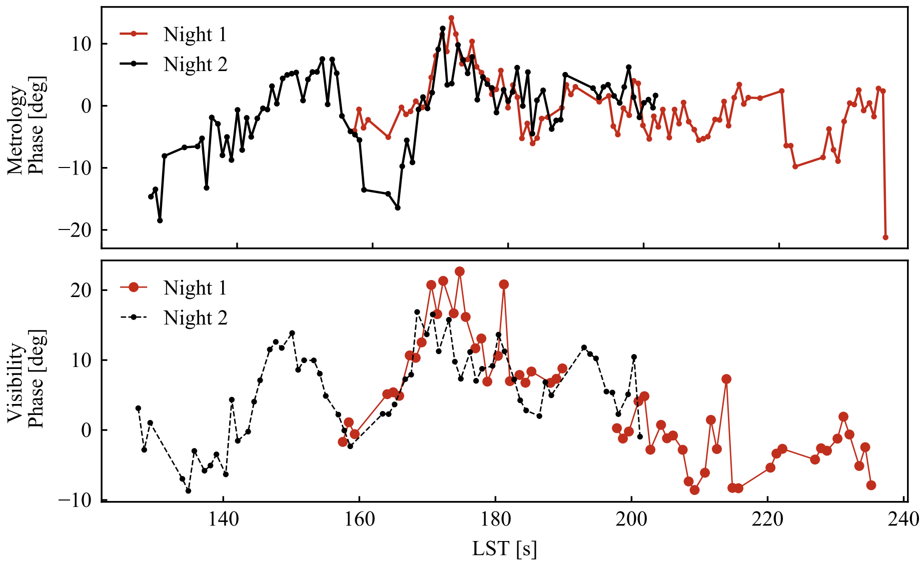

Figure 9.6: Comparison of the metrology phase and the visibility phase for two nights. The metrology phase is the metrology from UT3 minus the metrology from UT2, where we use the difference between telescope and fiber coupler metrology for both. The visibility phase is directly from the baseline UT 3-2. The red data shows the first night, and the black data the second night.

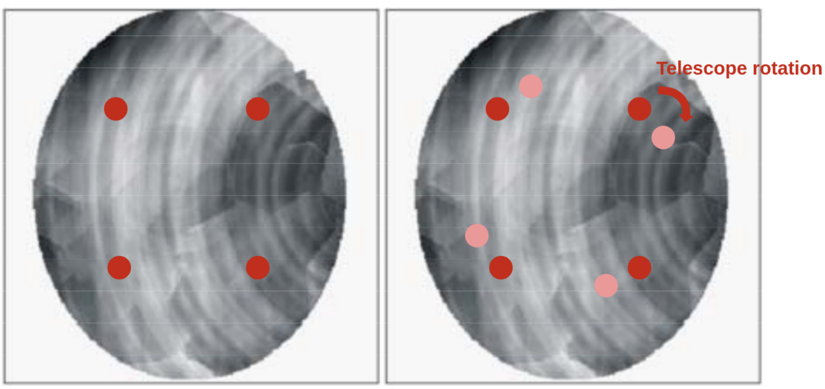

Figure 9.7: Schematic illustration of the introduced aberrations. The background shows an example mirror with scratches from the production, which are seen by the metrology diodes shown in red. The left figure shows the initial measurement and the right one how the metrology measurement rotates with the telescope and therefore samples the aberrations in the mirror.

imperfections in the optical train. Some optical aberration in the light path of the metrology beam can introduce a measurement error by introducing an OPD. Ideally, one would measure the metrology signal at the center of the telescope beam to be as close to the light path of the science light as possible. However, the center of the telescope is of course obscured by M2. Therefore the current scheme was chosen, where four receivers are mounted to the telescope spiders, and the used signal is the average of the four. Due to this set up, a spatially varying optical aberration can introduce different OPDs for the four receivers. The receivers are mounted so that any symmetric aberration (i.e. all low order Zernike polynomials such as astigmatism) is canceled out by the average. However, if there are asymmetric aberrations or symmetric aberrations on a small scale, the system is sensitive to them. As shown in chapter 6 the optical system of GRAVITY is affected by aberrations of higher order. Furthermore, imperfections in the production process of some of the mirrors may introduce asymmetric aberrations on small scales, which may also affect the measurement. Therefore, the conclusion is that we have field-dependent aberrations in some mirrors, which are measured by the metrology receivers. These optical aberrations appear as an error with beam motions and a different footprint between the starlight and the metrology. which is the beam-walk systematic (Lacour et al., 2014).

When we subtract the metrology signal from the science light, the beam-walk systematic introduces an error, as the footprint of the four receivers is in a different position on those mirrors than the science light and therefore sees different aberrations. The here discussed metrology error is therefore the difference between the Gaussian mode weighted phases of the FT and SC light and the sampling of the wavefront by the metrology receivers.

This would not be a problem for a static system, as one could just calibrate the effect. During an observation, however, the telescope rotates following the path of the source on the sky. This implies a rotation of the telescope spiders, and correspondingly the metrology receivers. Consequently, the aberration-induced OPD changes with time. An illustration of the aberrations and how the metrology diodes sample them is shown in Figure 9.7. This error is a time-varying telescope-based error that repeats if the telescope rotation is repeated on different nights. It explains the signal that we see: an OPD added to each telescope, which is time-varying and repeats over several nights. For an in-depth explanation as well as a mathematical treatment of how such aberrations affect the measurement, see Lacour et al., 2014.

Correction of metrology beam-walk:

Ideally, we need to run an extensive calibration program, where we map the mirrors' aberrations to correct them. Possibilities of how such a calibration

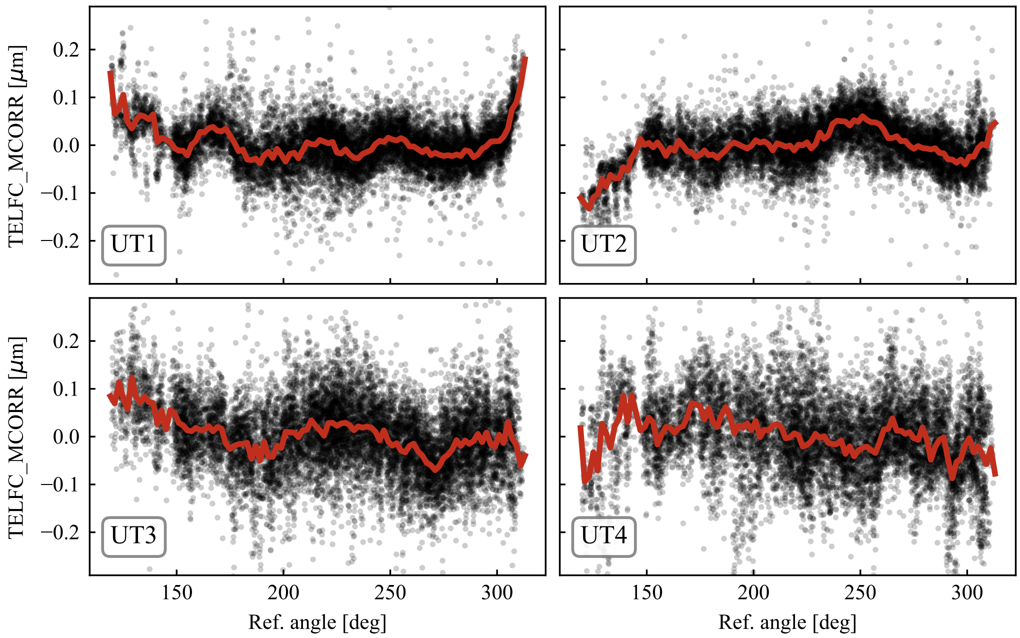

Figure 9.8: Combined metrology measurement for all the Galactic Center data of 2019. The four plots correspond to the four UTs. The individual data, binned to 0.1 deg is shown in black and the mean of all data in red.

could look are discussed in the next section. For now, we are using available data to achieve the best possible correction.

In order to correct this effect, we use the *telfc-corr metrology*, the signal measured at the telescope receivers and referenced to the metrology signal measured at the fiber coupler inside the instrument. This includes the full telescope metrology, but it is already corrected for the dOPD introduced in the fiber coupler, for example, by the differential delay lines. The telfc-corr metrology is a 2π-wrap-free quantity, which is easy to handle. In the following, I refer to telfc-corr to as "the metrology" to ease the understanding.

We construct our correction by combining the metrology measurement of all Galactic Center observations of 2019. These are data taken over 28 nights, with a total on-source time of 25.6 h. While the metrology error changes as a function of time, its time-dependence is introduced by the rotation of the telescope or, more correctly, by the rotation of the instrument's pupil plane. In order to correct the effect, we bin the metrology data of all nights as a function of the angle Φ_{ref} by which the pupil is rotated. This reference angle is determined according to the following formula:

$$\Phi_{ref} = -\tan^{-1}\left(\frac{s_x}{s_y}\right) - \mathrm{DROT}_{\mathrm{OFF}} + p + 315^\circ \tag{9.10}$$

where (s_x, s_y) is the separation vector between the fringe-tracking and science targets on sky; $\mathrm{DROT_{OFF}}$ is the offset angle of the K-mirror in GRAVITY, which depends on the observing mode; and p is the parallactic angle. This reference angle is defined so that it describes the rotation of the metrology pattern in GRAVITY. Meaning that at the same reference angle, the metrology pattern is the same in GRAVITY.

To remove constant offsets between the different nights, which depend on the metrology calibration, we allowed for an offset of the mean and adapted the offset such as that the combined data fits together. Figure 9.8 shows the raw metrology data of 2019 for each telescope as well as the median value binned by the reference angle. This figure is a strong evidence for us that we indeed have systematic effects that repeat at a given reference angle. The metrology signal is of course expected to measure a dOPD introduced by instrumental effects, which is then also seen in the phase and has to be corrected. However, we do not expect to see effects which repeat at a given reference angle and Figure 9.8 shows this behavior clearly. We therefore conclude that we have systematic effects in the metrology, which are directly propagated in our phase measurement. Using the reference angle here is based on the assumption that the aberrations are within GRAVITY, as the field rotation is different outside the instrument. Given that we see a clear correlation with the reference angle this assumption seems to be valid and we continue to consider aberrations within the GRAVITY instrument.

Averaging data over a significant fraction of a night leads to a cancellation of this effect (e.g. as in Gravity Collaboration et al., 2019) and only increases the uncertainty of the measurement. In the case of observations of time-variable sources, however, we want to use data from single exposures and must therefore take this effect into account.

Estimation of residual uncertainty

Due to the limited amount of metrology data available, we cannot perfectly correct the systematic metrology error. Any residual telescope error causes an error in the measured visibility phases and, therefore, a shift in the fitted centroid position. This position shift cannot be disentangled from a true source movement when we fit the visibility phases. Consequently, it is essential to estimate the residual systematic metrology error to derive a reliable measurement of the centroid motion.

If a white noise model describes the metrology error, the scatter of the fitted centroid position would also correspond to white noise. However, in the case of correlated noise (with respect to the reference angle), the motion of the phase centroid can appear correlated and systematic, mimicking an actual motion of the source on the sky.

Unfortunately, we cannot expect white noise since the metrology measurement is strongly correlated over time on any single night. If the number of data sets going into the averaged correction (as shown in Figure 9.8) is large, the mean will not be dominated by the trends of any individual night, and the remaining noise in the correction should be white. For the 2019 data set as shown in Figure 9.8 we have at most 12 overlapping observations at a given reference angle. When averaging this small number of data points, we must expect that some correlation remains between neighboring reference angles. This correlated error in the metrology correction would then be attributed to a physical motion of the source. This correlation is solely due to the small number of available metrology data sets and will decrease with the addition of more data sets. There is no technical limitation on the number of metrology data sets we can combine and thus on the quality of the correction of this systematic. The quality of the correction should improve with an increasing amount of observations.

In order to obtain an estimate of the residual systematic effect due to the uncertainty on the median metrology correction, we bootstrap 100 realizations of the metrology data and derive 100 realizations of the corrected phases of each data-set. We do this in an end-to-end fashion, using the bootstrapped metrology realizations to correct the phases and the correction of the measured astrometry.

9.3 CORRECTION OF AFFECTED DATA

In this section, we pick one data-set to show how the astrometric result improves when we take into account the systematic effects described in the previous section. For this analysis, we pick a data set from the Galactic Center observations of 2019. The data were taken on the night of the 20th of June 2019. We picked this night as it is a comparably long observation of Sgr A*, where we observed the black hole for a little more than two hours. We did not have any technical issues and good weather, making this data set a good one to illustrate the discussed effects. We discussed earlier that in dual beam astrometry, one simply has to fit a centroid model to the observed visibility phases. However, the Galactic Center is a very crowded field, so we usually have to take into account that there might be other stars in the field of view. We will shortly discuss the effect of those other stars before moving on to the data of Sgr A*.

9.3.1 INFLUENCE OF NEARBY STARS

In 2019 Sgr A* is not the only source in our interferometric field of view: S2 and S62 are observed as well (Gillessen et al., 2017; Gravity Collaboration

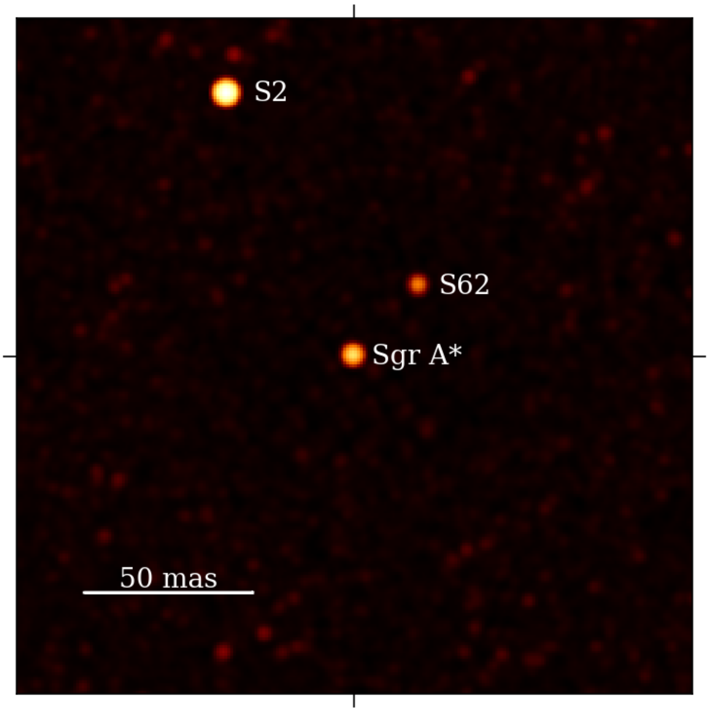

Figure 9.9: Image of the Galactic Center data from 2019-06-20. The image shows the three sources in the field: Sgr A*, S2 and S62. The off-center sources are damped by the fiber coupling profile, which is taken into account in the image. The image is produced with a newly developed imaging technique based on information field theory (Gravity Collaboration et al., 2021, in prep.)

et al., 2021). An image of the used data set is shown in Figure 9.9. The flux of S2 and S62 is highly damped by the fiber coupling profile and thus their contribution is small. Nevertheless, we take their pull on the image centroid into account.

In order to include these two additional sources we calculated the complex visibilities V with a three-source model:

$$V = \frac{I_{SgrA^*} + f_{S2} \cdot I_{S2} + f_{S62} \cdot I_{S62}}{I^0_{SgrA^*} + f_{S2} \cdot I^0_{S2} + f_{S62} \cdot I^0_{S62}} \tag{9.11}$$

In this equation f_i is the flux ratio of each source with respect to Sgr A*: $f_i = f(i)/f(Sgr\ A*)$. I is the interferometric signal from the individual source, integrated over a bandpass $P(\lambda)$ for each pixel:

$$I(\alpha, OPD) = \int_{\Delta\lambda} P(\lambda) \cdot \left(\frac{\lambda}{2.2\mu m}\right)^{-1-\alpha} \cdot \exp\left(-2\pi i \frac{OPD}{\lambda}\right) d\lambda \tag{9.12}$$

and I^0 is the same value with the OPD set to zero, which is needed for the correct normalization:

$$I^0(\alpha) = \int_{\Delta\lambda} P(\lambda) \cdot \left(\frac{\lambda}{2.2\mu m}\right)^{-1-\alpha} d\lambda \tag{9.13}$$

The OPD for a point source is the product of the source position $\vec{s}$ and the baseline $\vec{B}$:

$$OPD = \vec{s} \cdot \vec{B} \tag{9.14}$$

For a full deviation of these formulas see Waisberg, 2019.

The flux ratios f_{S2} and f_{S62} are given relative to the SgrA* brightness and corrected for the fiber damping (see chapter 6). Finally α is the spectral slope of the source. We used $\alpha = 0.5$ for SgrA* and $\alpha = 3$ for S2 and S62. In order to keep the fit as simple as possible, we do not fit the flux ratios and positions of S2 and S62 as free parameters, but take their values from Gravity Collaboration et al., 2020e; Gravity Collaboration et al., 2021. The number of free parameters in our model is therefore still two, but the fit to the data is much improved. We show an example of the fit with and without the metrology correction and the contributions of S2 and S62 in Figure 9.10.

9.3.2 CORRECTED DATA

The data presented here are taken in the usual scheme, where we predominantly observe with the fiber centered on Sgr A* and occasionally observe S2 as a calibrator. The goal is to measure the distance vector between the two sources. To correct the data for the various effects, we need to follow a couple of steps after the initial data reduction with the GRAVITY pipeline:

- First, the inaccurate separation vector needs to be corrected. For this, we fit for the $\vec{\Delta S}$, which removes the expected drift from the S2 data. This $\vec{\Delta S}$ is then added to the separation vector. We then recalculate the Sgr A* phases with the corrected separation vector.
- In the next step, we correct for the beam-walk systematic. For this correction, we calculate the reference angle for each integration. We then read out the metrology correction, which we derived from the combined data of 2019, as shown in Figure 9.8. As the correction is derived for each telescope, we need to get a baseline quantity by just using the correction from the two involved telescopes. This correction is then added as an OPD to the phases of this baseline. For an example on how it improves the phases, see Figure 9.10.
- To get the final astrometry of the measurement, we then fit a three source fit to Sgr A*, S2, and S62.

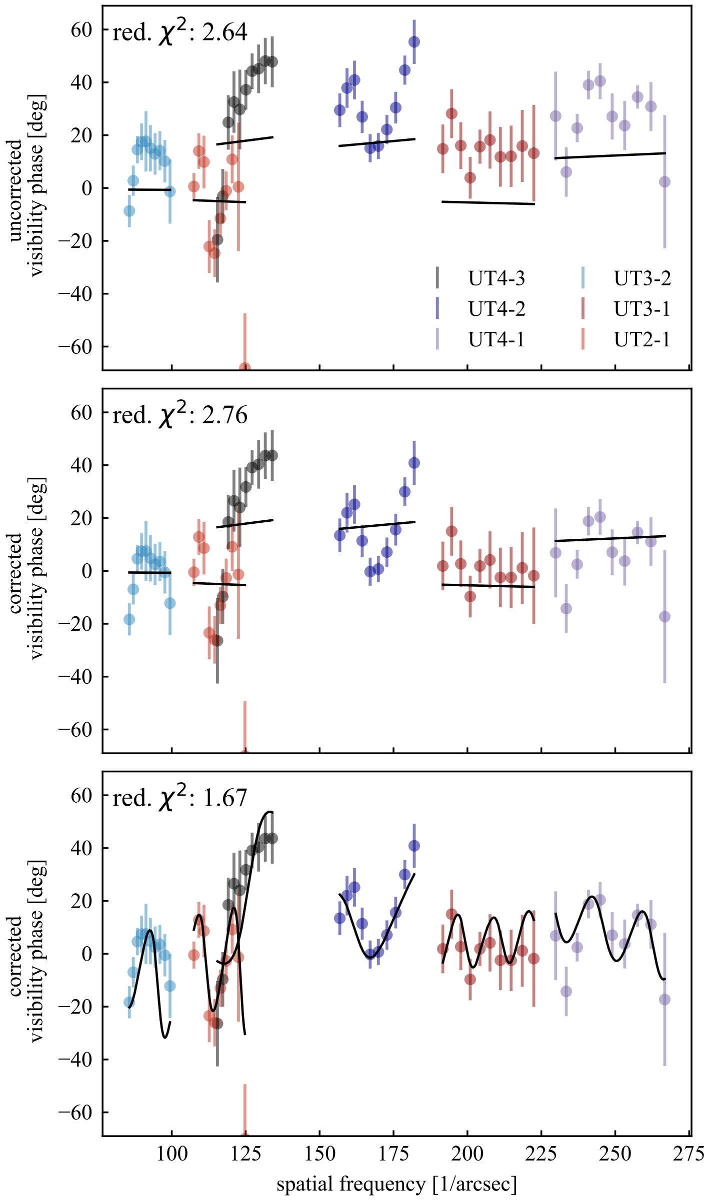

Figure 9.10: Example fit to uncorrected data and corrected data. The top panel shows a single source centroid fit to the data affected by metrology systematics. The beam-walk systematic effect leads to inconsistency of the data with a point source. This is visible when comparing fit lines with the data: systematically affected baselines are shifted w.r.t. the best fit point source. In the depicted case, baselines containing UT3 are affected the most (black 4-3, blue 3-2 and red 3-1). The middle plot shows the fit after the metrology systematic have been corrected. The data is now consistent with a point source, the center of weight of the phases matches that of the fit. The bottom panel shows the three-source centroid fit, which includes the phase signature of S2 and S62.

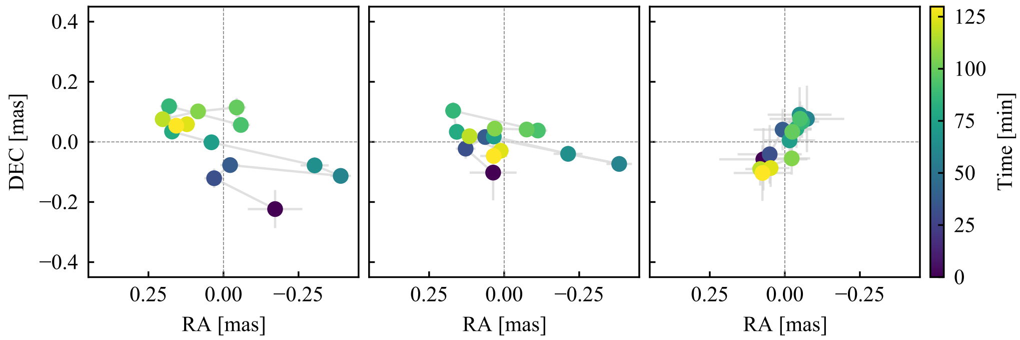

Figure 9.11: Astrometry of Sgr A* in the night 2019-06-20. The left plot shows the astrometry without any correction for systematic effects. In the center plot only the separation vector is corrected. The data in the right plot include the correction for the separation vector as well as for the beam-walk systematics. As we are interested in the relative movement of the source we removed the mean of each data set.

- The last two steps are repeated 100 times with different realizations of the bootstrapped metrology correction to get the errorbar on the measurement. The uncertainty from the metrology correction is added in a squared sum to the other contributions but is usually the dominant one.

The measured astrometric position of Sgr A* is shown in Figure 9.11, once without the corrections, with the separation correction and the fully corrected dataset. From this figure, one sees two main effects. Firstly in the uncorrected data, there is a strong drift in the astrometry. This is due to the slightly incorrect separation vector, which is then removed in the corrected data set in the middle. Secondly, the uncorrected data shows much more scatter than the corrected one, which is the dominant error in this case. This is due to the beam-walk systematics, which adds the scatter on short time scales. The right data also show bigger errorbars as the uncertainty estimated from the bootstrapping over the correction is added.

The data shown in Figure 9.11 is the astrometry of the black hole Sgr A*. From previous observations in single-beam mode we know that we expect motions on the order of 100 µas (Gravity Collaboration et al., 2018a; Gravity Collaboration et al., 2020c). The motions we see in the uncorrected data in Figure 9.11 are significantly bigger than this and cannot be physically explained, as they would exceed the speed of light. We can conclude that the corrections done to the data certainly improve the data-set. The corrected data show a believable motion. However, due to the comparably large errorbar, we cannot detect significant motions in the emission of Sgr A* in this case. The error bars can be reduced by adding more data to the correction shown in Figure 9.8. Another way to reduce them would be to start a dedicated calibration program, as discussed in the following.

With the correction of the data as shown in Figure 9.10 and Figure 9.11 we demonstrate that we can significantly improve our data by taking the discussed systematic effects into account. With the corrections applied we can reach an astrometric uncertainty of below 50 µas with the dual-beam observation. However, we are still limited by how well we know the corrections we need to apply to reach better uncertainties over short timescale.

9.4 CALIBRATION OF METROLOGY SYSTEMATIC

The described systematic effects are currently our limiting factor for the dual-beam astrometry. GRAVITY was built to reach astrometric accuracies on the order of 10 µas. Currently an accuracy on the order of 50 µas is achievable for dual beam astrometry (see e.g. Gravity Collaboration et al., 2020a; Gravity Collaboration et al., 2020d). The 50 µas are possible, as the systematic effects of the metrology average out over time, especially with long observing sequences. The long observing sequences usually have a significant telescope rotation and therefore cover a large range in reference angle, which means that the errors introduced by the metrology measurement average out. Over short timescales we can already reach a similar accuracy by correcting for the systematic effects as discussed before.

The effects become more problematic when we want to do reach the highest possible accuracy in dual-beam astrometry on short time scales. The science case for this is, for example, the orbital motions in the emission of the supermassive black hole Sgr A*. The first observations of orbital motions in Gravity Collaboration et al., 2018a were done in single beam mode, as S2 was at this point very close to Sgr A*. Ideally, we want to repeat such a measurement with dual-beam astrometry, which means that we need to reach an accuracy of a few 10 µas on timescales of a few minutes. To reach such a measurement accuracy, we need to even better calibrate the discussed effects. For the very best accuracy the corrections we have shown before are not sufficient, and we present the ongoing work towards a better calibration in the following.

The main problem is shown in Figure 9.7: the footprint of the metrology diodes samples inaccuracies on different mirrors. Considering only this picture, it would be enough to measure the metrology signal with a 360° scan and apply this measurement as a correction to each metrology measurement. This idea describes the first possibility of a calibration measurement: We can use the telescopes in an arbitrary state as long as the metrology laser is propagated from

GRAVITY to the diodes in the telescopes. We then rotate the internal K-mirror in GRAVITY, which has exactly the desired effect as it rotates the metrology footprint in the pupil plane. The rotation will be the same as indicated in Figure 9.7, except that we rotate the pattern regularly by using the K-mirror, instead of getting the rotation from the telescope position over the night. We can calculate the reference angle by taking the actual K-mirror position into account and get the full calibration. This scanning mode is theoretically the simplest way to get to a calibration measurement. However, there are several issues that complicate the problem:

- The K-mirror is used to align the field so that it can be split up into the science and fringe-tracking field and that the light is fed into the two fibers. By rotating the K-mirror, it is therefore impossible to keep the targets at the positions of the fringe-tracking and science fibers. We cannot get any science light to analyze in this scanning mode. The only observable is then the metrology signal.

- The SNR of the metrology measurement is relatively low. This is done by design, as the metrology laser shows some backscattering into the science wavelengths. The low SNR complicates any calibration measurement, as one probably has to scan several times (similar to the data in Figure 9.8).

- Lateral movements of the pupil plane shift the spots in Figure 9.7 accordingly, and the metrology signal measures slightly different aberrations. The pupil plane is controlled in GRAVITY in real-time, but small movements do still occur.

- The fiber separation is adjusted for each observation, depending on the separation of fringe-tracking and science target. While this should not change the overall picture, there still might be a slight change in the illumination of the metrology light, which modifies the measured effects.

We can adjust for the fourth problem in the scanning mode by using the same fiber separation as for a normal Galactic Center observation. For the other three points, we do not have a solution, except to do many scans and average out the effects.

There is, however, a second possibility. When we observe a point source on sky, we know that the phases should be zero. Any significant deviation from zero is expected to be from the beam-walk effect. Therefore, the second idea for a calibration is to observe a point source on sky and follow it through zenith. During the zenith passage of the target, the telescopes rotate a lot, and we get a good coverage in reference angle in a short period of time. We can fill the entire space in reference angle by adding several of those measurements and get a full calibration. In this mode, the big difficulties are the opposite ones than for the scanning mode: we do not suffer from SNR problems as we can use the visibility phase, which has for bright stars a much better SNR than the metrology signal. However, we need to have stars with the exact proper separation, as we otherwise might measure different aberrations. If the separation is indeed a real problem is not clear to us and has to be established in experiments.

9.4.1 ON-AXIS SCAN

There is one mode where we can combine the advantages of both calibration approaches, which is the on-axis mode of GRAVITY. GRAVITY can be operated in two different modes: on-axis or off-axis. In on-axis mode, the fringe-tracking and the science target are the same object, while they are two separate objects in the off-axis mode. The on-axis mode is used when the science target is bright enough to fringe track or no close stars suitable to fringe tracking are available. As the fringe-tracking and the science object are the same in this case, there is no need for a phase-referencing between the two, and the metrology signal is normally not needed in the on-axis mode.

By using the on-axis mode, we can rotate the K-Mirror, while staying with the fibers on the target. The field does not have to be spatially split up into the science and fringe-tracking field in this mode. The splitting of the light is done with a beam-splitter, which does not depend on the K-mirror position.

We did this experiment in the beginning of 2021, where we pointed at a single star in on-axis mode and rotated the K-Mirror. In total, we did three rotations, where we recorded the metrology data as well as the science and fringe-tracking data. The metrology data for UT2 is shown in Figure 9.12. In this case, we do not plot the averaged quantity but the signal from each diode individually. The diodes are separated by approximately 90°, so if there is an aberration in a mirror, it should show up at each diode with a 90° shift. In Figure 9.12 we can see that each diode shows an area with a strong high-frequency signal, which repeats at the next diode with a 90° shift. This repeated signal is a strong indication that our theory of aberrations in the mirrors is right, causing the systematic effects we see in the phases. In Figure 9.12 one also sees a strong low-frequency signal. This signal is from a tip in the metrology light, which is removed when the four diodes are averaged. We only show UT2 here as it shows the clearest effects, but the other three telescopes show a similar picture.

While this test shows that we indeed have aberrations in the mirrors, which are then sampled by the metrology and add an OPD to the measured phases, it is not directly applicable to the off-axis data. As mentioned before, the light is split with a beam splitter in the on-axis case, while a roof prism is used in the off-axis mode. This different element in the light path and the different positioning of the fibers makes for a different illumination of the metrology light,

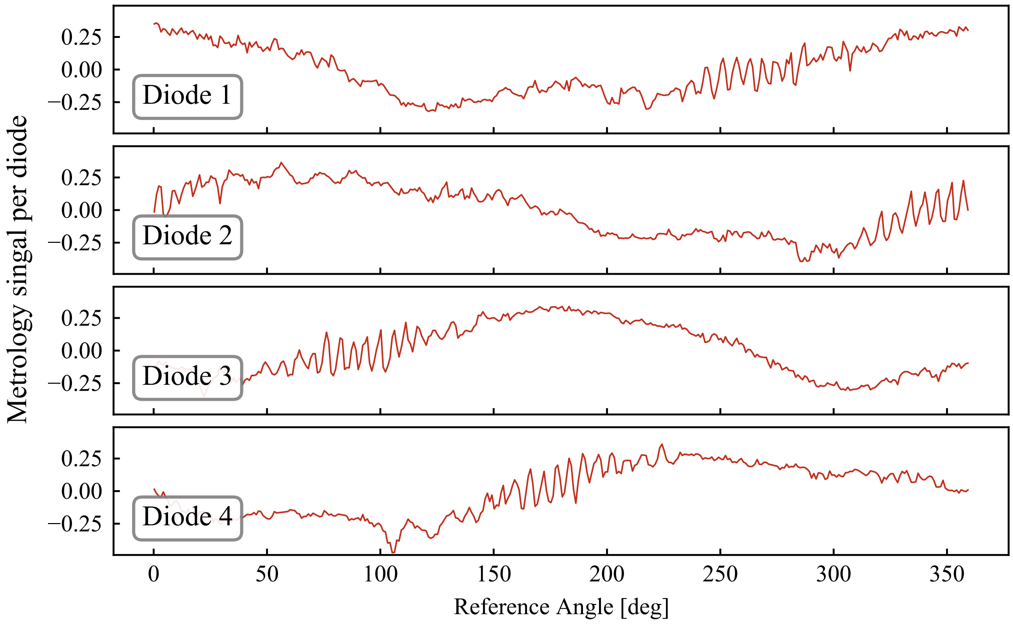

Figure 9.12: Measurement of the metrology scan for UT2. The four plots show the signal measured by each individual telescope diode.

which is propagated backward through the instrument. We, therefore, conclude this on-axis test as very helpful to show that we understand our problem, but not the final step to get to a calibration measurement.

9.4.2 OFF-AXIS CALIBRATION

The final calibration for the dual-beam observation has to be done in off-axis mode. We plan to make a two-fold approach to reach the best possible calibration. The first part will be a blind rotation, similar to what we have done in the on-axis mode. Due to the discussed problems in the off-axis mode, we will not have a phase measurement in this experiment, as the science fiber will be pointed into the sky. It will then rotate around the star, which we use as the fringe tracking star. This test could theoretically be done in an entirely blind mode (and even with closed telescopes during daytime), but many control loops in GRAVITY only function if there is light in the fringe-tracker. To ensure the best possible stability in GRAVITY we plan to do this test with the fringe-tracker active on a star and the majority of the control loops closed. This approach also ensures that the instrument is as close as possible to the state it would be in for regular observations.

The second experiment we plan to do is with starlight in the science fiber to get the high SNR phase measurement in addition to the metrology measurement. In

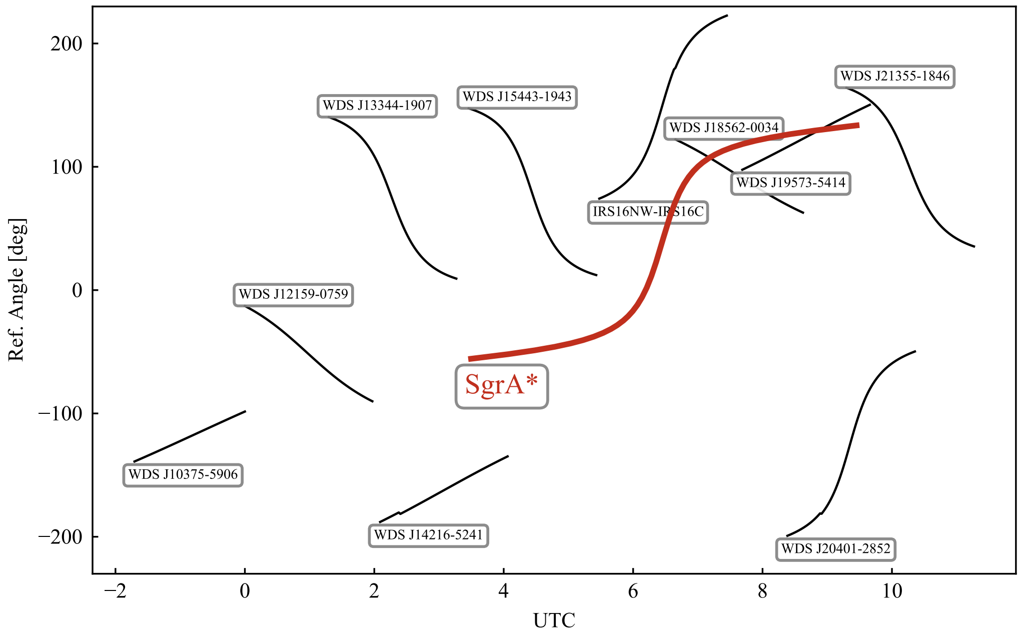

Figure 9.13: Example for a selection of binary stars to be observed to measure the off-axis metrology. The red line shows the track in reference-angle for Sgr A* as observed with the usual fringe-tracking star IRS 16C. The black curves show the reference angle curves for different binary stars, picked from the WDS catalog. Each track is shown for a two hour observation around the zenith passage of the target.

this case, we can not freely rotate the field but have to wait for the telescopes to rotate due to the target's motion on sky. This motion is fast around the zenith passage of the target and relatively slow otherwise. To only use the fast rotation, we plan to observe several stars and always only observe during their zenith passage. During the zenith passage, a two-hour observation of a target will give us up to 130° of reference angle, depending on the target's zenith distance. By adding several of such two-hour blocks, we will fill the full range of possible reference angles with a handful of observations and put together a complete calibration measurement from this. An example of reference-angle coverage for several targets is shown in Figure 9.13. The shown targets are known binary stars from the WDS catalog (The Washington Double Star Catalog[1]). We picked binary systems, which have a similar separation as Sgr A* and IRS 16C, to not bias the measurement with different fiber positions. From the figure, one can see that with a handful of targets and two hours of observation on each, we will be able to fill the entire reference angle space rather quickly and get to a complete calibration measurement from those stars.

[1] `http://www.astro.gsu.edu/wds/`

In theory, the two approaches measure the same thing: the aberrations in the mirrors, as seen by the metrology. Therefore, the approach of two different experiments will also convince us that our model of the systematic effects is correct if they fit nicely together. The time for these experiments was already granted to us from ESO. Due to the challenging situation over the last one and a half years, they were not fully executed yet.

9.5 CONCLUSION

We have presented the dual-beam observation mode and the systematic effects which currently limit it in this section. For the Galactic Center observations (Gravity Collaboration et al., 2020a) and the astrometry of exoplanets (Gravity Collaboration et al., 2020d) the dual-beam astrometry is already used. In those cases, we depend on longer observing sequences to average out the systematic effects, which currently limit the fully phase referenced astrometry. By using a night average, we can achieve astrometric results with an accuracy on the order of 50 µas, which is already an astonishing improvement to what is possible with single-dish observations of 10 m class telescopes. Nevertheless, to reach the goal of 10 µas accuracy over the timescale of five to ten minutes, we need to correct for the mentioned systematic effects. With the work we have presented in this section, we found the dominant effect, currently limiting our astrometry. By understanding the effect, we already did the first important step. We then outlined the calibration program, which we are currently running to correct for the systematic effects.

From what we know about the optical aberrations, we think that they mostly come from mirrors in the fiber coupler of GRAVITY. As they show up in the difference between the fringe-tracker and the science light, they have to be mirrors that are not seen by both beams or where the beams are not in focus. There is, therefore, only a small number of mirrors, which are most likely the reason for the strong aberrations. It is consequently even worth a thought to replace those mirrors with better ones, and we are currently looking into it as part of the significant upgrade of GRAVITY and VLTI under the project GRAVITY$^+$. However, until then, our best chance is to fully understand the effects that we see and calibrate them. The majority of this was done as we have outlined. With the work presented here, we are one big and essential step closer to unleashing GRAVITY's full astrometric potential in the fully phase-referenced dual-beam mode.

10 OUTLOOK & CONCLUSION

In this thesis, I present our work to improve the available instrumentation to study the Galactic Center and the supermassive black hole at its center. I show how a better understanding of the instrument opens up new observing modes and the possibility of new exciting science in the near future.

The first part of the work shows the improvements to existing data, both for the SINFONI and the GRAVITY instrument. I present several different improvements, which helped to reach new science results with the Galacitc Center stars:

- The part starts with the developments in the reduction and analysis of SINFONI data in chapter 4. We improved the reduction by tweaking the reduction algorithms and the calibration scheme. We implemented a cross-correlation-based approach to extract the velocities from the measured spectrum. The cross-correlation led to a significant improvement in accuracy, as it takes into account all available spectral features and not just one spectral line. With the improved methods, we can significantly improve the uncertainty in the radial velocities of the star S2. This allows to better constrain its orbit around the supermassive black hole Sgr A*. The revisited radial velocities helped us to improve the complete S2 data-set and to reach better scientific results. The results of these improvements are not limited to the work presented in this thesis. But it also contributed to other results, such as the detection of the Schwarzschild Presession in the orbit of S2 (Gravity Collaboration et al., 2020a). SINFONI was decommissioned in 2019. It is currently being upgraded to a new instrument that combines integral field spectroscopy and imaging into one: ERIS (Davies et al., 2018). ERIS will return to the VLT in 2022 and again be a workhorse for observations of the stars in the Galactic Center. The approaches presented in this thesis will be directly applicable to ERIS and will give us a great base to achieve the best possible measurements as soon as ERIS is available.
- The improvements in the SINFONI reduction played a vital part in the next part of this work presented in chapter 5. This chapter addresses one of the most fundamental challenges in astronomy: measuring the distances to astronomical objects. The data of the star S2, which orbits Sgr A*, offer the possibility to measure the distance to the Galactic

Center, as the distance is a parameter of the fit to the data. We measured the distance to the Galactic Center with unprecedented accuracy in the S2 orbit fit. With the renewed SINFONI results, more GRAVITY data points, and a slightly improved data analysis, we were able to significantly reduce the uncertainty on the distance in comparison to the previous result in Gravity Collaboration et al., 2018b.

- A further improvement to the analysis was done by taking field-dependent optical aberrations in GRAVITY into account. In chapter 6, we discuss the implications of these aberrations and how we can correct them. We find that especially the GRAVITY results in 2017 were affected by the optical aberrations and that they caused a slight inconsistency in the measured distance to the Galactic Center. With the correction for the field-dependent aberrations, we bring all the distance measurements in agreement and remove inconsistencies in the data. Therefore, this work not only studies the optical aberrations, but also further improves the distance measurement to the Galactic Center. This property can be used in many other fields as it helps to constrain the structure of the Milky Way.
- With the results from GRAVITY, we have measured the orbit of S2 better than ever before. Together with the improved radial velocity this opens a unique opportunity to test a prediction of General relativity, the Einstein Equivalence Principle. In chapter 7, we study whether the Hydrogen and Helium lines in the S2 spectrum couple differently to the potential of the supermassive black hole. A different coupling to the potential would violate the Local Position Invariance and hint towards inconsistencies in General Relativity. This work shows the first-ever test of the equivalence principle in the surroundings of a supermassive black hole. With this first experiment around Sgr A* we overcome the limitations of earlier measurements outside of the solar system and show that tests of the Equivalence Principle around the supermassive black hole are possible. Therefore, the Galactic Center offers a unique chance to test General Relativity in the future when larger telescopes can do this experiment with much higher precision.

While the first part of this thesis focuses on the improvements done to the available data and the science results reached with the increased understanding of GRAVITY and SINFONI, the second part develops new techniques and calibration methods for so far impossible science programs. There are two new modes discussed in this part:

- In chapter 8, we build up a calibration model for the instrumental polarization of the VLTI and GRAVITY. Polarization measurements are an established part of astronomy. However, for optical interferometry, they remain a very unusual topic. The lack of polarimetry is due to the need for a difficult calibration of the high number of mirrors in an optical interferometer. First polarimetric observations with an interferometer were done by Ireland et al., 2005, but until today it is not an established observing mode. The work presented in this thesis combines the unique capabilities of GRAVITY with an end-to-end calibration model. With this work we add polarimetry to the many possibilities of observations with GRAVITY. The outstanding precision of GRAVITY and its astrometric capabilities together with polarimetric measurements will allow us to continue the studies of the accretion processes of Sgr A* on the smallest scales around the black hole. With these studies we will be able to further constrain the magnetic field surrounding Sgr A*, as shown in Gravity Collaboration et al., 2020b. However, polarimetry with GRAVITY is not only interesting for the Galactic Center science. Many other fields, such as the study of young stellar objects and the disks around them, will benefit significantly from the unveiling of the polarimetric mode of GRAVITY.

- The second new mode is the dual-beam observing in chapter 9. This mode is already available but is currently limited by systematic effects. We explore where these effects come from and how we might be able to remove them. Similar to the effects in chapter 6, they are caused by optical aberrations but mainly affect the phase referencing in the dual-beam observation. To overcome the currently limiting systematic effects, we propose two solutions: The first one is to collect the average metrology measurement from the existing data and use it as a measurement of the systematic effect. We showed that this solution works and vastly improves the data. However, it still has considerable uncertainty. The second solution is a dedicated calibration scheme which we are currently implementing with the Paranal Observatory.

This second part of the thesis paves the way into the very near future with GRAVITY. Both the polarimetric mode and the dual-beam observation with the highest possible accuracy were planned from the beginning of the instrument, but, as lined out in this work, both need significant calibration schemes to become available. With the work presented here, we unlock both observing modes, making GRAVITY an even more versatile instrument than it already is. The new modes are especially interesting for the Galactic Center observations: With the fully calibrated dual-beam observing mode, we can observe the supermassive black-hole at all times, independent of the surrounding stars. This will allow us to study the black hole and its accretion mechanisms better than ever before. When we combine these observations with the newly available polarimetric mode, we can also study the magnetic field around Sgr A* and the influence of it on the supermassive black hole. This combination will push GRAVITY even further and reinforce its position as the best available instrument for studies of the Galactic Center. The new observing modes will add new possibilities for many other astronomical studies and open up new science cases with GRAVITY.

BIBLIOGRAPHY

Agachev, A. R. et al. (Jan. 2011). "Test of local position invariance at the detector "Dulkyn-1"". In: *Gravitation and Cosmology* 17, pp. 83–86. DOI: 10.1134/S0202289311010026.

Alexander, Tal (Nov. 2005). "Stellar processes near the massive black hole in the Galactic center [review article]". In: *Physics Reports* 419.2-3, pp. 65–142. DOI: 10.1016/j.physrep.2005.08.002. arXiv: astro-ph/0508106 [astro-ph].

Amorim, Antonio et al. (July 2012). "The final design of the GRAVITY acquisition camera and associated VLTI beam monitoring strategy". In: *Optical and Infrared Interferometry III*. Ed. by Françoise Delplancke, Jayadev K. Rajagopal, and Fabien Malbet. Vol. 8445. Society of Photo-Optical Instrumentation Engineers (SPIE) Conference Series, 844534, p. 844534. DOI: 10.1117/12.925993.

Angélil, R. and Saha, P. (June 2011). "Galactic-center S Stars as a Prospective Test of the Einstein Equivalence Principle". In: *Astrophysical Journal, Letters* 734, L19, p. L19. DOI: 10.1088/2041-8205/734/1/L19. arXiv: 1105.0918.

Angélil, R, Saha, P, and Merritt, D (Sept. 2010). "Toward Relativistic Orbit Fitting of Galactic Center Stars and Pulsars". In: *ApJ* 720.2, pp. 1303–1310.

Anglada-Escudé, G. and Torra, J. (Apr. 2006). "Astrometric light-travel time signature of sources in nonlinear motion. I. Derivation of the effect and radial motion". In: *Astronomy & Astrophysics* 449, pp. 1281–1288. DOI: 10.1051/0004-6361:20054500.

Armstrong, J. T. et al. (Mar. 1998). "The Navy Prototype Optical Interferometer". In: *The Astrophysical Journal* 496.1, pp. 550–571. DOI: 10.1086/305365.

Arsenault, Robin et al. (Feb. 2003). "MACAO-VLTI: An Adaptive Optics system for the ESO VLT interferometer". In: *Adaptive Optical System Technologies II*. Ed. by Peter L. Wizinowich and Domenico Bonaccini. Vol. 4839. Society of Photo-Optical Instrumentation Engineers (SPIE) Conference Series, pp. 174–185. DOI: 10.1117/12.458836.

Ashby, N. et al. (Feb. 2007). "Testing Local Position Invariance with Four Cesium-Fountain Primary Frequency Standards and Four NIST Hydrogen Masers". In: *PhysicalReview A: General Physics* 98.7, p. 070802. ISSN: 0031-9007. DOI: 10.1103/PhysRevLett.98.070802.

Bainbridge, M. et al. (Mar. 2017). “Probing the Gravitational Dependence of the Fine-Structure Constant from Observations of White Dwarf Stars”. In: *Universe* 3, p. 32. DOI: 10.3390/universe3020032. arXiv: 1702.01757.

Balick, B. and Brown, R. L. (Dec. 1974). “Intense sub-arcsecond structure in the galactic center.” In: *The Astrophysical Journal* 194, pp. 265–270. DOI: 10.1086/153242.

Bartko, H. et al. (June 2009). “Evidence for Warped Disks of Young Stars in the Galactic Center”. In: *The Astrophysical Journal* 697.2, pp. 1741–1763. DOI: 10.1088/0004-637X/697/2/1741. arXiv: 0811.3903 [astro-ph].

Bartko, H. et al. (Jan. 2010). “An Extremely Top-Heavy Initial Mass Function in the Galactic Center Stellar Disks”. In: *The Astrophysical Journal* 708.1, pp. 834–840. DOI: 10.1088/0004-637X/708/1/834. arXiv: 0908.2177 [astro-ph.GA].

Bauch, A. and Weyers, S. (Apr. 2002). “New experimental limit on the validity of local position invariance”. In: *Physical Review D* 65.8, 081101, p. 081101. DOI: 10.1103/PhysRevD.65.081101.

Beck, C., Schlichenmaier, R., Collados, M., Bellot Rubio, L., and Kentischer, T. (Dec. 2005). “A polarization model for the German Vacuum Tower Telescope from in situ and laboratory measurements”. In: *Astronomy & Astrophysics* 443.3, pp. 1047–1053. DOI: 10.1051/0004-6361:20052935.

Beckers, Jacques M. (Sept. 1990). “Instrumental factors affecting the fringe contrast in optical interferometers”. In: *Astrophysics and Space Science* 171.1-2, pp. 333–339. DOI: 10.1007/BF00646874.

Becklin, E. E., Gatley, I., and Werner, M. W. (July 1982). “Far-infrared observations of Sagittarius A - The luminosity and dust density in the central parsec of the Galaxy”. In: *The Astrophysical Journal* 258, pp. 135–142. DOI: 10.1086/160060.

Berengut, J. C. et al. (July 2013). “Limits on the Dependence of the Fine-Structure Constant on Gravitational Potential from White-Dwarf Spectra”. In: *Physical Review Letters* 111.1, 010801, p. 010801. DOI: 10.1103/PhysRevLett.111.010801. arXiv: 1305.1337 [astro-ph.CO].

Bhatnagar, S., Cornwell, T. J., Golap, K., and Uson, J. M. (Aug. 2008). “Correcting direction-dependent gains in the deconvolution of radio interferometric images”. In: *Astronomy & Astrophysics* 487.1, pp. 419–429. DOI: 10.1051/0004-6361:20079284. arXiv: 0805.0834 [astro-ph].

Bland-Hawthorn, Joss and Gerhard, Ortwin (Sept. 2016). “The Galaxy in Context: Structural, Kinematic, and Integrated Properties”. In: *Annual Review of Astronomy and Astrophysics* 54, pp. 529–596. DOI: 10.1146/annurev-astro-081915-023441. arXiv: 1602.07702 [astro-ph.GA].

Blind, N. et al. (July 2014a). “GRAVITY: the calibration unit”. In: *Proc. SPIE*. Vol. 9146. Society of Photo-Optical Instrumentation Engineers (SPIE) Conference Series, 91461U, 91461U. DOI: 10.1117/12.2055542. arXiv: 1407.6660 [astro-ph.IM].

Blind, N. et al. (July 2014b). “The GRAVITY metrology system: modeling a metrology in optical fibers”. In: *Optical and Infrared Interferometry IV*. Ed. by Jayadev K. Rajagopal, Michelle J. Creech-Eakman, and Fabien Malbet. Vol. 9146. Society of Photo-Optical Instrumentation Engineers (SPIE) Conference Series, 914624, p. 914624. DOI: 10.1117/12.2055553. arXiv: 1407.6669 [astro-ph.IM].

Boehle, A. et al. (Oct. 2016). “An Improved Distance and Mass Estimate for Sgr A* from a Multistar Orbit Analysis”. In: *The Astrophysical Journal* 830, 17, p. 17. DOI: 10.3847/0004-637X/830/1/17. arXiv: 1607.05726.

Bonnell, I. A. and Rice, W. K. M. (Aug. 2008). “Star Formation Around Supermassive Black Holes”. In: *Science* 321.5892, p. 1060. DOI: 10.1126/science.1160653. arXiv: 0810.2723 [astro-ph].

Bonnet, H. et al. (Sept. 2004). “First light of SINFONI at the VLT”. In: *The Messenger* 117, pp. 17–24.

Bower, Geoffrey C. et al. (July 2014). “The Intrinsic Two-dimensional Size of Sagittarius A*”. In: *The Astrophysical Journal* 790.1, 1, p. 1. DOI: 10.1088/0004-637X/790/1/1. arXiv: 1405.1456 [astro-ph.HE].

Brault, J. W. (1962). “The Gravitational Red Shift in the Solar Spectrum.” PhD thesis. PRINCETON UNIVERSITY.

Broderick, A E and Loeb, A (Oct. 2005). “Imaging bright-spots in the accretion flow near the black hole horizon of Sgr A*”. In: *MNRAS* 363.2, pp. 353–362.

Brummelaar, Theo A. ten et al. (2005). “First results from the CHARA Array. 2. A Description of the instrument”. In: *Astrophys. J.* 628, pp. 453–465. DOI: 10.1086/430729. arXiv: astro-ph/0504082.

Buchholz, R. M., Witzel, G., Schödel, R., and Eckart, A. (Sept. 2013). “Ks- and Lp-band polarimetry on stellar and bow-shock sources in the Galactic center”. In: *Astronomy & Astrophysics* 557, A82, A82. DOI: 10.1051/0004-6361/201220338. arXiv: 1308.0956 [astro-ph.GA].

Canovas, H., Rodenhuis, M., Jeffers, S. V., Min, M., and Keller, C. U. (July 2011). “Data-reduction techniques for high-contrast imaging polarimetry. Applications to ExPo”. In: *Astronomy & Astrophysics* 531, A102, A102. DOI: 10.1051/0004-6361/201116918. arXiv: 1105.2961 [astro-ph.IM].

Chatterjee, P., Hernquist, L., and Loeb, A. (June 2002). “Dynamics of a Massive Black Hole at the Center of a Dense Stellar System”. In: *The Astrophysical Journal* 572, pp. 371–381. DOI: 10.1086/340224. eprint: astro-ph/0107287.

Chatzopoulos, S. et al. (Feb. 2015). “The old nuclear star cluster in the Milky Way: dynamics, mass, statistical parallax, and black hole mass”. In: *Monthly Notice of the Royal Astronomical Society* 447.1, pp. 948–968. DOI: 10.1093/mnras/stu2452. arXiv: 1403.5266 [astro-ph.GA].

Christopher, M. H., Scoville, N. Z., Stolovy, S. R., and Yun, Min S. (Mar. 2005). “HCN and HCO^+ Observations of the Galactic Circumnuclear Disk”. In:

The Astrophysical Journal 622.1, pp. 346–365. DOI: 10.1086/427911. arXiv: astro-ph/0502532 [astro-ph].

Chu, D. S. et al. (Feb. 2018). "Investigating the Binarity of S0-2: Implications for Its Origins and Robustness as a Probe of the Laws of Gravity around a Supermassive Black Hole". In: *Astrophysical Journal* 854, 12, p. 12. DOI: 10.3847/1538-4357/aaa3eb. arXiv: 1709.04890 [astro-ph.SR].

Chupp, T. E. et al. (Oct. 1989). "Results of a new test of local Lorentz invariance: A search for mass anisotropy in ^{21}Ne". In: *Physical Review Letters* 63, pp. 1541–1545. DOI: 10.1103/PhysRevLett.63.1541.

Colavita, M. M. et al. (Jan. 1999). "The Palomar Testbed Interferometer". In: *The Astrophysical Journal* 510.1, pp. 505–521. DOI: 10.1086/306579. arXiv: astro-ph/9810262 [astro-ph].

Colavita, M. M. et al. (Oct. 2013). "The Keck Interferometer". In: *The Publications of the Astronomical Society of the Pacific* 125.932, p. 1226. DOI: 10.1086/673475.

Collett, Edward (1992). *Polarized light. Fundamentals and applications.*

Crawford, M. K. et al. (June 1985). "Mass distribution in the galactic centre". In: *Nature* 315.6019, pp. 467–470. DOI: 10.1038/315467a0.

Cutri, R. M. et al. (June 2003). "VizieR Online Data Catalog: 2MASS All-Sky Catalog of Point Sources (Cutri+ 2003)". In: *VizieR Online Data Catalog*, II/246, pp. II/246.

Damour, T. (Nov. 1996). "Testing the equivalence principle: why and how?" In: *Classical and Quantum Gravity* 13, A33–A41. DOI: 10.1088/0264-9381/13/11A/005.

Davies, R. I. (Mar. 2007). "A method to remove residual OH emission from near-infrared spectra". In: *Monthly Notice of the Royal Astronomical Society* 375.3, pp. 1099–1105. DOI: 10.1111/j.1365-2966.2006.11383.x. arXiv: astro-ph/0612257 [astro-ph].

Davies, R. et al. (Aug. 2016). "MICADO: first light imager for the E-ELT". In: *Ground-based and Airborne Instrumentation for Astronomy VI*. Vol. 9908. Proceedings of the SPIE, 99081Z, 99081Z. DOI: 10.1117/12.2233047. arXiv: 1607.01954 [astro-ph.IM].

Davies, R. et al. (July 2018). "ERIS: revitalising an adaptive optics instrument for the VLT". In: *Ground-based and Airborne Instrumentation for Astronomy VII*. Ed. by Christopher J. Evans, Luc Simard, and Hideki Takami. Vol. 10702. Society of Photo-Optical Instrumentation Engineers (SPIE) Conference Series, 1070209, p. 1070209. DOI: 10.1117/12.2311480. arXiv: 1807.05089 [astro-ph.IM].

Do, Tuan et al. (Aug. 2019). "Relativistic redshift of the star S0-2 orbiting the Galactic Center supermassive black hole". In: *Science* 365.6454, pp. 664–668. DOI: 10.1126/science.aav8137. arXiv: 1907.10731 [astro-ph.GA].

Dodds-Eden, K et al. (June 2009). “Evidence for X-Ray Synchrotron Emission from Simultaneous Mid-Infrared to X-Ray Observations of a Strong Sgr A* Flare”. In: *ApJ* 698.1, pp. 676–692.

Doeleman, S. S. et al. (Sept. 2008). “Event-horizon-scale structure in the supermassive black hole candidate at the Galactic Centre”. In: *Nature* 455, pp. 78–80. DOI: 10.1038/nature07245. arXiv: 0809.2442.

Doeleman, S. et al. (2009). “Imaging an Event Horizon: submm-VLBI of a Super Massive Black Hole”. In: *astro2010: The Astronomy and Astrophysics Decadal Survey*. Vol. 2010. arXiv Astrophysics e-prints. arXiv: 0906.3899 [astro-ph.CO].

Dorn, R. J. et al. (June 2014). “CRIRES+: Exploring the Cold Universe at High Spectral Resolution”. In: *The Messenger* 156, pp. 7–11.

Drimmel, R. and Poggio, E. (Nov. 2018). “On the Solar Velocity”. In: *Research Notes of the American Astronomical Society* 2.4, 210, p. 210. DOI: 10.3847/2515-5172/aaef8b.

Dzuba, V. A. and Flambaum, V. V. (Jan. 2017). “Limits on gravitational Einstein equivalence principle violation from monitoring atomic clock frequencies during a year”. In: *Physical Review D* 95.1, p. 015019. ISSN: 2470-0010. DOI: 10.1103/PhysRevD.95.015019.

Eckart, A. and Genzel, R. (Oct. 1996). “Observations of stellar proper motions near the Galactic Centre”. In: *Nature* 383.6599, pp. 415–417. DOI: 10.1038/383415a0.

— (Jan. 1997). “Stellar proper motions in the central 0.1 PC of the Galaxy”. In: *Monthly Notice of the Royal Astronomical Society* 284.3, pp. 576–598. DOI: 10.1093/mnras/284.3.576.

Eilers, A.-C., Hogg, D. W., Rix, H.-W., and Ness, M. K. (Jan. 2019). “The Circular Velocity Curve of the Milky Way from 5 to 25 kpc”. In: *The Astrophysical Journal* 871, 120, p. 120. DOI: 10.3847/1538-4357/aaf648. arXiv: 1810.09466.

Eisenhauer, F et al. (Nov. 2003). “A Geometric Determination of the Distance to the Galactic Center”. In: *ApJ* 597.2, pp. L121–L124.

Eisenhauer, F. et al. (Mar. 2003). “SINFONI - Integral field spectroscopy at 50 milli-arcsecond resolution with the ESO VLT”. In: *Instrument Design and Performance for Optical/Infrared Ground-based Telescopes*. Ed. by M. Iye and A. F. M. Moorwood. Vol. 4841. Proceedings of the SPIE, pp. 1548–1561. DOI: 10.1117/12.459468. eprint: astro-ph/0306191.

Eisenhauer, F. et al. (July 2005). “SINFONI in the Galactic Center: Young Stars and Infrared Flares in the Central Light-Month”. In: *The Astrophysical Journal* 628, pp. 246–259. DOI: 10.1086/430667. eprint: astro-ph/0502129.

Elias Nicholas M., II (Mar. 2001). “Optical Interferometric Polarimetry. I. Foundation”. In: *The Astrophysical Journal* 549.1, pp. 647–668. DOI: 10.1086/319046.

Elias Nicholas M., II (Aug. 2004). “Optical Interferometric Polarimetry. II. Theory”. In: *The Astrophysical Journal* 611.2, pp. 1175–1199. DOI: 10.1086/422212.

Elias Nicholas M., II et al. (Nov. 2008). “The case for optical interferometric polarimetry”. In: *arXiv e-prints*, arXiv:0811.3139, arXiv:0811.3139. arXiv: 0811.3139 [astro-ph].

Event Horizon Telescope Collaboration et al. (Mar. 2021). “First M87 Event Horizon Telescope Results. VII. Polarization of the Ring”. In: *The Astrophysical Journal Letters* 910.1, L12, p. L12. DOI: 10.3847/2041-8213/abe71d. arXiv: 2105.01169 [astro-ph.HE].

Falcke, H. and Markoff, S. B. (Dec. 2013). “Toward the event horizonthe supermassive black hole in the Galactic Center”. In: *Classical and Quantum Gravity* 30.24, 244003, p. 244003. DOI: 10.1088/0264-9381/30/24/244003. arXiv: 1311.1841 [astro-ph.HE].

Falcke, H., Melia, F., and Agol, E. (Jan. 2000). “Viewing the Shadow of the Black Hole at the Galactic Center”. In: *The Astrophysical Journal Letters* 528, pp. L13–L16. DOI: 10.1086/312423. eprint: astro-ph/9912263.

Flambaum, V. V. (2007). “Variation of the Fundamental Constants:. Theory and Observations”. In: *International Journal of Modern Physics A* 22, pp. 4937–4950. DOI: 10.1142/S0217751X07038293. arXiv: 0705.3704 [physics.atom-ph].

Flambaum, V. V. and Shuryak, E. V. (Apr. 2008). “How changing physical constants and violation of local position invariance may occur?” In: *Nuclei and Mesoscopic Physic - WNMP 2007*. Ed. by P. Danielewicz, P. Piecuch, and V. Zelevinsky. Vol. 995. American Institute of Physics Conference Series, pp. 1–11. DOI: 10.1063/1.2915601. eprint: physics/0701220.

Fritz, T K et al. (Jan. 2010). “What is limiting near-infrared astrometry in the Galactic Centre?” In: *MNRAS* 401.2, pp. 1177–1188.

Fritz, T. K. et al. (Apr. 2016). “The Nuclear Cluster of the Milky Way: Total Mass and Luminosity”. In: *The Astrophysical Journal* 821, 44, p. 44. DOI: 10.3847/0004-637X/821/1/44. arXiv: 1406.7568.

Gaia Collaboration et al. (Aug. 2018). “Gaia Data Release 2. Mapping the Milky Way disc kinematics”. In: *Astronomy & Astrophysics* 616, A11, A11. DOI: 10.1051/0004-6361/201832865. arXiv: 1804.09380.

Genzel, R., Eisenhauer, F., and Gillessen, S. (Oct. 2010). “The Galactic Center massive black hole and nuclear star cluster”. In: *Reviews of Modern Physics* 82, pp. 3121–3195. DOI: 10.1103/RevModPhys.82.3121. arXiv: 1006.0064.

Genzel, R et al. (Oct. 2003). “Near-infrared flares from accreting gas around the supermassive black hole at the Galactic Centre”. In: *Nature* 425.6, pp. 934–937.

Ghez, A. M., Klein, B. L., Morris, M., and Becklin, E. E. (Dec. 1998). “High Proper-Motion Stars in the Vicinity of Sagittarius A*: Evidence for a Supermassive Black Hole at the Center of Our Galaxy”. In: *The Astrophysical*

Journal 509.2, pp. 678–686. DOI: 10.1086/306528. arXiv: astro-ph/9807210 [astro-ph].

Ghez, A. M. et al. (Sept. 2003a). "Full Three Dimensional Orbits For Multiple Stars on Close Approaches to the Central Supermassive Black Hole". In: *Astronomische Nachrichten Supplement* 324, pp. 527–533. DOI: 10.1002/asna.200385103. eprint: astro-ph/0303151.

Ghez, A. M. et al. (Apr. 2003b). "The First Measurement of Spectral Lines in a Short-Period Star Bound to the Galaxy's Central Black Hole: A Paradox of Youth". In: *The Astrophysical Journal Letters* 586.2, pp. L127–L131. DOI: 10.1086/374804. arXiv: astro-ph/0302299 [astro-ph].

Ghez, A. M. et al. (Feb. 2005). "Stellar Orbits around the Galactic Center Black Hole". In: *The Astrophysical Journal* 620.2, pp. 744–757. DOI: 10.1086/427175. arXiv: astro-ph/0306130 [astro-ph].

Ghez, A. M. et al. (Dec. 2008). "Measuring Distance and Properties of the Milky Way's Central Supermassive Black Hole with Stellar Orbits". In: *The Astrophysical Journal* 689, pp. 1044–1062. DOI: 10.1086/592738. arXiv: 0808.2870.

Gil, J. J. (Oct. 2004). "A unified model for polarimetric magnitudes". In: *5th Iberoamerican Meeting on Optics and 8th Latin American Meeting on Optics, Lasers, and Their Applications*. Ed. by Aristides Marcano O. and Jose Luis Paz. Vol. 5622. Society of Photo-Optical Instrumentation Engineers (SPIE) Conference Series, pp. 725–730. DOI: 10.1117/12.592194.

Gillessen, S. et al. (Feb. 2009a). "Monitoring Stellar Orbits Around the Massive Black Hole in the Galactic Center". In: *The Astrophysical Journal* 692, pp. 1075–1109. DOI: 10.1088/0004-637X/692/2/1075. arXiv: 0810.4674.

Gillessen, S. et al. (Dec. 2009b). "The Orbit of the Star S2 Around SGR A* from Very Large Telescope and Keck Data". In: *The Astrophysical Journal Letters* 707.2, pp. L114–L117. DOI: 10.1088/0004-637X/707/2/L114. arXiv: 0910.3069 [astro-ph.GA].

Gillessen, S. et al. (Mar. 2017). "An Update on Monitoring Stellar Orbits in the Galactic Center". In: *The Astrophysical Journal* 837, 30, p. 30. DOI: 10.3847/1538-4357/aa5c41. arXiv: 1611.09144.

Gillessen, Stefan et al. (July 2012). "GRAVITY: metrology". In: *Optical and Infrared Interferometry III*. Ed. by Françoise Delplancke, Jayadev K. Rajagopal, and Fabien Malbet. Vol. 8445. Society of Photo-Optical Instrumentation Engineers (SPIE) Conference Series, 84451O, 84451O. DOI: 10.1117/12.926813. arXiv: 1209.2624 [astro-ph.IM].

Gitton, Ph. and Wilhelm, R. (2003). "Determination of the field and pupil rotation in the VLTI laboratory". In: *ESO Documentation* VLT-TRE-ESO-15000-3092.

Glindemann, Andreas (2011). *Principles of Stellar Interferometry*. DOI: 10.1007/978-3-642-15028-9.

Godone, A., Novero, C., and Tavella, P. (Jan. 1995). "Null gravitational redshift experiment with nonidentical atomic clocks". In: *Physical Review D* 51, pp. 319–323. DOI: 10.1103/PhysRevD.51.319.

Gravity Collaboration et al. (June 2017). "First light for GRAVITY: Phase referencing optical interferometry for the Very Large Telescope Interferometer". In: *Astronomy and Astrophysics* 602, A94, A94. DOI: 10.1051/0004-6361/201730838. arXiv: 1705.02345 [astro-ph.IM].

Gravity Collaboration et al. (Oct. 2018a). "Detection of orbital motions near the last stable circular orbit of the massive black hole SgrA*". In: *Astronomy & Astrophysics* 618, L10, p. L10. DOI: 10.1051/0004-6361/201834294. arXiv: 1810.12641 [astro-ph.GA].

Gravity Collaboration et al. (July 2018b). "Detection of the gravitational redshift in the orbit of the star S2 near the Galactic centre massive black hole". In: *Astronomy and Astrophysics* 615, L15, p. L15. DOI: 10.1051/0004-6361/201833718. arXiv: 1807.09409.

Gravity Collaboration et al. (May 2019). "A geometric distance measurement to the Galactic center black hole with 0.3% uncertainty". In: *Astronomy & Astrophysics* 625, L10, p. L10. DOI: 10.1051/0004-6361/201935656. arXiv: 1904.05721 [astro-ph.GA].

Gravity Collaboration et al. (Apr. 2020a). "Detection of the Schwarzschild precession in the orbit of the star S2 near the Galactic centre massive black hole". In: *Astronomy & Astrophysics* 636, L5, p. L5. DOI: 10.1051/0004-6361/202037813. arXiv: 2004.07187 [astro-ph.GA].

Gravity Collaboration et al. (Nov. 2020b). "Dynamically important magnetic fields near the event horizon of Sgr A*". In: *Astronomy & Astrophysics* 643, A56, A56. DOI: 10.1051/0004-6361/202038283. arXiv: 2009.01859 [astro-ph.HE].

Gravity Collaboration et al. (Mar. 2020c). "Modeling the orbital motion of Sgr A*'s near-infrared flares". In: *Astronomy & Astrophysics* 635, A143, A143. DOI: 10.1051/0004-6361/201937233. arXiv: 2002.08374 [astro-ph.HE].

Gravity Collaboration et al. (Jan. 2020d). "Peering into the formation history of β Pictoris b with VLTI/GRAVITY long-baseline interferometry". In: *Astronomy & Astrophysics* 633, A110, A110. DOI: 10.1051/0004-6361/201936898. arXiv: 1912.04651 [astro-ph.EP].

Gravity Collaboration et al. (June 2020e). "The flux distribution of Sgr A*". In: *Astronomy & Astrophysics* 638, A2, A2. DOI: 10.1051/0004-6361/202037717. arXiv: 2004.07185 [astro-ph.GA].

Gravity Collaboration et al. (Jan. 2021). "Detection of faint stars near Sagittarius A* with GRAVITY". In: *Astronomy & Astrophysics* 645, A127, A127. DOI: 10.1051/0004-6361/202039544. arXiv: 2011.03058 [astro-ph.GA].

Grould, M., Vincent, F. H., Paumard, T., and Perrin, G. (Dec. 2017). "General relativistic effects on the orbit of the S2 star with GRAVITY". In: *Astronomy*

& Astrophysics 608, A60, A60. DOI: 10.1051/0004-6361/201731148. arXiv: 1709.04492 [astro-ph.HE].

Gualandris, A, Gillessen, S, and Merritt, D (Dec. 2010). "The Galactic Centre star S2 as a dynamical probe for intermediate-mass black holes". In: *MNRAS* 409.3, pp. 1146–1154.

Guesten, R. et al. (July 1987). "Aperture Synthesis Observations of the Circumnuclear Ring in the Galactic Center". In: *The Astrophysical Journal* 318, p. 124. DOI: 10.1086/165355.

Habibi, M. et al. (Oct. 2017). "Twelve Years of Spectroscopic Monitoring in the Galactic Center: The Closest Look at S-stars near the Black Hole". In: *Astrophysical Journal* 847, 120, p. 120. DOI: 10.3847/1538-4357/aa876f. arXiv: 1708.06353 [astro-ph.SR].

Hamaker, J. P. (May 2000). "Understanding radio polarimetry. IV. The full-coherency analogue of scalar self-calibration: Self-alignment, dynamic range and polarimetric fidelity". In: *Astronomy and Astrophysics, Supplement* 143, pp. 515–534. DOI: 10.1051/aas:2000337.

Hamaus, N. et al. (Feb. 2009). "Prospects for Testing the Nature of Sgr A*'s Near-Infrared Flares on the Basis of Current Very Large Telescope and Future Very Large Telescope Interferometer Observations". In: *The Astrophysical Journal* 692, pp. 902–916. DOI: 10.1088/0004-637X/692/1/902. arXiv: 0810.4947.

Harrington, David M., Sueoka, Stacey R., and White, Amanda J. (July 2019). "Polarization modeling and predictions for Daniel K. Inouye Solar Telescope part 5: impacts of enhanced mirror and dichroic coatings on system polarization calibration". In: *Journal of Astronomical Telescopes, Instruments, and Systems* 5, 038001, p. 038001. DOI: 10.1117/1.JATIS.5.3.038001. arXiv: 1905.10370 [astro-ph.IM].

Haubois, X. et al. (Aug. 2019). "The inner dust shell of Betelgeuse detected by polarimetric aperture-masking interferometry". In: *Astronomy & Astrophysics* 628, A101, A101. DOI: 10.1051/0004-6361/201833258. arXiv: 1907.08594 [astro-ph.SR].

Hayes, C. R., Law, D. R., and Majewski, S. R. (Nov. 2018). "Constraining the Solar Galactic Reflex Velocity using Gaia Observations of the Sagittarius Stream". In: *The Astrophysical Journal Letters* 867, L20, p. L20. DOI: 10.3847/2041-8213/aae9dd. arXiv: 1809.07654.

Hills, J. G. (Mar. 1975). "Possible power source of Seyfert galaxies and QSOs". In: *Nature* 254, pp. 295–298. DOI: 10.1038/254295a0.

Hobbs, Alexander and Nayakshin, Sergei (Mar. 2009). "Simulations of the formation of stellar discs in the Galactic Centre via cloud-cloud collisions". In: *Monthly Notice of the Royal Astronomical Society* 394.1, pp. 191–206. DOI: 10.1111/j.1365-2966.2008.14359.x. arXiv: 0809.3752 [astro-ph].

Högbom, J. A. (June 1974). "Aperture Synthesis with a Non-Regular Distribution of Interferometer Baselines". In: *Astronomy and Astrophysics, Supplement* 15, p. 417.

Hrynevych, Michael A., Ligon Edgar R., III, and Colavita, M. M. (Oct. 2004). "Baseline monitoring for astrometric interferometry". In: *New Frontiers in Stellar Interferometry*. Ed. by Wesley A. Traub. Vol. 5491. Society of Photo-Optical Instrumentation Engineers (SPIE) Conference Series, p. 1649. DOI: `10.1117/12.552320`.

Hunziker, S. et al. (Apr. 2021). "HD 142527: quantitative disk polarimetry with SPHERE". In: *Astronomy & Astrophysics* 648, A110, A110. DOI: `10.1051/0004-6361/202040166`. arXiv: `2103.08462 [astro-ph.EP]`.

Hutter, Donald J. and Elias Nicholas M., II (Feb. 2003). "Array metrology system for an optical long-baseline interferometer". In: *Interferometry for Optical Astronomy II*. Ed. by Wesley A. Traub. Vol. 4838. Society of Photo-Optical Instrumentation Engineers (SPIE) Conference Series, pp. 1234–1245. DOI: `10.1117/12.459763`.

Ireland, M. J., Tuthill, P. G., Davis, J., and Tango, W. (July 2005). "Dust scattering in the Miras R Car and RR Sco resolved by optical interferometric polarimetry". In: *Monthly Notice of the Royal Astronomical Society* 361.1, pp. 337–344. DOI: `10.1111/j.1365-2966.2005.09181.x`. arXiv: `astro-ph/0505112 [astro-ph]`.

Issaoun, S. et al. (Jan. 2019). "The Size, Shape, and Scattering of Sagittarius A* at 86 GHz: First VLBI with ALMA". In: *The Astrophysical Journal* 871.1, 30, p. 30. DOI: `10.3847/1538-4357/aaf732`. arXiv: `1901.06226 [astro-ph.HE]`.

Jenkins, R. E. (Sept. 1969). "A Satellite Observation of the Relativistic Doppler Shift". In: *Astronomical Journal* 74, p. 960. DOI: `10.1086/110889`.

Jocou, L. et al. (July 2014). "The beam combiners of Gravity VLTI instrument: concept, development, and performance in laboratory". In: *Optical and Infrared Interferometry IV*. Ed. by Jayadev K. Rajagopal, Michelle J. Creech-Eakman, and Fabien Malbet. Vol. 9146. Society of Photo-Optical Instrumentation Engineers (SPIE) Conference Series, 91461J, 91461J. DOI: `10.1117/12.2054159`.

Johnson, M. D. et al. (Dec. 2017). "Dynamical Imaging with Interferometry". In: *Astrophysical Journal* 850, 172, p. 172. DOI: `10.3847/1538-4357/aa97dd`. arXiv: `1711.01286 [astro-ph.IM]`.

Keller, Christoph U. (Jan. 2002). "Instrumentation for astrophysical spectropolarimetry". In: *Astrophysical Spectropolarimetry*. Ed. by J. Trujillo-Bueno, F. Moreno-Insertis, and F. Sánchez, pp. 303–354.

Kendrew, S. et al. (Sept. 2012). "GRAVITY Coudé Infrared Adaptive Optics (CIAO) system for the VLT Interferometer". In: *Ground-based and Airborne Instrumentation for Astronomy IV*. Ed. by Ian S. McLean, Suzanne K. Ramsay, and Hideki Takami. Vol. 8446. Society of Photo-Optical Instrumentation Engineers (SPIE) Conference Series, 84467W, 84467W. DOI: 10.1117/12.926558. arXiv: 1207.2945 [astro-ph.IM].

Krichbaum, T. P. et al. (July 1993). "First 43 GHz VLBI detection of the compact source SGR A in the Galactic Center." In: *Astronomy & Astrophysics* 274, pp. L37–L40.

Krichbaum, T. P. et al. (July 1998). "VLBI observations of the galactic center source SGR A* at 86 GHz and 215 GHz". In: *Astronomy and Astrophysics* 335, pp. L106–L110.

Krisher, T. P., Anderson, J. D., and Campbell, J. K. (Mar. 1990). "Test of the gravitational redshift effect at Saturn". In: *Physical Review Letters* 64, pp. 1322–1325. DOI: 10.1103/PhysRevLett.64.1322.

Lacour, S. et al. (July 2014). "Reaching micro-arcsecond astrometry with long baseline optical interferometry. Application to the GRAVITY instrument". In: *Astronomy & Astrophysics* 567, A75, A75. DOI: 10.1051/0004-6361/201423940. arXiv: 1404.1014 [astro-ph.IM].

Lacour, S. et al. (Apr. 2019). "The GRAVITY fringe tracker". In: *Astronomy & Astrophysics* 624, A99, A99. DOI: 10.1051/0004-6361/201834981. arXiv: 1901.03202 [astro-ph.IM].

Lacy, J. H., Townes, C. H., Geballe, T. R., and Hollenbach, D. J. (Oct. 1980). "Observations of the motion and distribution of the ionized gas in the central parsec of the Galaxy. II." In: *The Astrophysical Journal* 241, pp. 132–146. DOI: 10.1086/158324.

Layden, D., Wood, M. F. G., and Vitkin, I. A. (Aug. 2012). "Optimum selection of input polarization states in determining the sample Mueller matrix: a dual photoelastic polarimeter approach". In: *Optics Express* 20.18, p. 20466. DOI: 10.1364/OE.20.020466.

Lazareff, B., Blind, N., Jocou, L., and Schoeller, M (2014a). "Measurement of the Jones matrix of the VLTI/UT from laboratory to M9". In: *ESO Documentation* VLT-TRE-GRA-15884-6513.

Lazareff, B. et al. (2014b). "Telescope birefringence and phase errors in the Gravity instrument at the VLT interferometer". In: *Proc. SPIE*. Society of Photo-Optical Instrumentation Engineers (SPIE) Conference Series 9146, 91460X, p. 91460X. DOI: 10.1117/12.2056304.

Lenzen, R., Hofmann, R., Bizenberger, P., and Tusche, A. (Aug. 1998). "CONICA: the high-resolution near-infrared camera for the ESO VLT". In: *Infrared Astronomical Instrumentation*. Ed. by A. M. Fowler. Vol. 3354. Proceedings of the SPIE, pp. 606–614. DOI: 10.1117/12.317287.

Lindegren, Lennart and Dravins, Dainis (Apr. 2003). "The fundamental definition of "radial velocity"". In: *Astronomy & Astrophysics* 401, pp. 1185–1201. DOI: 10.1051/0004-6361:20030181. arXiv: astro-ph/0302522 [astro-ph].

Lippa, Magdalena et al. (Aug. 2016). "The metrology system of the VLTI instrument GRAVITY". In: *Optical and Infrared Interferometry and Imag-*

ing V. Ed. by Fabien Malbet, Michelle J. Creech-Eakman, and Peter G. Tuthill. Vol. 9907. Society of Photo-Optical Instrumentation Engineers (SPIE) Conference Series, 990722, p. 990722. DOI: 10.1117/12.2232272. arXiv: 1608.04888 [astro-ph.IM].

Lippa, Magdalena et al. (July 2018). "Learnings from the use of fiber optics in GRAVITY". In: *Optical and Infrared Interferometry and Imaging VI*. Ed. by Michelle J. Creech-Eakman, Peter G. Tuthill, and Antoine Mérand. Vol. 10701. Society of Photo-Optical Instrumentation Engineers (SPIE) Conference Series, 107011Y, 107011Y. DOI: 10.1117/12.2312477.

Lo, K. Y. and Claussen, M. J. (Dec. 1983). "High-resolution observations of ionized gas in central 3 parsecs of the Galaxy: possible evidence for infall". In: *Nature* 306.5944, pp. 647–651. DOI: 10.1038/306647a0.

Lopresto, J. C., Schrader, C., and Pierce, A. K. (Aug. 1991). "Solar gravitational redshift from the infrared oxygen triplet". In: *Astrophysical Journal* 376, pp. 757–760. DOI: 10.1086/170323.

Lu, J. R. et al. (Dec. 2006). "Galactic Center Youth: Orbits and Origins of the Young Stars in the Central Parsec". In: *Journal of Physics Conference Series*. Vol. 54. Journal of Physics Conference Series, pp. 279–287. DOI: 10.1088/1742-6596/54/1/044.

Lu, J. R. et al. (Jan. 2009). "A Disk of Young Stars at the Galactic Center as Determined by Individual Stellar Orbits". In: *The Astrophysical Journal* 690.2, pp. 1463–1487. DOI: 10.1088/0004-637X/690/2/1463. arXiv: 0808.3818 [astro-ph].

Lynden-Bell, D. and Rees, M. J. (Jan. 1971). "On quasars, dust and the galactic centre". In: *Monthly Notice of the Royal Astronomical Society* 152, p. 461. DOI: 10.1093/mnras/152.4.461.

Marconi, A. et al. (Aug. 2016). "EELT-HIRES the high-resolution spectrograph for the E-ELT". In: *Ground-based and Airborne Instrumentation for Astronomy VI*. Vol. 9908. Proceedings of the SPIE, 990823, p. 990823. DOI: 10.1117/12.2231653. arXiv: 1609.00497 [astro-ph.IM].

Martins, F. et al. (Jan. 2008). "On the Nature of the Fast-Moving Star S2 in the Galactic Center". In: *Astrophysical Journal, Letters* 672, p. L119. DOI: 10.1086/526768. arXiv: 0711.3344.

McGaugh, S. S. (Aug. 2018). "A Precise Milky Way Rotation Curve Model for an Accurate Galactocentric Distance". In: *Research Notes of the American Astronomical Society* 2.3, 156, p. 156. DOI: 10.3847/2515-5172/aadd4b. arXiv: 1808.09435.

Merritt, D., Berczik, P., and Laun, F. (Feb. 2007). "Brownian Motion of Black Holes in Dense Nuclei". In: *Astronomical Journal* 133, pp. 553–563. DOI: 10.1086/510294. eprint: astro-ph/0408029.

Meyer, L. et al. (Oct. 2012). "The Shortest-Known-Period Star Orbiting Our Galaxys Supermassive Black Hole". In: *Science* 338, p. 84. DOI: 10.1126/science.1225506. arXiv: 1210.1294.

Michel, A. (2000). “MIRROR POSITIONS AND DISTANCES IN THE VLT UT COUDE”. In: *ESO Documentation* VLT-TRE-ESO-15000-2165.

Monnier, John D. (May 2003). “Optical interferometry in astronomy”. In: *Reports on Progress in Physics* 66.5, pp. 789–857. DOI: 10.1088/0034-4885/66/5/203. arXiv: astro-ph/0307036 [astro-ph].

Monnier, John D. and Allen, Ronald J. (2013). “Radio and Optical Interferometry: Basic Observing Techniques and Data Analysis”. In: *Planets, Stars and Stellar Systems. Volume 2: Astronomical Techniques, Software and Data*. Ed. by Terry D. Oswalt and Howard E. Bond, p. 325. DOI: 10.1007/978-94-007-5618-2_7.

Montero-Castaño, María, Herrnstein, Robeson M., and Ho, Paul T. P. (Apr. 2009). “Gas Infall Toward Sgr A* from the Clumpy Circumnuclear Disk”. In: *The Astrophysical Journal* 695.2, pp. 1477–1494. DOI: 10.1088/0004-637X/695/2/1477. arXiv: 0903.0886 [astro-ph.GA].

Mróz, P. et al. (Jan. 2019). “Rotation Curve of the Milky Way from Classical Cepheids”. In: *The Astrophysical Journal Letters* 870, L10, p. L10. DOI: 10.3847/2041-8213/aaf73f. arXiv: 1810.02131.

Neumann, Ernst-Georg (1988). *Single-mode fibers*.

Norris, Barnaby R. M. et al. (Apr. 2012a). “A close halo of large transparent grains around extreme red giant stars”. In: *Nature* 484.7393, pp. 220–222. DOI: 10.1038/nature10935. arXiv: 1204.2640 [astro-ph.SR].

Norris, Barnaby R. M. et al. (July 2012b). “Probing dusty circumstellar environments with polarimetric aperture-masking interferometry”. In: *Optical and Infrared Interferometry III*. Ed. by Françoise Delplancke, Jayadev K. Rajagopal, and Fabien Malbet. Vol. 8445. Society of Photo-Optical Instrumentation Engineers (SPIE) Conference Series, 844503, p. 844503. DOI: 10.1117/12.925838.

Norris, Barnaby et al. (Mar. 2015). “The VAMPIRES instrument: imaging the innermost regions of protoplanetary discs with polarimetric interferometry”. In: *Monthly Notice of the Royal Astronomical Society* 447.3, pp. 2894–2906. DOI: 10.1093/mnras/stu2529.

Ong, A., Berengut, J. C., and Flambaum, V. V. (Nov. 2013). “Measuring chemical evolution and gravitational dependence of α using ultraviolet Fe v and Ni v transitions in white-dwarf spectra”. In: *PhysicalReview A: General Physics* 88.5, 052517, p. 052517. DOI: 10.1103/PhysRevA.88.052517. arXiv: 1310.2685 [physics.atom-ph].

Osterbrock, Donald E. et al. (Mar. 1996). “Night-Sky High-Resolution Spectral Atlas of OH and O2 Emission Lines for Echelle Spectrograph Wavelength Calibration”. In: *The Publications of the Astronomical Society of the Pacific* 108, p. 277. DOI: 10.1086/133722.

Ott, Thomas, Eckart, Andreas, and Genzel, Reinhard (Sept. 1999). “Variable and Embedded Stars in the Galactic Center”. In: *The Astrophysical Journal* 523.1, pp. 248–264. DOI: 10.1086/307712.

Paumard, T., Maillard, J. P., and Morris, M. (Oct. 2004). "Kinematic and structural analysis of the <ASTROBJ>Minispiral</ASTROBJ> in the Galactic Center from BEAR spectro-imagery". In: *Astronomy & Astrophysics* 426, pp. 81–96. DOI: 10.1051/0004-6361:20034209. arXiv: astro-ph/0405197 [astro-ph].

Peil, S., Crane, S., Hanssen, J. L., Swanson, T. B., and Ekstrom, C. R. (Jan. 2013). "Tests of local position invariance using continuously running atomic clocks". In: *PhysicalReview A: General Physics* 87.1, 010102, p. 010102. DOI: 10.1103/PhysRevA.87.010102. arXiv: 1301.6145 [physics.atom-ph].

Perraut, K. and Berger, J. P. (2010). "Polarization Analysis". In: *ESO Documentation* VLT-TRE-GRA-15884-3202.

Perraut, K. et al. (June 2018). "Single-mode waveguides for GRAVITY. I. The cryogenic 4-telescope integrated optics beam combiner". In: *Astronomy & Astrophysics* 614, A70, A70. DOI: 10.1051/0004-6361/201732544.

Perrin, G. and Woillez, J. (May 2019). "Single-mode interferometric field of view in partial turbulence correction. Application to the observation of the environment of Sgr A* with GRAVITY". In: *Astronomy & Astrophysics* 625, A48, A48. DOI: 10.1051/0004-6361/201834013. arXiv: 1903.10937 [astro-ph.IM].

Pfuhl, O. et al. (July 2014). "The fiber coupler and beam stabilization system of the GRAVITY interferometer". In: *Proc. SPIE*. Vol. 9146. Society of Photo-Optical Instrumentation Engineers (SPIE) Conference Series, 914623, p. 914623. DOI: 10.1117/12.2055080. arXiv: 1412.1696 [astro-ph.IM].

Plewa, P. M. and Sari, R. (June 2018). "Unrecognized astrometric confusion in the Galactic Centre". In: *Monthly Notice of the Royal Astronomical Society* 476, pp. 4372–4382. DOI: 10.1093/mnras/sty512. arXiv: 1802.08043.

Plewa, P. M. et al. (Nov. 2015). "Pinpointing the near-infrared location of Sgr A* by correcting optical distortion in the NACO imager". In: *Monthly Notices of the RAS* 453, pp. 3234–3244. DOI: 10.1093/mnras/stv1910. arXiv: 1509.01941.

Pound, R. V. and Rebka, G. A. (Nov. 1959). "Gravitational Red-Shift in Nuclear Resonance". In: *Physical Review Letters* 3, pp. 439–441. DOI: 10.1103/PhysRevLett.3.439.

Pound, R. V. and Snider, J. L. (Nov. 1965). "Effect of Gravity on Gamma Radiation". In: *Physical Review* 140, pp. 788–803. DOI: 10.1103/PhysRev.140.B788.

Reddy, Salla Gangi et al. (Mar. 2014). "Measuring the Mueller matrix of an arbitrary optical element with a universal SU(2) polarization gadget". In: *Journal of the Optical Society of America A* 31.3, p. 610. DOI: 10.1364/JOSAA.31.000610. arXiv: 1211.2416 [physics.optics].

Reid, M. J. (2009). "Is There a Supermassive Black Hole at the Center of the Milky Way?" In: *International Journal of Modern Physics D* 18, pp. 889–910. DOI: 10.1142/S0218271809014820. arXiv: 0808.2624.

Reid, M. J. and Brunthaler, A. (Dec. 2004). “The Proper Motion of Sagittarius A*. II. The Mass of Sagittarius A*”. In: *Astrophysical Journal* 616, pp. 872–884. DOI: 10.1086/424960. eprint: astro-ph/0408107.

Reid, M. J., Menten, K. M., Trippe, S., Ott, T., and Genzel, R. (Apr. 2007). “The Position of Sagittarius A*. III. Motion of the Stellar Cusp”. In: *Astrophysical Journal* 659, pp. 378–388. DOI: 10.1086/511744. eprint: astro-ph/0612164.

Reid, M. J. et al. (July 2009). “Trigonometric Parallaxes of Massive Star-Forming Regions. VI. Galactic Structure, Fundamental Parameters, and Noncircular Motions”. In: *The Astrophysical Journal* 700, pp. 137–148. DOI: 10.1088/0004-637X/700/1/137. arXiv: 0902.3913 [astro-ph.GA].

Reid, M. J. et al. (Mar. 2014). “Trigonometric Parallaxes of High Mass Star Forming Regions: The Structure and Kinematics of the Milky Way”. In: *The Astrophysical Journal* 783, 130, p. 130. DOI: 10.1088/0004-637X/783/2/130. arXiv: 1401.5377 [astro-ph.GA].

Reid, M. J. et al. (Nov. 2019). “Trigonometric Parallaxes of High-mass Star-forming Regions: Our View of the Milky Way”. In: *The Astrophysical Journal* 885.2, 131, p. 131. DOI: 10.3847/1538-4357/ab4a11. arXiv: 1910.03357 [astro-ph.GA].

Roddier, F. (Jan. 1981). “The effects of atmospheric turbulence in optical astronomy”. In: *Progess in Optics* 19, pp. 281–376. DOI: 10.1016/S0079-6638(08)70204-X.

Rousselet-Perraut, K. et al. (June 2006). “First sky validation of an optical polarimetric interferometer”. In: *Astronomy & Astrophysics* 451.3, pp. 1133–1137. DOI: 10.1051/0004-6361:20054296.

Rousselet-Perraut, Karine, Vakili, Farrokh, and Mourard, Denis (Oct. 1996). “Polarization effects in stellar interferometry”. In: *Optical Engineering* 35, pp. 2943–2955. DOI: 10.1117/1.600978.

Rousselot, P., Lidman, C., Cuby, J.-G., Moreels, G., and Monnet, G. (Feb. 2000). “Night-sky spectral atlas of OH emission lines in the near-infrared”. In: *Astronomy & Astrophysics* 354, pp. 1134–1150.

Rousset, G. et al. (Sept. 1998). “Design of the Nasmyth adaptive optics system (NAOS) of the VLT”. In: *Adaptive Optical System Technologies*. Ed. by D. Bonaccini and R. K. Tyson. Vol. 3353. Proceedings of the SPIE, pp. 508–516. DOI: 10.1117/12.321686.

Rousset, Gerard et al. (Feb. 2003). “NAOS, the first AO system of the VLT: on-sky performance”. In: *Adaptive Optical System Technologies II*. Ed. by Peter L. Wizinowich and Domenico Bonaccini. Vol. 4839. Society of Photo-Optical Instrumentation Engineers (SPIE) Conference Series, pp. 140–149. DOI: 10.1117/12.459332.

Sabatke, D. S. et al. (June 2000). “Optimization of retardance for a complete Stokes polarimeter”. In: *Optics Letters* 25.11, pp. 802–804. DOI: 10.1364/OL.25.000802.

Schiff, L. I. (Apr. 1960). “On Experimental Tests of the General Theory of Relativity”. In: *American Journal of Physics* 28, pp. 340–343. DOI: 10.1119/1.1935800.

Schödel, R., Merritt, D., and Eckart, A. (July 2009). “The nuclear star cluster of the Milky Way: proper motions and mass”. In: *Astronomy and Astrophysics* 502, pp. 91–111. DOI: 10.1051/0004-6361/200810922. arXiv: 0902.3892.

Schödel, R. et al. (Oct. 2002). “A star in a 15.2-year orbit around the supermassive black hole at the centre of the Milky Way”. In: *Nature* 419, pp. 694–696. DOI: 10.1038/nature01121. eprint: astro-ph/0210426.

Schödel, R. et al. (Oct. 2003). “Stellar Dynamics in the Central Arcsecond of Our Galaxy”. In: *The Astrophysical Journal* 596.2, pp. 1015–1034. DOI: 10.1086/378122. arXiv: astro-ph/0306214 [astro-ph].

Schönrich, R., Binney, J., and Dehnen, W. (Apr. 2010). “Local kinematics and the local standard of rest”. In: *Monthly Notice of the Royal Astronomical Society* 403, pp. 1829–1833. DOI: 10.1111/j.1365-2966.2010.16253.x. arXiv: 0912.3693.

Schreiber, J. et al. (July 2004). “Data Reduction Software for the VLT Integral Field Spectrometer SPIFFI”. In: *Astronomical Data Analysis Software and Systems (ADASS) XIII*. Ed. by Francois Ochsenbein, Mark G. Allen, and Daniel Egret. Vol. 314. Astronomical Society of the Pacific Conference Series, p. 380.

Setterholm, Benjamin R. et al. (Dec. 2020). “MIRC-X polarinterferometry at CHARA”. In: *Society of Photo-Optical Instrumentation Engineers (SPIE) Conference Series*. Vol. 11446. Society of Photo-Optical Instrumentation Engineers (SPIE) Conference Series, 114460R, 114460R. DOI: 10.1117/12.2562407.

Shao, M. and Colavita, M. M. (Aug. 1992). “Potential of long-baseline infrared interferometry for narrow-angle astrometry”. In: *Astronomy & Astrophysics* 262.1, pp. 353–358.

Shen, Zhi-Qiang, Lo, K. Y., Liang, M. C., Ho, Paul T. P., and Zhao, J. H. (Nov. 2005). “A size of ~1AU for the radio source Sgr A* at the centre of the Milky Way”. In: *Nature* 438.7064, pp. 62–64. DOI: 10.1038/nature04205. arXiv: astro-ph/0512515 [astro-ph].

Smirnov, O. M. (Mar. 2011). “Revisiting the radio interferometer measurement equation. II. Calibration and direction-dependent effects”. In: *Astronomy & Astrophysics* 527, A107, A107. DOI: 10.1051/0004-6361/201116434. arXiv: 1101.1765 [astro-ph.IM].

Smirnov, O. M. and Tasse, C. (May 2015). “Radio interferometric gain calibration as a complex optimization problem”. In: *Monthly Notice of the Royal Astronomical Society* 449.3, pp. 2668–2684. DOI: 10.1093/mnras/stv418. arXiv: 1502.06974 [astro-ph.IM].

Snider, J. L. (Mar. 1972). "New Measurement of the Solar Gravitational Red Shift". In: *Physical Review Letters* 28, pp. 853–856. DOI: 10.1103/PhysRevLett.28.853.

Straubmeier, Christian et al. (2014). "The GRAVITY spectrometers: optical design and first light". In: *Proc. SPIE*. Society of Photo-Optical Instrumentation Engineers (SPIE) Conference Series 9146, 914629, p. 914629. DOI: 10.1117/12.2054736.

Tasse, C. et al. (Apr. 2018). "Faceting for direction-dependent spectral deconvolution". In: *Astronomy & Astrophysics* 611, A87, A87. DOI: 10.1051/0004-6361/201731474. arXiv: 1712.02078 [astro-ph.IM].

Tecza, Matthias et al. (Aug. 2000). "SPIFFI image slicer: revival of image slicing with plane mirrors". In: *Optical and IR Telescope Instrumentation and Detectors*. Ed. by Masanori Iye and Alan F. Moorwood. Vol. 4008. Society of Photo-Optical Instrumentation Engineers (SPIE) Conference Series, pp. 1344–1350. DOI: 10.1117/12.395451. arXiv: astro-ph/0008322 [astro-ph].

Thompson, A. Richard, Moran, James M., and Swenson George W., Jr. (2017). *Interferometry and Synthesis in Radio Astronomy, 3rd Edition*. DOI: 10.1007/978-3-319-44431-4.

Tinbergen, Jaap (1996). *Astronomical Polarimetry*.

— (2005). *Astronomical Polarimetry*.

Trippe, Sascha (Feb. 2014). "[Review] Polarization and Polarimetry". In: *Journal of Korean Astronomical Society* 47.1, pp. 15–39. DOI: 10.5303/JKAS.2014.47.1.015. arXiv: 1401.1911 [astro-ph.IM].

Tsuboi, Masato et al. (June 2017). "ALMA View of the Galactic Center Minispiral: Ionized Gas Flows around Sagittarius A*". In: *The Astrophysical Journal* 842.2, 94, p. 94. DOI: 10.3847/1538-4357/aa74e3. arXiv: 1608.08714 [astro-ph.GA].

Turneaure, J. P., Will, C. M., Farrell, B. F., Mattison, E. M., and Vessot, R. F. C. (Apr. 1983). "Test of the principle of equivalence by a null gravitational red-shift experiment". In: *Physical Review D* 27, pp. 1705–1714. DOI: 10.1103/PhysRevD.27.1705.

Vessot, R. F. C. and Levine, M. W. (Feb. 1979). "A test of the equivalence principle using a space-borne clock". In: *General Relativity and Gravitation* 10, pp. 181–204. DOI: 10.1007/BF00759854.

Waisberg, Idel Reis (2019). "Optical interferometry of compact objects". URL: http://nbn-resolving.de/urn:nbn:de:bvb:19-245673.

Waisberg, Idel et al. (May 2018). "What stellar orbit is needed to measure the spin of the Galactic centre black hole from astrometric data?" In: *Monthly Notice of the Royal Astronomical Society* 476.3, pp. 3600–3610. DOI: 10.1093/mnras/sty476. arXiv: 1802.08198 [astro-ph.GA].

Wallace, L. and Hinkle, K. (Aug. 1997). "Medium-Resolution Spectra of Normal Stars in the K Band". In: *Astrophysical Journal, Supplement* 111, pp. 445–458. DOI: 10.1086/313020.

Wallner, Oswald, Leeb, Walter R., and Winzer, Peter J. (Dec. 2002). "Minimum length of a single-mode fiber spatial filter". In: *Journal of the Optical Society of America A* 19.12, pp. 2445–2448. DOI: 10.1364/JOSAA.19.002445.

Wegg, C., Gerhard, O., and Bieth, M. (May 2019). "The gravitational force field of the Galaxy measured from the kinematics of RR Lyrae in Gaia". In: *Monthly Notice of the Royal Astronomical Society* 485, pp. 3296–3316. DOI: 10.1093/mnras/stz572. arXiv: 1806.09635.

Will, C. M. (Mar. 1993). *Theory and Experiment in Gravitational Physics*, p. 396.

— (June 2014). "The Confrontation between General Relativity and Experiment". In: *Living Reviews in Relativity* 17, 4, p. 4. DOI: 10.12942/lrr-2014-4. arXiv: 1403.7377 [gr-qc].

Witzel, G. et al. (Jan. 2011). "The instrumental polarization of the Nasmyth focus polarimetric differential imager NAOS/CONICA (NACO) at the VLT. Implications for time-resolved polarimetric measurements of Sagittarius A*". In: *Astronomy & Astrophysics* 525, A130, A130. DOI: 10.1051/0004-6361/201015009. arXiv: 1010.4708 [astro-ph.IM].

Witzel, G. et al. (Aug. 2018). "Variability Timescale and Spectral Index of Sgr A* in the Near Infrared: Approximate Bayesian Computation Analysis of the Variability of the Closest Supermassive Black Hole". In: *The Astrophysical Journal* 863, 15, p. 15. DOI: 10.3847/1538-4357/aace62. arXiv: 1806.00479 [astro-ph.HE].

Wizinowich, Peter L. et al. (July 2000). "Performance of the W.M. Keck Observatory Natural Guide Star Adaptive Optic Facility: the first year at the telescope". In: *Adaptive Optical Systems Technology*. Ed. by Peter L. Wizinowich. Vol. 4007. Society of Photo-Optical Instrumentation Engineers (SPIE) Conference Series, pp. 2–13. DOI: 10.1117/12.390368.

Woillez, J. and Lacour, S. (Feb. 2013). "Wide-angle, Narrow-angle, and Imaging Baselines of Optical Long-baseline Interferometers". In: *The Astrophysical Journal* 764, 109, p. 109. DOI: 10.1088/0004-637X/764/1/109.

Woillez, J. et al. (Sept. 2019). "NAOMI: the adaptive optics system of the Auxiliary Telescopes of the VLTI". In: *Astronomy & Astrophysics* 629, A41, A41. DOI: 10.1051/0004-6361/201935890. arXiv: 1908.06651 [astro-ph.IM].

Wollman, E. R., Geballe, T. R., Lacy, J. H., Townes, C. H., and Rank, D. M. (Dec. 1977). "Ne II 12.8 micron emission from the galactic center. II." In: *The Astrophysical Journal Letters* 218, pp. L103–L107. DOI: 10.1086/182585.

Yelda, Sylvana et al. (Jan. 2013). "The Kinematic Structure of the Young Stellar Disk in the Galactic Center". In: *American Astronomical Society*

Meeting Abstracts #221. Vol. 221. American Astronomical Society Meeting Abstracts, 254.03, p. 254.03.

Zhao, Jun-Hui, Morris, Mark R., Goss, W. M., and An, Tao (July 2009). "Dynamics of Ionized Gas at the Galactic Center: Very Large Array Observations of the Three-dimensional Velocity Field and Location of the Ionized Streams in Sagittarius A West". In: *The Astrophysical Journal* 699.1, pp. 186–214. DOI: 10.1088/0004-637X/699/1/186. arXiv: 0904.3133 [astro-ph.GA].

de Boer, J. et al. (Jan. 2020). "Polarimetric imaging mode of VLT/SPHERE/IRDIS. I. Description, data reduction, and observing strategy". In: *Astronomy & Astrophysics* 633, A63, A63. DOI: 10.1051/0004-6361/201834989. arXiv: 1909.13107 [astro-ph.IM].

van Holstein, R. G. et al. (Jan. 2020). "Polarimetric imaging mode of VLT/-SPHERE/IRDIS. II. Characterization and correction of instrumental polarization effects". In: *Astronomy & Astrophysics* 633, A64, A64. DOI: 10.1051/0004-6361/201834996. arXiv: 1909.13108 [astro-ph.IM].

van de Ven, G., van den Bosch, R. C. E., Verolme, E. K., and de Zeeuw, P. T. (Jan. 2006). "The dynamical distance and intrinsic structure of the globular cluster ω Centauri". In: *Astronomy & Astrophysics* 445, pp. 513–543. DOI: 10.1051/0004-6361:20053061. eprint: astro-ph/0509228.

ACKNOWLEDGMENTS

I am very grateful for the help and support I have received from many people over the last years. First of all, I want to especially thank Prof. Reinhard Genzel for the supervision of my PhD and for the many opportunities the work in the infrared group has given me. The chance to celebrate a Nobel Price, travel to one of the world-leading observatories, and of course, work in this team on fantastic projects and science are opportunities I always cherish. I thank my advisors Frank Eisenhauer and Stefan Gillessen, for your great support over the last four years and that you always had an open door for my issues and fruitful discussions about my work. And of course, I want to thank the infrared group for the trust put into me to continue as a member of the GRAVITY+ team. I am very thankful that I can continue the adventure in the group and am looking forward to the many opportunities and challenges to come.

Many people have helped me over the last years, and they are too many to name everybody individually. I thank all the members of the infrared group from which I have always got great support, I thank the technical staff at MPE for the support with the IT, in the LAB, and especially for the support of experiments in Paranal and the many people in the institute (low- as well as high-energy) for the inspiring discussions. And of course, I thank everybody at Paranal who has worked with me, for the assistance in the on-site experiments, and of course for the support in many observing nights, in person and virtually.

Lastly, I want to thank my partner, my friends, and my family for the continuous support, understanding, and for always showing genuine interest in my work.